Analysis of Wave and Current Data in a Tidal Energy Test Site

Emmanuel Osalusi

Submitted for the degree of Doctor of Philosophy

Heriot-Watt University
Institute of Petroleum Engineering

April, 2010

Abstract

Characterisation of a tidal stream site before device deployment is important for the marine tidal industry, in order to optimise the device design and accurately predict its performance during operation. Understanding the short-term fluctuations in tidal stream velocity, resulting from turbulence and wave-current interactions, is essential for proper evaluation of the transient performance of a tidal stream turbine. Several aerodynamic models have been proposed for the design of tidal stream turbines and energy production calculation, most of which have proved to predict accurately mean quantities within the flow regime. Unfortunately, these models cannot accurately predict the instantaneous flow variation and resulting forces within the flow regime acting on tidal stream systems which is of central importance to the tidal energy industry. The reasons for this may not be unconnected to the significant differences between wind and tidal turbines. Given the uncertainties which exist in the assumptions of resource modelling and the need for an accurate energy capture assessment at a specific site, accurate on-site measurements that can predict the flow velocity (and its directional component) at a given location, are needed.

This thesis is devoted to characterisation of flow in a typical tidal stream site (the Fall of Warness, of the European Marine Energy Center (EMEC), Orkney) through measured data. The high-frequency Acoustic Doppler Current Profiler (ADCP) surveys were conducted at different locations within this site by EMEC. This dataset allows for the first time a statistical and thorough analysis of the vertical turbulence structure at the EMEC's tidal stream test site. Detailed analyses of the directional components of the wave fields using a non-phase-locked method and influences of seabed and tidal stream on wave fields, were performed. The bulk turbulence parameters within the tidal streams were estimated using the variance method. The results suggest a significant effect of directionality and short-term fluctuations in stream velocity resulting from turbulence and wave-current interactions, on the hydrodynamics in a typical tidal energy test site. The results from this study can be used to validate and improve/develop proposed hydrodynamic models and can play a vital role in tidal energy resource planning.

. . . most affectionately dedicated to Orkney Islands.

Acknowledgements

The completion of such strenuous a task as Ph.D. thesis research is impossible without adequate support, with which I was definitely blessed. First and foremost, I wish to thank my supervisor, Professor Jonathan Side for his enthusiastic supervision, advice and encouragement throughout the duration of this course of study. He has provided for an optimum working environment at the International Centre for Island Technology (ICIT), where a lack of resources is something unimaginable due to his managerial skills and foresight. His uncompromising quest for excellence significantly shapes everyone at the institute. I am also indebted to my co-supervisor, Dr. Robert Harris, who has been a source of inspiration and invaluable source of support throughout the duration of this course of study.

The PhD studentship award received from TOTAL E & P Ltd, Aberdeen (Dir. Scientifique), without which this research would not have even started, let alone be completed, is appreciated.

I would certainly like to thank all of the staff members of EMEC for providing the data and permitting its use in the thesis.

The discussions and cooperations with all of my colleagues have contributed substantially to this work. I am privileged to have been part of such a brilliant, stimulating and fun group of people as this one, which has done a lot to foster my creative growth. John Ruscoe has fearlessly attacked the most intricate of problems, drawing from a rich expertise in software engineering and numerics; Mark Wemyss and Bob Beharie have been helpful during this study, shaping my mind during many technical and non-technical discussions along the way. Piya (Zan) Parnphumeesup has put a lot of enthusiasm and energy into eliminating many shortcomings in various areas, closing the gap between academic research and practical applications.

I also extend my appreciation to all staff members of the ICIT for their assistance and support. I would be amiss not to mention the place where I have discovered the world

of both humour and acceptance; the Islands that gave me and my family the love, I am not sure, I could have received anywhere else. I truly appreciate all that I received from Orkney Islands.

Finally, last but not least, I want to thank my family for their generous part in making me who I am, without whom I would not have had all that it takes to succeed.

I wish to thank my dearest wife, Victoria, who made some important sacrifices to follow me to a new place, bore the cross of a postgraduate student's wife, took care of me, loved, endured and supported me through all the ups and downs during this study period. To her and Fortune I owe more than I can ever express.

ACADEMIC REGISTRY
Research Thesis Submission

Name:	Emmanuel Osalusi		
School/PGI:	Institute of Petroleum Engineering		
Version: *(i.e. First, Resubmission, Final)*		Degree Sought (Award **and** Subject area)	Ph.D

Declaration

In accordance with the appropriate regulations I hereby submit my thesis and I declare that:

1) the thesis embodies the results of my own work and has been composed by myself
2) where appropriate, I have made acknowledgement of the work of others and have made reference to work carried out in collaboration with other persons
3) the thesis is the correct version of the thesis for submission and is the same version as any electronic versions submitted*.
4) my thesis for the award referred to, deposited in the Heriot-Watt University Library, should be made available for loan or photocopying and be available via the Institutional Repository, subject to such conditions as the Librarian may require
5) I understand that as a student of the University I am required to abide by the Regulations of the University and to conform to its discipline.

* *Please note that it is the responsibility of the candidate to ensure that the correct version of the thesis is submitted.*

Signature of Candidate:		Date:	

Submission

Submitted By *(name in capitals):*	
Signature of Individual Submitting:	
Date Submitted:	

For Completion in Academic Registry

Received in the Academic Registry by *(name in capitals):*			
Method of Submission *(Handed in to Academic Registry; posted through internal/external mail):*			
E-thesis Submitted ***(mandatory from January 2009)***			
Signature:		Date:	

Contents

List of Tables

List of Figures

Full list of Publications During the Course of the PhD Studentship

[1] E. Osalusi, J. Side, R. Harris, *Reynolds stress and turbulence estimates in bottom boundary layer of Fall of Warness*, Int. Comm. Heat and Mass Transfer, **36**, 5, 412-421, (2009)

[2] E. Osalusi, J. Side, R. Harris, *Structure of turbulent flow in EMECs tidal energy test site*, Int. Comm. Heat and Mass Transfer, **36**,5, 422-431, (2009)

[3] E. Osalusi, J. Side, R. Harris, *Thermo-Diffusion and Diffusion-Thermo effects on combined heat and mass transfer of a steady MHD convective and slip flow due to a rotating disk with viscous dissipation and Ohmic heating*, Int. Comm. Heat and Mass Transfer, **35**, 908-915, (2008)

[4] E. Osalusi, J. Side, R. Harris, *Ohmic heating and viscous dissipation effects on unsteady hydromagnetic flow and heat transfer over a porous rotating disk with variable properties, hall and ion-slip currents*, Far East Journal of Applied Mathematics, **32**, 3,381-407, (2008)

[5] E. Osalusi, J. Side, R. Harris, *Viscous and Ohmic dissipations effect on MHD and slip flow, heat and mass transfer of Maxwellian fluids over a stretching sheet considering Soret and Dufour effects*, Advances and Applications in Fluid Mechanics, **4**, (1), 59-76, (2008)

[6] E. Osalusi, J. Side, R. Harris, *The effect of thermo-diffusion and diffusion-thermo on combined heat and mass transfer of a steady hydromagnetic convective flow due to a rotating disk with viscous dissipation and Ohmic heating*, JP Journal of Heat and Mass Transfer, **2**, 1, 29-53, (2008)

[7] E. Osalusi, J. Side, R. Harris, P. Clark, *The effects of combined viscous dissipation and Joule heating on unsteady mixed convection MHD flow on a rotating cone in a rotating fluid with variable properties in the presence of Hall and ion-slip currents*, Int. Comm. Heat and Mass Transfer, **35**, 413-429, (2008)

[8] E. Osalusi, J. Side, R. Harris, B. Johnston, *On the effectiveness of viscous dissipation and Joule heating on steady MHD and slip flow of a Bingham fluid over a porous rotating disk in the presence of Hall and Ion-slip currents*, JP Journal of Heat and Mass Transfer, **1**, 3, 303-330, (2007)

[9] E. Osalusi, J. Side, R. Harris, B. Johnston, *On the effectiveness of viscous dissipation and Joule heating on steady MHD flow and Heat transfer of a Bingham fluid over a porous rotating disk in the presence of Hall and Ion-slip currents*, Int. Comm. Heat and Mass Transfer, **34**, 9-10, 1030-1040, (2007)

[10] E. Osalusi, J. Side, R. Harris, *The effects of Ohmic heating and viscous dissipation on unsteady MHD and slip flow over a porous rotating disk with variable properties in the presence of Hall and Ion-slip currents*, Int. Comm. Heat and Mass Transfer **34**, 9-10, 1017-1029, (2007)

[11] E. Osalusi, *Effects of thermal radiation on MHD an slip flow over a porous rotating disk with variable properties*, Romania Journal of Physics, **52**, 3-4, 193-205, Bucharest, (2007)

Nomenclature

a	wave amplitude, m
A_{rms}	orbital-semi excursion
Az	Eddy viscosity, m^2/s
b_i	along-beam velocitie, m/ss
d_0	near-bed orbital diameter, m
f	frequency, Hz
f_{br}	representative wave frequency, Hz
H	wave height, m
h	water depth, m
H_s	significant wave height, m
Ht	mean tidal height, m
i	integer
k	wave number, $1/m$
L	wavelength, m
M	ensemble number
M_e/M_f	ebb/flood rates of mean current
Mx_e/Mx_f	ebb/flood rates of maximum current
n	integer

P	TKE production, Wm^{-3}
rb_1	ADCP radial beam 1 velocity, m/s
rb_2	ADCP radial beam 2 velocity, m/s
rb_3	ADCP radial beam 3 velocity, m/s
rb_4	ADCP radial beam 4 velocity, m/s
Re	Reynolds number
S	TKE density, m^2/s^2
S_n	spectral density of water elevation, $m^2 s$
T	wave period, s
t_e/t_f	rate between durations of ebb and flood periods
T_p	wave peak period, s
T_z	zero-crossing period, s
$T_{e\rightarrow f}$	duration from ebb to flood
$T_{f\rightarrow e}$	duration from flood to ebb
Tt	tidal cycle duration
u	along-stream velocity, m/s
u_*	shear velocity, m/s
u_{br}	representative bottom orbital velocity, m/s
u_{bs}	significant bottom orbital velocity, m/s
u_{bt}	magnitude of particle velocity, m/s
u_{rms}	root-mean-square orbital velocity, m/s
v	across-stream velocity, m
w	vertical velocity, m/s

z	height above bed (z<0 below still-water surface), m
α	Kolmogorov constant
γ	constant
μ	dynamic viscosity, kg/ms
ω	radian frequency, Hz
$\overline{u}$	mean velocity, m/s
$\overline{x_i'^2}$	along-beam velocity variance due to turbulent fluctuations, m/s
ϕ_1	pitch angle, deg
ϕ_2	roll angle, deg
ρ	fluid density, kg/m^3
σ_b^2	along-beam velocity variance due to instrument noise
σ_{pr}	TKE production uncertainties, W/m^3
σ_{sh}	Shear estimate uncertainties, $1/s$
σ_{st}	Reynolds stress uncertainties, Pa
τ	shear stress, Pa
τ_b	bed shear stress, Pa
τ_x	along-stream vertical turbulent stress, Pa
τ_y	across-stream vertical turbulent stress, Pa
θ	direction, deg
θ	beam angle, deg
$\tilde{u}, \tilde{v}, \tilde{w}$	velocities instrument coordinate system
ε	TKE dissipation, W/m^3

Glossary of Terms and Abbreviations

2SFM	Second Order Structure Function Method
ADCP	Acoustic Doppler Current Profiler
BDM	Bayesian Directional Spectrum Estimation Method
CFD	Computational Fluid Dynamics
CMPT	The Centre for Marine and Petroleum Technology
CPSD	Cross Power Spectrum Density
DFTM	Direct Fourier Transformation Method
DGPS	Differential Global Positioning System
DTI	Department of Trade and Industry
EC	European Commission
EMEC	European Marine Energy Center
EMEP	Extended Maximum Entropy Principle Method
EMLM	Extended Maximum Likelihood Method
FHATT	Floating Horizontal Axis Tidal Turbine
HAWT	Horizontal Axis Wind Turbine
ICIT	International Centre for Islands Technology
IDM	Inertial Dissipation Methods
MEPM	Maximum Entropy Principle Method
MHD	Magnetohydrodynamics
MLM	Maximum Likelihood Method
PIV	Particle Image Velocimetry
RTT	Lunar Energy Rotech Tidal Turbine
SRTT	Scotrenewables Tidal Turbine
TKE	Turbulent kinetic energy
TSED	Tidal Stream Energy Devices
TWh	Terawatt (10^{12}) hour
USGS-OSW	United States Geological Survey-Office of Surface Water

Chapter 1

Introduction

1.1 Introduction

The world's energy demand over the next 30 years is estimated to increase by at least 70% due to the increase in the population. The current major source of energy is from fossil fuels, which provide 95% of the world's total energy demand and comes with the cost of devastating environmental impact through the emission of carbon dioxide (CO_2). This is assumed to be the major cause of climate change. As fossil fuel shortages are predicted because of oil reservoir depletion, the supply will potentially become more difficult. As a result of this, renewable energy issues have become a priority in order to meet the world energy demand.

Tidal streams are large movements of water driven mostly by the tides with the resulting kinetic energy of the moving water used to power turbines. One of the advantages of the tidal stream resource is that, being a feature of the gravitational forces of planetary orbits unlike wind, it is essentially quantifiable and predictable.

The technologies of energy extraction from tidal streams are virtually identical to those of wind which can be argued have mostly reached maturity. It is therefore not surprising that the lift dependent devices found to be efficient in wind turbines are being applied to tidal stream devices.

As tidal stream turbine prototypes are now being tested in the real marine environment, the understanding of such environments, such as the short-term variations as a result of turbulence or wave-current interaction are becoming crucial.

As no model that can accurately predict the instantaneous behaviour of the tidal stream systems currently exists, obtaining measured data to describe the environment, and using it to best advantage in the design of tidal stream turbines, is therefore of cen-

tral importance to the tidal energy industry (Jennings [49], Singer [100], Fraenkel [25], VanZwieten *et al.* [119], BC Hydro [33], Scotrenewables [98]).

1.2 Aims

The main objective of this thesis is to improve the understanding of the transient flow due to short-term fluctuations in stream velocity, resulting from turbulence and wave-current interactions in a typical tidal stream site, the EMEC's tidal energy test site, Orkney. This study aims to achieve this objective through the high-frequency sampling data collected by EMEC at different times of the year. The field data are then processed, analysed and interpreted to characterise the flow hydrodynamics at the test site. In order to achieve this, intermediate aims were set as follows:

1. To estimate the directional wave spectrum and current profiles through the water column and to investigate the influence of wave-current interaction on the water particle kinematics;
2. To estimate the shear stresses due to the combined effect of wave, current and turbulent bottom boundary layer; and
3. To estimate the bulk turbulence parameters of the flow

The author believes that the understanding of the flow due to short-term fluctuations in stream velocity, at a typical tidal stream site, gained from this study will assist in the modeling of a tidal test site and improve design optimisation of tidal stream turbine design. The author is satisfied, that this investigation will have a positive impact, on the improved future tidal turbine design, quality of life and energy security in the foreseeable future.

1.3 Thesis Outline

This thesis consists of seven Chapters through which the development of the research work carried out for this project is presented. It has been structured in the format of a series of papers. Two of these papers have been published and they are attached in Appendices E and F.

The contents of the Chapters are summarised below. Chapter 1 presents a brief introduction to tidal resource and tidal stream energy devices. The aims and objectives of this research are explained so that a suitable approach is planned and executed. This is followed by reviewing closely related relevant literature.

Chapter 2 provides a detailed overview of the theoretical concepts underlying this study and the description of post-processing techniques and analysis methodology used in processing data collected by an ADCP. Apart from highlighting the achievements from the instrument and analysis methods used in dealing with the measured data, the review also discusses the limitations and sources of errors and how they can be minimised. The outcome then assists in establishing an effective approach and methodology for fulfilling the aims and objectives set in Chapter 1.

Chapter 3 presents analyses of directional wave spectra and current profiles from data collected between 18 and 30 August, 2005. Key results from the current profiles and directional wave field are presented and discussed.

In Chapter 4, the effects of current and seabed-induced effects on directional energy spectrum and wave energy dissipation are investigated from data recorded between 12 March to 13 April, 2007. Key results are presented and discussed.

In the fifth Chapter, the effect of wave-current interaction within the bottom boundary layer on the hydrodynamics of the Fall of Warness from the data collected between 16-29 October, 2007 is presented. The author used the eddy viscosity wave-current interaction model proposed by Christoffersen and Jonsson [17] discussed in Chapter 2 to achieve this objective. Results from this Chapter are presented and discussed.

Chapter 6 investigates the structure of turbulence flow in the EMEC's tidal test site. The Chapter aims to identify the bulk turbulence parameters (Reynolds stresses, Turbulent Kinetic Energy (TKE) production, Eddy viscosity and TKE dissipation) in the flow. Results are presented and analysed accordingly. The final Chapter gives the conclusions of the studies presented in the preceding Chapters. This is followed by design implications of the results from this thesis and recommendations for future study.

The Appendices provide the theoretical development of methods presented in Chapter 2, pre-processing analysis of data and code functions.

1.4 Review of the Literature

1.4.1 Introduction

Tides are the main source of the global marine current energy resource. The inward flow (flood tide) and seaward flow (ebb tide) of water caused by the tide can be twice each day (semidiurnal), with a period of approximately 12 hours and 24 minutes and once each day (diurnal) with a period of 24 hours and 48 minutes. However, there are certain locations that experience a combination of semi-diurnal and diurnal tidal effects. Gravitational forces of the Sun and Moon on the ocean waters of the rotating Earth are responsible for tides, with a significant effect on the proximity of the Moon and the Sun relative to the Earth.

The two tides observed a day are as a result of the two bulges in the Earth's ocean water created by the gravitational forces with one directly closest to the Moon and the other on the opposite side of the Earth. The Earth tilts at 23.5 degree to the Moon's orbit thereby giving unequal two bulges in the ocean relative to fixed point (i.e. latitude), unless the Moon is over the equator.

These unequal bulges give rise to the difference in tidal height between the two day tides (diurnal inequality) and this repeats on a 14-day cycle as the Moon rotates around the the Earth. When the Sun and Moon's gravitational pull is aligned and the semi-diurnal tide is dominant, the largest marine currents occur at new Moon and full Moon (spring tides), and lowest currents at the the first and third quarters of the Moon (neap tides), where the Sun and Moon's gravitational pull are 90^o out of phase. The largest currents occur during the diurnal tide, at the extreme declination of the Moon and lowest currents at zero declination. Since the differences in currents observed in ocean water occur due to changes between the distances of the Moon and Sun from the Earth relative to the Earth and angles of declination, the strength of the marine currents generated by the tide varies, depending on their position on the Earth. Other factors such as the shape of the coastline and the bathymetry (shape of the sea bed) also affect the strength of marine currents. Narrow passages between islands and around headlands (e.g., the Fall of Warness EMEC's tidal test site) have an effect on the magnitude of the tidal stream due to the concentration of tidal flow and this is accompanied by energy loss due to seabed roughness and enhanced current boundary layer by the oscillatory, turbulent wave boundary layer (VanZwieten *et al.* [119]).

Energy from the tidal stream is less vulnerable to climate change than wind and wave which are weather dependent. Due to this, the tidal stream resource is predictable and quantifiable (spatially and temporally) because it is driven by gravitational forces of planetary orbits. The high capital and environmental problems associated with the first commercial scale tidal generating barrage (La Rance, France) has brought about the horizontal and vertical axis models. The difference in these two models is based on the orientation of the rotating shaft (see Figures 1.1 and 1.2). Horizontal axis model technology (e.g., Scotrenewables Tidal Turbine (SRTT)), which is more advanced and presently favoured by the tidal energy developers, was adapted from the wind energy industry while the vertical axis model (e.g., Blue Energy Ocean Turbine) technology was developed from the technology used in the oil industry. Most of these tidal turbines are in prototype research development. Horizontal axis tidal turbine rotors can be fixed in space (e.g, Marenergie Tidal Turbine (MTT)) or freer free-floating (e.g., SRTT).

The horizontal axis model and in particular the floating horizontal axis tidal turbine (FHATT) come with some design challenges (that do not occur when such system are operated in air) due to differences in fluid density. The variation in static pressure and velocity across the vertical water column imposes dynamic effects on the rotor blades and with increased thrust on the FHATT which is over three times greater (due to high density of water) than that experienced by horizontal axis wind turbine (HAWT).

A good understanding of waves, currents, winds, tides and other environmental factors is critical for the design of FHATT which often have more complicated dynamic responses than seabed mounted tidal turbines. The main features of the environment are largely random in nature and unpredictable in any long-term deterministic sense.

Even though the statistical properties of these processes can be defined, predicting the probability of extreme events, or in selecting design conditions, especially when limited measured data exists, is a challenge. Since there is no model capable of describing this environment to the best advantage of FHATT design, obtaining best and long-term data from this inhospitable tidal site is of central importance if the marine tidal industry is going to succeed.

Recently, Grant and Stallard [32] and Sun [111], have investigated the steady and unsteady flow past tidal current turbine blades modeled as a porous disk. The general conclusion is that large energy extraction can cause a free surface drop immediately downstream of the tidal current turbine. The blockage effect which can alter the flow within the channel was also considered as a crucial factor due to the confined space

between sea surface and seabed where tidal current turbines operate. Sun [111], in particular confirms that energy extraction from tidal currents is very sensitive to the freestream flow velocity. The Grant and Stallard [32] CFD model investigated the effect of large-scale flow oscillations on the wake of the turbine. Their result indicated shorter wakes are produced due to unsteady/turbulent flows in the incident flow field which were absent in the case of steady flows.

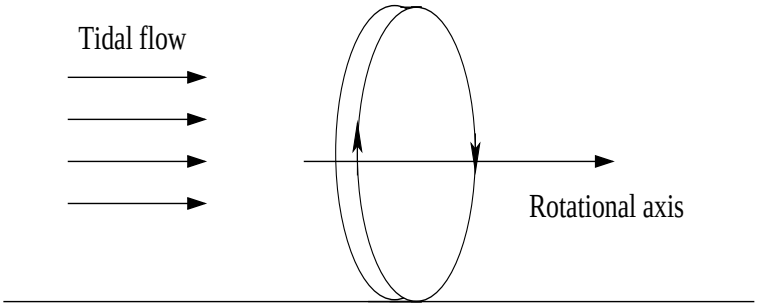

Figure 1.1: Schematic of a horizontal axis tidal current turbine; source Bryden [12]

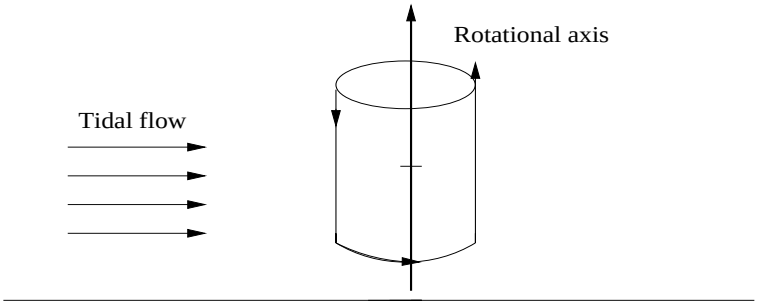

Figure 1.2: Schematic of a vertical axis tidal current turbine; source Bryden [12]

1.4.2 Wave-current Interaction

Accurate prediction of instantaneous forces (resulting from the combined wave and current flows) acting on the tidal turbine blades is of great interest in the tidal energy industry. This is because the load exerted on the turbine systems by the flow of fluid, acting in the direction of the fluid flow (drag force) and the load perpendicular to it (lift force), are proportional to the square of this total fluid velocity. Most of the tidal stream

sites fall within shallow water regions (less than 50 m depth) where relatively strong currents are predominant (e.g., Fall of Warness) and as such, wave-current interactions will be most significant (CMPT [24], Christoffersen and Jonsson [17]).

Longuet-Higgins and Stewart [64], [65] were the first to use the radiation concept to describe the interaction between waves and currents by proving the existence of energy transfer between them. The conservation principle of waves and currents through wave action in the absence of wave generation or dissipation was proposed by Bretherton and Garret [9]. The mathematical formulation of wave-current interactions for linear waves can be seen as the ratio between wave energy density and frequency with respect to current (wave action). Current modifies the wavelength, height, steepness, velocity and direction and most especially alters the relationship between the observed wavelength and period. The equation describing the effect of current field on wave spectra without the occurrence of wave breaking induced by opposing current was first introduced by Huang *et al.* [40] . Later Hedges [37] modified Huang's equation to take the effect of wave breaking into account. Kemp and Simon [51] and Hedges *et al.* [37], [38] reported on the modifications in wave spectra in the presence of current. Their results were based on the measurements of waves in a flume propagating without refraction into a following and opposing current.

This experimental work was extended by Nwogu [77] to directional wave spectra. However, there was limited experimental proof due to the amount of data available to support the theoretical formulations of wave spectra in the presence of a current. Recently, Soares *et al.* [102] confirmed that the wave spectrum increases (or decreases) in magnitude when a wave system is met by an opposing (following) current, and the showed that the theoretical models proposed by Huang *et al.* [40] gave a reasonable approximation to the measured values.

1.4.3 Hydrodynamic Loading

Understanding the loading regime in the design and analysis of a tidal stream turbine structure is a fundamental prerequisite especially considering the effect of wave-current interaction. Wave-current interaction through changes in their frequency spectra may produce significant changes in the probability distribution of the induced fluid loading on the tidal blades and the main hull of a tidal stream turbine (Hedges *et al.* [38] and Burrows *et al.* [13]). The hydrodynamic loading may be underestimated (or over-

estimated) when waves encounter opposing (or following) current by neglecting the interaction.

Tung and Huang [117] used the wave-current interaction model developed by Huang *et al.* [38] to study the influence of wave-current interaction on fluid loading. Their results showed that the effect of wave-current interaction is to an appreciable extent to increase or decrease the fluid loading in following or opposing currents, as compared with the case when simple superposition is used. In another study, Tung and Huang [117] investigated the effect of wave-current interaction on a single pile. They concluded that wave-current interactions have more effect on the forces on a cylinder near the surface than on those deeper in the water. Interestingly, they proposed that wave-current interactions have more effect on the spectrum of the overturning moment than the total force.

Taylor and Rajagopalan [113] studied the influence of the wave-current interaction on the fluid loading on a deep water jacket. In spite of the increase in damping, they found that the responses increase strongly with an increase in current. This is because of the marked increase in forcing when a current is interacting with waves. In the laboratory experiments for predicting the water particle velocity for a wave and current coexisting field in an intermediate water depth conditions, Li [127] demonstrated that this wave-current interaction model proposed by Huang *et al.* [38] gave a picture of the measured water particle velocities.

All of these studies above are based on the assumption that waves are generated where current velocity is zero. However, when waves are generated in water where the current already exists, the wave-current interaction will be different from that described above. When waves are generated in a current, there will be a correlation between significant wave height and the wind speed due to wave-current interaction when waves are generated in current. Based on these findings, Hedges *et al.* [38] developed a model to include current velocity in the development of sea elevation spectrum. The following three conclusions were drawn from their work:

- *"the current is steady and uniform and does not vary in horizontal plane;*
- *the Pierson-Moskowitz spectrum can be applied in the relative frame of reference where the current is effectively zero;*
- *the wind speed used to define the Pierson-Moskowitz spectrum is that relative to the water*

surface."

Even though the relative wind speed was used for the calculation of significant wave height and the associated Pierson-Moskowitz spectrum, it was shown that the current velocity affected the significant wave height and the sea elevation spectrum.

The most established model for axial force on bodies generating axial resistance in oscillatory flow is Morison's equation, in which the force F_x in the flow direction on the device (area A, volume V) subject to velocity $u(t)$ is :

$$F_x(t) = \frac{1}{2}\rho u(t)|u(t)|AC_d + \rho\dot{u}(t)VC_m \tag{1.4.1}$$

where A is the facing area $\pi D^2/4$ and it is usual for disc-like bodies such as a tidal stream turbine rotor to take V as the volume of the circumscribing sphere $\pi D^3/6$. D is the rotor diameter, $u(t)$ and $\dot{u}(t)$ are the velocity and acceleration of the flow, respectively. Experimental results of inline axial force on the device in the presence of currents has shown that for usual frequencies and amplitude of motion, the damping will be overpredicted and structure response underestimated (e.g. Verley and Moe [73], Zhou and Graham [130]). There is still little information about the effects of current (especially the fluctuating part of the current velocity) and about combined effect of current and waves on hydrodynamic loading of the tidal turbine structures. Verley and Moe [73] investigated the damping of vibrations of offshore structures excited by waves and current. They suggested that the drag coefficient in Morison's equation has to represent both the mean and oscillatory force. Through their analysis and experimental work for a combined flow of a cylinder oscillating in a current, Verley and Moe [73] offered an alternate form of equation 1.4.1 to account for the fluctuating part of the current velocity as:

$$F_x(t) = \frac{1}{2}\rho u'(t)|u'(t)|AC'_d + \frac{1}{2}\rho U^2 AC_d + \rho\dot{u}(t)VC_m \tag{1.4.2}$$

where $u'(t) = u(t) - U$, U is the mean velocity and C'_d is the oscillatory drag coefficients. Their results indicated that the current did affect the oscillatory component of force, and neglecting the effect of a current may result in overestimating the oscillatory part of the force and hence the fluid damping.

1.4.4 Wave Kinematics

In the design of FHATT it is crucial to accurately compute the total water particle velocities of the wave-current flow field. It is of interest to the designer of floating tidal turbine systems because:

- The combined effect of current and waves potentially gives rise to the largest instantaneous water particle velocities, and thus the largest fluid drag forces. This is likely to be most important for smaller components of the FHATT.
- Strong current fields have a marked influence on the properties of the wave which pass through them. Waves can become much steeper, and wave energy can be focused in particular locations, giving rise to wave of much greater steepness and height than might otherwise be expected.
- The wave-period: wave-length relationship is changed.

Longuet-Higgins and Stewart ([64]) were the first to describe the interaction between waves and currents. They introduced the radiation stress concept and proved the existence of the energy transfer between waves and currents. Later, Bretherton and Garret [9] defined the wave action, which is important in the study of the interaction of waves and currents, as it is conserved in the absence of the wave generation or dissipation. For linear waves, the wave action is equal to the ratio between wave energy density and frequency with respect to current and its introduction leads to some simplifications in the mathematical formulations of wave-current interactions. When waves propagate through a region with variable current, some of their characteristic parameters, such as their length, height, steepness, celerity and direction will suffer modifications. The presence of a current alters the velocity of the waves and affects the relation between the observed wave length and period. The current also produces changes in other properties of the waves, as happens with the velocity (and acceleration) of water particles. The interaction between waves and currents does not only change the waves characteristics, but at the same time it transforms the current flow field. Huang *et al.* [40] proposed the first equations describing the change of the spectral shape due to the presence of currents. However, they did not take into account the occurrence of wave breaking induced by opposite currents, especially for the waves associated with the equilibrium limit of the spectra, that is, with the high frequency tail of the spectrum. Hedges [37] modified

the theoretical model of Huang *et al.* [40] so as to take that effect into account. The basic formulations of wave-current interaction have been verified experimentally by Kemp and Simons [51] in wave flumes. Hedges *et al.* [38] also reported on measurements made on waves in a flume propagating without refraction into a steady almost uniform opposing current, showing how the spectra was changing. However, the experimental validation of these spectral models has not been extensive and it was mainly done in wave flumes, which basically limit the waves to a long crested situation. Unfortunately, there does not seem to exist many full scale measurements of wave spectra and simultaneous surface current that could be used to verify the theoretical formulations of the change in spectral form. Therefore, the offshore basins that are able to reproduce directional sea states and also current are a good option to study these effects, despite the difficulty that most basins have in reproducing accurately the current fields. Nwogu [77] was probably the first who conducted an experimental investigation on the effect of steady currents on directional wave spectra. He conducted laboratory tests in a multi-directional wave basin using both regular and irregular waves, with different angles between the current and wave fields. The amount of experimental data available to support the theoretical formulations of wave spectra in the presence of a current is still limited as only Hedges *et al.* [37] and Nwogu [77] presented limited experimental results on the change in wave spectra caused by currents, in deep water. This was the motivation of the work initiated by Soares *et al.* [102] and continued here, which aims at providing additional experimental data on those phenomena, furthering their understanding and attempting to validate the theoretical models. Soares *et al.* [102] have confirmed that when a current meets a wave system, differences are observed in the distribution of the spectral energy of the waves. When a wave system is met by a following current, the wave spectrum decreases in terms of its energy, and the contrary happens when the current has the opposite direction. When comparing the experimental results with the theoretical models, it was found that the models proposed by Huang *et al.* [40], tend to give very similar values and to give reasonable approximations to the measured values. However in both cases of following current and opposite current, the theoretical predictions of both models underestimate the change produced by the current in the shape of the spectrum, which recommends further study.

The wave and current interaction acts through a number of mechanisms, (Soulsby *et al.* [104]):

1. refraction of the waves by horizontal sheared currents

2. modification of the wave kinematics by the (possibly vertically sheared) current
3. generation by the waves of mass transport or streaming currents
4. generation by the waves of radiation stresses given rise to currents, particularly longshore currents in the surf zone
5. enhancement of the bottom friction felt by the currents, due to interaction with the wave boundary layer
6. enhancement of the bed shear stresses and energy dissipation of the waves due to interaction with the current boundary layer.

If the current velocity is U (U is positive when current flows with the waves) in a train of regular waves traveling on a steady current, and the waves have an apparent angular frequency ω_a in a stationary frame of reference and ω_r in a frame of reference moving along with the current, then

$$\omega_a = \omega_r + kU \tag{1.4.3}$$

where k ($2\pi/L$) is the wave number and L is the wave length. According to linear wave theory, the relative wave angular frequency ω_r is given by:

$$\omega_r = (gk \tanh kd)^{0.5} \tag{1.4.4}$$

where g is the acceleration of gravity and d is the water depth. In reality, waves and current coexist and the change in significant wave height and thereby the sea elevation spectrum is already taken care of in the measurements (stationary frame of reference).

In the experiments conducted by Ismail [44] with regular waves and current, the observed velocity profile were compared with the computed profile using three methods. They are:

- *"wave-current interaction including Doppler effect with uniform current;*
- *wave-current interaction including Doppler effect with linear shear current and;*
- *linear superposition of waves induced velocity (using linear wave theory) and measured current velocity."*

His conclusion from this investigation revealed that, both the current profiles yielded reasonable predictions for following current but linear shear current profile predicted velocities for opposing currents more accurately. The method of linear superposition underpredicted the horizontal velocities for waves in shallow waters on following current up-to 30% near the bottom and overpredicted the velocity near the water surface. The prediction from this method for opposing current is far larger than the measured values. The main limitation of this model is the assumption that the current profile is uniform over depth. In reality, currents velocity varies over the water column height. Skop [101] proposed an approximate dispersion relationship for water waves on a depth dependent current using perturbation expansion. The dispersion relationship for a linear sheared current for finite water depth is given (Skop [101]) as:

$$\omega_a - kU_s = (gk\tanh kd)^{0.5} + \frac{U_s}{2d}\tanh kd \tag{1.4.5}$$

where ω_a is the wave frequency in stationary position, U_s is the surface current, $U_c = U_s(1 + z/d)$ and d is the water depth. At the surface (i.e. $z = 0$ and $U_c = U_s$), equation 1.4.5 becomes:

$$\omega_a - kU_c = (gk\tanh kd)^{0.5} + \frac{U_c}{2d}\tanh kd \tag{1.4.6}$$

As water depth becomes infinite i.e. $d \to \infty$ and $\tanh kd \approx 1$, equations 1.4.3 and 1.4.6 converge to:

$$\omega_a = \sqrt{gk} + kU \tag{1.4.7}$$

The computed error difference between the exact relation and his approximate relation is small. Kirby and Chen [52] also developed the approximate dispersion relation for waves on arbitrary varying currents using an asymptotic method. Their dispersion relation is given as:

$$(\omega_a - k\overline{U})^2 = gd\tanh kd \tag{1.4.8}$$

where $\overline{U}$ is the weighted mean current and

$$\overline{U} = \frac{2k}{\sinh 2kd}\int_{-d}^{0} U(z)\cosh 2k(z+d)dz \tag{1.4.9}$$

In the limit of $kd \to \infty$, equation (1.4.9) becomes,

$$\overline{U} = 2k \int_{-\infty}^{0} U(z) e^{2kz} dz \tag{1.4.10}$$

where these expressions contain only the first order approximations in the asymptotic technique. This method was further advanced to compute the phase velocity for different current profiles and the result compared with the exact solution of phase speed. The result shows that the first order approximation,

$$\omega_a = (gk \tanh kd)^{0.5} + kU_s - \frac{(s \tanh kd)}{2d} \tag{1.4.11}$$

is sufficient for deep water but second order approximations,

$$\omega_a = (gk \tanh kd)^{0.5} + kU_s - \frac{s \tanh kd}{2} + (gk \tanh kd)^{0.5} \frac{(s^2 \tanh kd)}{8g} \tag{1.4.12}$$

are required for higher accuracy at shallow water depth. Here s is the vorticity (the local angular rate of rotation) of current. The stream function formulation for calculation of water kinematics for waves on current with an arbitrary profile was developed by Dalrymple and Heideman [19]. Their results which were in agreement with the approximation model by Kirby and Chen [52], indicate that the approximation model predicts the wave-current loads accurately on drag-dominated structures.

1.5 Boundary layer Turbulence

The bottom boundary layer is defined to be the vertical distance between the no-slip bottom boundary conditions and outer free-stream motion. Boundary layer thickness is mostly determined by the magnitude of the stream velocity and the seabed roughness. The bottom boundary layer of a typical tidal channel, like the EMEC's tidal test site, is mostly turbulent due to the strong tidal stream velocity (greater than $3ms^{-1}$) and seabed roughness (particle grain size greater than 256 mm [82]). Also, since the water depth at this region is shallow (with respect to the waves), the orbital motion due to surface waves may create horizontal oscillatory currents in the bed region. Under this condition of waves and current interaction, the entire flow over the water column becomes more complicated. Since the length and time scales associated with current and waves are differing in magnitude (e.g. tidal current time and length scales are greater

than that of surface waves), two separate boundary layers are formed naturally: the wave and current boundary layers. The wave boundary layer, which is thinner (few centimeters thick) than current boundary layer, has a steeper velocity gradient and is more turbulent than the current boundary layer that occupies almost the entire water column. The overlying current boundary layer perceives the wave boundary layer as an additional bed roughness resulting in increased friction velocity (due to bed increased shear) and enhanced mean current profiles (Kemp and Simons [51]). This interaction between these two boundary layers, at a typical tidal site, creates a transient and non-linear flow. ZhenGang's [129] work on the coexistence of these two boundary layers showed that the effect of waves on the current boundary layer is generally more than the effect of current on the wave boundary layer. This is because the wave boundary layer is oscillatory and more turbulent than current boundary layer. Accurate measurement of turbulence in an inhospitable environment, like the EMEC's tidal site, is challenging. This is because, the fluctuating part of the velocity must be recorded in four dimensions (three space and one time dimension), and temporally sufficient to fulfill the statistical properties of bulk turbulence parameter (Reynolds stress, Turbulent Kinetic Energy (TKE) production, eddy viscosity and TKE dissipation) computations.

Only recently have ADCPs proved capable of measuring instantaneous velocities over the entire water column in shallow water. The ADCP transmits sound at a fixed frequency along its beams and listens to echoes returning from sound scattered by water particles and this is used to calculate the velocity of water. An ADCP normally has three or four beams inclined at 20^o or 30^o. Estimation of bulk turbulence parameters have been achieved recently through the availability of high-frequency, broad-band ADCPs. Recently, Osalusi *et al.* [83], Osalusi *et al.* [84], Stacey *et al.* [106], Fugate and Chant [27], Rippeth *et al.* [93] and Simpson [99] have used these capabilities of ADCPs to estimate bulk turbulence parameters in tidal channels and estuaries. Lohrmann *et al.* [63] obtained turbulent Reynolds stresses using the difference in the velocity variance between opposing beams. This method is discussed in Chapter 2.

The uncertainties in Reynolds stresses from the use of ADCPs have been discussed by Williams and Simpson [124]. They found that the uncertainties are due to the combined instrument and flow dependent noise and proposed that the error can be reduced by increasing the number of samples or bursts and the use of faster-ping broadband ADCPs (e.g., mode 12). Mode 12 is an operational mode that allows Teledyne RDI's ADCPs to measure fast flows in shallow gauging sites. By operating in mode 12, the ADCP can

measure a large range of flow velocities with smaller depth cells, making it capable of taking measurements in much shallower flows and to measure the highly sheared profile of fast flows near boundaries. It (mode 12) achieves this by increasing the ping rate, allowing the depth cell size to be small without increasing the averaging time or data noise (RDI [90]).

1.5.1 Characteristics of Tidal Streams in the Fall of Warness

Tidal stream variations in the Fall of Warness are dominated by semi-diurnal variations (twice per day) and the spring/neap cycles. Figure 1.3 illustrates the 10 min mean spring peak and neap velocities from a profile of current speed measured by an ADCP over one month (12 March 2007 - 13 April, 2007). The survey was conducted approximately 4 km West of the Island of Eday in the Orkney Islands, the EMEC's tidal energy test site at the Fall of Warness, test location, $59^o08.147N; 2^o48.391W$ (Figure 1.4). Current velocity profiles were sampled every 30 s with 1 m bin vertical spacing while directional wave data were sampled for 10 min every hour at a sampling rate of 2 Hz. It can be seen that the mean spring peak (around 200 hours) is the greatest velocity, while the mean neap peak velocity (around 365 hours) is a maximum when the spring/neap cycle is at a trough. Figure 1.5 shows the variation of one month mean current velocity over the water column. As expected, maximum value of mean current is noticed at the water surface and decreases to it minimum down the water column due to shear at the seabed. It is this seabed roughness that brings about the increased seabed friction and bottom boundary layer turbulence. Figure 1.6 shows an averaged power density for the 360^o of current direction. Theoretically, the tidal stream power density is given by:

$$P_w = 0.5\rho U_c^3 \tag{1.5.1}$$

where ρ is the water density and U_c is the stream velocity. As expected, the power density is mainly distributed over two peaks located approximately 180^o to each other. These reflect the approximately bi-directional nature of the tidal stream in the Fall of Warness. The power captured by a tidal turbine is expected to decrease as the direction of the stream departs from the turbine axis – the advantage of bidirectional horizontal-axis tidal turbine (e.g., Lunar Energy Rotech Tidal Turbine (RTT)).

A further one-month set of ADCP data was used to validate the result discussed above. The data refers to a 600-kHz four-beam broadband ADCP (RD Instruments Workhorse

monitor) deployed on the seabed in approximately 37 m (mean water depth) of water between 5 October - 5 November 2007 test location, $59^o09.046N; 2^o48.935W$ (Figure 1.7). The data was sampled at 2 Hz for 10 min in every 20 min record. The plot corresponding to the figures discussed above are shown in Figures 1.8-1.10. Though the magnitude of the current is much smaller than the one discussed above (which resulted in smaller power density) , the same trends are shown in all corresponding plots.

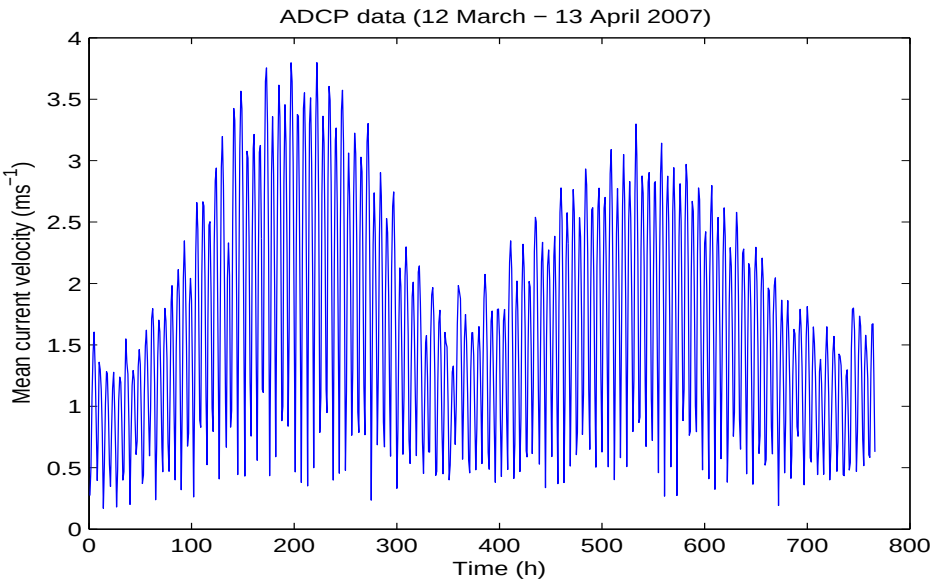

Figure 1.3: Mean (10 min) tidal stream velocity (ms^{-1}) variation in the Fall of Warness (Time in Hours)

1.6 ADCP Measurements

The ADCP uses sound to sense current velocities in the water (sonar) on the basis of the Doppler Effect. The Doppler Effect refers to the compression or expansion (i.e., a change in frequency) of the transmitted sonar signal caused by the relative motion between the ADCP and the scattering material in the water column (Figure 1.11). Since this material is moving with the water currents, and at the same speed, the magnitude of the

Figure 1.4: ADCP location in 12 March-13 April, 2007; (source: Google Earth)

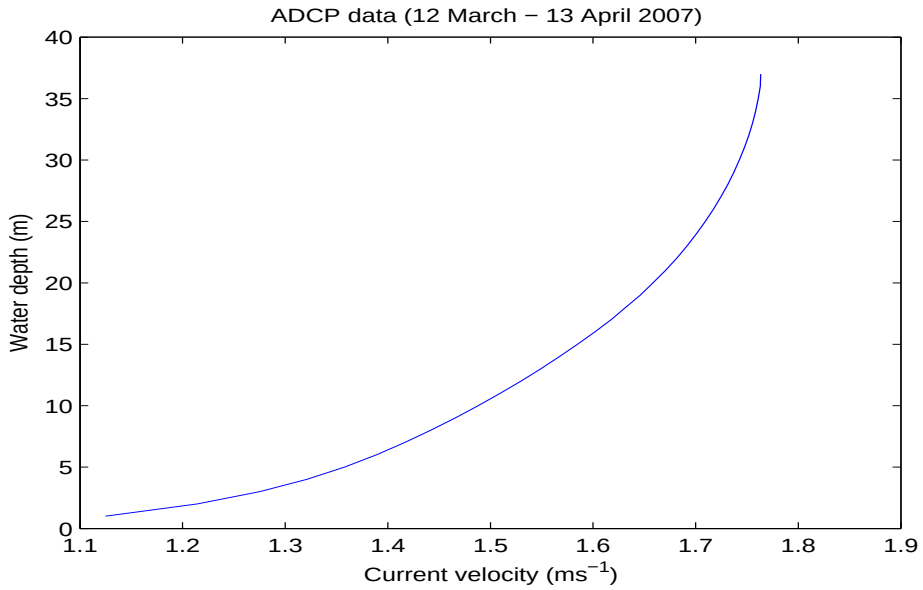

Figure 1.5: Mean (10 min) tidal stream velocity (ms^{-1}) variation in the Fall of Warness (over water column)

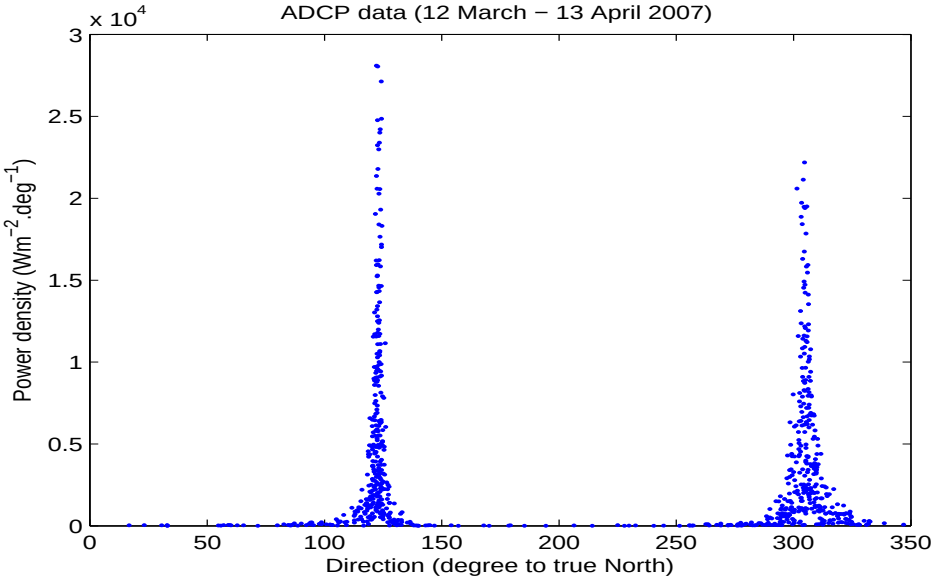

Figure 1.6: Average power density

Doppler Effect is directly proportional to the velocity of the currents. The ADCP determines the velocity of the water currents by measuring the frequency of backscattered echoes (echoes returned from the scattering material) and comparing it to the transmit-

Figure 1.7: ADCP location in 5 October-5 November, 2007; (source: Google Earth)

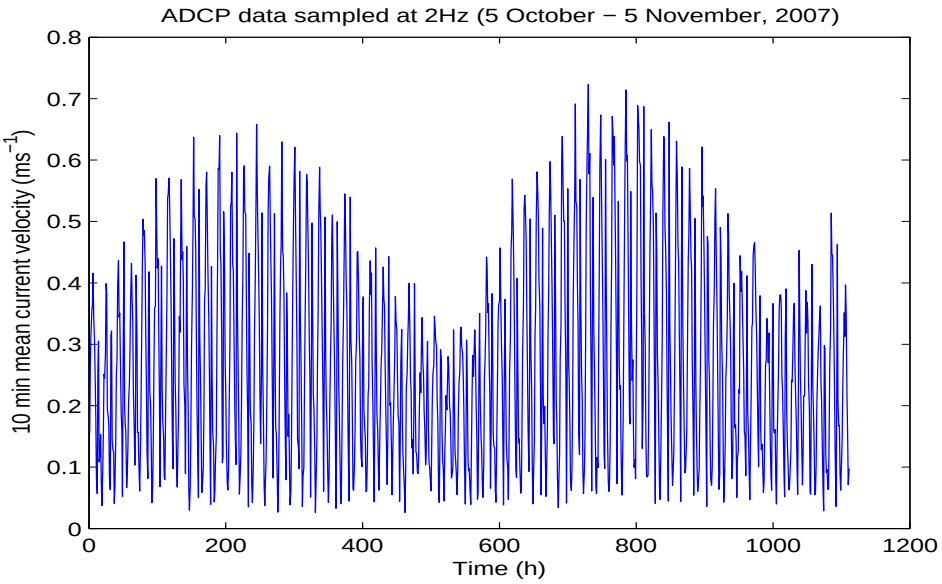

Figure 1.8: Mean (10 min) tidal stream velocity (ms^{-1}) variation in the Fall of Warness (Time in Hours)

ted frequency. ADCPs measure the pressure at the head of the instrument, the range to the surface and orbital velocities. The pressure sensor of the ADCP measures the water depth above the instrument which is also a time series of wave fluctuations. The intensity of the sound that is reflected back to the ADCP (the Returned Signal Strength Intensity or RSSI) is measured as a quality control parameter. Since the water surface will reflect sound much more strongly than the particles within the water, the RSSI allows an accurate measurement of the range to the surface along each of the four beams of the ADCP. The along-beam velocities in a series of bins are measured by the ADCP extending along each beam away from the instrument transducers. This is done by measuring the Doppler shift of sound reflected from scatterers assumed to be moving with the water currents. The measurements are range-gated into series of bins along each of the four beams of the ADCP and then combined to infer the velocity profile encompassed by the beams.

The Doppler effect is directional. Any shift in frequency corresponds to a velocity component along the transmitters direction of send/receive. Velocities perpendicular to the direction of send/receive produce no Doppler shift. The opposite beams of an ADCP measure two different components of the water-current vector. Because these components are not in the same direction, they can be transformed into two orthogonal vectors

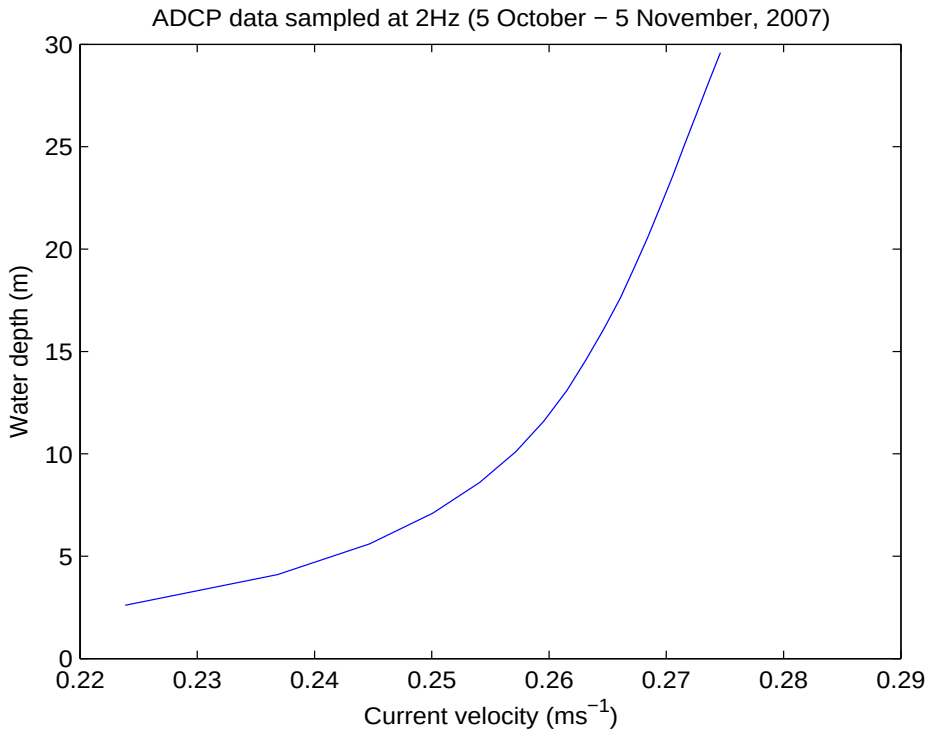

Figure 1.9: Mean (10 min) tidal stream velocity (ms^{-1}) variation in the Fall of Warness (over water column)

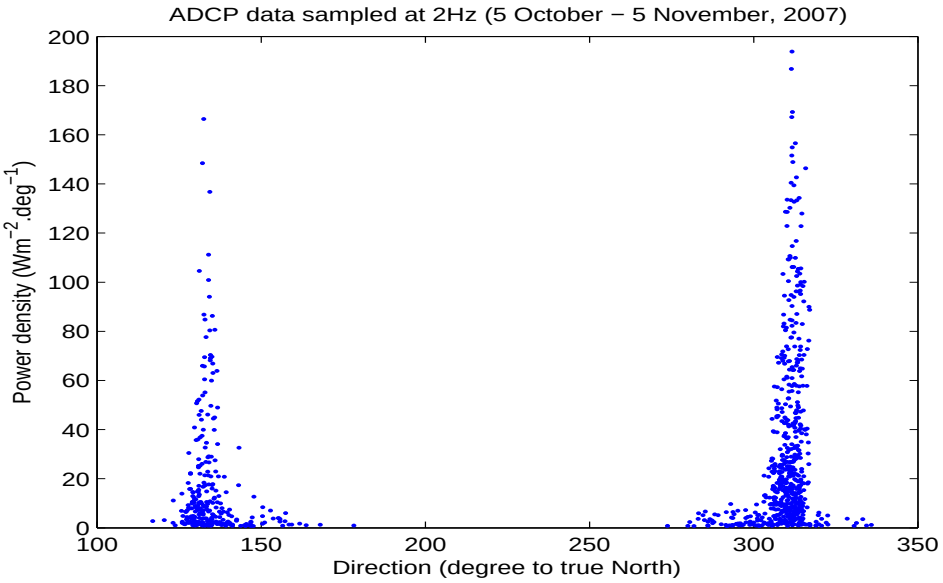

Figure 1.10: Average power density

one horizontal, one vertical. A second pair of beams, rotated 90^o in azimuth from the first pair, generate another set of horizontal and vertical vectors. This gives a total of three orthogonal vectors (x,y,z), which are the three vector components of water current (u,v,w). ADCP uses depth cell mapping to ensure accurate computation of horizontal velocity u and v. This is done by matching the velocity at a particular depth with corresponding opposite cell at the same depth.

Thus with two pairs of acoustic beams, ADCPs estimate two horizontal velocity components and two independent vertical velocities. Two horizontal velocities are orthogonal to each other. Horizontal velocity components are converted from ADCP coordinate system into Earth coordinates by means of heading data, which are measured by the compass of the ADCP. The difference between the independent estimates of vertical velocity is referred to as the error velocity. This error velocity can be used to test the assumption that flow volume of water bounded by the four measurement beams is homogeneous. Velocity homogeneity means that the water velocities do not change significantly in magnitude or direction within the confines of the acoustic beam footprint.

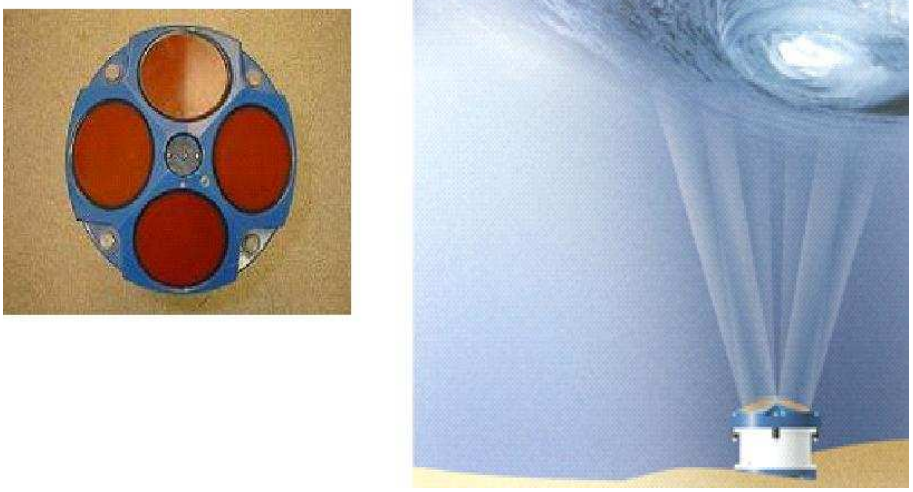

Figure 1.11: RDI Workhorse Sentinel ADCP 600kHz (Source: RDI [90])

The availability of higher-frequency, broad-band ADCP has enabled the estimation of turbulence parameters. Gargett [28] developed a method for estimating the rate of dissipation of TKE from measurements of larger-scale turbulent structures using an ADCP with one beam oriented in the vertical. The ADCP's ability to measure profiles of mean

current and turbulent stresses, and hence turbulent shear production throughout the water column, has made it an invaluable tool in studies of vertically sheared flows where bottom or surface boundary layers compose a significant portion of the water column. The increasing popularity of the ADCP is at least partially due to its nonintrusive measurement method, its tolerance to biofouling, and its ability to synoptically sample nearly the entire water column. These capabilities are particularly well suited for work in shallow systems where ADCPs have been used to observe currents and dynamical quantities such as Reynolds stresses (Stacey *et al.* [106]), near-bed velocity gradients (Fugate and Chant [27]), eddy viscosity (Rippeth *et al.* [93]) and tidal straining mechanisms (Simpson [99]). In highly frictional systems, the behavior of turbulent Reynolds stresses (e.g., Kundu and Cohen [59]) is often of interest and can be obtained from ADCP measurements using the difference of velocity variances between opposing beams (Lohrmann *et al.* [63]). Error analyses of the variance method (Stacey *et al.* [106], Lu and Lueck [68]), Williams and Simpson [124] have demonstrated that uncertainties in Reynolds stress calculations are a combination of instrument- and flow-dependent noise and are inversely dependent on the number of samples, M, used in obtaining the variance estimate. Until recently, the ability to reduce error (by increasing M) was limited by the sampling rate of the ADCP (commonly 2 Hz), which is set by acoustical constraints and signal processing rates of the instrument hardware. Thus, ADCP measurements of large Reynolds stresses have been typically noisy and measurement of small Reynolds stresses problematic. Ideally, one would have an instrument that could sample and record velocities at rates fast enough for resolution of turbulent fluctuations; however, this would require changes to the signal processing hardware found in the current generation of ADCPs. To partially address this issue, RD Instruments (RDI) recently introduced a firmware option that provides a faster-ping capability for their existing broadband ADCPs. This firmware option (known as water mode 12) allows an order of magnitude faster sampling rates (up to 20 Hz) by collecting a user-specified number of unprocessed sub-pings and then averaging the sub-pings into a single recorded velocity profile. Slowly varying flow such as tidal flow exhibits some peculiarities. When the water column is accelerated from a situation in which the near-bed velocity is zero (as after slack tide), shear stress propagates upwards from the bed. Other turbulent properties such as shear production, TKE and dissipation rate also propagate upwards, all with a height dependent time lag behind the phase of the bed stress. This has been clearly demonstrated by means of analytical models while observational evidence of the phase lag of dissipation has been provided, for example, by Simpson [99]. Recent

independent observations of turbulence production and dissipation rate by Rippeth *et al.* [93] in a narrow strait allow the study of the production-dissipation phase lag, which is often ignored in modeling exercises for boundary layer flow. The turbulent structure of tidal bottom boundary layers may also be strongly influenced by horizontal density gradients. Rippeth *et al.* [93] found $\sim 4.5Pa$ for a current speed of $1.2ms^{-1}$, Rippeth *et al.* [94] observed $\sim 0.5Pa$ for a current speed of $\sim 0.6ms^{-1}$ and Williams and Simpson [124]) got $\sim 6Pa$ for a current speed of $\sim 1.2ms^{-1}$. Dyer [22] proposed a turbulence intensity value of the order of 10% near the boundary of an estuary.

In a less energetic flow like the studies described above, separating the wave and turbulent components of velocity may not be as challenging as in an energetic tidal test site like the Fall of Warness.

Extracting waves and turbulence parameters in an energetic ocean state where the mean spring Peak is greater than 4 m/s (like the Fall of Warness), is challenging because the two processes overlap in frequency, or in wavenumber. Even though it is assumed that the turbulent and wave process would not overlap in the combined wavenumber-frequency spectrum, due to each having a different dispersion relationship, (the turbulent process assumed to obey a linear dispersion relationship, as turbulent flow is advected with the mean current (Taylors frozen turbulence approximation)), the ADCP looks at radial wavenumbers and frequencies and finds overlap.

This is because near the bottom boundary layer of the ocean it can be assumed that the process responsible for creating the turbulence is independent of the process creating the surface waves. When two processes are independent, the cross correlation between turbulent fluctuations and wave induced velocities is zero. In that case the cross covariances of the two measured velocity components will consist of a turbulent term and a wave induced term. The horizontal wave velocities are out of phase with vertical wave velocities, and the cross-covariance wave term is zero. Therefore when there is uncertainty between the axes of the ADCP and the principle wave axes, the measured radial velocities have wave and turbulent components which are correlated. Separating the wave and turbulent components of the velocity in an energetic tidal channel is a challenge and such is one of the differences between earlier studies in less energetic environment and this study.

1.7 Design of the Experiment

The summary of the dataset used in each Chapter of this study are presented in Table 1.1. Each experiment was performed at the test berths location at depths ranging from 29m to 45m (mean water depth) where prototype tidal stream turbines are marked to be tested.

Water velocities recorded in the beam coordinate system of the ADCP (i.e. individual Doppler shift along each beam logged independently) are instantaneous velocities containing waves, mean and fluctuating component of the current velocities. Records of three dimensional velocity vector, the echo amplitude and correlations between four beams are provided (Table 1.1). The movement of the instrument was recorded by the compass and pressure sensors. Ensemble averaging is done automatically inside the ADCP (if it is configured to do so) and the velocities are rotated from the beam coordinate system to the Earth's reference frame. If the ADCP is configured to record in *packets*, then waves and mean current can be extracted. If in *ensemble* setting (data within intervals of time), only the mean value (current) can be read from the dataset. *Packets* dataset split waves and mean current during the experiment. Since Chapters 3 and 4 are centered on waves and mean current analysis, datasets recorded in Earth coordinate system and in *packets* are suitable and are used. In Chapter 5, the instantaneous velocities were time averaged over 20 minutes based on the stability of the statistics (Figure 1.12). The velocities appeared to be stable from 20 minutes upwards. The purpose of Chapters 6 is to examine the stress associated with the fluctuating part of the current velocity (Reynolds stress) and so the beam-recorded datasets containing both the mean and fluctuating components of the velocities were used.

Different datasets were chosen for a particular analysis. For example for mean current analysis, ensemble averaged data recorded in Earth cordinates (in Chapters 3 and 4) were used and for turbulence processes, beam cordinates (non-averaged) data (Chapters 5 and 6) were chosen. The reasons being that beam cordinates contain waves, mean current and fluctuations whereas ensembled averaged data contain only mean current.

It should be noted here that there is no data from an energetic tidal site to validate the wave measurement used in this study. Though there is a good correlation with wave measurements from a less energetic site, but a validation with a different instrument is required in order to be 100% confident in this aspect of measurements.

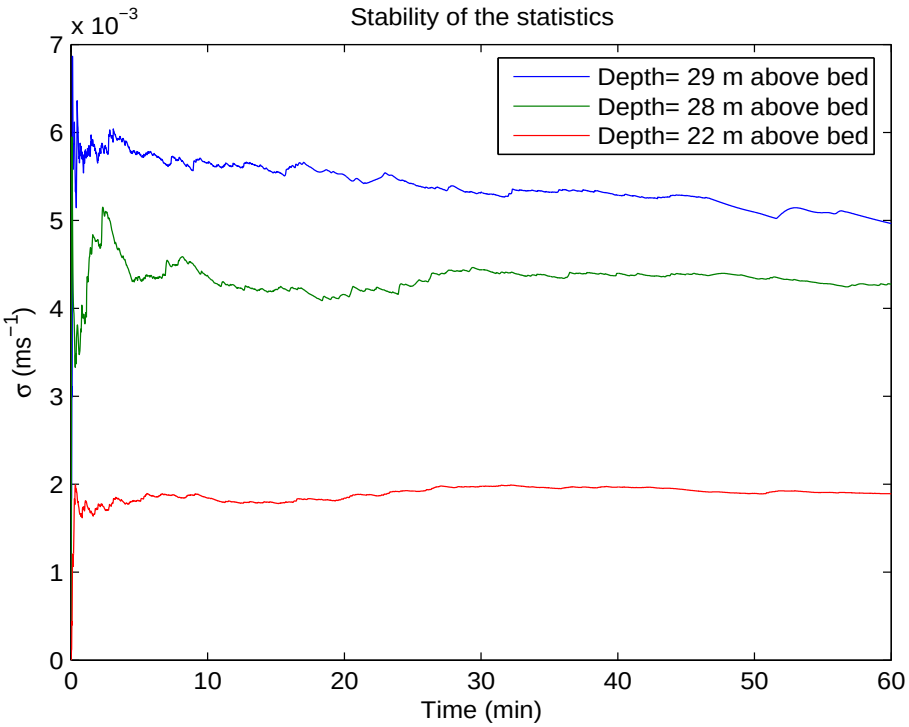

Figure 1.12: Stability of the statistics

Table 1.1: Design of the Experiment

	Chapter 3	**Chapter 4**	**Chapter 5**	**Chapter 6** *Deployment 1*	*Deployment 2*
Instrument	RDI ADCP	RDI ADCP	RDI ADCP	RDI ADCP	RDI ADCP
Acoustic Frequency	600 kHz	600 kHz	600 kHz	600 kHz	600 kHz
Test location	59^o09.323N, 2^o49.515W	59^o08.147N, 2^o 48.391W	59^o09.046N, 2^o48.935W	59^o08.208N, 2^o 48.469W	59^o09.046N, 2^o 48.935W
Record time	18 - 30 Aug. 2005	12 Mar - 13 Apr 2007	16-29 Oct 2007	2-5 Jul 2006	5 Oct - 5 Nov, 2007
Water depth (m)	29	45	37	42	37
Sample interval for currents (sec)	24	30	0.5	1	0.5
Sample interval for waves (sec)	0.5	0.5	0.5	1	0.5
Vertical bin size (m)	0.75	1	1.5	1	1.5
Pinging mode	12	12	12	12	12
Beam angle (deg)	20	20	20	20	20
Coordinate system	Earth	Earth	Beam	Beam	Beam
Main measurements	3D velocity, Velocity direction and Magnitude, Echo amplitude, Pitch, Roll, Heading,Range to the bottom, Pressure, Temperature	3D velocity, Velocity direction and Magnitude, Echo amplitude, Pitch, Roll, Heading,Range to the bottom, Pressure, Temperature	3D velocity, Velocity direction and Magnitude, Echo amplitude, Pitch, Roll, Heading,Range to the bottom, Pressure, Temperature	3D velocity Velocity direction and Magnitude, Echo amplitude, Pitch, Roll, Heading,Range to the bottom, Pressure, Temperature	3D velocity Velocity direction and Magnitude Echo amplitude Pitch, Roll Heading,Range to the bottom Pressure Temperature

1.8 General Information and Site Specific Background Data

Meteorological data (horizontal components of wind velocity at 10 m) were provided by Orkney Islands Council Department of Harbours. The wind data, recorded at Sandy Hill ($58^o46.15, -2^o58.05$) which is 92 m above sea level, was supplied at 15 minute intervals. The wind data was converted to the 10 m level using the power-law wind profiles ($U_{10} = U_z(10/z)^{0.14}$) proposed by Wantz *et al.* [122], where U_z was the wind speed at a given elevation z. This dataset are used consequently in the proceeding Chapters.

Chapter 2

Analysis Methods

The purpose of this Chapter is to explore methods for analysing data used in this study. Application of these methods on the field data are presented in Chapters 3 to 6. This Chapter begins with ADCP configurations and transformation of beam velocities measured to velocity vectors. This is followed by the description of the theoretical concepts underlying the study. These include directional wave spectrum, spectral estimates of wave-generated bottom orbital velocities, wave-current interaction and bottom boundary layer turbulence. The details of the derivation of these methods can be found in Appendix A.

2.1 ADCP Configuration

The data used in this study were collected by EMEC using the RDI sentinel, four-transducer 600 kHz broadband ADCP with a tilt angle of 20^o from the vertical axis. The data were collected over the entire water column. It is assumed that the direction of all four beams of the ADCP deviates by the angle $\theta = 20^o$ from a single axis that forms the centerline of the instrument and the beams are orthogonal when viewed from along the centerline. Rotation around the centerline, ξ_1, defines heading (Figure 2.1). The ADCP was also equipped with pitch (ξ_2) and roll (ξ_3) sensors which measure the tilt about horizontal x and vertical y axis (Figure 2.1). If the flow is homogeneous i.e. each velocity component at different beams are identical (or the water velocities do not change significantly in magnitude or direction within the confines of the acoustic beam footprint), the measured instantaneous beam velocities $r_{bi}(i = 1 \ldots 4)$ can be transformed to instantaneous velocities vectors u and w velocities in x and z axis and v and w velocities in y and z directions. For homogeneous flow (Figure 2.5) the error velocity

is approximately zero. Due to the inherent error associated with the individual ping, numbers of pings are averaged and the mean velocities $\overline{u}, \overline{v}$ and $\overline{w}$ are given as (Lu and Lueck [68], RDI [91]) (details of derivations are provided in Appendix A.1.2):

$$\overline{u} = \frac{\overline{r_{b2}} - \overline{r_{b1}}}{2\sin\theta}, \quad \overline{v} = \frac{\overline{r_{b4}} - \overline{r_{b3}}}{2\sin\theta}, \quad \overline{w} = \sum_{i=1}^{4} \frac{\overline{r_{bi}}}{4\cos\theta} \tag{2.1.1}$$

In turbulent flow (e.g., tidal stream site), the assumption of homogeneity will fail and the concept leading to equation (2.1.1) will not be appropriate (see Figure 2.6) . This is because equation (2.1.1) averages out the fluctuating part of the velocities as the beams increasingly diverge from the transducer. The velocities seen by opposite beams will not be the same i.e. $r_{b1} \neq r_{b2}$, $r_{b3} \neq r_{b4}$. It is this inhomogeneous flow that introduces high uncertainty in the ADCP measurements. Research has shown (e.g., Nezu and Nakagawa [75]) that even though the instantaneous velocities are chaotic, the statistics of this chaos can give very good information about the turbulence parameters. Based on this, the Reynolds stress tensor approach, which is based on higher moment flow, has been used in this study to estimate the bulk turbulence parameters. The method, called the *variance method* will be discussed in a proceeding section.

2.2 Wave Spectra

The spectra of random ocean waves can be interpreted as a linear superposition of progressive waves and can be represented mathematically as (Longuet-Higgins [64]):

$$\eta = \eta(x,y,t) = \sum_{n=1}^{\infty} a_n \cos(k_n x \cos\theta_n + k_n y \sin\theta_n - 2\pi f_n t + \epsilon_n) \tag{2.2.1}$$

where a is the wave amplitude, k is the wavenumber, f is the wave frequency, θ is the angle between the x-axis and the direction of wave propagation, f is the wave frequency, ϵ is the phase angle, x, y and t are the space and time coordinates and η represents the water elevation of the water surface above the mean water level. If a wave is observed at a fixed point in the sea, the wave profile is given as (Goda [29]):

$$\eta = \eta(t) = \sum_{n=1}^{\infty} a_n \cos(2\pi f_n t + \epsilon_n) \tag{2.2.2}$$

where a_n and ϵ_n are amplitudes and phase angles of freely propagating independent waves. Since the summation of the squares of wave amplitude in equation (2.2.2) is finite and unique over an interval from f and $f + df$, the sum is given as:

$$\sum_{f}^{f+df} \frac{1}{2} a_n^2 = S(f)df \tag{2.2.3}$$

where $S(f)$ is known as the frequency spectrum.

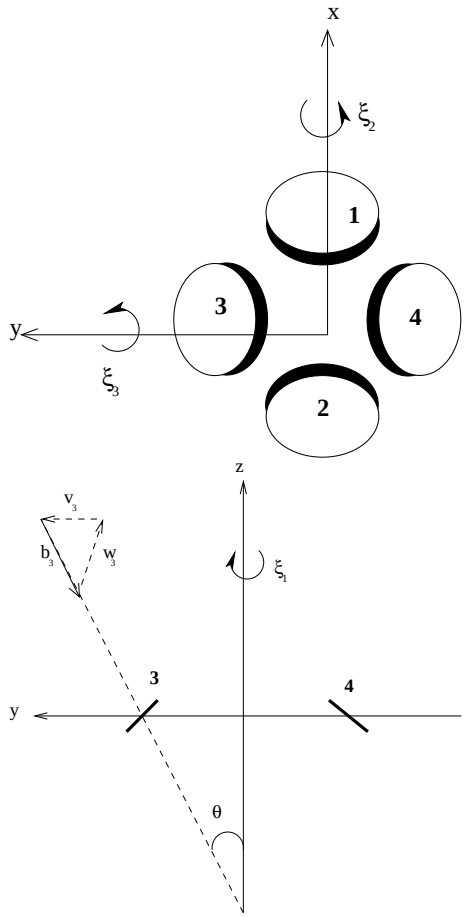

Figure 2.1: Transducer geometry and beam orientation of the ADCP. The beams are inclined by $\theta = 20^o$ from the axis of the instrument, which is normally vertical. Here, ξ_1, ξ_2 and ξ_3 are heading, pitch, and roll angles; (source: Lu and Lueck [68]

The moments of the wave spectrum are defined as:

$$m_n = \int_0^\infty f^n S(f)df \tag{2.2.4}$$

and the zero moment (i.e. $n = 0$) is the area under the spectrum. The significant wave-height, derived from the zero moment is given as:

$$H_{mo} = 4\sqrt{m_o} = 4\sqrt{\int S(f)df} \tag{2.2.5}$$

where $S(f)$ is the spectral density of surface elevation (Ochi [80]). In practice, m_o can be computed from water-level time series or from the integral of the surface elevation. The discrete approximation of equation (2.2.5) can be written as:

$$H_s = 4\sqrt{\sum S_{\eta,i}\Delta f_i} \tag{2.2.6}$$

where the summation is taken over all frequency bins in the spectrum. The mean and energy period is given as $T_m = m_0/m_1$ and $T_e = m_{-1}/m_0$, respectively. The peak period T_p, which is defined as the measure of spectral wave period and is useful for locating the peak in the wave energy spectrum (Tucker and Pitt [116]). The peak period is the period corresponding to period at which the one-dimensional frequency spectrum reaches its maximum. DT_p is the main direction of the peak period (i.e. the highest point in the two-dimensional directional spectrum) and D_p is the dominant direction defined as the direction with the highest energy integrated over all frequencies.

Since the interpretation of random waves is assumed to be a linear superposition of free progressive waves, the correctness cannot be proven, but is supported through evidence of agreement between the properties of real waves and those derived from a mathematical model. Studies (e.g. Longuet-Higgins [66], Goda [29]) have shown that most properties of sea waves have been successfully explained with equation 2.2.1 rather than equation 2.2.2.

For equation (2.2.1) to be a full description of ocean waves, Goda [29] suggested that f_n must have a relatively high density distribution between zero and infinity, θ must be closely distributed between $-\pi$ and π and ϵ_n must be randomly and uniformly distributed between 0 and 2π. Therefore the sum which represents the way wave energy is distributed with respect to frequency and direction is given as:

$$\sum_{f}^{f+df}\sum_{\theta}^{\theta+d\theta}\frac{1}{2}a_n^2 = S_k(k,\theta)dkd\theta = S(f)G(\theta,f) \tag{2.2.7}$$

where $G(\theta, f)$ is the directional spreading function and $S(f, \theta)$ is called the directional wave spectrum. Further details are provided in Appendix A.3.

2.2.1 Methods of Directional Wave Analysis

Several conventional methods for estimating directional wave spectrum have been proposed by several authors. Nwogu [77] reviewed some of these methods. They include Direct Fourier Transform Method (DFTM), the Iterative Maximum Likelihood Method (IMLM), and the Maximum Entropy Method (MEM). However, the shortcoming of these methods is that the algorithms are based on the homogeneity of a sea state. Based on this inherent drawback, Hashimoto [35] developed non-phase-locked methods (Extended Maximum Entropy Principle method (EMEP) and Bayesian Directional spectrum estimation (BDM)) which have been tested and widely used as reliable estimating methods for directional wave spectrum of ocean waves (Hashimoto [35], Horikawa [39]). Further details are provided in Appendix A.3.

Among these methods, BDM seems to provide the highest resolutions but it is computational intensive. The EMEP method has been developed to decrease the time of iterative refinement that is found in the BDM. It uses a Newtonian iterative technique which helps to minimise the errors contained in the cross-spectra. The general expression for EMEP directional spreading function $G(\theta, f)$ is given as (Benoit *et al.* [6]):

$$G(\theta,f) = \frac{\exp\left[\sum_{n=1}^{M}\left\{a_n(f)\cos n\theta + b_n(f)\sin n\theta\right\}\right]}{\int_{-\pi}^{\pi}\exp\left[\sum_{n=1}^{M}\left\{a_n(f)\cos n\theta + b_n(f)\sin n\theta\right\}\right]\mathrm{d}\theta} \tag{2.2.8}$$

where $a_n(f)$ and $b_n(f)$ are the unknown parameters and M is the order of the model. Hashimoto [35] gave more detailed expressions and discussions concerning procedures of the iterative computation. The application of equation (2.2.7) to the field data need to account for the errors in the cross-power spectra. The error in the EMEP estimation is given as:

$$\epsilon_n = \left[\int_{-\pi}^{\pi}\theta_i - H_i(\theta)\right] \times \frac{\exp\left[\sum_{n=1}^{M}\left\{a_n(f)\cos n\theta + b_n(f)\sin n\theta\right\}\right]}{\int_{-\pi}^{\pi}\exp\left[\sum_{n=1}^{M}\left\{a_n(f)\cos n\theta + b_n(f)\sin n\theta\right\}\right]\mathrm{d}\theta}, \quad i = 1,\ldots,M$$

(2.2.9)

where M is the number of remaining independent equations following the elimination of meaningless equations, $a_n(f)$ and $b_n(f)$ are computed iteratively. Details of derivations are provided in Appendix A, section A.2.

2.2.2 Calculating Scheme

The raw output file in binary format from the ADCP was analysed first by the application of Python® open-source programming language [88] and the output is imported into Matlab® [72] for processing. The raw binary ADCP data is split into raw waves and current data by a Python® program. The Python® codes identify the raw data byte header, the type of data and the byte length field in order to separate waves and current raw data. The wave data is further separated into orbital velocities, pressure, ADCP configuration data and range data. Finally the wave data is then imported into Matlab® for directional spectrum computation. The flow chart is shown in Figure 2.2. Due to space limitation, some of the functions (pre-processing code (in Python® and Matlab®), directional wave spectra and turbulence) are provided in Appendix G.1 (Pages 219-252).

2.2.3 A Comparison of Directional Spectrum Estimators: A Case Study Using ADCP data from the Fall of Warness

A 600-kHz four-beam broadband ADCP (RD Instruments Workhorse monitor) was deployed on the seabed, looking upward, in approximately 45 m (mean water depth) of water between 12 March and 13 April 2007. In this section, the DFTM, IMLM and EMEP are applied to estimate the directional wave spectrum of the wave observation records described above and their spectra resolutions are compared.

Figures 2.3 and 2.4 show the directional spectra in polar plots and their corresponding directional wave spectra integrated over frequency for DFTM, IMLM and EMEP.

The resolution potential of each directional spectrum estimating methods was examined. Figure 2.3 presents typical results of the directional spreading for low spectral energy (low waveheight) case and Figure 2.4 for high spectral energy (large waveheight) case. From these figures, it is found that DFTM and IMLM over-predict the directional spreading. Figure 2.4 shows that the performance of DFTM gets poor as the spectral en-

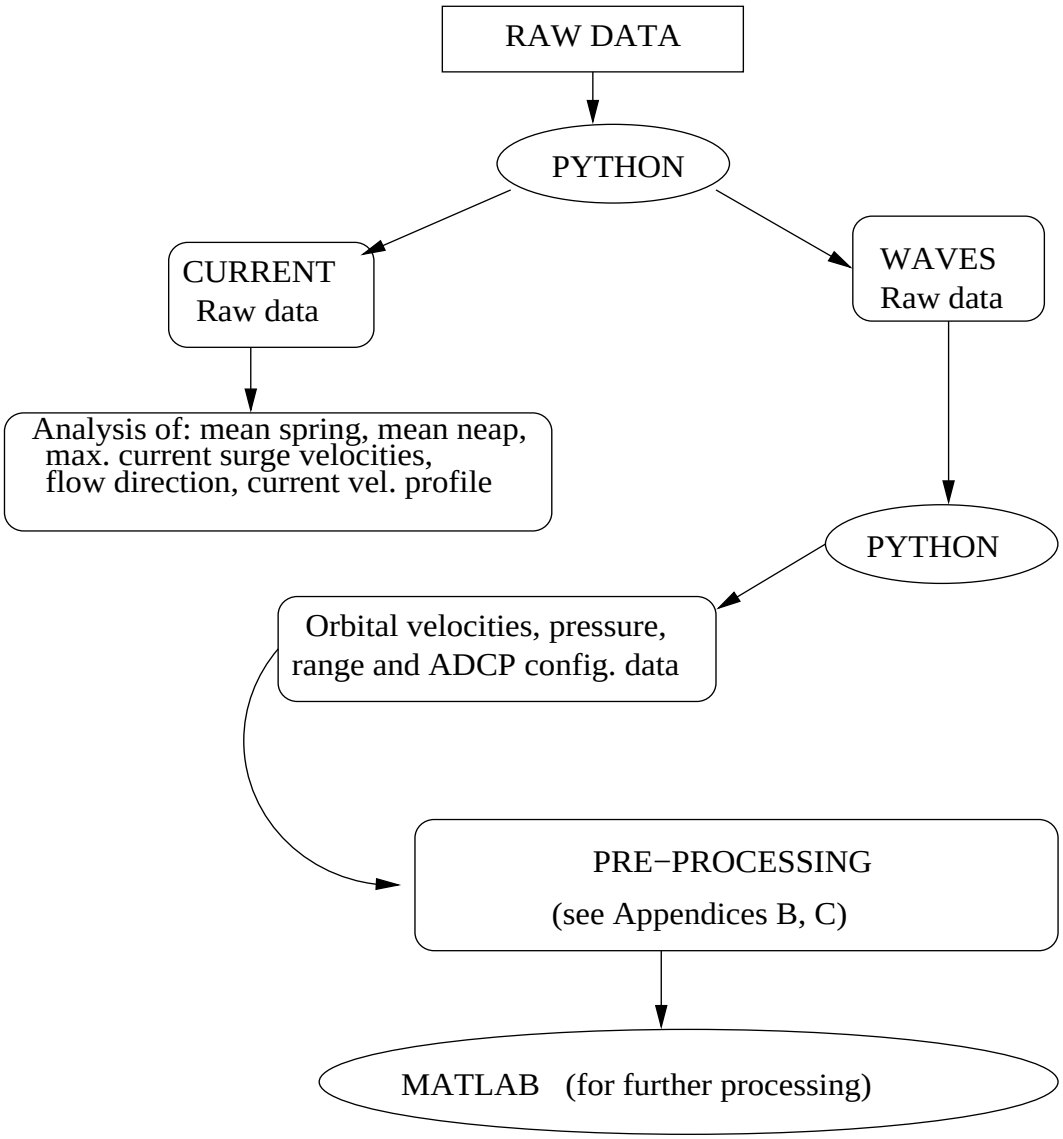

Figure 2.2: Flow chart of ADCP directional wave processing used in this thesis

ergy decreases. On the performance of the bimodal spreading, it can be seen in Figure 2.3 that due to the limited terms of the Fourier series expression in DFTM (Appendix A, section A.3), the capability of DFTM is comparatively poor to other methods. The IMLM seems to be too sensitive to noise contamination and provides poor predictions of the energy distribution especially in the case of large spectral energy (Figure 2.4-middle panel). EMEP performs better with one distinct direction correctly predicted.

The implementation of DFTM does not require lengthy computation but gives a low spectral resolution because of the low order of Fourier series which over-predict the directional spreading. Generally, the DFTM returned skewed estimates and could not distinguish the energy peaks. IMLM estimates are consistent with the data, but the out-

puts are too sensitive to noise contamination and inconsistent from one frequency band to the other and small changes in the noise level can produce significant differences in the returned estimates. It is not also certain if the estimate will iteratively converge in every case. It has also been reported (e.g., Benoit *et al.* [6]) that IMLM is not stable and can give significant directional spreading difference between neighbouring frequency bands. The performance of EMEP on the test ADCP data (low and large spectra energies) has shown that it is capable of giving high-resolution spectra estimates and will be used in the subsequent Chapters to obtain accurate and high-resolution directional spreading.

Similar conclusions were reported by other investigators (e.g., Suzuki *et al.* [112], Huang *et al.* [41], Park *et al.* [85], Cruz and Sarmento [18]).

General observation shows that the estimates of cross-spectrum density in IMLM encounter singularity due to errorneous or dropped data (since the cross-spectrum model from IMLM is based on the ration of Fourier transform of two signals (equation A.3.15)), the IMLM estimator may perform unsatisfactorily with the ADCP data from energetic tidal tidal site and hence EMEP is preferred for directional wave spectra in this study.

2.3 Spectral Estimates of Wave-generated Bottom Orbital Velocities

The spectrum of bottom boundary layer wave-generated orbital velocities can be computed from a surface-wave spectrum S_η defined in equation (2.2.3). By applying each frequency band of the wave spectrum from wave orbital velocity, the resulting equation gives (Soulsby [104]):

$$S_{u,i} = \frac{4\pi^2}{T_i^2 \sinh^2(k_i h)} S_{\eta,i} = \frac{\omega_i^2}{\sinh^2(k_i h)} S_{\eta,i} \tag{2.3.1}$$

where T is the wave period, h is the water depth, k is the wavenumber. Summing up the $S_{u,i}$ in equation (2.3.1) over each frequency gives:

$$u_{br}^2 = 2\sum_i S_{u,i} \Delta f_i \tag{2.3.2}$$

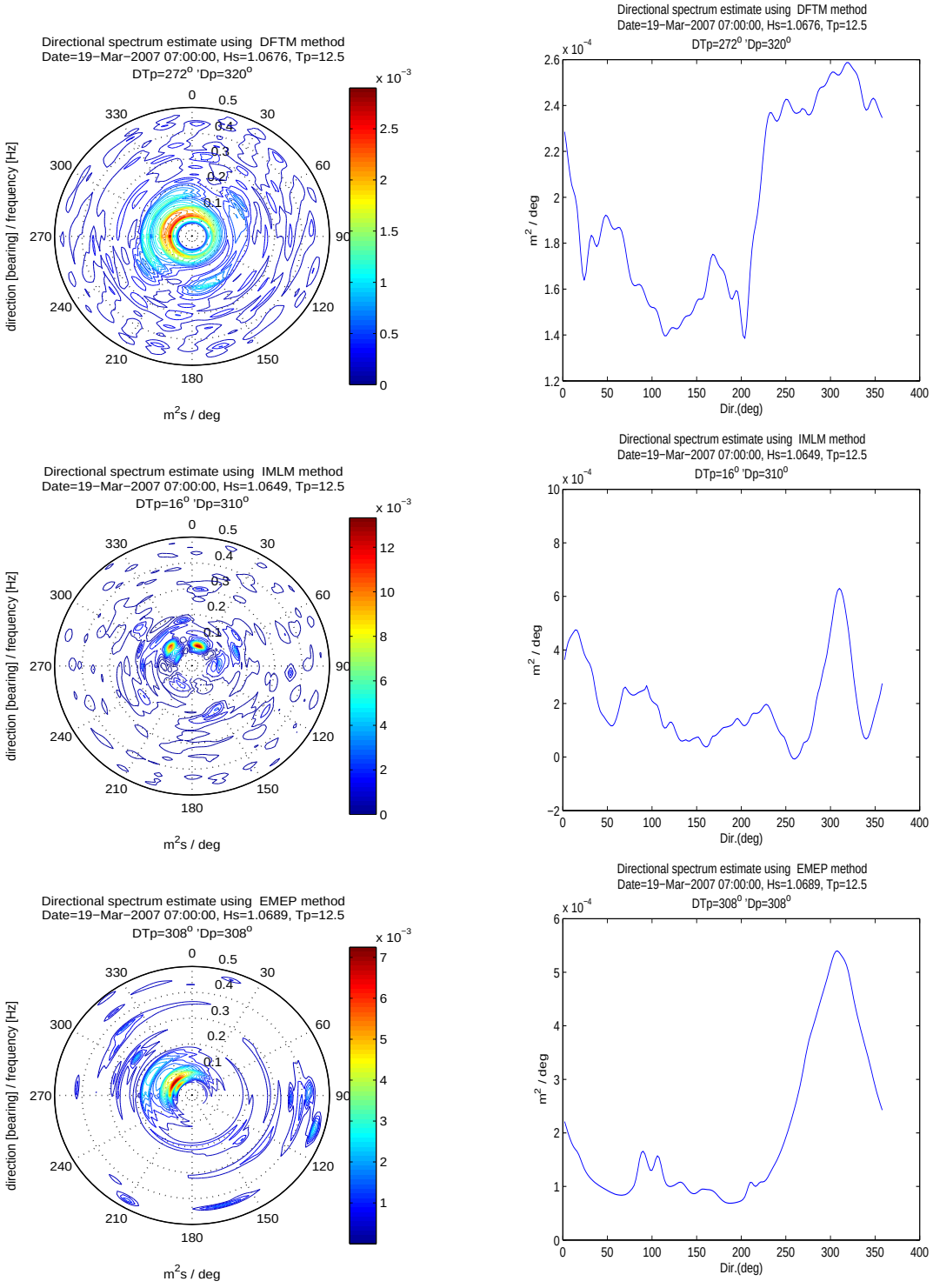

Figure 2.3: Directional spectrum estimated using DFTM, IMLM and EMEP methods: 19 March 2007 07:00:00

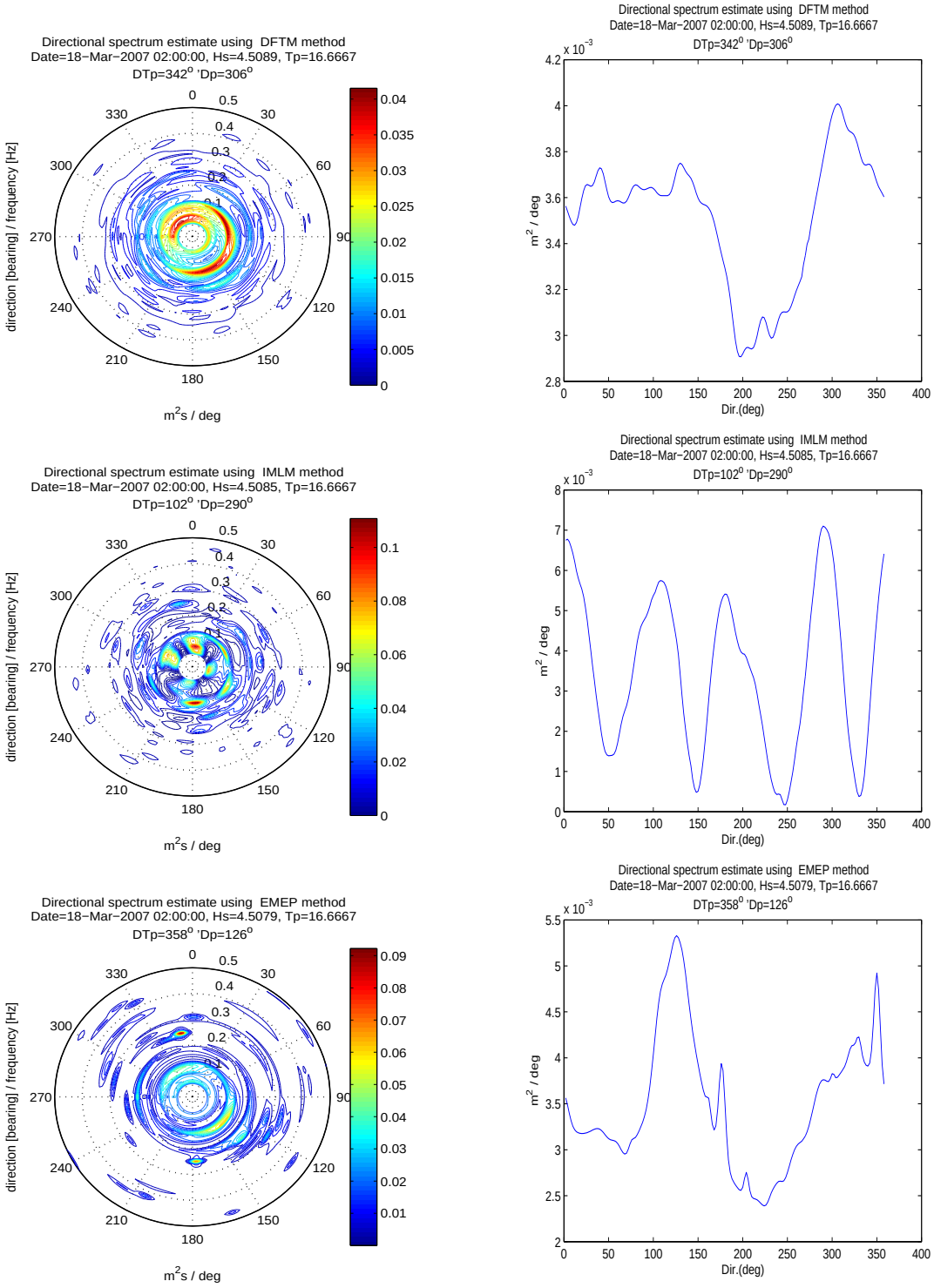

Figure 2.4: Directional spectrum estimated using DFTM, IMLM and EMEP methods: 18 March 2007 02:00:00

(Note: $a_{rms}^2 = H_{rms}^2/4 = 2m_0 = 2\int S_\eta df$ and $u_b =$ amplitude of wave orbital velocity at the bed). The bottom orbital velocity can be derived by substituting equation (2.3.1) into equation (2.3.2) to yield (Madsen [71]):

$$u_{br} = \sqrt{2}\left(\sum_i \left[\frac{4\pi^2}{T_i^2 \sinh^2(k_i h)} S_{\eta,i} \Delta f_i\right]\right)^{0.5} \tag{2.3.3}$$

The u_{br} can also be defined as the root-mean squared value of the bottom orbital velocity. The significant orbital velocity can be defined with respect to significant wave height as (Madsen [71]):

$$u_{bs} = \sqrt{2}u_{br} = 2\left(\sum_i \left[\frac{4\pi^2}{T_i^2 \sinh^2(k_i h)} S_{\eta,i} \Delta f_i\right]\right)^{0.5} \tag{2.3.4}$$

Further details are provided in Appendix A.4.

2.4 Wave-current Interaction Model

As discussed in Chapter 1, the boundary layer consists of the current boundary layer (relatively steady low frequency) overlaid with a wave boundary layer (oscillatory, turbulent, high frequency). Greater bottom shear stress induced by wave action can be felt at the bed if the maximum bottom orbital velocity of the waves (described in section 2.3) has the same or higher order of magnitude as the current stream velocity. Grant and Madsen [31] found that a nonlinear wave-current interaction process generates a shear stress that is different from the sum of the two components and they proposed a detailed method to calculate shear stress and velocities near the bed. Later, Christoffersen and Jonsson [17] discovered some weaknesses in the Grant and Madsen model, such as the introduction of fictitious reference velocity at an unknown level which may be different for different current velocities. They proposed a simpler solution which has been shown to give a better result than the previous model (e.g., Jacobs [46], Tanaka and Dang [114], Rosales *et al.* [96]).

The Christoffersen and Jonsson's model is described as follows:

If

$$\frac{\partial \mathbf{u}}{\partial t} + (\mathbf{u} \cdot \nabla)\mathbf{u} + w\frac{\partial \mathbf{u}}{\partial z} + \frac{1}{\rho}\nabla p = \frac{\partial}{\partial z}\left(\frac{\tau}{\rho}\right) \tag{2.4.1}$$

$$p = p_c + p_w \quad ; \quad \mathbf{u} = \mathbf{u}_c + \mathbf{u}_w \tag{2.4.2}$$

represents the horizontal equilibrium, where $\mathbf{u}$ is the total horizontal particle velocity, t is time, z is the vertical distance measured upwards from the bed, w is the vertical particle-wave velocity, $\nabla(= \partial/\partial x)$ is the horizontal gradient operator, x and y are horizontal Cartesian coordinates, ρ is the water density, p is the total pressure, and τ is the total shear stress in a horizontal section, c and w indicate the components caused by the current and the wave. Here, p and u consist of a steady current part and oscillatory wave part.

The shear stress can be defined as:

$$\tau = \tau_c + \tau_w \quad ; \quad \tau_b = \tau_{cb} + \tau_{wb} \tag{2.4.3}$$

and the current motion as:

$$\rho\epsilon_c\frac{\partial \mathbf{u}_c}{\partial z} = \tau_c(1 - \frac{z}{h}) \tag{2.4.4}$$

where the subscript b indicates a quantity at the bed, ϵ_c is the eddy viscosity in the current-boundary layer and h is the water depth.

$$\frac{\partial}{\partial t}(\mathbf{u}_w - \mathbf{u}_{wb}) = \frac{\partial}{\partial z}\left(\frac{\tau_w}{\rho}\right) = \frac{\partial}{\partial z}\left(\epsilon_w\frac{\partial \mathbf{u}_w}{\partial z}\right) \tag{2.4.5}$$

is defined as the wave motion within the wave-boundary layer, where ϵ_w is the eddy viscosity and $\mathbf{u}_{wb}$ is the horizontal-wave orbital-velocity at the top of the wave-boundary layer.

The current f_c and wave f_w friction factors for wave-current flows are determined from:

$$\sqrt{\frac{2}{f_c}} = \frac{1}{\kappa}\ln\frac{30h}{ek_N} + \frac{1}{\kappa}\ln\frac{k_A}{k_b} \tag{2.4.6}$$

where $e(= exp(1) = 2.718\ldots)$ and

$$\frac{m}{4.07\sqrt{mf_w}} + \log\frac{1}{4.07\sqrt{mf_w}} = -0.1164 + \log\left(\frac{a_{bm}\omega_r}{k_b\omega_a}\right) \tag{2.4.7}$$

The total bed shear-stress can be calculated as:

$$\tau_{bm} = \frac{1}{2}f_w\rho u_{br}^2 m \tag{2.4.8}$$

where

$$m = \left(1 + \sigma^2 + 2\sigma|\cos(\delta - \alpha)|\right)^{0.5} \tag{2.4.9}$$

and

$$\sigma \equiv \frac{\tau_{cb}}{\tau_{wbm}} = \frac{f_c}{f_w}\left(\frac{U}{u_{br}}\right)^2 \tag{2.4.10}$$

From equations (2.4.9) and (2.4.10)

$$m \equiv \left(1 + \frac{\tau_{cb}^2}{\tau_{wbm}^2} + 2\frac{\tau_{cb}\cos(\delta - \alpha)}{\tau_{wbm}}\right)^{0.5} \tag{2.4.11}$$

or

$$m \equiv \left(1 + \frac{f_c^2U^4}{f_w^2u_{br}^4} + 2\frac{f_cU^2\cos(\delta - \alpha)}{f_wu_{br}^2}\right)^{0.5} \tag{2.4.12}$$

where κ is the von Kármán constant (=0.40), k_N is the Nikuradse roughness, and k_A is the apparent roughness, k_b is the bottom roughness, log denotes the base 10, $a_{bm}(= u_{bs}/\omega_r)$ (section 2.3, equation 2.3.4) is the wave orbital semi-excursion, $\omega_a(= 2\pi/T_a)$ is the absolute wave angular-frequency, and $\omega_r(= \sqrt{gh\tanh kh})$ is the relative wave angular-frequency, σ is the ratio of τ_{cb} (bottom shear stress due to currents) to τ_{wbm}, the

amplitude of τ_{wb}, (i.e., τ_{wbm} is the maximum value of the oscillatory bed shear stress τ_{wb} due to waves). δ is the angle of the current direction and α is the angle of the wave direction. Note that if $\tau_{cb} \gg \tau_{wbm}$, then:

$$m \rightarrow \frac{f_c}{f_w}\left(\frac{U}{u_{br}}\right)^2 \tag{2.4.13}$$

i.e. the second term in equations (2.4.11) or (2.4.12) will dominate over the third term. For example if $U = 1, u_{br} = 0.1, f_c = 0.1, f_w = 0.01, \delta = 270, \alpha = 90$, the second term in equation (2.4.11) (i.e. τ_{cb}^2/τ_{wbm}^2) gives 10^6 while the third (i.e. $2\tau_{cb}\cos(\delta - \alpha)/\tau_{wbm}$) equals -1.1969×10^3.

Thus $\tau_{bm} \rightarrow \tau_{cb}$. Similarly, if $\tau_{cb} \rightarrow \tau_{wbm}$ (i.e. $\sigma \rightarrow 1, m = 2$ forces $(\delta - alpha) = 1$), then $m \rightarrow 1$ and $\tau_{bm} \rightarrow \tau_{wbm}$.

2.4.1 Wave-current Interaction Calculating Scheme

The following calculating scheme, which was proposed by Christoffersen and Jonsson [17] has been used in this study.

1. *"Compute f_c from equation (2.4.6) with $k_A = k_N$ (pure current);*
2. *Compute f_w from equation (2.4.10) and equation (2.4.7) with $m = 1$ (pure waves);*
3. *Keeping f_c fixed, iterate through equation (2.4.10), equation (2.4.9) and equation (2.4.7) until sufficient accuracy is obtained for sigma, m and f_w;*
4. *Compute a new f_c value from equation (2.4.6);*
5. *Repeat steps 2-4 until sufficient accuracy has been obtained for f_c".*

A Matlab® function that implements these calculations is provided in Appendix G.

2.5 The Variance method

As discussed in section 2.1 in a inhomogeneous sea state, equation (2.1.1) will not be suitable because it will average out turbulent contributions as the ADCP beams increasingly diverge from the transducer. It is therefore not possible to use ADCP data directly

in order to estimate both vertical and horizontal Reynolds stresses. One method of addressing this is to estimate the covariances from velocity variance of opposing ADCP beams. This approach is called the variance method. This method was firstly applied to ADCP data by Lohrmann [63] and has been developed by many researchers (e.g., Stacey *et al.* [106], Lu and Lueck [68], [69], Gross and Nowell [34]) over the last decade.

As discussed in section 2.1, each ADCP beam ($b_i, i = 1, \ldots, 4$) measures a weighted sum of the local horizontal and vertical velocity. The beam velocities are given as:

$$\begin{aligned} b_1 &= -u\sin\theta - w\cos\theta \\ b_2 &= u\sin\theta - w\cos\theta \\ b_3 &= -v\sin\theta - w\cos\theta \\ b_4 &= v\sin\theta - w\cos\theta \end{aligned} \tag{2.5.1}$$

where u, v represent horizontal velocities, w is the vertical velocities and θ is the beam angle (20^o for the ADCP used for this study). Instantaneous velocity is the sum of the mean (e.g., $\overline{u}$) and the fluctuating part (e.g., u') of the velocity. Therefore by separating each velocity into a mean and the fluctuating quantity gives:

$$\begin{aligned} u' &= u - \overline{u} \\ v' &= v - \overline{v} \\ w' &= w - \overline{w} \\ b'_1 &= b_1 - \overline{b_1} \\ b'_2 &= b_2 - \overline{b_2} \\ b'_3 &= b_3 - \overline{b_3} \\ b'_4 &= b_4 - \overline{b_4} \end{aligned} \tag{2.5.2}$$

Substituting equation (2.5.2) into equation (2.5.1) gives the variance of the along beam velocities as:

$$\overline{b'^2_1} = \overline{u'^2}\sin^2\theta + \overline{w'^2}\cos^2\theta + 2\overline{u'w'}\sin\theta\cos\theta \tag{2.5.3}$$

$$\overline{b'^2_2} = \overline{u'^2}\sin^2\theta + \overline{w'^2}\cos^2\theta - 2\overline{u'w'}\sin\theta\cos\theta \tag{2.5.4}$$

$$\overline{b'^2_3} = \overline{v'^2}\sin^2\theta + \overline{w'^2}\cos^2\theta + 2\overline{v'w'}\sin\theta\cos\theta \tag{2.5.5}$$

$$\overline{b'^2_4} = \overline{v'^2}\sin^2\theta + \overline{w'^2}\cos^2\theta - 2\overline{v'w'}\sin\theta\cos\theta \tag{2.5.6}$$

Taking the difference of the variance of opposite beams (i.e. equation (2.5.3 minus equation (2.5.4) and equation (2.5.5 minus equation (2.5.6), the along - and cross-stream Reynolds stresses are derived as (Stacey *et al.* [106], Lu and Lueck [68], [69]):

$$\overline{u'w'} = \frac{\overline{b'^2_1} - \overline{b'^2_2}}{4\sin\theta\cos\theta} \tag{2.5.7}$$

and

$$\overline{v'w'} = \frac{\overline{b'^2_3} - \overline{b'^2_4}}{4\sin\theta\cos\theta} \tag{2.5.8}$$

Application of this method on ADCP data has shown (e.g., Lu and Lueck [69], Gross and Nowell [34]) additional assumptions must be made before the turbulent kinetic energy (TKE), $q^2/2 = (\overline{u'^2} + \overline{v'^2} + \overline{w'^2})/2$ can be estimated from ADCP data. Lu and Lueck proposed the TKE density S as:

$$S = \frac{1}{1+\alpha}\left(1 + \frac{2\alpha}{\tan^2\theta}\right)\frac{q}{2} \tag{2.5.9}$$

and

$$\alpha = \frac{\overline{w'^2}}{(\overline{u'^2} + \overline{v'^2})} \tag{2.5.10}$$

where α represents the turbulence anisotropy. For measurement in unstratified flow,

Stacey *et al.* [106] and Nezu and Nakagawa [75] found empirically the value of α to be 0.17, and this value was determined appropriate to be used in this study. This is because the water column in the Fall of Warness is well mixed (density gradient approximately constant) and the flow unstratified.

The transfer of energy from the mean flow to TKE, which is known as TKE production, P, is given as:

$$P = -\rho\left(\overline{u'w'}\frac{\partial\overline{u}}{\partial z} + \overline{v'w'}\frac{\partial\overline{v}}{\partial z}\right) \tag{2.5.11}$$

where ρ is the water density and $\partial\overline{u}/\partial z$ is the vertical velocity gradient. Shear stress in the water column is proportional to the vertical velocity gradient and the constant of the proportionality is the eddy viscosity. It is defined as:

$$A_z = \frac{1}{\rho}\frac{P}{\left[\left(\frac{\partial\overline{u}}{\partial z}\right)^2 + \left(\frac{\partial\overline{v}}{\partial z}\right)^2\right]} \tag{2.5.12}$$

Equation (2.5.12) will break down when the vertical velocity gradient is close to zero, most especially during slack water. The eddy viscosity is responsible for the dynamic of mixing in the water column.

Stacey *et al.* [106] and Williams and Simpson [124] estimated the level of uncertainties in the stress estimate caused by the ADCP, velocity variability and averaging. According to Williams and Simpson [124], the uncertainties in stress, shear and the rate of shear production estimates are given respectively as:

$$\sigma_{st}^2 = \rho^2\gamma\left(\frac{\sigma_b^2 + \overline{x_i^2}}{M\sin^2 2\theta}\right)^2 \tag{2.5.13}$$

$$\sigma_{sh} = \gamma_s\frac{(\mathrm{var}[u_{2(n+1)} - u_{1(n+1)} - u_{2(n-1)} + u_{1(n-1)}])}{4M(\Delta z)^2\sin^2\theta} \tag{2.5.14}$$

and

$$\sigma_{pr}^2 = (\overline{u'w'})^2\sigma_{sh}^2 + \left(\frac{\partial u}{\partial z}\right)^2 \sigma_{st}^2 + \sigma_{st}^2\sigma_{sh}^2 \tag{2.5.15}$$

where σ_b^2 is the variance in beam-velocity due to instrument noise, $\overline{x_i^2}$ is the variance due to velocity variability, M is the number of samples in a variance computation period. From equation (2.5.15), if $\overline{u'w'} \to 0$ and $(\partial u/\partial z) \to 0$, then the last term will dominate for the low-flow case, and the other two terms are expected to be more significant at higher flow.

2.5.1 Inertial Dissipation Method (IDM)

The dissipation rate ε of TKE is important especially when considering the energy balance. There are several definitions of IDM given in the literature but the author considers the description from Stapleton [109] the most succinct. It states that *"IDM is based on the assumption that if the wavenumbers at which the turbulent energy is produced and dissipated are well separated, (the region of separation is known as the inertial subrange) the flux of energy from low to high wavenumber is equal to the dissipation rate, as there are no sinks or sources of energy within the wavenumbers of the sub-range"*.

According to Lorke and Wuest [67], the spectrum in a given direction can be written as

$$\phi_i(k) = \alpha_i \varepsilon^{2/3} k^{-5/3} \tag{2.5.16}$$

where k is the one dimensional wave number, α_i is the one dimensional Kolmogorov constant, ϵ is the energy dissipation rate and the subscript i represents a given direction.

The drawback of the above definition is that it assumes that there is a local equilibrium between the production and dissipation of turbulent energy. In reality, this may not be the case.

$$\phi_i(f) = \alpha_i \varepsilon^{2/3} \left(\frac{2\pi}{\overline{u}}\right)^{-2/3} f^{-5/3} \tag{2.5.17}$$

where $\phi_i(k) = \phi(f)\overline{u}/2\pi$ represents the Taylor concept of *frozen turbulence* to convert the wavenumber spectra to velocity spectra (Nezu and Nakagawa [75]).

From equation (2.5.17), ϕ_i is estimated from the ADCP time series data and thus ε by spectral fitting (e.g., Gross and Nowell [34], Lorke and Wuest [67], Stapleton [109], Stapleton and Huntley [110]).

Stapleton and Huntley provided a simpler algorithm for calculating ϕ_i and it has been adopted for use in this study. The procedures are given below:

1. *" Calculate the spectrum of the time series; averaging is done automatically within Matlab® dividing the time series into segments of the specified length (usually a power of 2 for simplicity when calculating using fast Fourier transforms) which overlap by 50% of the length of the segment. For example, if the time series has 8192 points, it can be divided into 15 shorter series of 1024. This overlapping is done to increase the number of degrees of freedom of the spectrum.*
2. *Calculate predicted limits of inertial sub-range;*
3. *Plot the spectrum on log-log axes to check for $-5/3$ roll-off;*
4. *The main algorithm is to calculate the inertial sub-range frequency and amplitude, $\phi(f)$. This gives a mean point within the inertial sub-range through which a line with a gradient of $-5/3$ may be plotted. The intercept of this line with the $log\phi$ (i.e. where $log f = 0$) axis gives a value for $log\alpha_i\epsilon^{2/3}(2\pi/\bar{u})^{-2/3}$, i.e.*

$$\phi_i(f) = \alpha_i\epsilon^{2/3}(2\pi/\bar{u})^{-2/3}f^{-5/3} \tag{2.5.18}$$

taking logs gives

$$log[\phi_i(f)] = log[\alpha_i\epsilon^{2/3}(2\pi/\bar{u})^{-2/3}] - \frac{5}{3}log(f) \tag{2.5.19}$$

so where $log(f) = 0$, (i.e. $f = 1$):

$$log[\phi_i(f)] = log[\alpha_i\epsilon^{2/3}(2\pi/\bar{u})^{-2/3}]'' \tag{2.5.20}$$

A Matlab® function that implements these calculations is provided in Appendix G, Page 250.

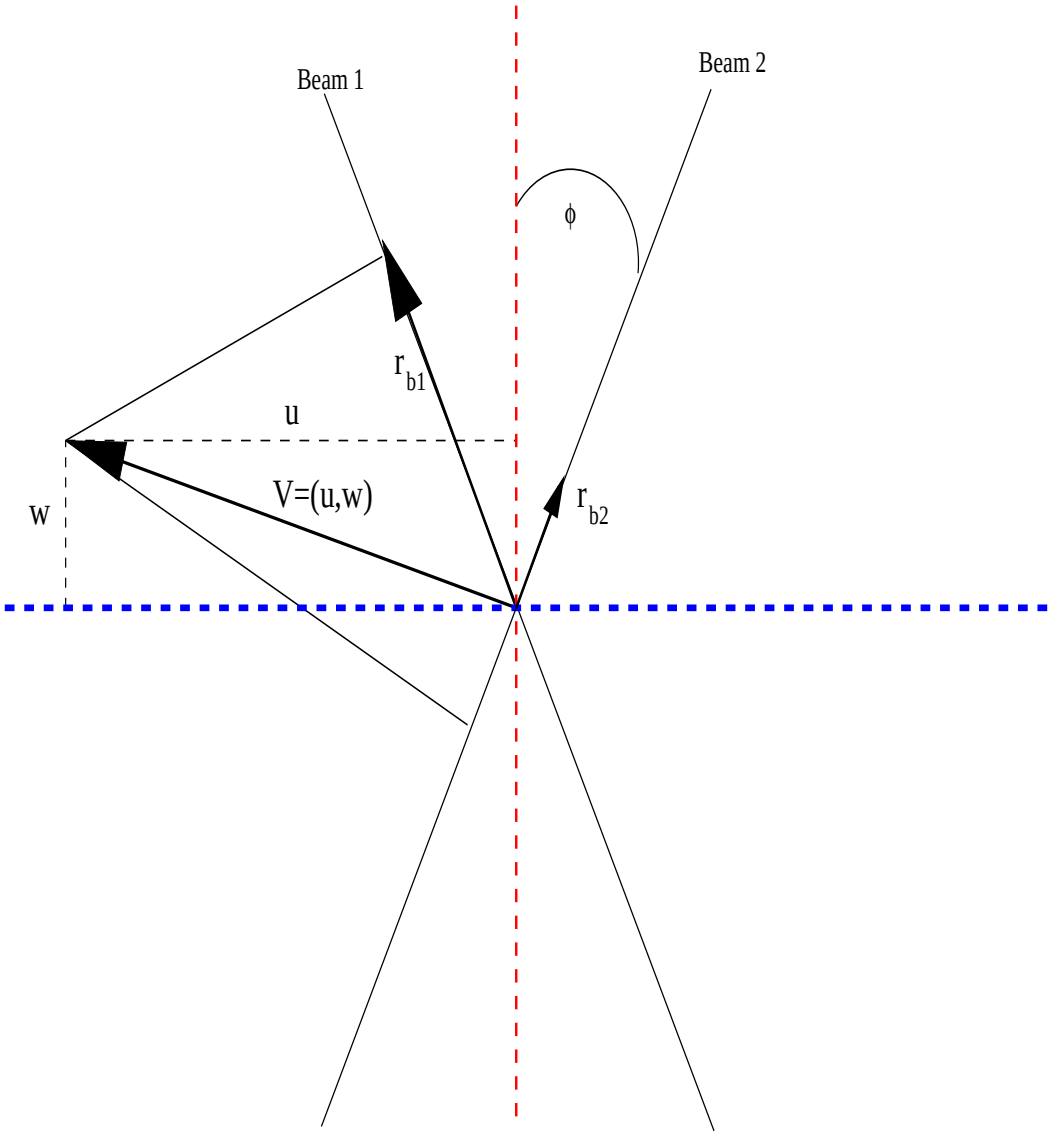

Figure 2.5: Projections of mean velocities $\overline{u}$ and $\overline{w}$ onto acoustic radial lines (r_{rb1} and r_{rb2}) ; Homogeneous flow case

2.5.2 *The Second Order Structure Function Method (2SFM)*

The second order structure function method was used in this thesis as the second method to calculate the dissipation rate ε. Lhermitte [61] was the first to apply this method to compute ε from radar measurements. Wiles *et al.* [123] recently extended this method to estimate ε from ADCP data. It is based on the assumption of isotropic turbulence. The major drawback has been that it underestimates the dissipation values. The method is based on the theory that a second order structure function $Z(z,r)$ at any depth z can be defined as:

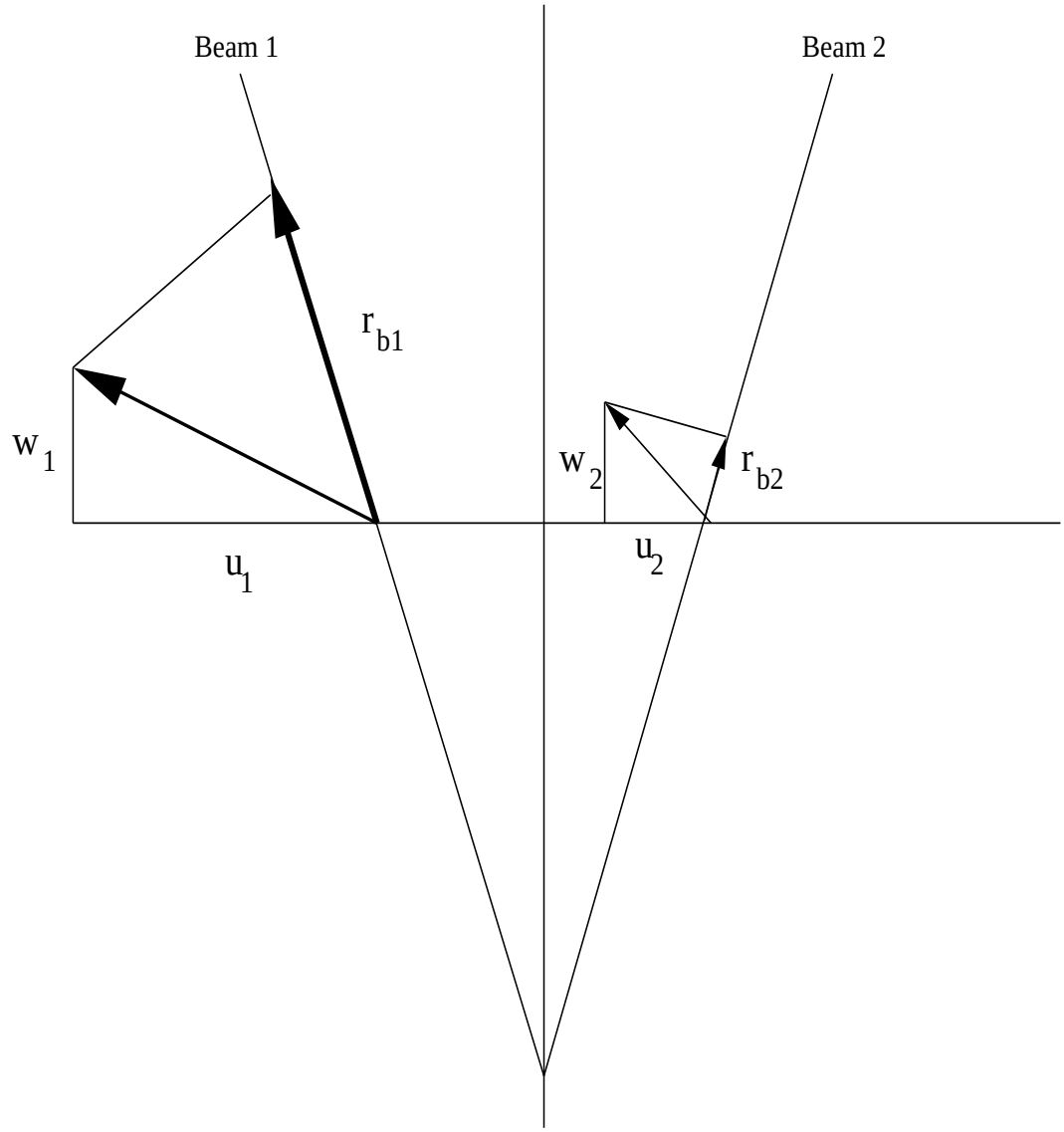

Figure 2.6: Projections of mean velocities $\overline{u}$ and $\overline{w}$ onto acoustic radial lines (r_{b1} and r_{b2}) ; Nonhomogeneous flow case

$$Z(z,r) = \overline{(u(z) - u(z+r))^2} \tag{2.5.21}$$

where $Z(z,r)$ is the mean-square of the along beam velocity fluctuation (u') difference between two point separated by a distance r. The assumption that the velocity difference due to eddies of the length scale equal to r was the basis upon which Wiles *et al.* [123] obtained his result.

Using the Taylor's cascade theory to relate the length scales and velocity scales to isotropic eddies, $Z(z,r)$ can be defined as:

$$Z(z,r) = C_v^2 \varepsilon^{2/3} r^{2/3} \tag{2.5.22}$$

where C_v^2 is known as the Kolmogorov constant (Yeung and Zhou [128]). The value of C_v^2 varies between 2 and 2.2 which depends on the ratio of r/ϑ where ϑ is the Kolmogorov microscale. For atmospheric and marine studies, Sauvageot [97] suggested C_v^2 to be between 2 and 2.2. A value of 2.1 is used in this study which is assumed to be a good approximation as suggested by other studies (e.g., Mohrholz *et. al* [74], Wiles *et. al* [123]). If a straight line is fitted to $Z(z,r)$ versus r, then

$$Z(z_i,r) = Ar^{2/3} + N, \quad \text{with} \quad A = C_v^2 \varepsilon^{2/3} \tag{2.5.23}$$

where N is an offset representing the uncertainly due to noise. From equation (2.5.23), the dissipation rates ε can be estimated as:

$$\varepsilon = \left(\frac{A}{C_v^2} \right)^{3/2} \tag{2.5.24}$$

Wiles *et al.* proposed a central difference method algorithm to calculate the dissipation rates ε. The description is given in Table 2.1.

Table 2.1: 2SFM Method Description

Separation	General Algorithm	Example ($i = 6$)
$r = 2$	$u(i+1) - u(i-1)$	$u(7) - u(5)$
$r = 3$	$u(i+2) - u(i-1), u(i+1) - u(i-2)$	$[\{u(8) - u(5)\} + \{u(7) - u(4)\}]/2$
$r = 4$	$u(i+2) - u(i-2)$	$u(8) - u(4)$
$r = 5$	$u(i+3) - u(i-2), u(i+2) - u(i-3)$	$[\{u(9) - u(4)\} + \{u(8) - u(3)\}]/2$

A Matlab® function that implements these calculations is provided in Appendix G, Page 252.

Summary of the data used in this study are listed in Table 1.1.

2.6 Analysis Flowchart

Figures 2.7 - 2.11 shows flowcharts of the ADCP data processing used in this study. The raw ADCP data contains binary files of orbital velocities for each ADCP depth cells, pressure, and range to the surface in each of the four beams and instrument configuration data, which has not been subjected to processing or any other manipulation. Figure 2.7 depicts the summary of the algorithm beginning from the raw data obtained from the ADCP. The raw data is split by Python code into separated waves and currents binary files. The raw waves data file is further process (as described in Figure 2.8) into 4 separate text files ready to be loaded into Matlab. These include a pressure record, a range record for each of 4 beams, a radial velocity record for each of 4 beams at 5 particular bin depths (for a total of 20 radial velocities), and a system configuration file which contains information such as the bin layout, date and time, heading, pitch and roll.

The orbital velocities are the along-beam velocities measured at very high data rates (e.g. 0.5 s) in a series of bins extending along each beam away from the ADCP transducers. Choosing bins near the surface allows measurement of much higher frequency waves to be measured. During a turbulent sea states, sound may glance off the surface without sending any signal back in the direction of the ADCP (RDI [90]). Under this situation, unlike range measurements, the velocity measurements remain robust. Such conditions are expected at the Fall of Warness and the reason for using orbital velocities measurements over range measurements for the computation of situation directional wave spectra.

The binary currents file is output and processed as describe in Figure 2.9 and the binary waves file (Figure 2.10) with Matlab code. The raw data were quality controlled and screened for spikes and missing data using methods described in Appendix B. Figure 2.9 is a flowchart depicting in more the detail directional wave spectra presented in section 2.2 and equations 2.2.1 - 2.2.9 which include calculating the cross-spectral matrix (equations A.3.35 - A.3.39). The method begins at equation B.0.2 where initial processing is performed (Appendix B). Next, the cross-spectral matrix, $\phi_j(f)$, is calculated (equation A.3.38). Proceeding to equation A.3.39, the directional spectrum is calculated at each observed frequency and wave number. This calculation includes estimating the directional spectrum using EMEP (section A.3.3) which is normalized at each observed frequency and wave number. The wave power spectrum is calculated utilizing the normalized directional spectrum and the normalized directional spectrum is scaled using

the wave power spectrum. Figure 2.11 shows a flowchart of the turbulence estimation using the variance method (section 2.5). The measurements of velocity which are made instantaneously, without any temporal averaging, but have a time resolution of typically of 1 and 2 (depending on the configuration of the instrument (section 1.6). The instantaneous velocity data undergo extensive quality control analysis to ensure that they meet stringent accuracy standards. The quality indices apply to these data are: (a) side-lobe contamination near the sea surface (b) statistical non-homogeneity of beams over the variance computation period (c) statistical non-homogeneity of horizontal and vertical velocities over the distance between beams (d) frequent values below the noise floor (e) surface or internal wave bias, and (f) ADCP motion. The quality analysis involves automatic flagging of data that fall outside of broad error specifications. Next, remaining data are checked against a narrower range of error specifications, and those that fall outside this range generate an error alert message. However, questionable data are not automatically removed. The suspect data are checked for validity. Using the individual velocity measurements ('single-ping data'), the Reynolds stresses in the flow can be calculated by first evaluating the variance of each along-beam velocity component, and then differencing opposite beams (equations 2.5.7-2.5.8). By summing the variances of the opposite beams, the cross terms (involving the Reynolds stresses) cancel one another, and the result contains contributions from individual components of the turbulent kinetic energy.

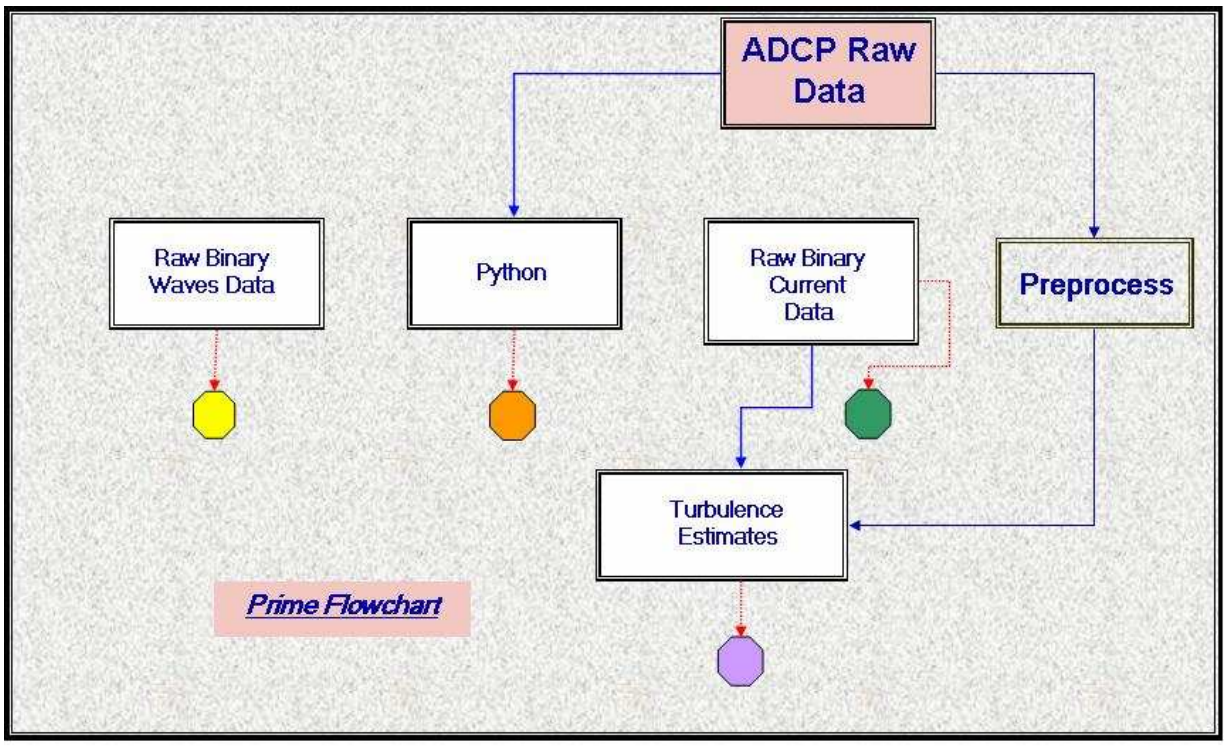

Figure 2.7: Prime flowchart: Spliter

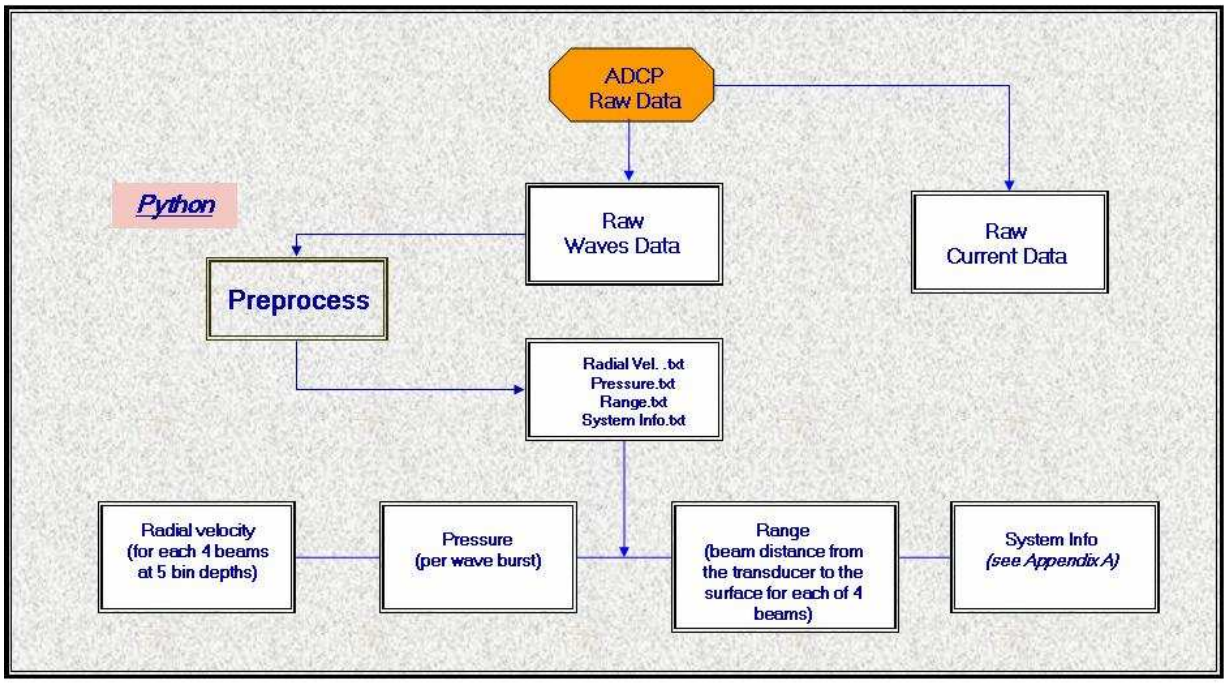

Figure 2.8: Raw wave data Prime flowchart

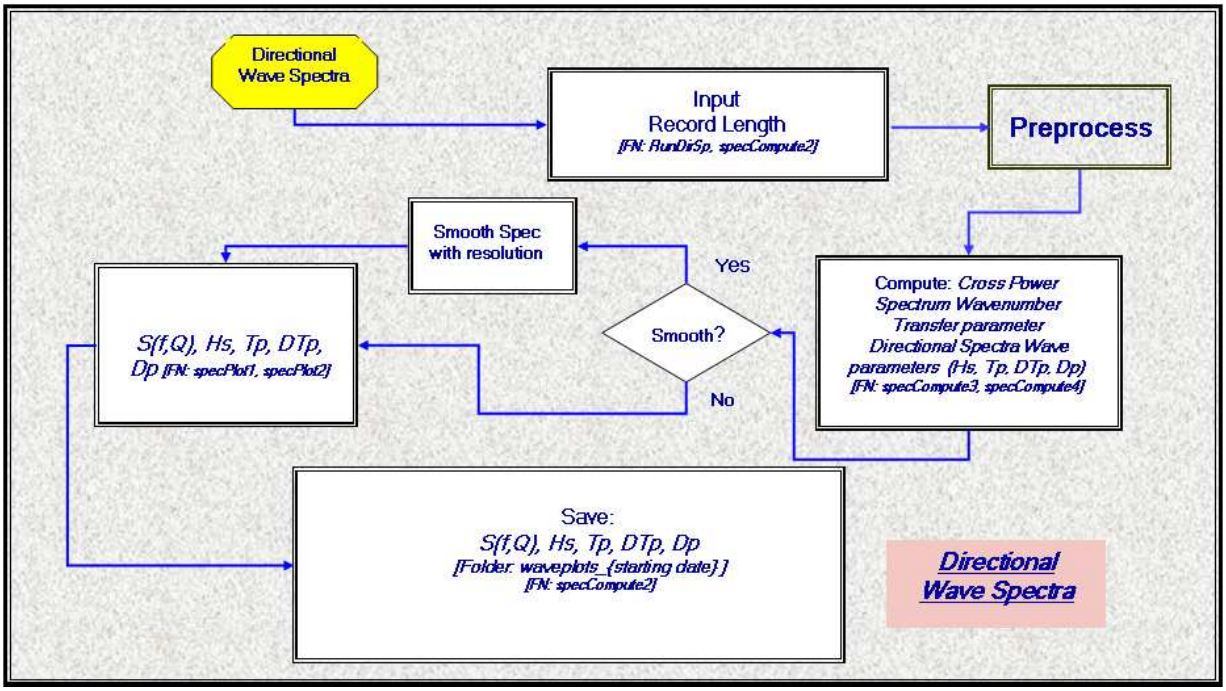

Figure 2.9: Directional wave spectra analysis flowchart

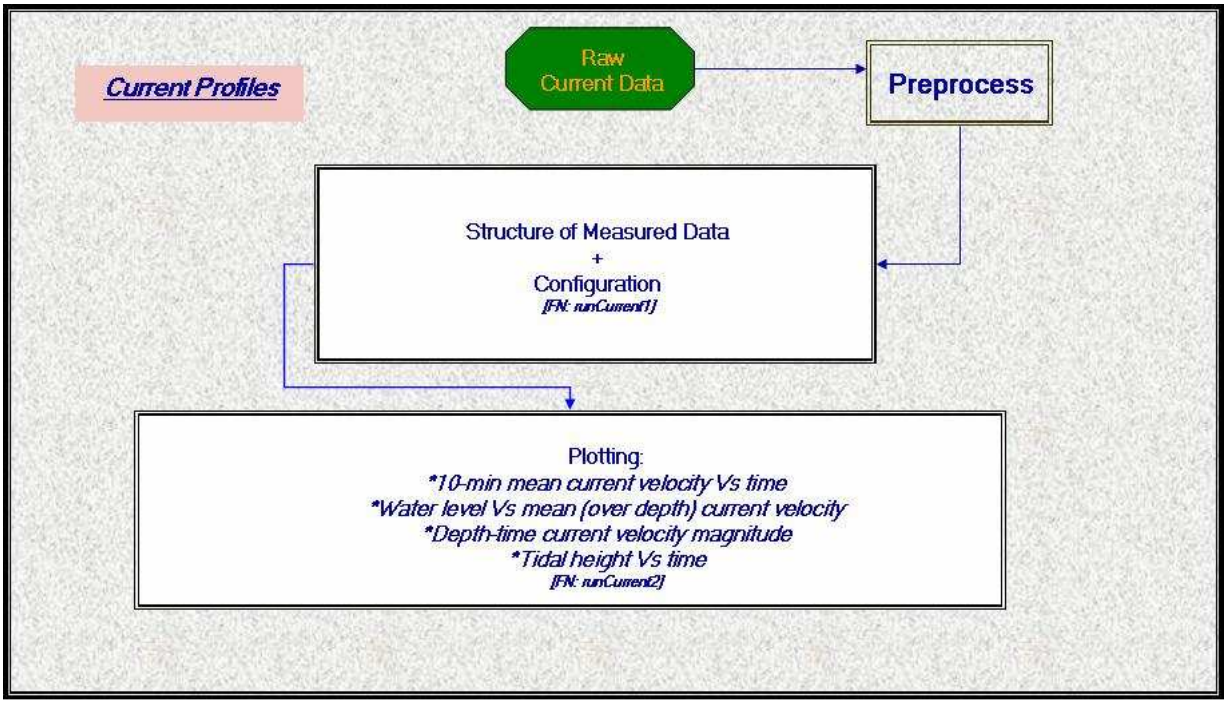

Figure 2.10: Current analysis flowchart

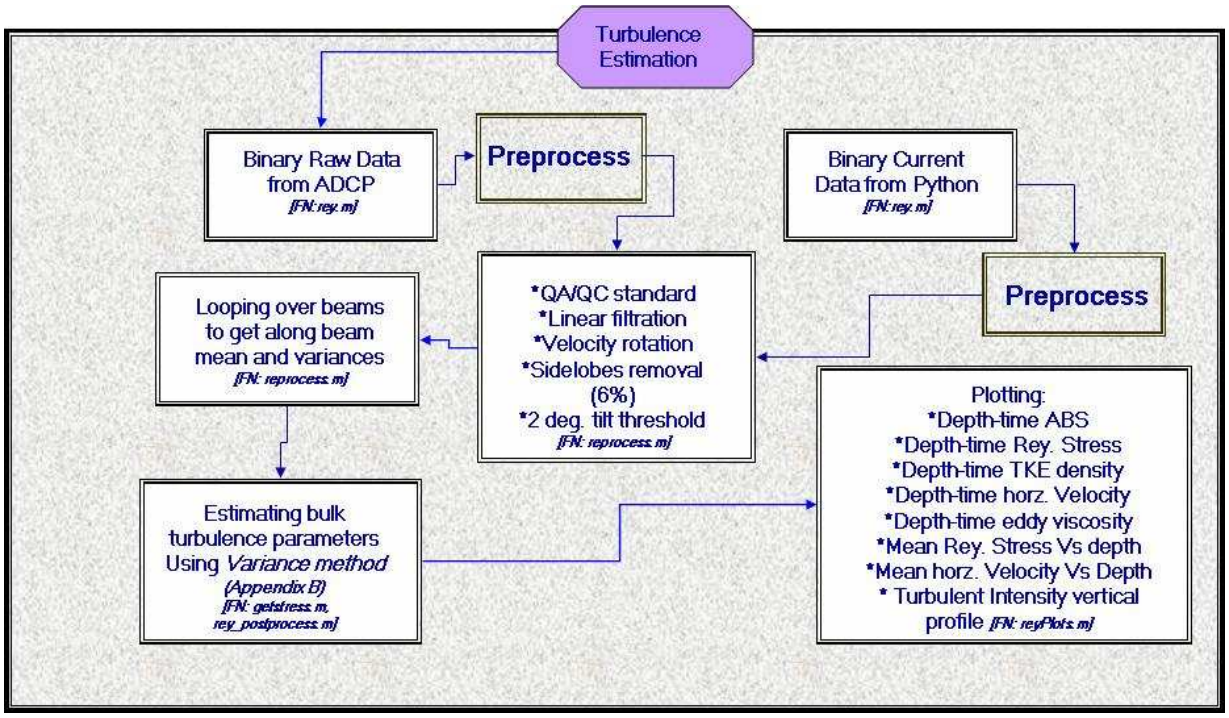

Figure 2.11: Turbulence analysis flowchart

Chapter 3

Observations of the Directional Spectrum of Ocean Waves and Current Profiles at the European Marine Energy Centre's Fall of Warness Tidal Test Site, Orkney Islands

In this Chapter, the estimates of the directional wave spectrum and current profiles have been obtained from ADCP measurements undertaken by EMEC and recorded between 18th-30th August 2005, at the EMEC's Fall of Warness tidal test site in Orkney Islands (Figure 3.1).

The data was collected at 29 m mean water depth. The temporal characteristics of the dynamics in the Fall of Warness tidal inlets are captured well by the ADCP, and show that the maximum ebb velocity slightly exceeds the maximum flood velocity (Admiralty [1]). The maximum speed was up to $\sim 3.6ms^{-1}$ at the water surface during spring and $\sim 2.5ms^{-1}$ during the neap tide. The wave climate over the recorded period was dominated by Northwesterly swells ($10-20s$) and Southerly wind-waves ($5-10s$). Maximum significant wave height recorded was $\sim 3.80m$. Currents in the Fall of Warness are mainly bi-directional, and are stronger during the ebbing tide [23]. A major asymmetry was revealed between the time $T_{e\rightarrow f}$ needed for the transition between maximum ebb and maximum flood as compared to the time needed for the inverse transition $T_{f\rightarrow e}$. During the a spring cycle, ebb periods were $\sim 1.08\%$ longer than the flood, and mean ebb currents were $\sim 4.12\%$ higher. Maximum ebb currents were $\sim 3.88\%$ larger than the flood ones. Neap tides presented a change in the degree of asymmetry between ebb and flood stages both in terms of duration, mean and maximum velocity.

Figure 3.1: ADCP location in 18-30 August 2005; (source: Google Earth)

3.1 Introduction

As discussed in Chapter 1, the success of tidal stream devices is dependent on the understanding of how these devices behave when interacting with waves and tidal streams. It is therefore essential that the characterisation of the tidal stream site is crucial to the success of the marine tidal energy industry. In a tidal stream sites, waves and currents are the dominant hydrodynamics. While surface waves may be driven by ocean storms and local wind, currents are mainly driven by tides. Since most of the tidal stream sites fall below 50 m water depth (classified as shallow water, based on mean water depth), orbital velocities near the seabed can become significant and a turbulent wave boundary layer (as discussed in Chapter 1, section 1.5) is evident. Oscillatory seabed shear-stress will characterise such a flow (Dean and Dalrymple [20]). Dean and Dalrymple [20] investigated waves travelling over finite depth. They reported that bottom friction, through a nonlinear process, contributes to the dissipation of wave energy which takes place within the thin turbulent wave boundary layer above the seabed. As discussed in Chapter 1, section 1.5, the strength of the overlying current boundary layer will be enhanced.

The combined functionality of the ADCP to measure both waves and currents in a single package had attracted the interest of many researchers in exploring their efficacy as a wave sensor e.g., as opposed to a waverider buoy. A waverider buoy uses two acceleration sensors (vertical - oscillation of the sea surface and horizontal - correction for undesired accelerations) to measure waves. The significant wave height is measured by integrating the vertical acceleration. However, accurate measurement requires that the buoy be designed to follow the water surface and the accelerometer remain vertical. Tucker and Pitt [116] pointed out that a waverider buoy equipped with accelerometers may produce distorted horizontal displacement measurements due to mooring constraints in currents greater than $2.5ms^{-1}$ (the drawback of using a waverider buoy in an energetic tidal site).

Recently, Jeans *et al.* [47], Hathaway and Long [36] and Work [126] compared the efficiency of ADCPs and other instruments (e.g., waverider buoy, ADV) to measure waves correctly. They concluded that the directional estimates from the ADCP gave similar results for all wave parameters and compared well with other sensors. Though measurement were done in calm conditions and the author knows no measurement comparisons in a turbulent environment like the Fall of Warness.

3.2 Study Area and ADCP Deployment

A 600-kHz four-beam broadband ADCP (RD Instruments Workhorse monitor) was deployed on the seabed, looking upward, in approximately 29 m (mean water depth) of water between 18th-30th August, 2005. The survey was conducted by EMEC approximately 4 km West of the Island of Eday in the Orkney Islands, the EMEC's tidal energy test site at the Fall of Warness, location $59^o09.323'$, $2^o49.515'$ (Figure 3.1).

This location is characterised by high velocity marine currents which reach almost $3.6ms^{-1}$ at spring tides and 2.5 ms^{-1} during neap tides. The instrument was bolted into a frame on a gimbal with the transducers located about 1.86 m above the seabed. Current velocity profiles were sampled every 24 s with 0.75 m vertical cell spacing. Directional wave data were sampled for 20 min (2400 samples) every hour at a sampling rate of 2 Hz.

Strong winds of speeds up to $23ms^{-1}$ incident from Southwest were generally noticed (Figure 3.2 - first two upper panels), except on the 19 August, 2005 when the wind direction changed from the South to the North with a wind speed reduced to $3ms^{-1}$.

3.3 Results and Discussions

Figure 3.3 shows the vertical profiles of the tidal stream velocity magnitude and direction. Variations in velocity magnitude can been seen for the spring (18-26 August, 2005) and neap (26- 30 August, 2005) tides (upper panel). Current speed reached $\sim 3.6ms^{-1}$ at mean spring peak velocity close to the water surface and $\sim 2.5ms^{-1}$ during the neap. ADCP data captured the temporal (on a diurnal scale) characteristics of the dynamics in the Fall of Warness and show that the maximum ebb velocity slightly exceeds the maximum flood velocity.

Pre-processing of the data was performed as discussed in Appendix B (Pages 219-252) and the processing steps undertaken are shown in Figure 2.2. In Matlab®, any invalid (erroneus spikes) values in the text files were removed through interpolation with the neighboring elements (discussed in Appendix B) and the radial velocities in instrument coordinates were converted into u,v,w velocities in Earth coordinates. The analysis programs also use the heading, pitch and roll to compute the surface locations of each of the 4 range beams, and the x,y,z positions of each of the radial velocities. Range data with EMEP estimation method proposed by Hashimoto [35], gave the best resolution

for spectral and directional peak (as demonstrated in section 2.2.3), and this was used in this study. Range data is the along beam distance from the ADCP to the surface of the water for each of four beams. The vertical component of this distance is then calculated and de-meaned. This gives the surface elevation change at four distinct x,y locations at the surface, enabling the estimation of a directional wave spectrum. In this analysis, the directional resolution of 2 degrees and a frequency resolution of 0.01 Hz ranging from 0.01 to 0.4 Hz were used (Figure 3.4). The significant wave heights H_s, peak wave periods T_p, dominant wave direction DT_p were obtained as discussed in Chapter 2, section 2.2. The zeroth moments (m_0) of this frequency spectra can be defined as:

$$m_0 = \int_{f_1=0.01}^{f_2=0.4} S_\eta(f)\mathrm{d}f \tag{3.3.1}$$

where f is the frequency, $S_\eta(f)$ is the surface elevation spectrum, f_1 and f_2 are, respectively, the minimum and maximum frequencies of the spectra. Orbital velocity spectra $S_u(f)$ were determined by transforming the directional wave spectra and integrating over direction (0 to 360^o) (Chapter 2, section 2.3) ; then integrating the orbital velocity spectra over frequency (0.01 to 0.04 Hz). The near-bed orbital diameter is given as:

$$d_0 = 2A_{rms} \tag{3.3.2}$$

where $A_{rms} = u_{bs}/\omega$ is the orbital semi-excursion, u_{bs} is the significant orbital velocity, defined in Chapter 2, section 2.3 and $\omega = 2pi/f$ is the radial frequency.

Figure 3.4 shows the spectra for selected two hour periods for neap (26 August 2005) cycle. The directional spectra (left hand side) show the peak energy incident from West-Northwest (WNW) during the obervational period. The frequency spectra of the same data were plotted in the right hand side of Figure 3.4. As expected, the two spectra show the same trend with highest energy recorded around 10 seconds, but a reduced magnitude for near-bed orbital velocity frequency spectra (left hand side) due to the fact that shorter waves attenuate with water depth more rapidly than longer waves.

Table 3.1 reveals the asymmetry between the maximum ebb and flood at the Fall of Warness. The transition time between ebb and flood (represented by $T_{e\rightarrow f}$) was compared with the time needed for the reverse flow i.e. flood to ebb ($T_{f\rightarrow e}$). It is clear from

Table 3.1 columns 3 and 5 that the tidal asymmetry is not constant but changes between ebb and flood, spring and neap tides. Table 3.1 columns 4, 6 and 7 show the comparison of tidal heights, mean and maximum velocities for ebb and flood, spring and neap tides. Interestingly, the ebb periods were $\sim 1.08\%$ longer than the flood during spring tides while the mean ebb currents were up by $\sim 4.12\%$. Maximum ebb current were $\sim 3.88\%$ higher than the flood current. The maximum flood current for each tidal cycle was computed as the maximum value of the current between the corresponding higher low water and higher high water while the maximum ebb current was estimated as the maximum current value between corresponding lower high and lower low water. Generally, the neap tides showed a change in the degree of asymmetry between ebb and flood more distinctly than flood to ebb in terms of duration, mean and maximum velocity than during the spring tide.

Tables 3.2-3.3 show the significant wave height H_s (column 3), peak wave period, T_p (column 4), peak wave direction DT_p (column 5), near-bottom orbital velocity u_{br} (column 6) and orbital diameter d_0 (column 7) (equation 3.3.2) calculated during two tidal cycles for spring (20/08/2005 00:40 - 20/08/2005 23:40) and neap (26/08/2005 00:40 - 26/08/2005 23:40). The H_s ranged from $\sim 0.2 - 3.8$ and $\sim 0.4 - 1.28$ m, spring and neap respectively. The T_p observed were between $\sim 7.5 - 20$ and $\sim 2.8 - 11.6$ s, spring and neap, respectively.

The largest H_s during the spring ($\sim 3.8m$ with longer peak period of $\sim 16s$) and neap cycles ($\sim 1.28m$ with short peak period of $\sim 7.8s$) are due to waves coming from the WNW. Generally, the peak wave direction for both spring and neap data observed for the chosen dates is from the West-Northwest. It appears that WNW seas travelling from the Atlantic produce increased significant wave heights (see Figure 3.2). As expected, the values of significant wave height H_s, near-bottom orbital velocity u_{br} and orbital diameter d_0 during the spring tide are higher compared to these values during the neap tide.

3.4 Conclusions

This Chapter discussed the observations of the directional spectrum of ocean waves and current profiles at the EMEC's tidal energy test site. Analysis of the current profiles and directional wave field were performed. The directional wave data collected in the Fall of Warness during late summer (August 2005) clearly shows the wave response to the

changing wind direction and intensity. The temporal characteristics of the dynamics in the Fall of Warness tidal inlets are captured well by the ADCP, and show that the maximum ebb velocity slightly exceeds the maximum flood velocity. The following conclusions can be drawn from this Chapter:

1. The tidal stream velocity reached $\sim 3.6ms^{-1}$ at mean spring peak velocity close to the water surface and $\sim 2.5ms^{-1}$ during the neap tide. The tidal height changes with the current speed;

2. Tidal asymmetry changes between ebb and flood, spring and neap at the Fall of Warness (Based on 24 tidal cycles). The ebb duration, mean and maximum values were $\sim 1.08\%$, $\sim 4.12\%$ and $\sim 3.88\%$ higher than flood current values, respectively;

3. During the spring tide (e.g.,Figure 3.5), the significant wave height H_s ranges between ~ 0.2 and ~ 3.8 m and ~ 0.4 and ~ 1.28 m during neap tide. An increase in H_s value corresponds to an increase in wave-induced orbital velocity;

4. The WNW seas from the Atlantic corresponds to severe sea states in term of significant wave heights;

5. The shorter peak periods and smaller significant wave heights were observed during the neap tides compared with the spring tide, suggesting that the magnitude of current has an influence on the wave field.

It should be noted that the rapid variability in the wave analysis (see Figure 3.5) has further showed the drawback of using ADCP to measure waves in an energetic environment.

These results are further examined with different datasets in the subsequent Chapters.

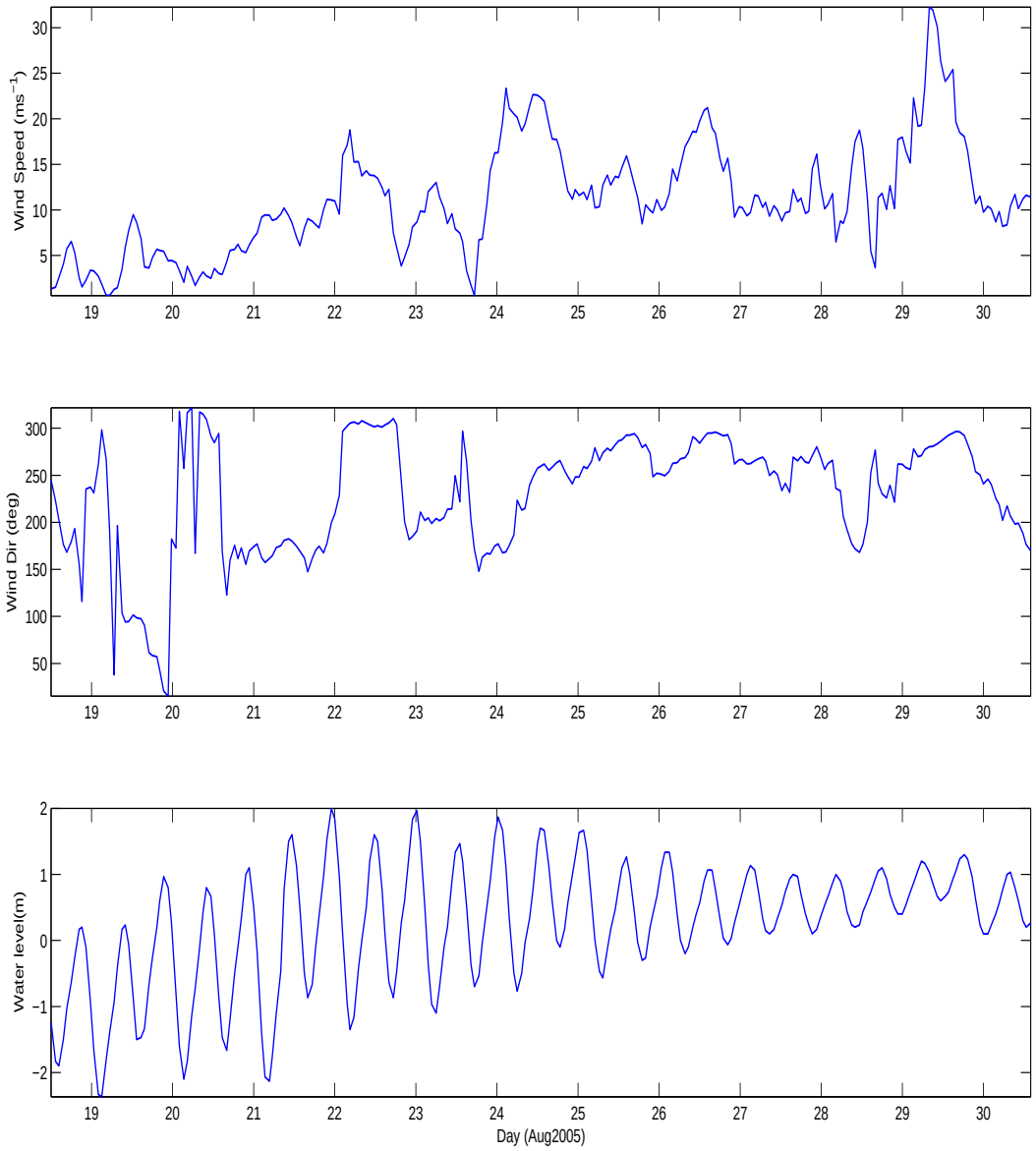

Figure 3.2: Time series of (a) wind speed (ms^{-1}), (b) wind direction (deg), (c) water level (m): (a)-(c)= upper - bottom panel

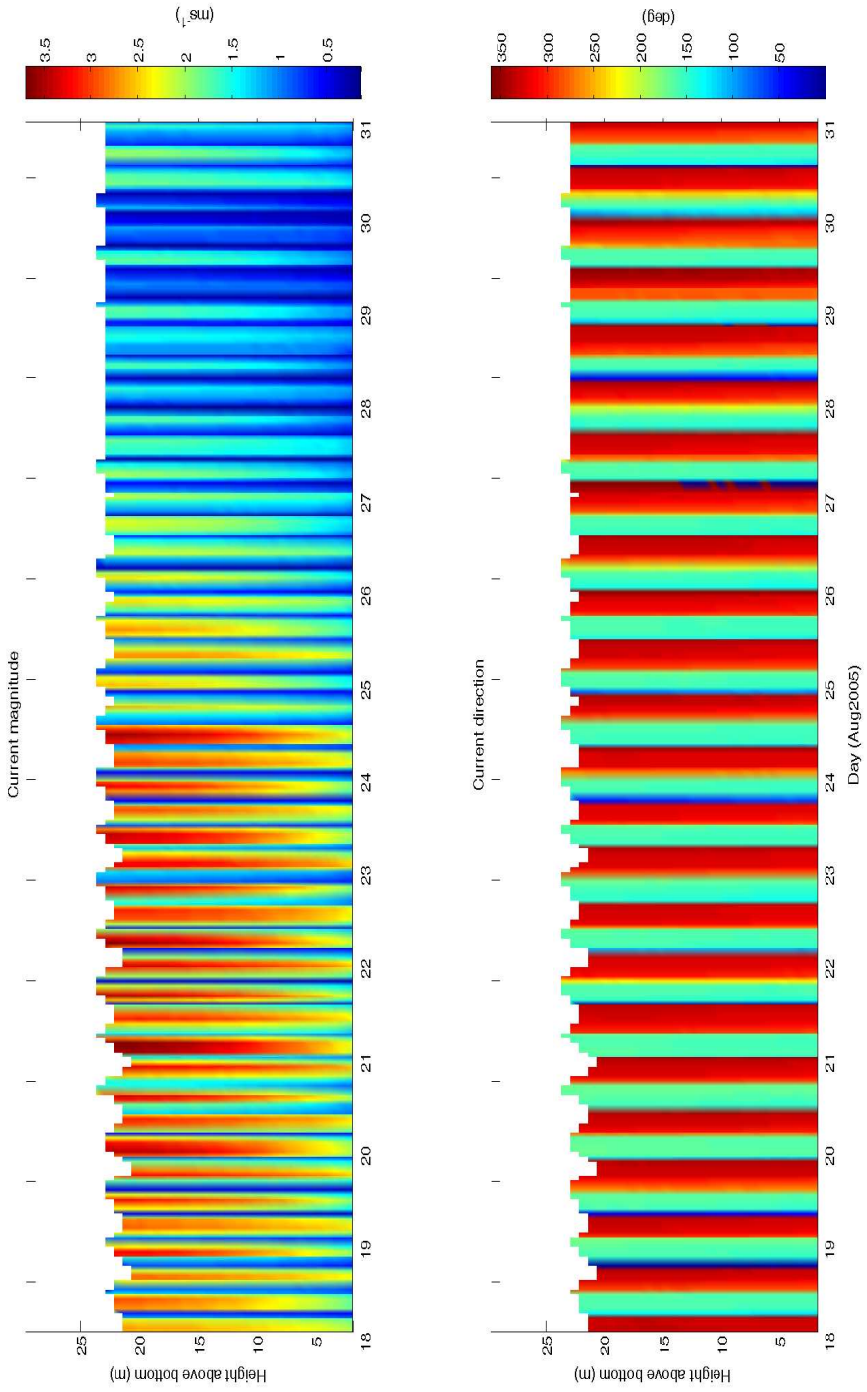

Figure 3.3: Depth-time series of current velocity (ms^{-1}) (flood flow=positive, ebb flow=negative) (upper panel) and current direction (deg) (bottom panel); (Spring: 18-24 August, Neap: 25-31 August)

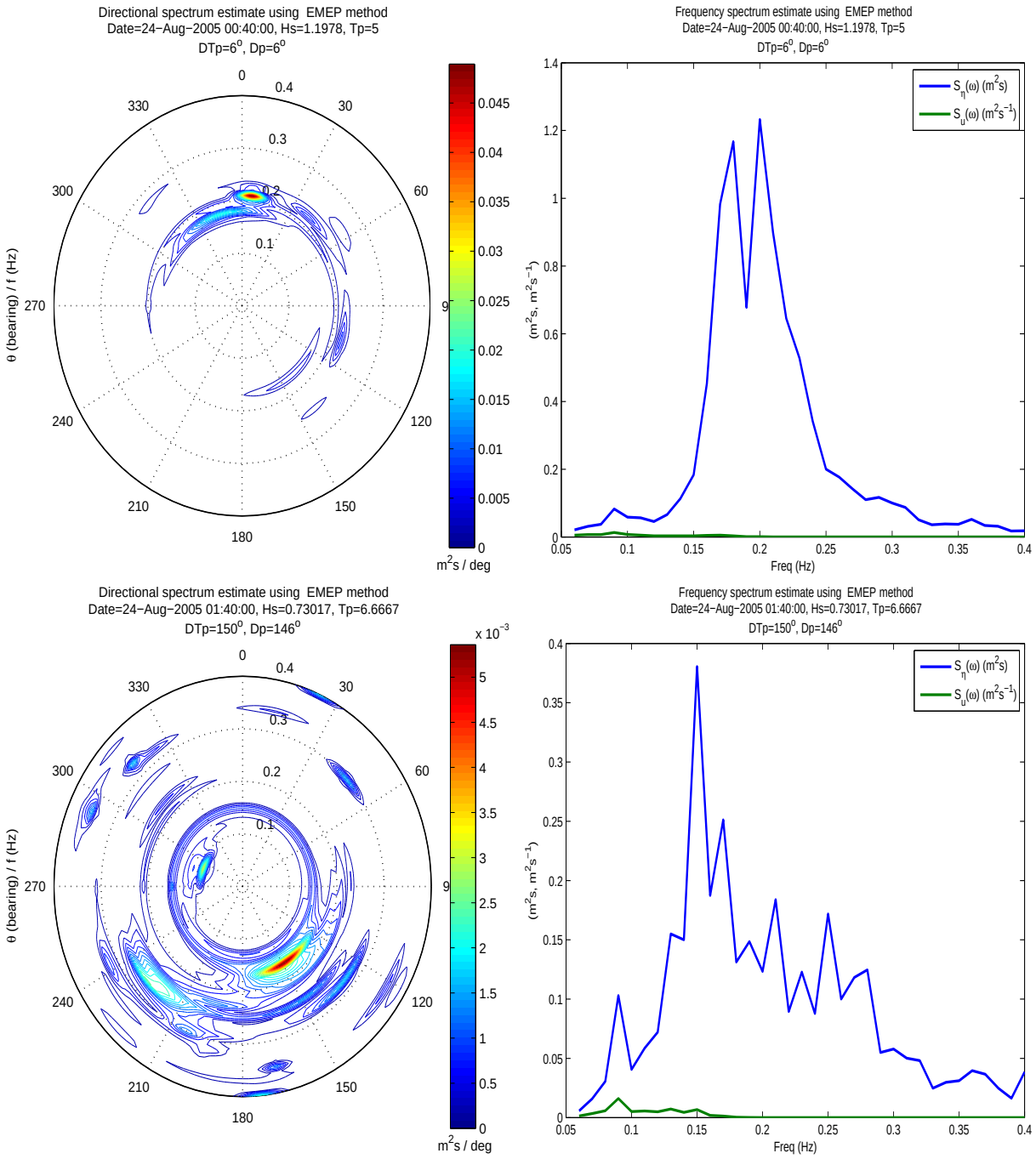

Figure 3.4: Directional spectrum (left hand side) , frequency spectra of surface elevation, $S_\eta(\omega)$ (right hand side - blue colour), and bottom orbital velocity (right hand side - green colour), $S_u(\omega)$ during a neap tide cycle

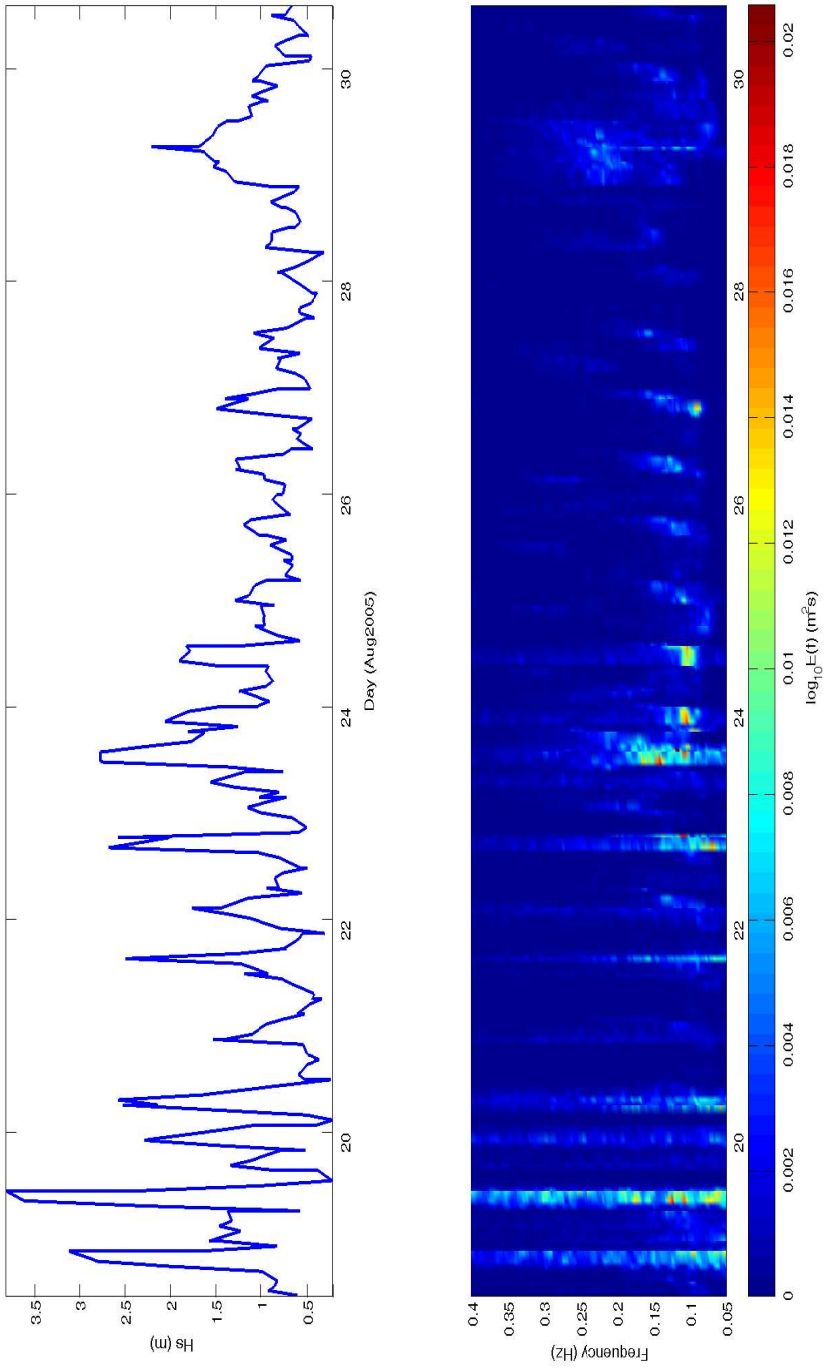

Figure 3.5: Time series of significant wave height (H_s) and contour plot showing the time history of wave spectra at the site

Date		$Tt(hr)$	$Ht(m)$	t_e/t_f	M_e/M_f	Mx_e/Mx_f
19-August-05	Spring	12.6667	0.8947	1.1111	1.0929	1.0667
20-August-05	Spring	11.6667	1.2021	1.0588	1.0880	1.0936
21-August-05	Spring	12.6667	0.8500	1.2353	1.0922	1.0574
22-August-05	Spring	12.6667	1.0500	1.1111	1.0697	1.0543
23-August-05	Spring	12.6667	0.7417	1.2353	1.1285	1.1676
24-August-05	Spring	11.3333	0.5839	1.0606	0.9834	0.9850
25-August-05	Neap	12.6667	0.5042	0.8095	0.9934	0.9972
26-August-05	Neap	13.6667	0.4095	1.4118	0.9543	0.9425
27-August-05	Neap	13.6667	0.3622	1.4118	1.1165	1.1409

Table 3.1: Description of 9 semi-diurnal tidal cycles for cycle duration (Tt), observed mean tidal heights (Ht), rate between durations of ebb and flood periods (t_e/t_f), ebb/flood rates of mean current (M_e/M_f) at 25m above seabed and ebb/flood rates of maximum current (Mx_e/Mx_f) at 25m above seabed

Spring

	Date	$H_s(m)$	$T_p(s)$	$DT_p(deg)$	$u_{br}(ms^{-1})$	$d_0(m)$
1	20/08/2005 00:40	0.6070	12.4510	334	0.0675	0.2676
2	20/08/2005 01:40	0.9245	10.6276	330	0.0924	0.3127
3	20/08/2005 02:40	0.8493	10.6276	342	0.0798	0.2700
4	20/08/2005 03:40	0.8257	10.0395	270	0.0928	0.2965
5	20/08/2005 04:40	0.8128	8.0380	270	0.0721	0.1845
6	20/08/2005 05:40	0.9870	18.9552	70	0.1160	0.7000
7	20/08/2005 06:40	1.9959	15.6790	350	0.1985	0.9906
8	20/08/2005 07:40	2.7862	11.6514	270	0.2370	0.8791
9	20/08/2005 08:40	3.1101	10.6276	270	0.2908	0.9838
10	20/08/2005 09:40	1.6741	20.0000	22	0.1568	0.9983
11	20/08/2005 10:40	0.8271	10.6276	138	0.0955	0.3232
12	20/08/2005 11:40	1.4353	15.0296	278	0.1385	0.6624
13	20/08/2005 12:40	1.5691	18.9552	138	0.1845	1.1135
14	20/08/2005 13:40	1.2266	14.4318	142	0.1335	0.6131
15	20/08/2005 14:40	1.4605	9.5131	26	0.1455	0.4406
16	20/08/2005 15:40	1.3215	9.7692	278	0.1283	0.3990
17	20/08/2005 16:40	1.3674	7.5371	350	0.1347	0.3232
18	20/08/2005 17:40	0.5782	5.0297	274	0.0384	0.0616
19	20/08/2005 18:40	2.3096	18.9552	242	0.1890	1.1402
20	20/08/2005 19:40	3.6037	8.0380	270	0.3097	0.7923
21	20/08/2005 20:40	3.8044	16.3871	270	0.2961	1.5443
22	20/08/2005 21:40	2.3091	16.3871	278	0.1953	1.0185
23	20/08/2005 22:40	0.9733	7.8638	270	0.0709	0.1776
24	20/08/2005 23:40	0.2226	8.2201	270	0.0165	0.0431

Table 3.2: A summary of wave measurements: Significant wave height (H_s), peak period (T_p), peak wave direction (DT_p), near-bottom orbital velocity u_{br} and the orbital diameter d_0 for a monitored day during spring cycle (20 August, 2005)

Neap

	Date	$H_s(m)$	$T_p(s)$	$DT_p(deg)$	$u_{br}(ms^{-1})$	$d_0(m)$
1	26/08/2005 00:40	0.7568	8.8194	278	0.0726	0.2038
2	26/08/2005 01:40	0.6609	9.7692	286	0.0559	0.1737
3	26/08/2005 02:40	0.6616	6.4631	302	0.0476	0.0980
4	26/08/2005 03:40	0.8948	3.2944	258	0.0633	0.0664
5	26/08/2005 04:40	0.7247	11.6514	270	0.0786	0.2914
6	26/08/2005 05:40	0.9476	8.4106	270	0.1006	0.2693
7	26/08/2005 06:40	1.0275	8.8194	270	0.1046	0.2935
8	26/08/2005 07:40	1.1960	8.0380	270	0.1059	0.2709
9	26/08/2005 08:40	1.1135	7.2365	270	0.0748	0.1723
10	26/08/2005 09:40	0.7278	6.2408	270	0.0328	0.0652
11	26/08/2005 10:40	0.6806	2.8766	270	0.0298	0.0273
12	26/08/2005 11:40	0.8171	4.3643	274	0.0467	0.0649
13	26/08/2005 12:40	0.8686	10.0395	270	0.0647	0.2068
14	26/08/2005 13:40	0.8262	9.7692	270	0.0613	0.1905
15	26/08/2005 14:40	0.7630	9.7692	298	0.0525	0.1632
16	26/08/2005 15:40	0.7344	11.2889	290	0.0488	0.1754
17	26/08/2005 16:40	0.9602	3.6599	326	0.0511	0.0595
18	26/08/2005 17:40	0.9607	11.2889	302	0.0915	0.3288
19	26/08/2005 18:40	1.2821	8.2201	270	0.1160	0.3036
20	26/08/2005 19:40	1.2273	8.6102	270	0.1017	0.2789
21	26/08/2005 20:40	1.2812	7.8638	270	0.0901	0.2256
22	26/08/2005 21:40	0.7588	6.3500	270	0.0400	0.0809
23	26/08/2005 22:40	0.6731	5.0297	334	0.0324	0.0519
24	26/08/2005 23:40	0.4407	10.3252	270	0.0286	0.0939

Table 3.3: A summary of wave measurements: Significant wave height (H_s), peak period (T_p), peak wave direction (DT_p), near-bottom orbital velocity u_{br} and the orbital diameter d_0 for a monitored day during neap cycle (26 August, 2005)

Chapter 4

Current- and Seabed-induced Effects on Directional Energy Spectrum and Wave Energy Dissipation in the Fall of Warness

This Chapter investigates the effects of current and bottom friction due to wave generated bottom orbital velocities on wave propagation and its energy deformation in the Fall of Warness during spring and neap tidal cycles. The ADCP survey was conducted between the 12 March and 13 April 2007 by EMEC. The mean water depth at this site was 45 m. Directional spectra were computed using the EMEP method (Chapter 2, section 2.2.1) which utilises twelve time series of orbital velocities, and the surface-wave spectra approach was used to estimate the wave-generated bottom orbital velocities. Results from this study show a correlation between the wind observation, wave height, and directional wave spectrum with winds incident from the North-westerly direction. The estimation of wave energy dissipation due to bottom friction showed that an increase in orbital motion was accompanied by a decrease in friction.

4.1 Study Area and ADCP Deployment

A 600-kHz four-beam broadband ADCP (RD Instruments Workhorse monitor) was deployed on the seabed, looking upward, in approximately 45 m (mean water depth) of water between 12 March and 13 April 2007. This water depth is the proposed depth and location for SRTT installation at the Fall of Warness. The survey was conducted approximately 4 km West of the Island of Eday in the Orkney Islands, the EMEC's tidal energy test site at the Fall of Warness, test location, $59^o08.147N; 2^o48.391W$ (Figure 4.1). The ADCP was bolted into a frame on a gimbal and the transducer mounted approximately 2.1 m above the seabed. Table 4.1 records the sampling and analysis parameters. Current velocity profiles were sampled every 30 s with 1 m bin vertical spacing while

directional wave data were sampled for 10 min every hour at a sampling rate of 2 Hz. Figure 4.2 shows the wind speed and direction together in comparison with the wave energy spectra over the duration of the deployment.

Figure 4.1: ADCP location in 12 March-13 April 2007; (source: Google Earth)

4.2 Results and Discussions

Figure 4.2 shows that the wind speed and direction influences the development of the observed directional spectra at the Fall of Warness. Wind directions were typically from the North-Northwest during the measurement period though there was a short period

Water depth	:	45 m mean
Sensor height above bed	:	2.1 m
Burst interval for currents	:	30 s
Ping per ensemble (current)	:	10
Burst interval for waves	:	10 min in every hour (start at top of hour)
Sampling rate	:	2 Hz for waves
Burst samples for waves	:	1200
Vertical bin size	:	1 m
Number of vertical bins	:	52

Table 4.1: ADCP deployment parameters

(between 20-26 March, 2007) of wind burst from the South-Southeast. The range of maximum wind speed observed were between $\sim 0.76ms^{-1}$ and $\sim 53ms^{-1}$. Generally, it was noticed that an increase in wind speed correlates with increased wave energy. Of particular interest is the measurement during the storm event of 18th March 2007 because of its significant influence on the wave field. Uncertainties in the spectra during the storm event are very high (as can be seen in Figure 4.2 - panels 3 and 4). The author assumed that the ADCP shifted from its original position coupled with large titlt angle as a result of turbulent flow during the storm and it is suggested that devices may be shut down during storm event.

According to Admiralty the [1], South-Southwest (SSW) and West-Northwest (WNW) wind seas are dominant in the Fall of Warness. During the winter (December, January, February and March), WNW wind (gale) seas were mainly observed, with violent turbulent during the Northwest-going tidal stream. .

Table 4.2 and Figures 4.3-4.7 show the development and decay of waves during a storm event of 18 March 2007. The polar representation of directional wave spectra are shown in Figures 4.4-4.7 and the waves parameters detailed in Table 4.2 The dominant direction was mainly WNW (Admiralty [1]) during the observational periods. Peak periods varying between ~ 4.3 to 20 s and the significant wave heights ranging from ~ 0.4 and ~ 7.9 m. As pointed out by the Admiralty [1], wind conditions during the observational periods correspond to some of the most severe sea states in the Fall of Warness in term of significant wave heights because of the fact that the WNW winds act over the longer dimension of the North Atlantic (Huthnance [42], [43]). Figure 4.3 (and Table 4.2) illustrates the changes in significant wave heights, peak period, wind speed and direction

associated with the generation of WSW wind sea during a 24-hour period (18 march 2007).

The wave field was dominated, firstly by the development of the WSW sea condition with long peak period ($\sim 12 \rightarrow 20$s) and large significant wave height ($\sim 2 \rightarrow 7.9$m). As the wind speed increases (Figure 4.2a) wave amplitude (and significant waveheight) increase and the waves become longer in order to satisfy the dispersion relationship. Long period waves suggest waves with swell characteristics. Waves that travel a significant distance, incident from distant storms and arrive at an angle that differs from the wind direction are known as swells. The storm progressively decays in wave periods and significant wave heights, due to the dispersive nature of WSW wind waves. This suggests that the longer distances traveled by swell act as a filter in both the frequency and the directional domains (Goda [29]).

In general, the rapid change in wind speed as observed in Figure 4.2 (first and second panels) from West-Northwest (WNW) to South-Southeast (SSE) before finally settling at West-Northwest, indicates several stages of WSW sea event generation. Due to the fact that the SSE seas gradually superimposed on the pre-existing WNW wave field, a directional bimodal wave field is expected (Figures 4.4-4.7).

The correlations between tidal elevation, significant wave heights and current speeds (at 5 and 43 m above bed) are shown in Figure 4.8. The tidal heights were between 1.5 to 3 m over the spring/neap cycle, the significant wave height was above 7.9 m (Table 4.2) during a major storm in Orkney (18 March, 2007) and the current speed had a maximum of about 4 ms^{-1} close to surface during the 18 March, 2007 storm event. This storm event correlates with the wind development during this time (see Figure 4.2-upper panel).

Figure 4.9 shows the significant wave height H_s and bottom orbital velocity u_{bs} during the deployment cycle. As expected, an increase in significant waveheight is accompanied by an increase in wave-induced bottom orbital velocity, with the maximum of $0.97ms^{-1}$ which corresponds to the significant waveheight of $\sim 7.9m$ during a storm event (around 18 March, 2007). The later end of the data (circled in red) are unreliable due to the interference with the acoustic pulses of the ADCP during the recovery period.

The likelihood that the ADCP frame shifts or the gimbal tilt to one direction during storm events are very high due to the effect of strong current and waves. This will

increase the uncertainties in the measurement and as a result data recorded at this date (e.g. 17 and 18 March 2007) may contain high degree of noise.

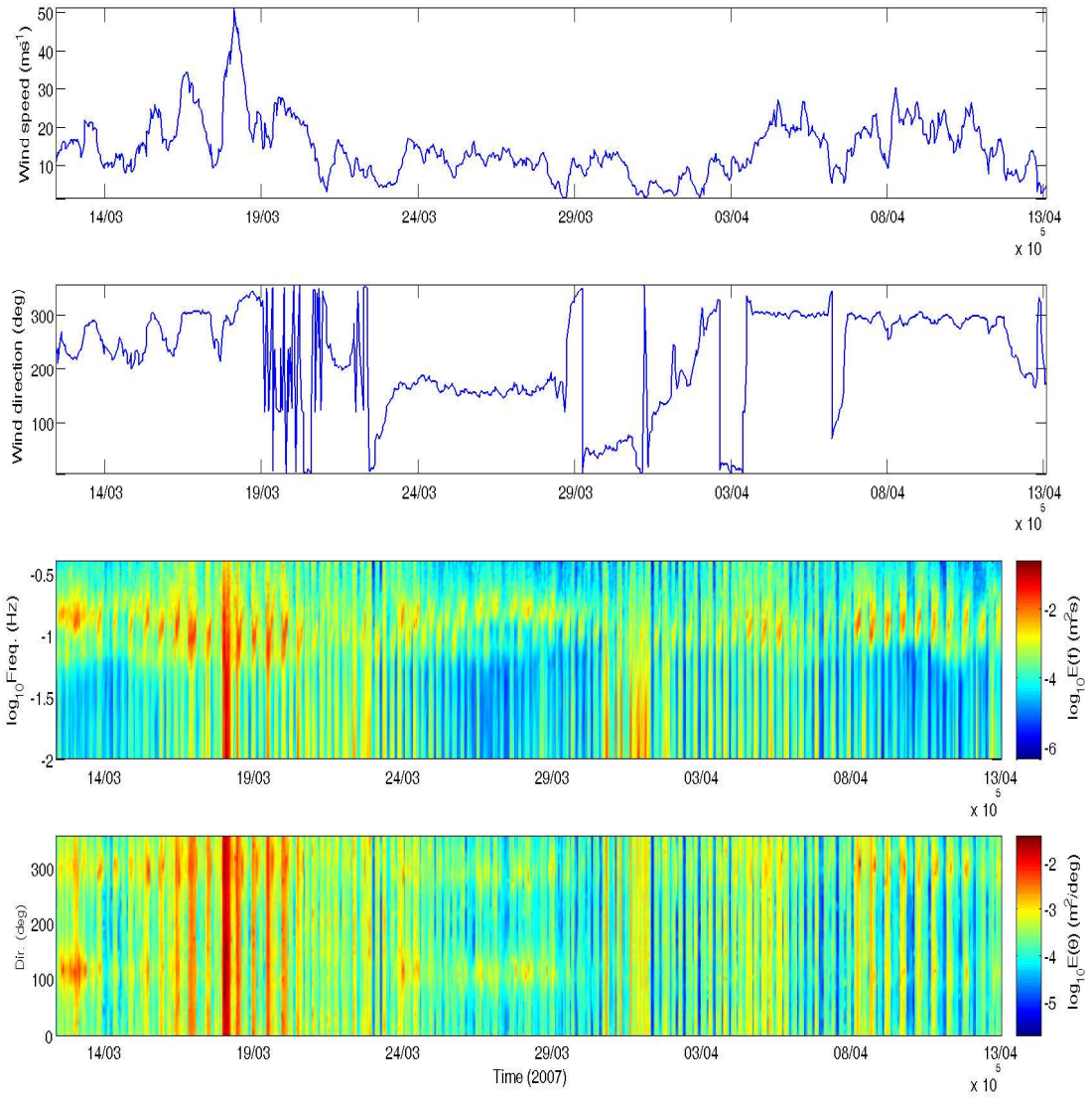

Figure 4.2: (a) Wind speed (ms^{-1}), (b) Wind direction (degree) (c) surface energy spectrum (m^2s) (d) directional surface wave spectrum ($m^2.degree^{-1}$); (a… d)=(first… last panel)

Time	$H_s(m)$	$T_p(s)$	$DT_p(deg)$	$D_p(deg)$
18-Mar-2007 00:00:00	1.99	9.09	332	336
18-Mar-2007 01:00:00	4.57	16.67	316	314
18-Mar-2007 02:00:00	5.49	12.50	320	174
18-Mar-2007 03:00:00	7.97	16.67	270	318
18-Mar-2007 04:00:00	3.73	20.00	144	306
18-Mar-2007 05:00:00	4.66	16.67	156	126
18-Mar-2007 06:00:00	4.58	20.00	340	50
18-Mar-2007 07:00:00	3.61	20.00	270	98
18-Mar-2007 08:00:00	1.88	16.67	270	302
18-Mar-2007 09:00:00	1.49	14.29	324	328
18-Mar-2007 10:00:00	1.19	4.35	336	322
18-Mar-2007 11:00:00	1.81	5.26	158	310
18-Mar-2007 12:00:00	3.27	7.69	268	80
18-Mar-2007 13:00:00	4.28	11.11	34	302
18-Mar-2007 14:00:00	2.66	12.50	270	140
18-Mar-2007 15:00:00	2.68	11.11	270	282
18-Mar-2007 16:00:00	2.08	7.69	270	100
18-Mar-2007 17:00:00	1.43	7.14	330	326
18-Mar-2007 18:00:00	0.93	12.50	270	300
18-Mar-2007 19:00:00	1.14	12.50	330	282
18-Mar-2007 20:00:00	1.01	16.67	296	64
18-Mar-2007 21:00:00	0.71	11.11	268	286
18-Mar-2007 22:00:00	0.61	7.14	316	320
18-Mar-2007 23:00:00	0.43	16.67	318	316

Table 4.2: 24-hour wave parameters from directional wave spectral estimate recorded on the 18 March 2007; H_s=Significant wave height, T_p= Peak wave period, DT_p=Peak direction, D_p= Dominant direction

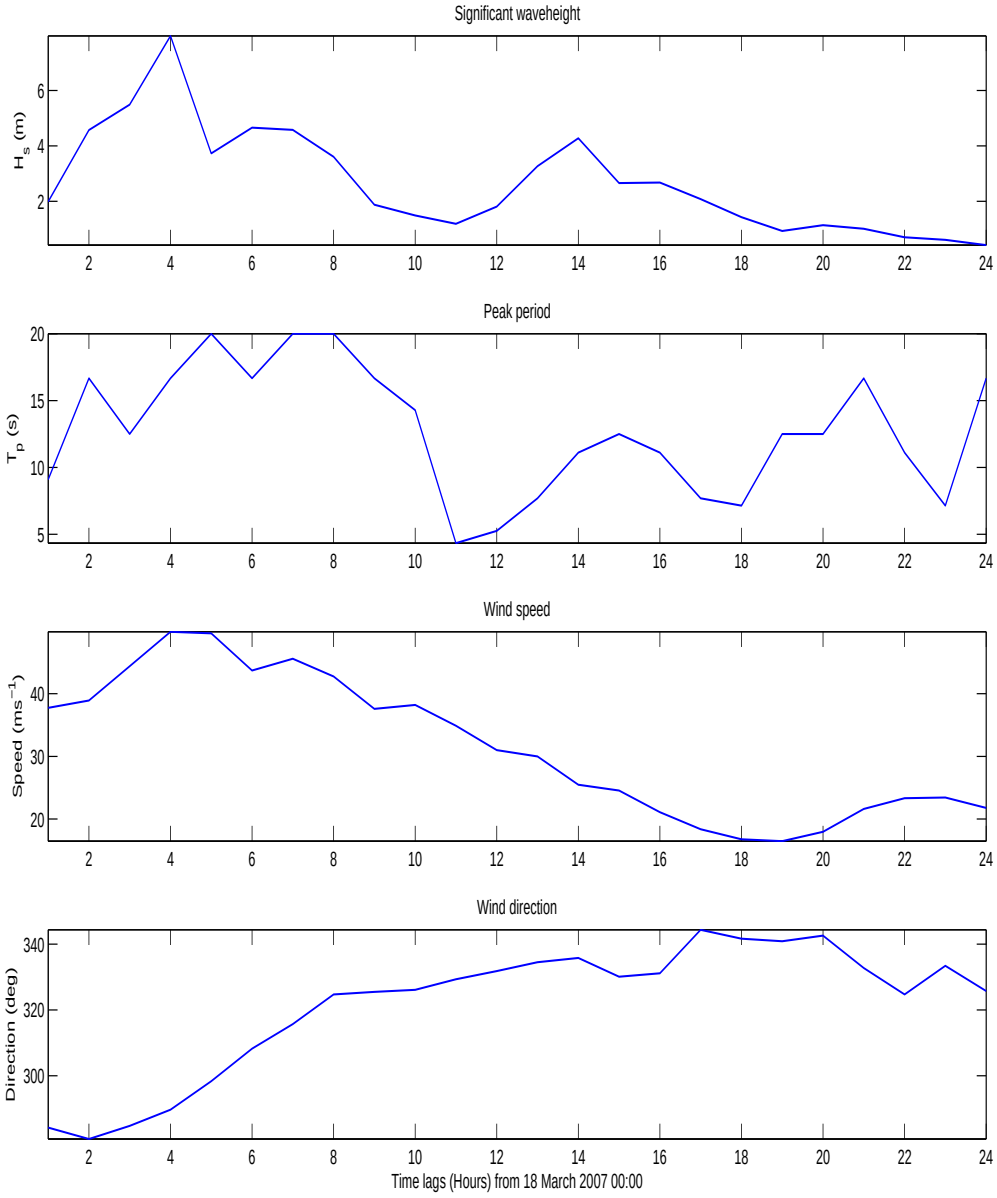

Figure 4.3: Time series of (a) Significant wave height (m) (b) Peak period (s) (c) wind speed (ms^{-1}), (d) wind direction (deg) during (18-March 2007): (a)-(d)= upper - bottom panel

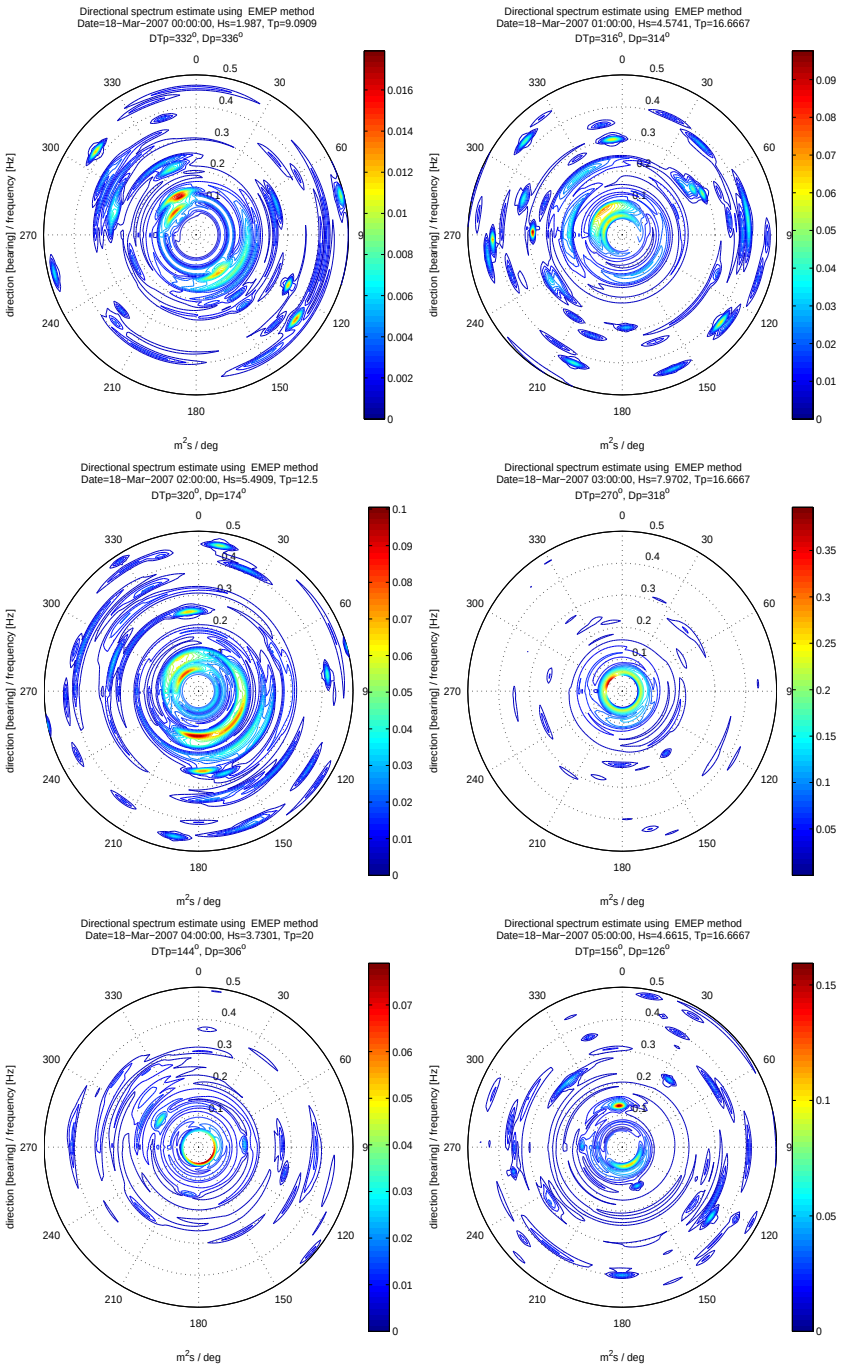

Figure 4.4: One hour average of Directional wave spectrum on the 18-Mar-2007 (00:00:00 - 05:00:00 Hours)

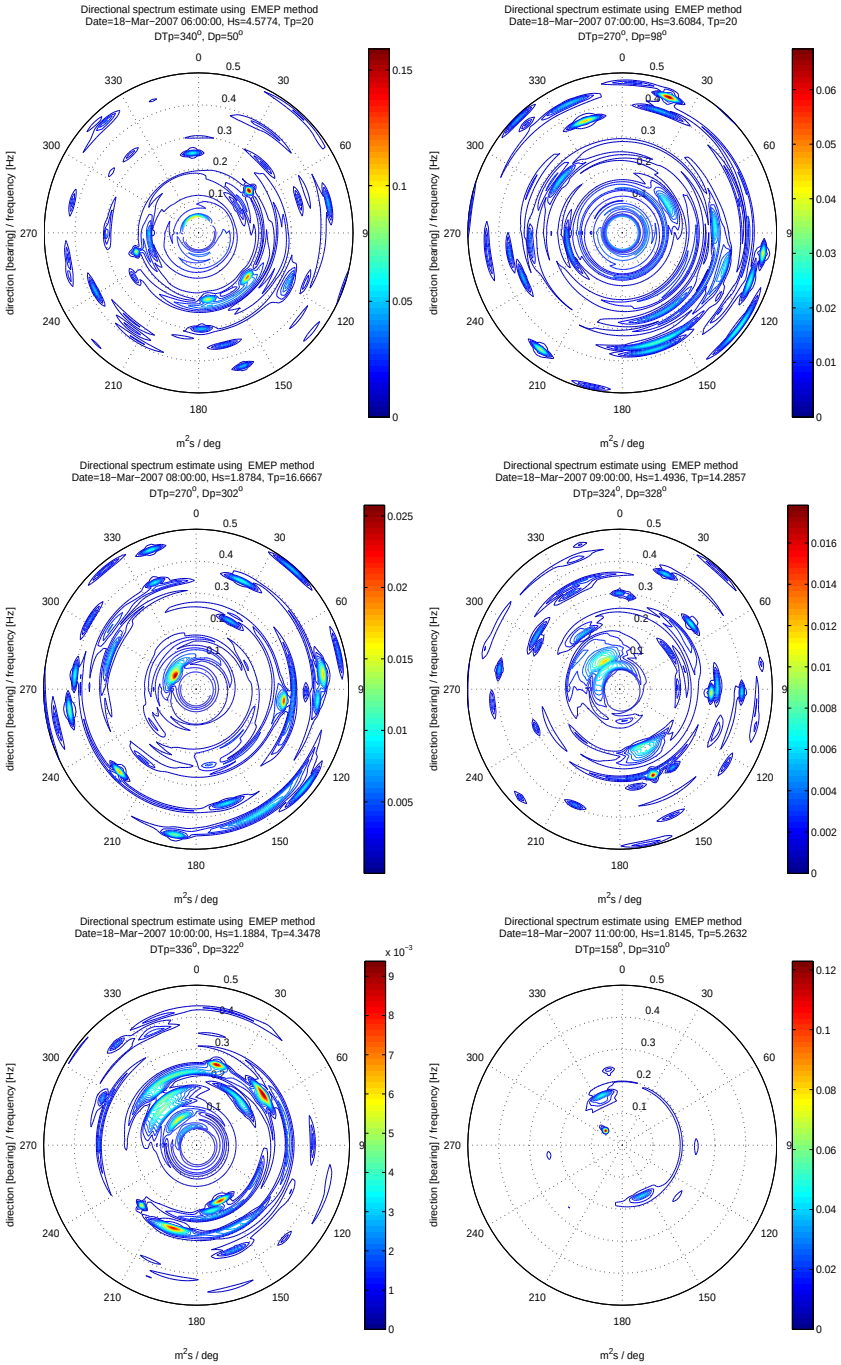

Figure 4.5: One hour average of Directional wave spectrum on the 18-Mar-2007 (06:00:00 - 11:00:00 Hours)

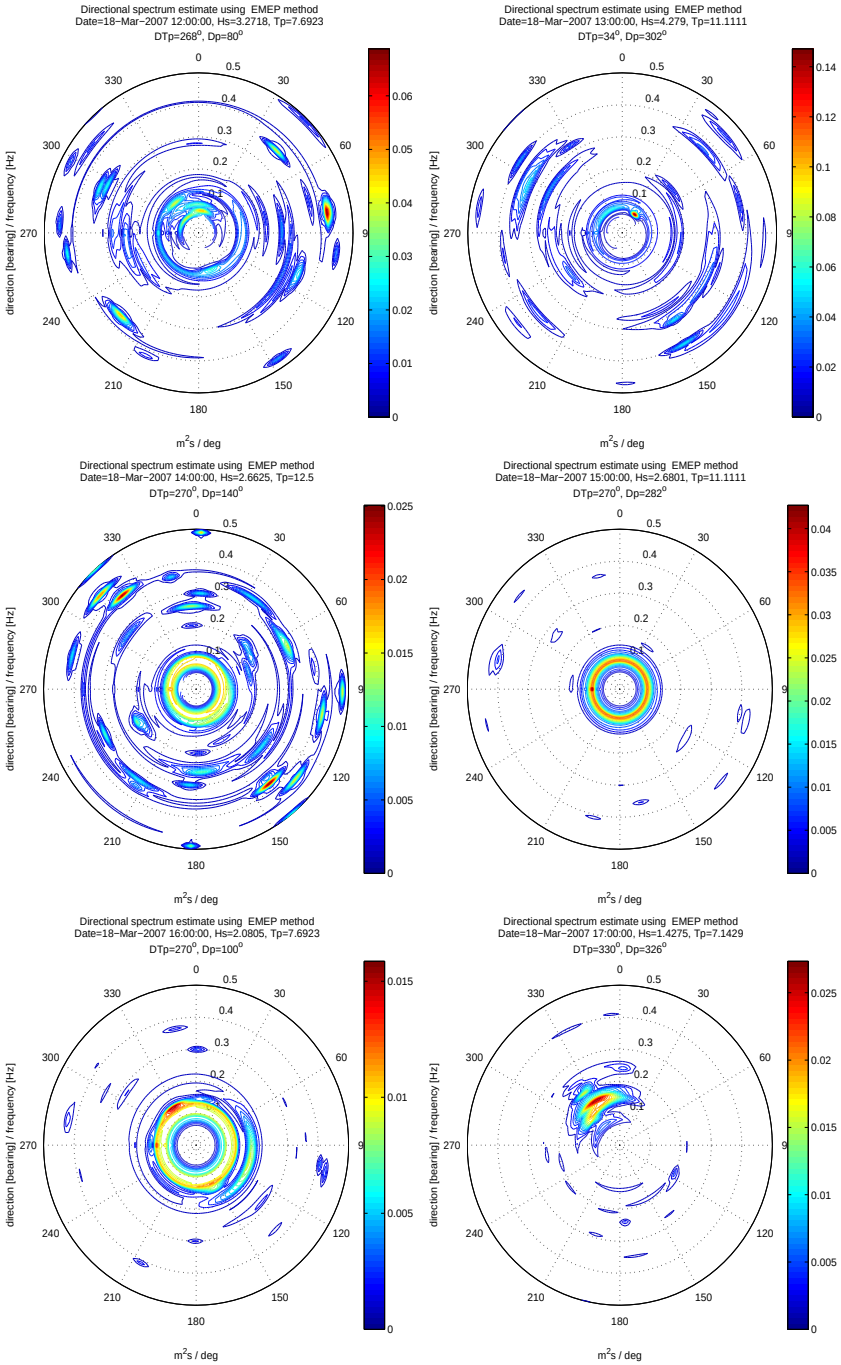

Figure 4.6: One hour average of Directional wave spectrum on the 18-Mar-2007 (12:00:00 - 17:00:00 Hours)

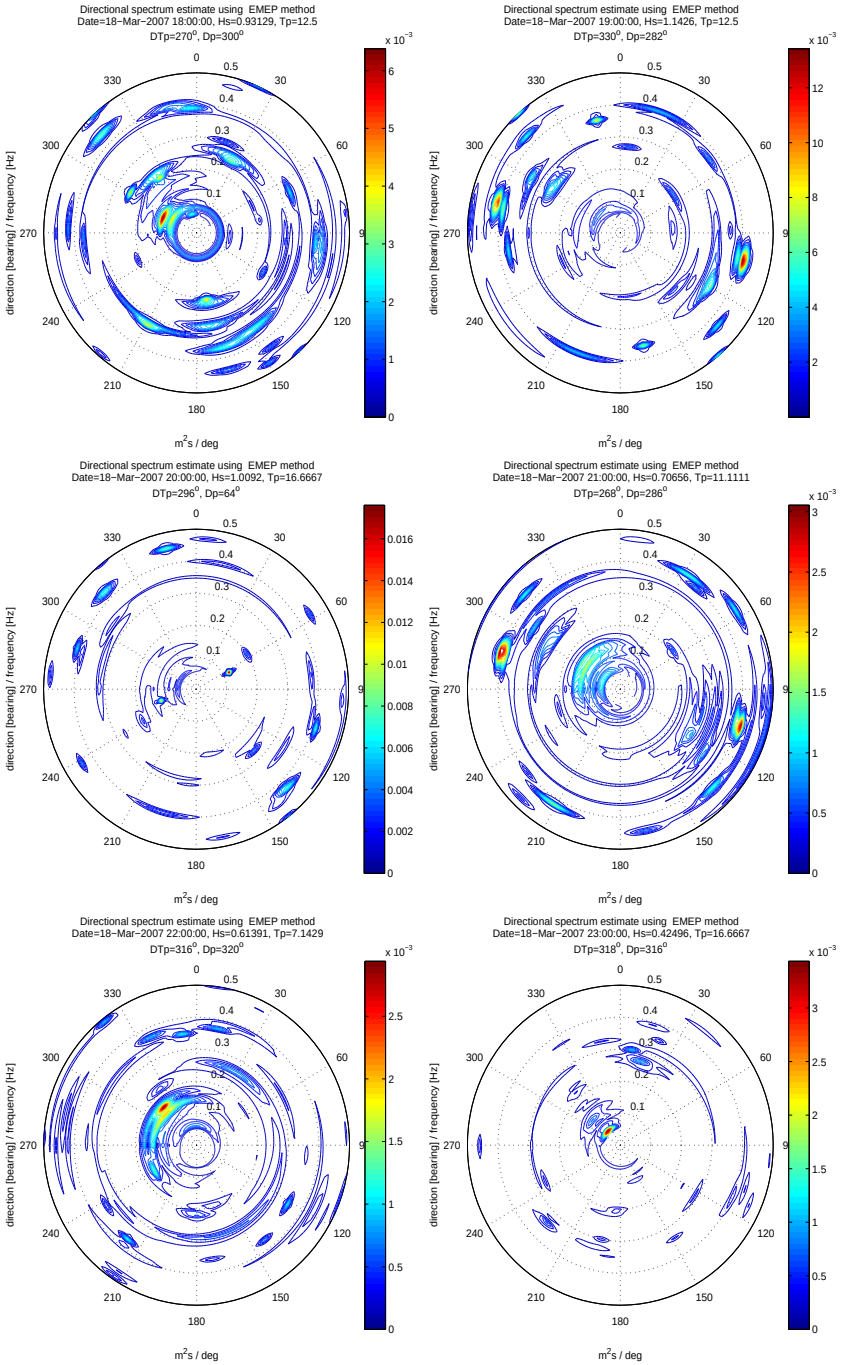

Figure 4.7: One hour average of Directional wave spectrum on the 18-Mar-2007 (18:00:00 - 23:00:00 Hours)

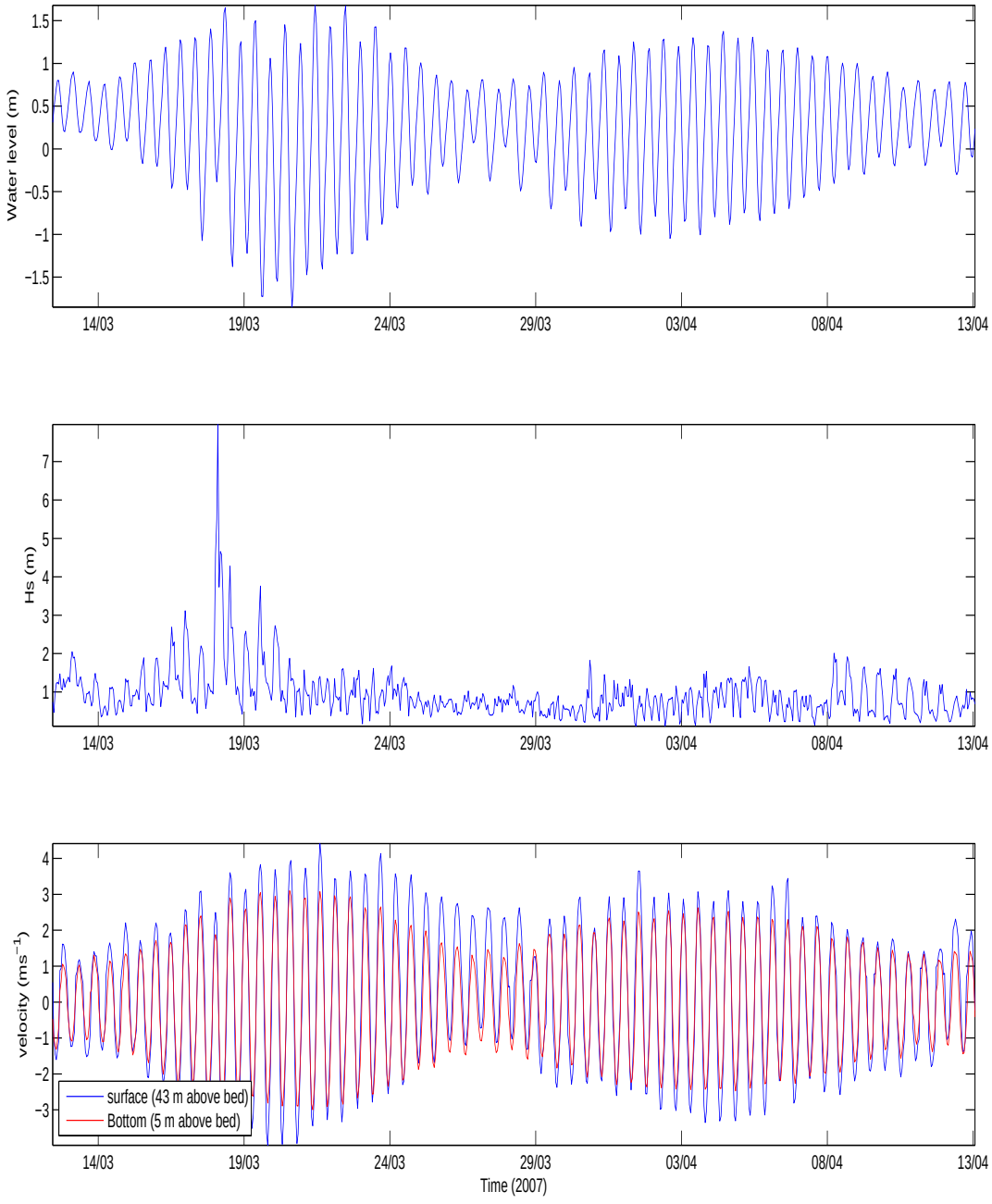

Figure 4.8: Tidal elevation (upper panel), significant wave height H_s (m) (middle panel) and current velocities (ms^{-1}) (surface-blue colour; bottom-red colour) (lower panel)

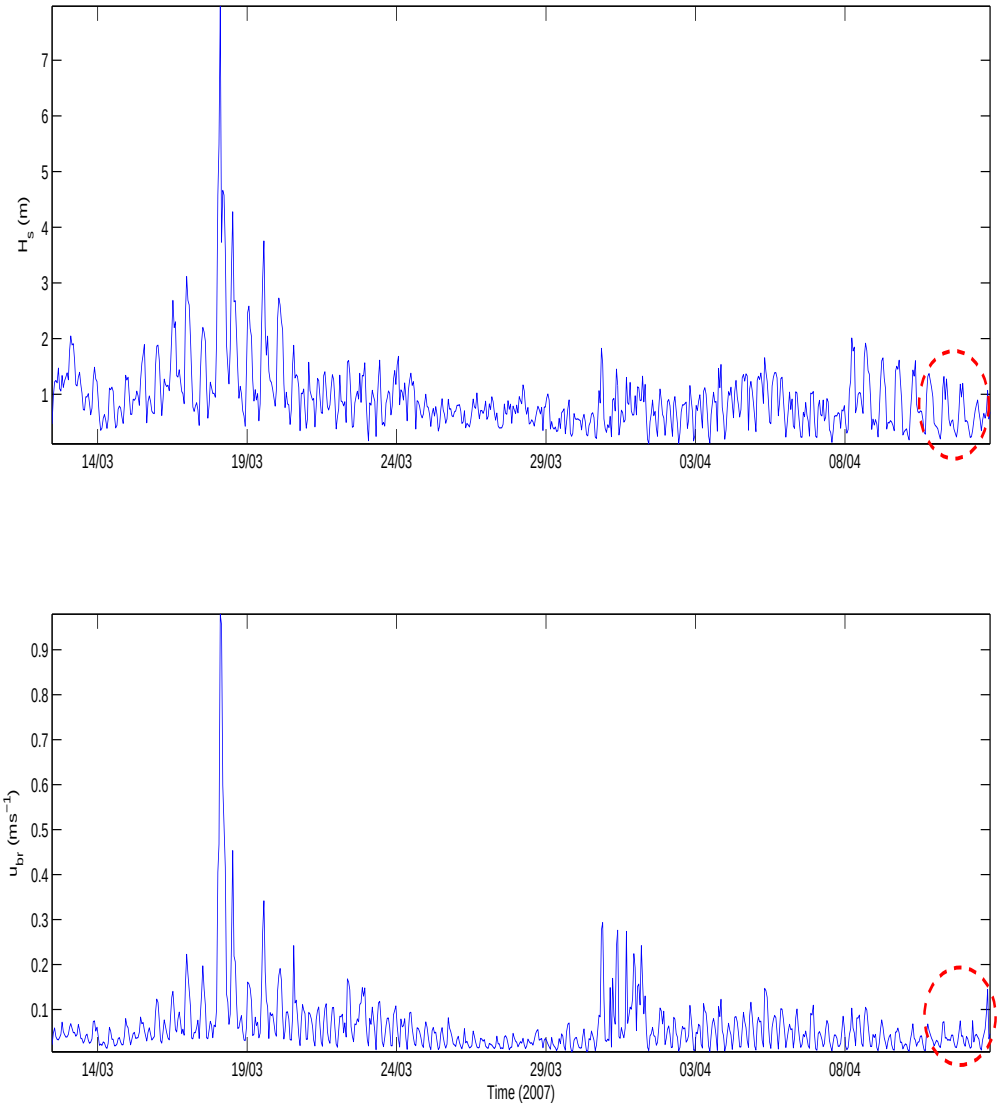

Figure 4.9: Plots of significant waveheight (H_s) and orbital velocity (ms^{-1}); data points within the red circle are suspects corresponding to ADCP recovery period

Chapter 5

Hydrodynamic Response Due to Wave-current Interaction Within Bottom Boundary Layer of an energetic tidal channel

Wave-current interaction within the bottom boundary layer and its effect on hydrodynamics at the Fall of Warness are investigated in this Chapter. The data used have been collected by EMEC between 16-29 October, 2007. This location has been marked for the prototype test berth for testing tidal turbine. The results show that waves were generally from West-Northwest (WNW) (corresponding to the direction of the wind) with a mean peak period of $\sim 7s$. There is high correlation between the significant wave height, wind speed, bottom shear stress and velocity. The bed shear stress values were estimated from the linear extrapolation to the bed from the bottom five stress estimates while the wave shear stress and maximum total shear stress values, due to the combined wave and current interaction, were calculated with the wave-current interaction model proposed by Christoffersen and Jonsson [17](Chapter 2, section 2.4). The bottom-shear stresses due to the combined effects of wave-current interaction and those which were wave-induced were considered and compared. The results show a significant difference between the wave-current interaction and wave-induced shear stresses. Shear stresses computed under the combined wave and current flows are of higher values (about an order of magnitude) than when wave alone is considered. This suggests that shear stresses at the tidal stream site are being predominantly influenced by tidal stream velocity and the seabed roughness.

5.1 Study Area and ADCP Deployment

The data were recorded using a 600-kHz four-beam broadband ADCP (RD Instruments Workhorse monitor) deployed on the seabed, ($59^o09.046N; 2^o48.935W$), in approximately

37 m (mean water depth) of water between 16-29 October, 2007 (Figure 5.1). The survey was conducted by EMEC. The data were recorded in beam coordinates (ie., individual Doppler shift along each beam logged independently) at 0.5 s sampling interval for current while wave observations were sampled for 10 minutes in every hour at 0.5 s sampling interval.

Figure 5.1: ADCP location in 16-29 October 2007; (source: Google Earth)

5.2 Results and Discussions

The wind direction was predominantly steady (at WNW) during the measurement period except for the period between 6-8 October 2007 when the direction changed to the North, with the lowest wind speed of about 2 ms^{-1}. The maximum value of WNW wind speed recorded during the observational period was 30 ms^{-1}(Figure 5.2b and c).

The time series of tidal current and direction measured at 2.6 m above bed is plotted in Figure 5.2d and 5.2e. As expected, current direction of Northwest flow was strongest and a maximum of about 1.4 ms^{-1} current speed was recorded near the bed. During the spring tide, the maximum value of H_s recoded was 1.65 m (Figure 5.2f).

The estimates of bulk turbulence parameters from this data are discussed in detail in Chapter 6.

It is interesting to note also in Figure 5.3, that the current speed near the surface (20 m above bed) during the observation period reached up to $\sim 1.92ms^{-1}$ during the spring tide while the direction remain predominantly WNW and South-Southeast (SSE) for both near-surface and near-bottom current.

Figure 5.4 shows time series variation of significant wave height H_s, current speed and wave-induced orbital velocity (the wave-generated velocity just above the seabed-at the top of the wave boundary layer) (discussed in Chapter 2 and in Appendix A.4). It was noted that the significant wave height and near-bottom orbital velocity respond to changes in current speed. This also confirms the earlier result in Chapter 4.

The time-varying maximum nearbed orbital velocity interacts with the seabed resulting in frictional dissipation of energy and modification of wave boundary bottom shear stress (Chapter 1, Section 1.5). An increase in nearbed orbital velocity might result in sand particles being stirred, picked up and transported away from the tidal turbine structure thus creating a hole around the turbine structure (scour) (You [131]). Though the uncertainties in the wave parameters from this analysis are high, however, the influence of currents on both significant wave heights and maximum orbital velocity are clearly shown in Figure 5.4.

Figure 5.5 shows the effect of wave-current interaction on the bottom shear stress. The result from this plot shows that the magnitude of the maximum bottom stress determined from the combined wave and current flow τ_{CW} (Figure 5.5-lower panel) is greater than the estimate from wave properties (τ_W) (Figure 5.5, upper panel). The difference is greater than an order of magnitude. It can also be seen from Figure 5.5 that the wave-induced shear stress contributed less that 2% to the combined stress due to wave-current interaction. This shows that the bottom stresses at the Fall of Warness (on energetic tidal channel) are mainly driven by tidal current.

The data used in this study was a high frequency sampled data recorded in beam coordinates. Due to the fast pinging rate and the flow dynamics, large uncertainties in the

wave parameters (e.g. Figure 5.4) are expected. This is unexpected because ADCPs are not designed to measure waves and the uncertainties in wave parameters increase in fast moving flow and single ping measurements (beam coordinate ADCP data). However, the major point observed in this study is the influence of tidal current on the wave kinematics and wave-induced orbital velocities.

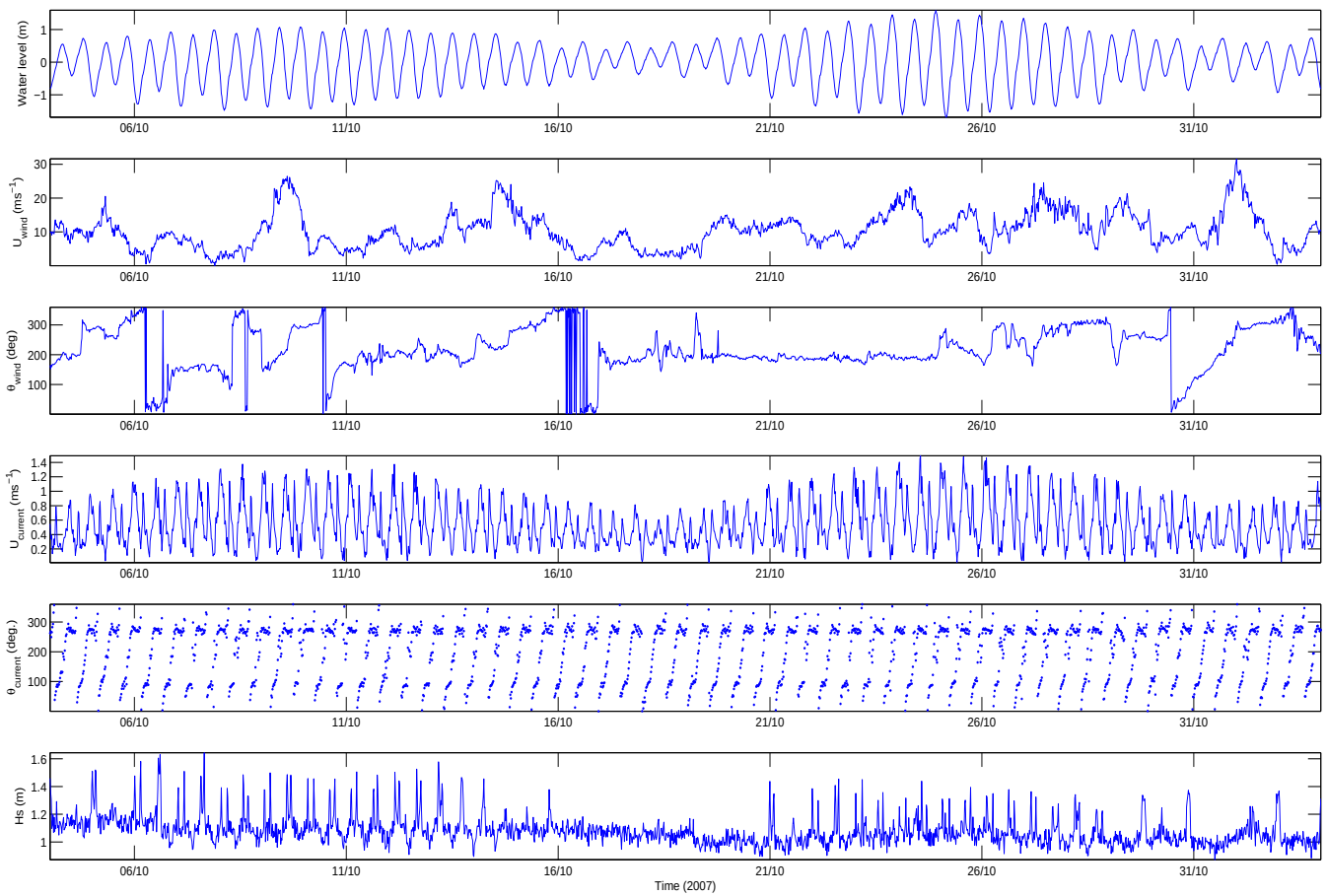

Figure 5.2: Time series of (a) water level (m), (b) wind speed (ms^{-1}) (c) wind direction (*degree*), (d) tidal current speed (ms^{-1}) (e) tidal current direction (*degree*) at 2.6 m above bed and (f) significant wave height (m) between 6 October - 5 November 2007: ((a)-(f)=upper panel - lower panel)

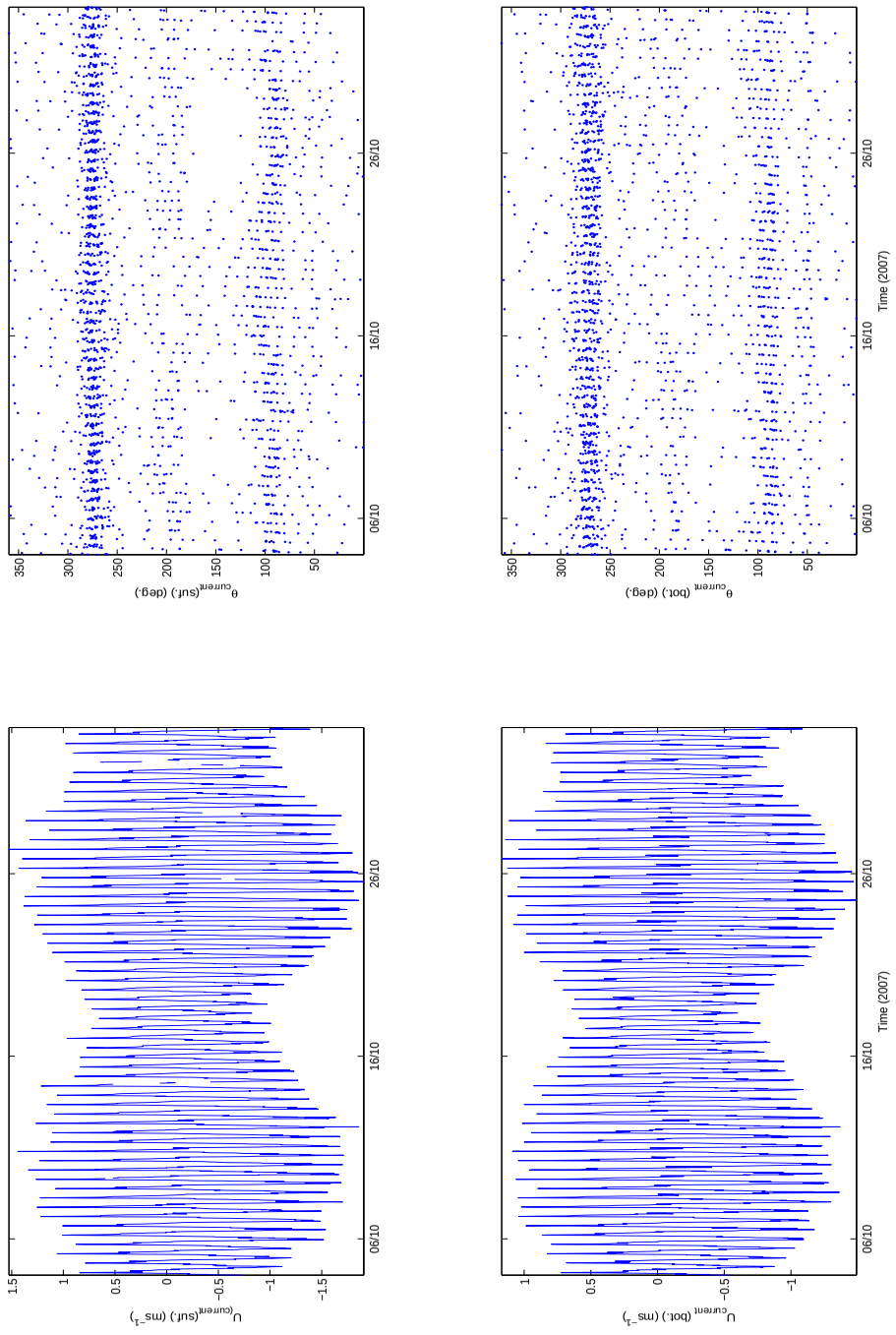

Figure 5.3: Time series of tidal current speed (ms^{-1}) and direction (*degree*) at 20 m (upper panel) and 2.6 m (lower panel) above bed

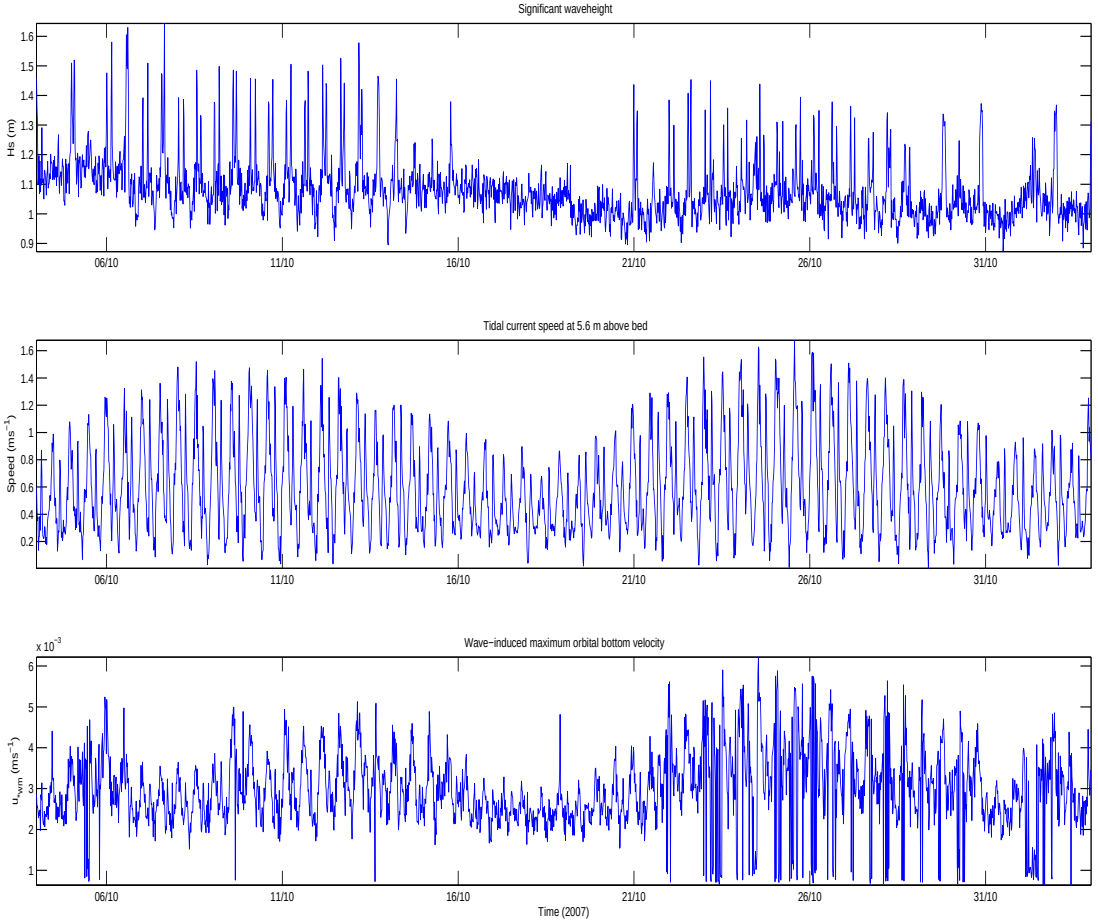

Figure 5.4: Time series of (a) significant waveheight, (b) tidal current speed at 5.6 m above bed, and (c) maximum orbital velocity (ms^{-1}); (a)-(c)=upper panel - lower panel)

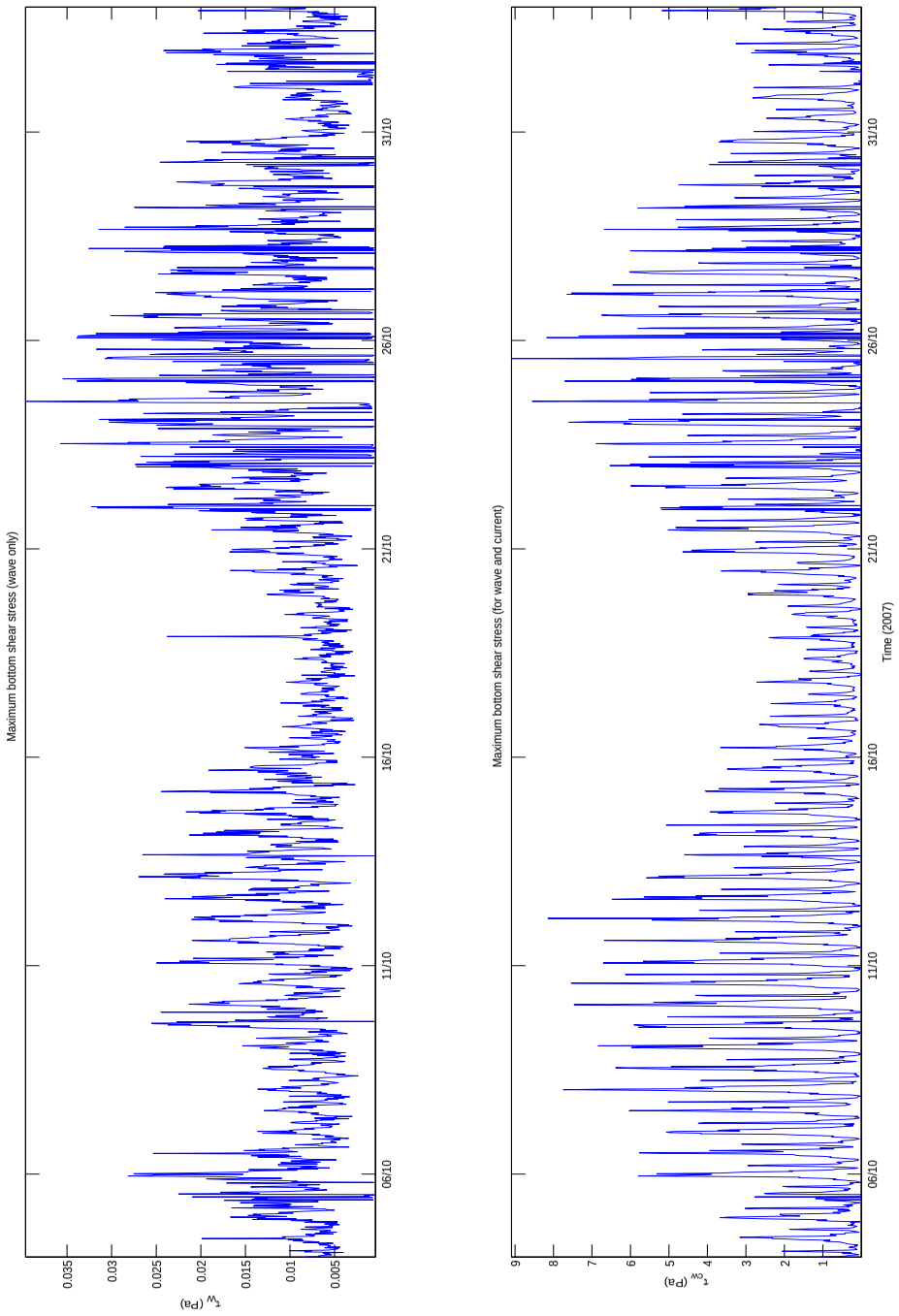

Figure 5.5: Time series of maximum bottom shear stress (Pa) (upper panel) and (b) maximum bottom shear stress (wave and current) (Pa) (lower panel)

Chapter 6

Structure of Turbulent Flow in EMEC's Tidal Energy Test Site

Estimates of bulk turbulence parameters (TKE production, Reynolds stress, TKE dissipation, eddy viscosity) were determined from the high frequency sampling data collected by EMEC in a tidally energetic test site for two locations: For the first survey (Deployment 1), data were collected over a period of 5 days in a water of ~ 46 m mean depth and for the second survey (Deployment 2), 30 days of continuous data were recorded at ~ 37 mean water depth. In the first deployment, flood and ebb currents exceed $1.8 ms^{-1}$ near the seabed (at 2.73 mab) and generate $> 7 Pa$ stresses while the maximum currents and stresses observed during the second deployment were $\sim 2.21 ms^{-1}$ and $\sim 19 Pa$. The TKE dissipation rate ε was estimated using two techniques: Inertial Dissipation (IDM) and Second-order Structure Function Methods (2SFM). The requirements for local turbulence isotropy were not met for both IDM and 2SFM due to the influence of noise. The bulk turbulence parameters for the two surveys were discussed and their estimates compared. The best turbine position with respect to vertical profiles of Reynolds stresses were determined over 8 tidal cycles for Deployment 1 and 60 tidal cycles for Deployment 2 covering neap and spring tides. The result from the study shows that the Reynolds stress estimate is an important factor in turbine design and performance and most especially, a reliable parameter to optimise the best position for turbine installation in the water column.

6.1 Study Area and ADCP Deployment

The data was provided by a 600-kHz four-beam broadband ADCP (RD Instruments Workhorse monitor) deployed on the seabed in approximately 46 m (mean water depth) of water between 2 and 5 July 2006 ($59^o 08.208N; 2^o 48.469W$) (Deployment 1) and 37 m

mean water depth between 5 October to 5 November 2007 (59^o09.046N; 2^o 48.935W) (Deployment 2) (Figure 6.1 and Table 6.1). The instrument was programmed to operate in fast pinging mode 12, recording one velocity profile per second for Deployment 1 and two velocity profiles per second for Deployment 2. Velocities were recorded in beam coordinates; that is, one along-beam velocity was obtained for each of the instrument's four acoustic beams. The surveys were conducted by EMEC approximately 4 km West of the Island of Eday in the Orkney Islands, the tidal test site at the Fall of Warness. The ADCP was mounted in a $\pm 20^o$ gimbal to adjust for uneven bottoms. The instrument was slightly tilted with respect to the vertical which varied between 0^o and 8^o during the experiment because of scour around the frame. For an isotropic flow typical of the coastal ocean, 2^o tilts resulted in no more than a 17% bias in stress estimate (Lu and Lueck [68]). The bias of 2^o tilts angle for an ADCP is acceptable (Lu and Lueck [68], Williams and Simpson [124], Rippeth *et al.* [93]) for the estimation of Reynolds stresses and thus, 2^o was used as a reasonable cutoff for a maximum instrument tilt. Current speeds regularly exceeded 2 ms^{-1} at the surface, and the majority of the velocity shear was near the seabed. The ambiguity velocity (the maximum allowable radial motion for phase measurements [91]) was set at 2 ms^{-1} and the standard deviation of the uncertainty (measured by ADCP) associated with each horizontal velocity estimate was 0.0393 ms^{-1}.

6.2 Results and Discussions

6.2.1 Deployment 1

The results presented here are an extension of the results from Osalusi *et al.* [83], Osalusi *et al.* [84] recent publications, which were based on 2 tidal cycles. In the series of figures presented, gaps in data analysis (see Figure 6.2e) occur where one of the following is detected (a) side-lobe contamination near the sea surface (6%) (b) statistical non-homogeneity of b_i over the variance computation period (c) statistical non-homogeneity of u, v and w over the distance between beams (d) frequent values below the signal-to-noise threshold (e) surface or internal wave bias, and (f) ADCP motion.

Figure 6.2 shows the time-depth profiles of the backscatter intensity (a qualitative measurement (in decibels) of scatterer concentration), tidal stream velocity (positive and negative for flood- and ebb-directed flows, respectively), Reynolds stress, TKE density

Figure 6.1: ADCP location in 2-5 July 2006; (source: Google Earth)

(measures the root-mean-squared (RMS) of the velocity fluctuations) and TKE production. The effect of surface waves is seen near the surface (clearly seen between yearday 187.4 and 187.6 - Figure 6.3) and is reflected in all the contour plots in Figure 6.2. As expected, current (stream) velocity (Figure 6.2b) attained its maximum ($\sim 2ms^{-1}$) at the surface and decreases with water depth. The ebb-directed flow seems to be stronger than the flood. Contour plots of Reynolds stress τ_x (Figure 6.2c), TKE density S (Figure 6.2d) and TKE production P (Figure 6.2e) have their largest values ($\sim 8Pa$ for τ_x, $\sim 0.26m^2s^{-2}$ for S and $\sim 0.01Wm^{-3}$ for P) near the bed.

The asymmetry between flood and ebb was noticed with larger currents occurring on the flood than on the ebb. Maximum values are observed at every second flood (Figure 6.2b). This might be due to the diurnal contribution with two low (lower low water and higher low water) and high (lower high water and higher high water) waters each day at the Fall of Warness.

Figure 6.4 shows 1 hour mean stress and current velocity over two tidal cycles. These data were taken from yearday 187.4 and 187.6 as presented in Figure 6.3. From the first (upper panel) and the second (lower panel) tidal cycles, the current velocities attained their maximum value of about $2ms^{-1}$ during ebb and flood. The Reynolds stresses reached their peak values near the bed and decreased to minimum values near the surface. These minimum values are of great interest in determining the best position for tidal turbine installation within the water column. The slight increase at the water surface is due to the strong effect of waves. It appears also that the effect of a wave boundary layer at the bed on the Reynolds stress assumes to be seen in both the first and second tidal cycles (e.g., profile i (upper panel) and L (lower panel)). This is speculation because the effect of waves has been minimized from this data.

Figures 6.5-6.6 show Reynolds stress profiles at hourly intervals for a 12-h period (a tidal cycle) over 8 tidal cycles. The profiles are obtained with a 60-min averaging period. The purpose of these graphs is to determine the best position for a floating tidal turbine rotors with respect to vertical profiles of Reynolds stresses. The minimum value of the sum for each depth is determined and the lowest value of Reynolds stress per depth (given 20 m clearance above the seabed and 8 m clearance below water surface) is considered as the best position for turbine rotor installation. Table 6.5 lists the 8 tidal cycles discussed above with their corresponding 'best position' values (with respect to depths below mean water level (MWL)) for turbine rotor installation. The mean of $\sim 12.58m$ (26.97%) below mean water level (Table 6.2 and Figure 6.22) which fluctuates within

95% confidence interval of $\pm 2.8m$ (Figure 6.7), was found to be the best installation position for a floating tidal turbine rotor for a mean water depth of 46 m at the Fall of Warness.

The 95% confidence intervals are estimated as follows:

- identifying the range of depths (10 m below water surface and 10 m above bed) for each mean of Reynolds stress estimate. The mean and standard deviation were computed.
- the standard error margin, critical value and margin of error were computed from: Margin of error = Critical value $\times$ Standard error. The standard error of the mean is defined as the ration of the standard deviation and the square root of the range of depths under consideration while the critical value is the t-score having 999 degrees of freedom and a cumulative probability equal to 0.975.
- the uncertainty in the best turbine position for each tidal cycle denoted by the confidence level is computed by: 95% confidence interval = critical value $\pm$ Margin of error

Figure 6.8a shows the contour plot of vertical velocity gradient or shear. As expected, shear is maximum near the bed and decreases sharply towards the surface. Theoretically, the shear stress in the water column is assumed to be proportional to the vertical velocity gradient (Chapter 2, section 2.5). The constant of proportionality is the eddy viscosity. Eddy viscosity A_z controls the dynamics of mixing in the water column. From Figure 6.8b, eddy viscosity A_z is seen to attain its maximum close to the peak flow and decreases to low values near slack water. The estimates of A_z are subject to large uncertainties, particularly when the magnitudes of the shear are close to zero (around slack water) since $A_z \propto (\partial \bar{u}/\partial z)^{-1}$, or near the surface where wave effect is significant. Due to this effect, only the real part of A_z is plotted since the equation (equation 2.5.12) breaks down where mean shear is approximately zero. Vertical eddy viscosity A_z, shear or friction velocity u_* and turbulence intensity (S normalised by u_*) are shown in Figure 6.9. Figure 6.9a shows the time-averaged eddy viscosity profiles. Theoretically, turbulence theory suggests a parabolic profile of eddy viscosity with maximum value at the middepth provided there is no wake effect (Nezu and Nakagawa [75]). As expected due to the effect of unsteadiness in the flow, A_z increases from the bed, attains its maximum below the middepth and decreases towards the surface.

This is of great importance in marine tidal industry because A_z influences not only the tidal elevations but also the structure of the current profiles significantly (Davies [2]). Pohlmann [87] used a turbulent energy approach proposed by Kochergin [56] together with baroclinic circulation model to simulate the hydrographic situation of the North Sea and in particular to quantify the cause of mixing over twelve months. He found that vertical profiles of A_z are influenced by high-frequency variability in meteorological forcing and increase towards the surface and bottom due to the intensification of vertical mixing caused by the wind stress and bottom friction, respectively. In the Northwestern North Sea in particular, during the winter months, Pohlmann [87] found that the maximum vertical A_z decreases nearly linearly from the surface ($300cm^2s^{-1}$) to the bottom ($150cm^2s^{-1}$) and in the summer, mean values of vertical A_z distribution dropped to $75cm^2s^{-1}$ at the surface and about $100cm^2s^{-1}$ at the bottom. Based on his result, he concluded that in the summer season, the vertical profiles of A_z rates depend more on topographic and tidal induced effects. Kraav [57] used a barotropic storm surge model in combination with a one-equation turbulent closure scheme to determine the relationship between the A_z and the maximum tidal current velocities along the British coast and he found the A_z exceeded 500 cm^2s^{-1}. The minimum and maximum values of vertical A_z from this deployment are found to be $\sim 0.013m^2s^{-1}$ ($\sim 130cm^2s^{-1}$) and $\sim 0.067m^2s^{-1}$ ($\sim 670cm^2s^{-1}$) (Figure 6.9a). These values can be improved with larger datasets.

The time series of friction velocity $u_*(=(\tau_b/\rho)^{0.5})$ is displayed in Figure 6.9b. The values of u_* were estimated for the lowest five bins (i.e. depth 2.76, 3.76, 4.76, 5.76, 6.76 m above bed) by linear extrapolation to the bed of the portion of the Reynolds stress profile that displayed decreasing stress for increasing elevation above the bed. Here, τ_b is the bed stress and ρ is the density of water. The maximum values of the friction velocities (Figure 6.9b) are expected to record peak flows during flood and ebb. This is seen to be out of phase with the Reynolds stress. The cause of this phase shift is not clear. The author assumes that phase shift between Reynolds stress and friction velocities might be due to the asymmetry between the ebb and flood. Friction velocities fluctuate with the tidal cycles and diminish towards slack water. Figure 6.9c shows the 'S' like-vertical profiles of turbulence intensity. The TKE S (which is equally the standard deviation of the fluctuating velocities), is normalised by the square of the friction or shear velocity. The turbulence intensity profile reached its maximum (~ 12.59 at $\sim 6.8m$) near to the bed high shear region, and decreases rapidly to its minimum

value of ~ 5.73 at $\sim 37.76m$ near the surface. Figure 6.10 shows the standard deviation of the Reynolds stresses and TKE production rate, calculated from the observations using equations (2.5.14 and 2.5.15) (Chapter 2, section 2.5) plotted against their associated Reynolds stress and TKE production rate. The purpose of this figure is to quantify the uncertainties in flow-related noise due to turbulent motions. The ordinate (y) axes of Figure 6.10 is proportional to the instrument noise. By using the least squares fitting method with equations (2.5.14 and 2.5.15) (Chapter 2, section 2.5), the minimum uncertainty of $\sim 1.73 \times 10^{-4} Pa$ in Reynolds stress estimate was found.

Following Williams and Simpson [124], the linear regression equation

$$\sigma_{st} = 0.0018\tau_x + 0.0009 \tag{6.2.1}$$

is obtained. The slope of equation (6.2.1) above (0.0018) represents the increase in the flow-related component of the uncertainty. Williams and Simpson [124] suggested that the uncertainties in Reynolds stress estimate σ_{st}^2 can be reduced by increasing the number of samples used in the computation (1200 samples were used in this study). From equation (2.5.15), it is clear that uncertainties in the Reynolds stress estimates has a large influence on the uncertainties in TKE production rate σ_{sh}^2. Therefore a decrease in σ_{st}^2 will correspond to a gradual decrease in σ_{sh}^2.

Figure 6.11 shows the contour plots of the time series of the rates of dissipation of turbulent kinetic energy using IDM and 2SFM. The largest values of dissipation rate are observed near the seabed, and decrease with height above the seabed. However, the results reported here are noisy and the assumptions that the turbulent velocity fluctuations are statistically homogeneous in horizontal space over the distances separating the beams were not met and this provides a poor correlation.

The difference in the dissipation rate can be seen between the two techniques. It has been reported by other investigators (e.g., Wiles *et al.* [123] , Rippeth *et al.* [93]) that 2SFM underestimate dissipation rate in the presence of noise. This is evident in Figure 6.11a. No vertical variance is noticed and white spaces in the profiles are largely due to noise. This make 2SFM values unreliable, at least in this study and with this dataset. However, IDM performed better with gradual changes in the vertical profiles and maximum at the seabed. At the seabed, maximum value of $2.06 \times 10^{-2} Wm^{-3}$ was recoded using IDM method. The result from IDM is consistent with what other investigators reported. For example Lorke and Wüest [67] estimated the dissipation rate at the

bottom boundary layer (BBL) in Lake Alpnach (Switzerland) during low energetic flow (maximum current speed equal to 3 cms^{-1}). The dissipation rates found was between 9.7×10^{-15} and $1 \times 10^{-5} Wm^{-3}$. This is much smaller than the result from this study as expected owing to a much slower flow. Wiles *et al.* [123] also estimated the dissipation rate in a more energetic tidal flow (Red Warf Bay) with maximum velocity of $0.2ms^{-1}$) using the 2SFM. They found the dissipation rate to be around $1 \times 10^{-3} Wm^{-3}$. As expected, the result from this study must be higher owing to greater energy flow. Since these results are consistent with the IDM maximum value from this study, the author considers the TKE dissipation rate estimate from IDM as a better choice. This result is examined further with a larger dataset, in the next section. The distribution of P and ε is shown in Figure 6.12b. There is a clear distinction between P and ε. The cause of this difference between P and ε is not clear. The author assumes that differences might be due to the inherent errors associated with the ADCP data, and the isotropic turbulence assumption made in the estimate of ε.

	Deployment 1	Deployment 2
Instrument	RDI ADCP	RDI ADCP
Acoustic frequency (kHz)	600	600
Pinging mode	Mode 12	Mode 12
Time/ping (s)	1	0.5
Time/ensemble (s)	1	1
Duration (days)	4	30
Water depth (mean)	46	37
Depth cell size (m)	1	1.5
Height above seabed (m)	1.63	2.6
Referential coordinate	Beam	Beam

Table 6.1: ADCP configuration settings for Deployments 1 and 2

Tidal Cycle	Best Turbine Position (Turbine position below MWL) (m)	Depth (below MWL) (%)	95% conf. (m)
1	11.62	24.91	2.95
2	12.50	26.81	3.35
3	11.62	24.91	2.64
4	12.50	26.81	1.87
5	12.77	27.38	3.16
6	11.97	25.67	3.01
7	13.83	29.65	2.86
8	13.83	29.65	2.67
Mean	**12.58**	**26.97**	**2.81**

Table 6.2: Best turbine position at depth below water surface for 8 tidal cycles (Deployment 1): 2 -5 July 2006

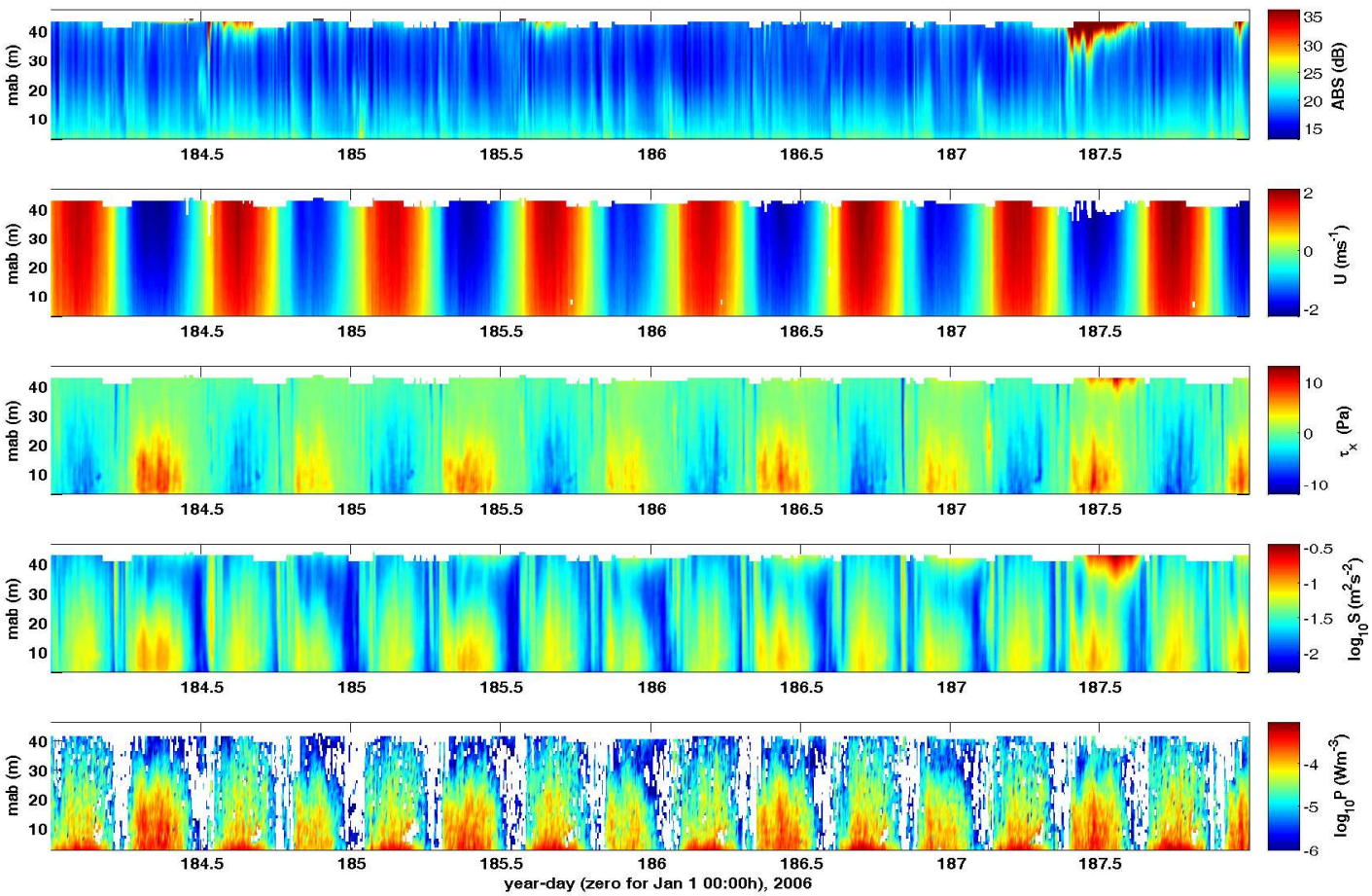

Figure 6.2: Depth-time series of (a) acoustic backscatter signal strength (dB) (b) stream velocity (ms^{-1}) (c) Reynolds stress (Pa) (d) TKE density (Jm^{-3}) (e) TKE production (Wm^{-3}) ; (a… e)=(first… last panel) : DEPLOYMENT 1

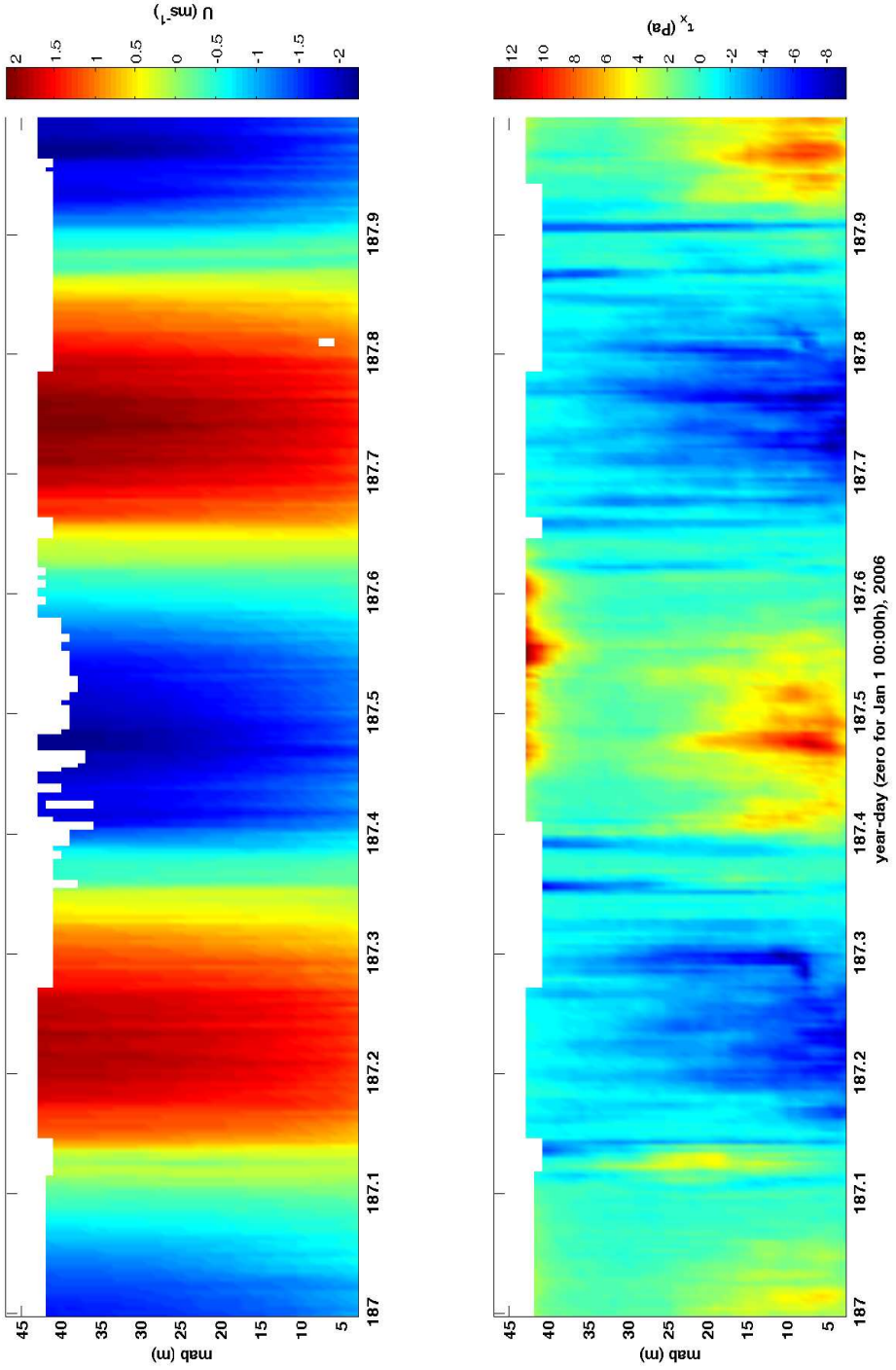

Figure 6.3: Depth-time series of (a) current velocity (ms^{-1}) and (b) Reynolds stress (Pa): DEPLOYMENT 1

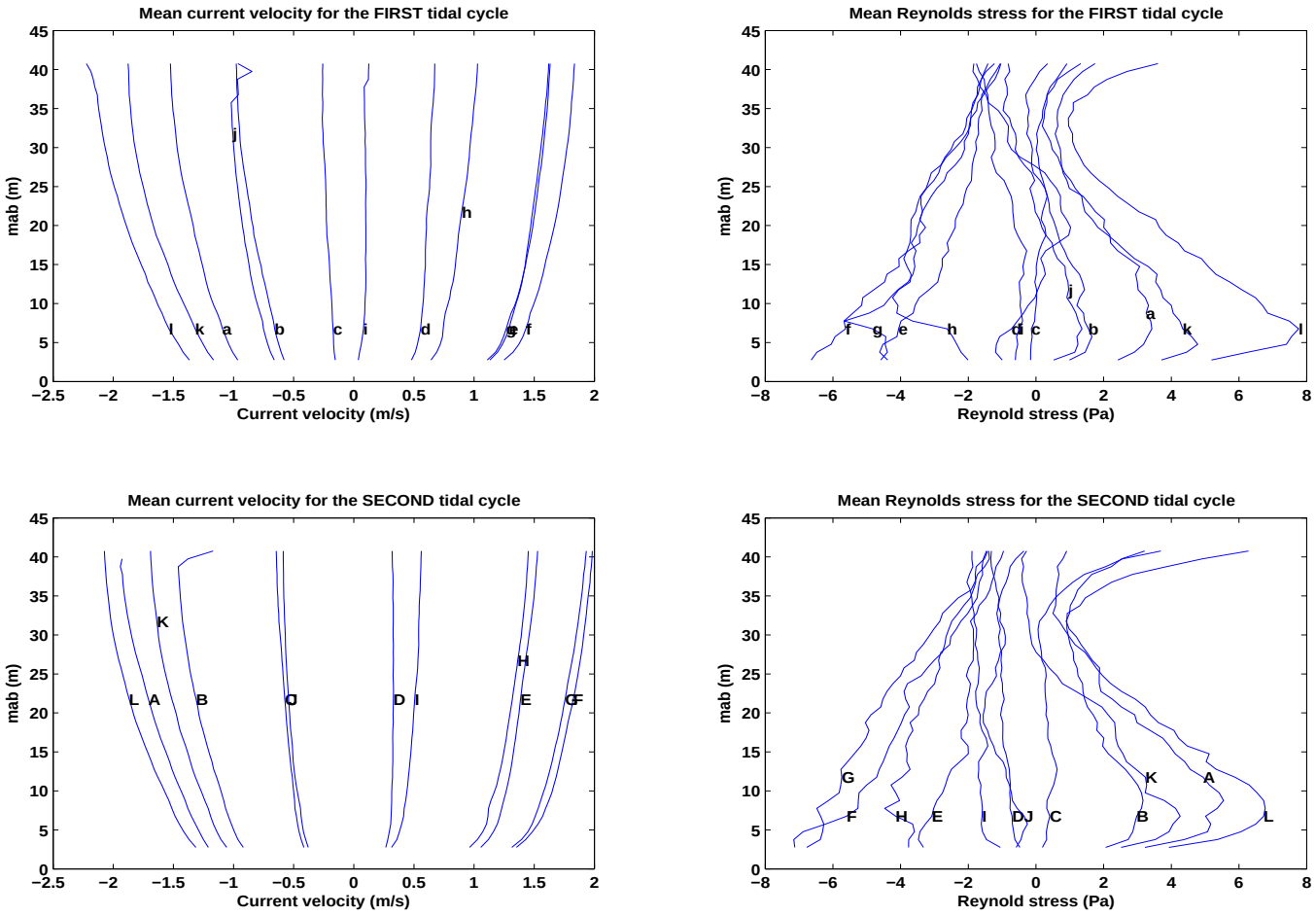

Figure 6.4: Mean velocity (ms^{-1}) profiles for 2 tidal cycles (24 hours) (yearday 186.9969-187.9969) (left). Hourly mean Reynolds stress (Pa) profiles at times corresponding to the stress profiles in (a) (right): Letters a-l and A-L correspond to mean profiles for currents and Reynolds stresses over 12 hours: DEPLOYMENT 1

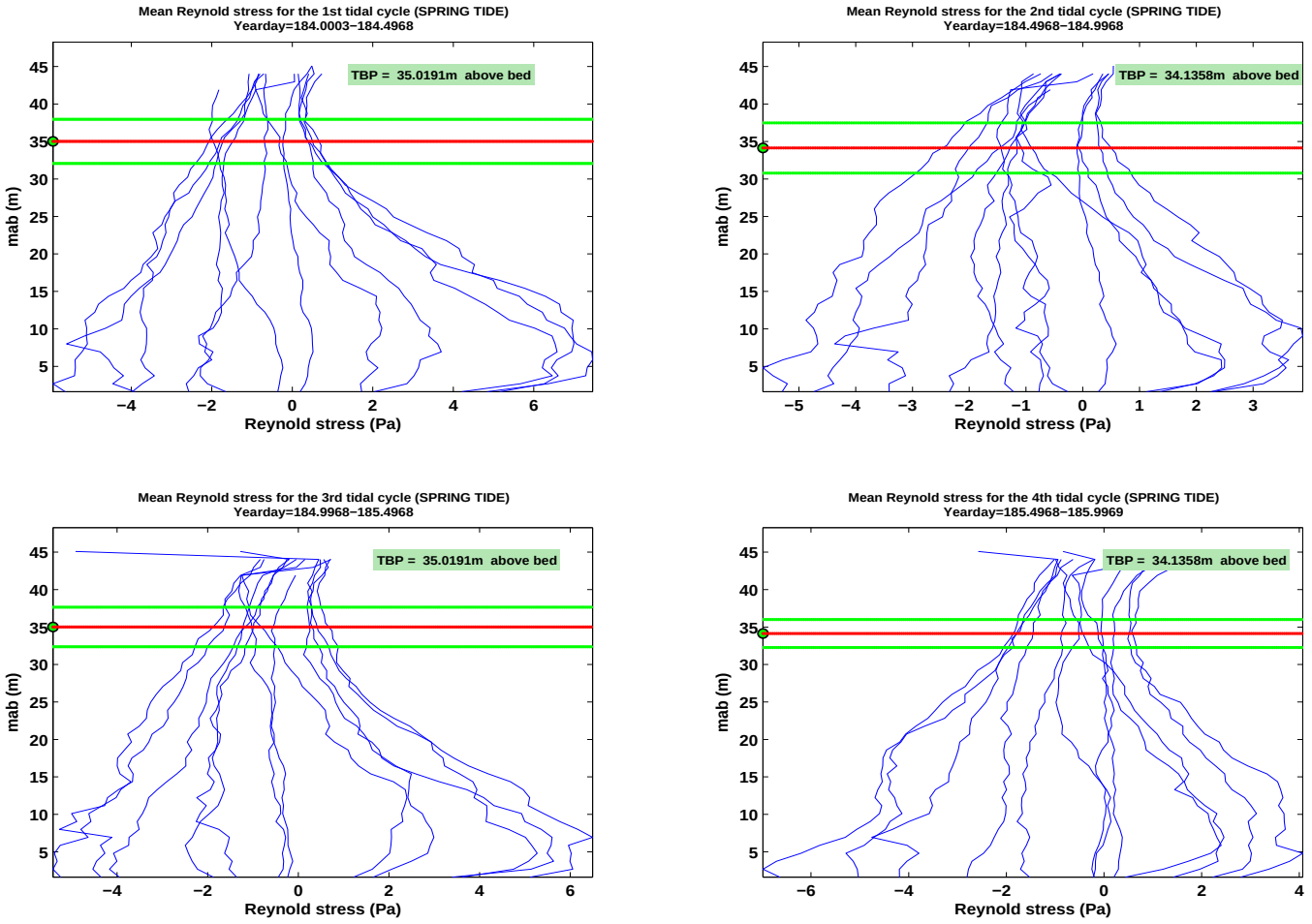

Figure 6.5: Hourly mean Reynolds stress (Pa) profiles for 4 tidal cycles (48 hours) (yearday 184.0003-185.9969); The red line is the (mean) best position and the green lines indicate the 95% confidence interval calculated as the standard error multiplied by the critical two-tailed value of t-distribution: DEPLOYMENT 1

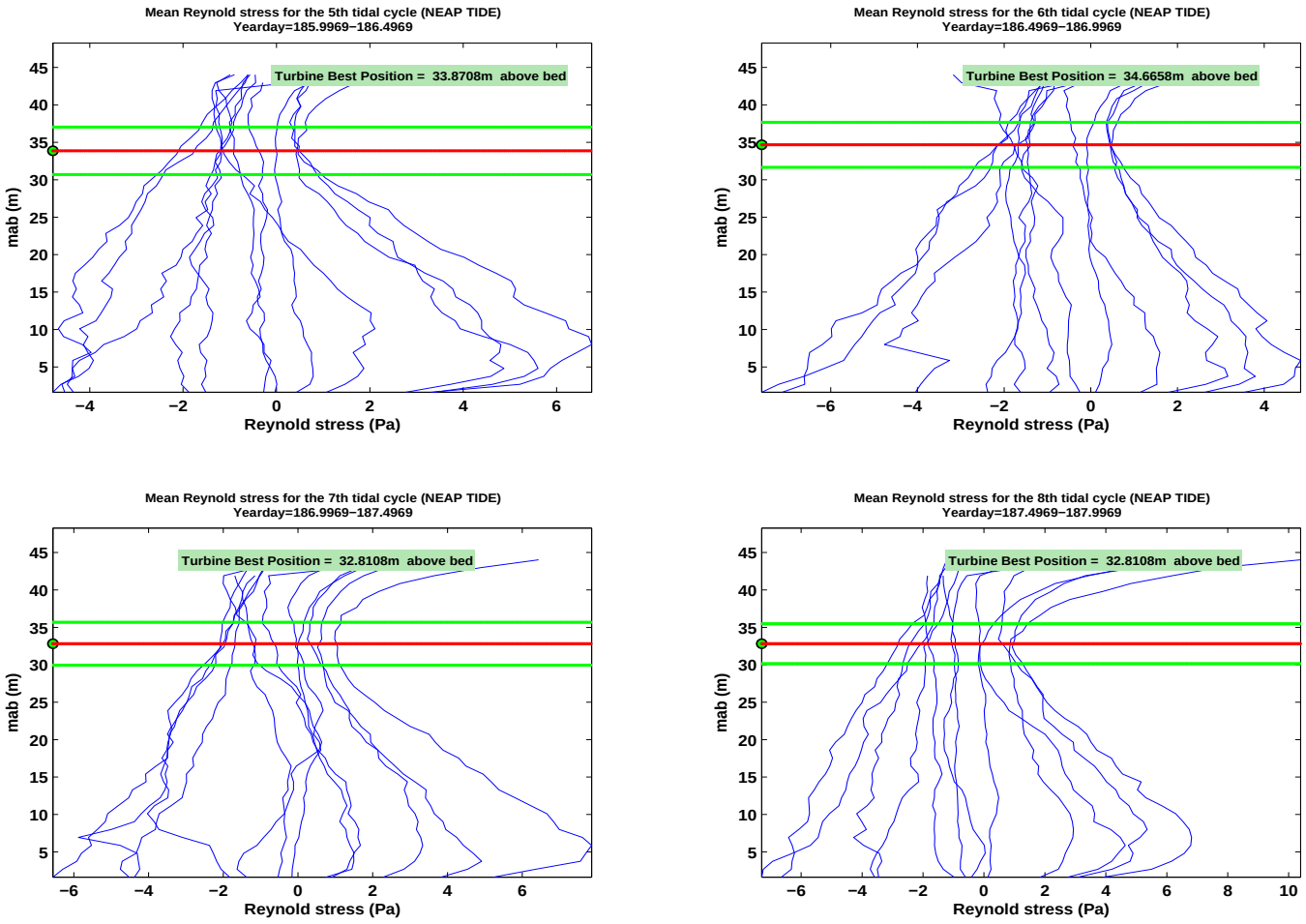

Figure 6.6: Hourly mean Reynolds stress (Pa) profiles for 4 tidal cycles (48 hours) (yearday 185.9969-187.9969) ; The red line is the (mean) best position and the green lines indicate the 95% confidence interval calculated as the standard error multiplied by the critical two-tailed value of t-distribution:: DEPLOYMENT 1

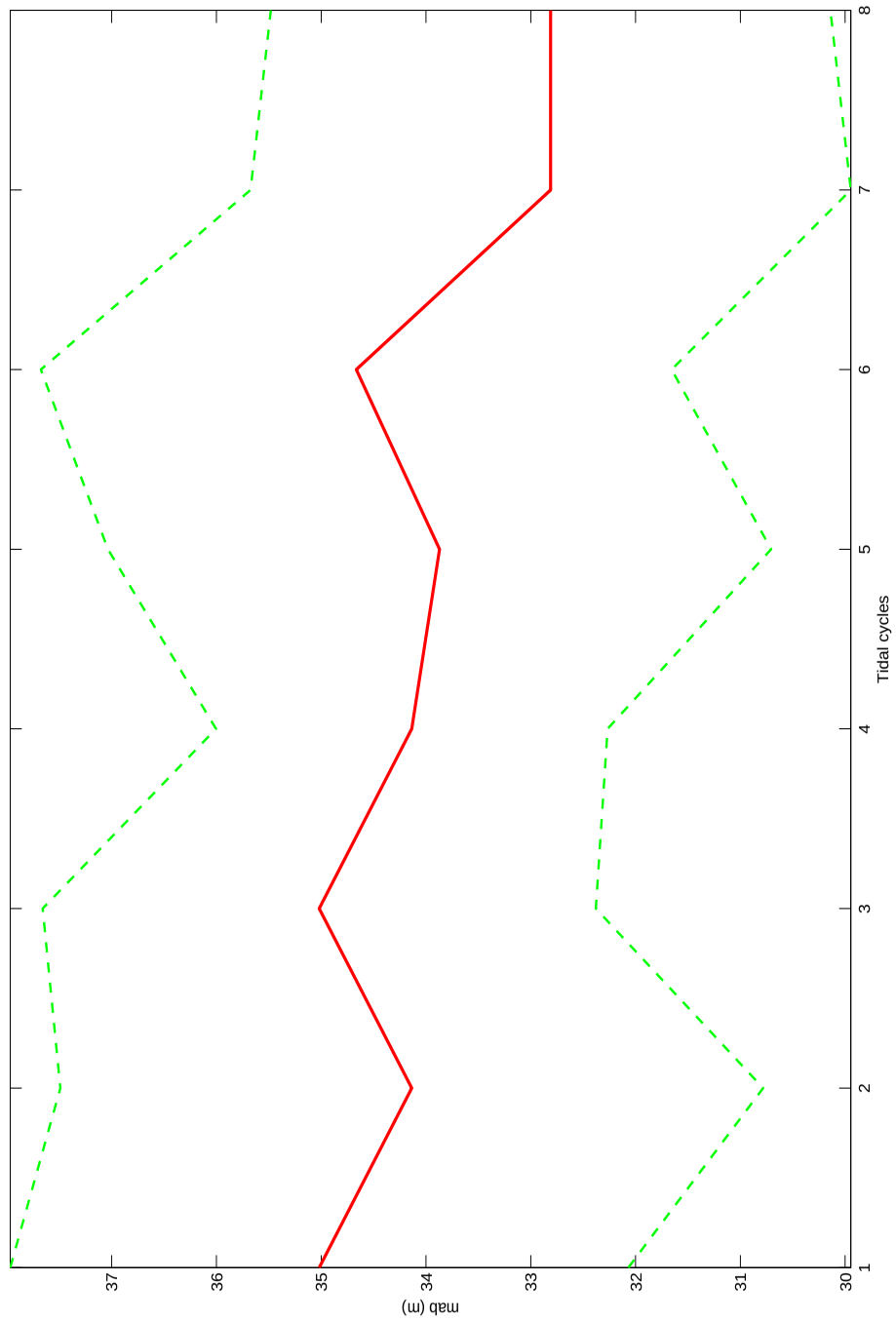

Figure 6.7: Mean of best turbine positions versus tidal cycles (red line) and the green lines indicate the 95% confidence interval calculated as the standard error multiplied by the critical two-tailed value of t-distribution: DEPLOYMENT 1

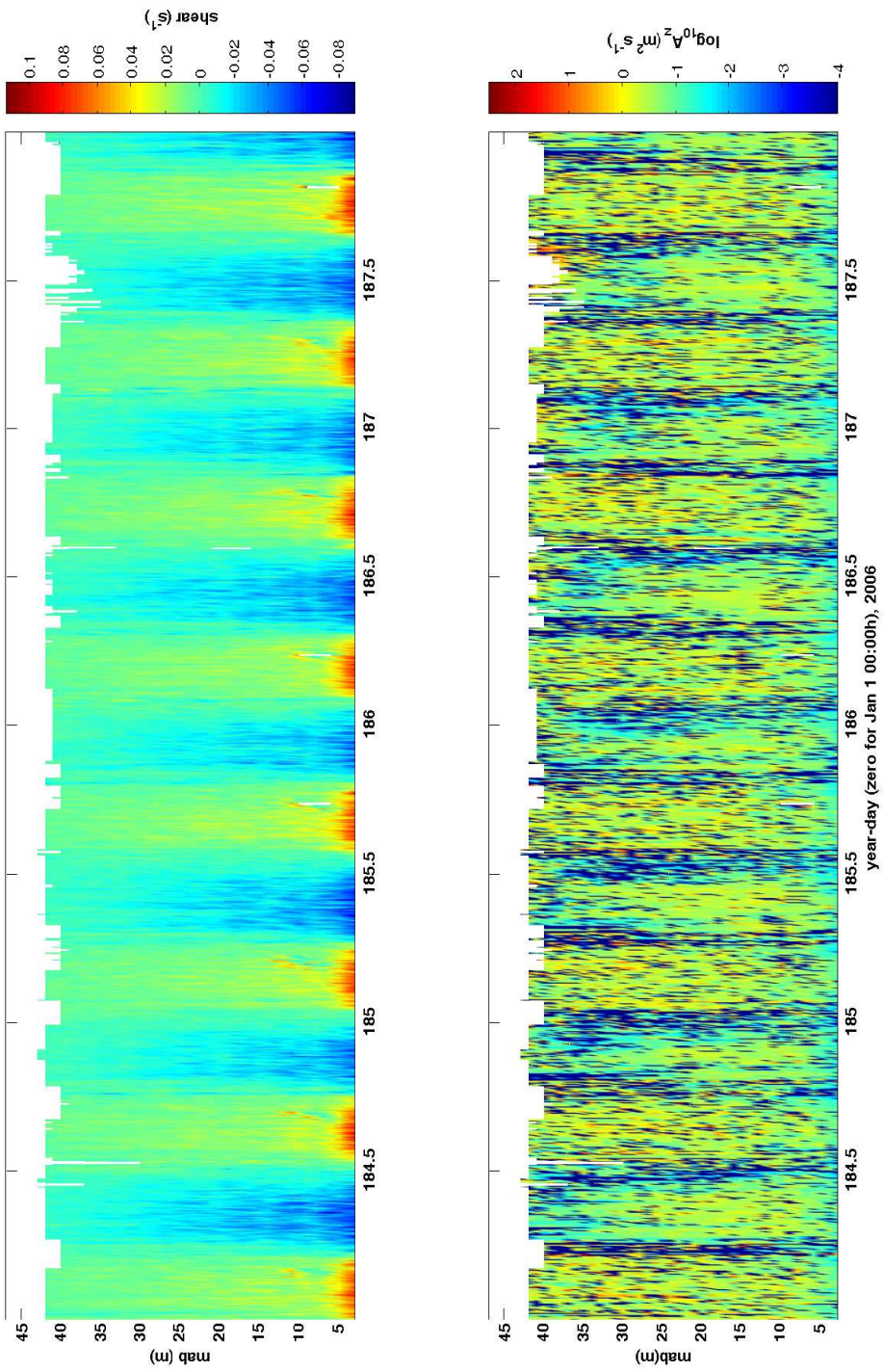

Figure 6.8: Depth-time series of (a) vertical shear (s^{-1}) (upper panel) (b) eddy viscosity ($m^2 s^{-1}$) (lower panel): DEPLOYMENT 1

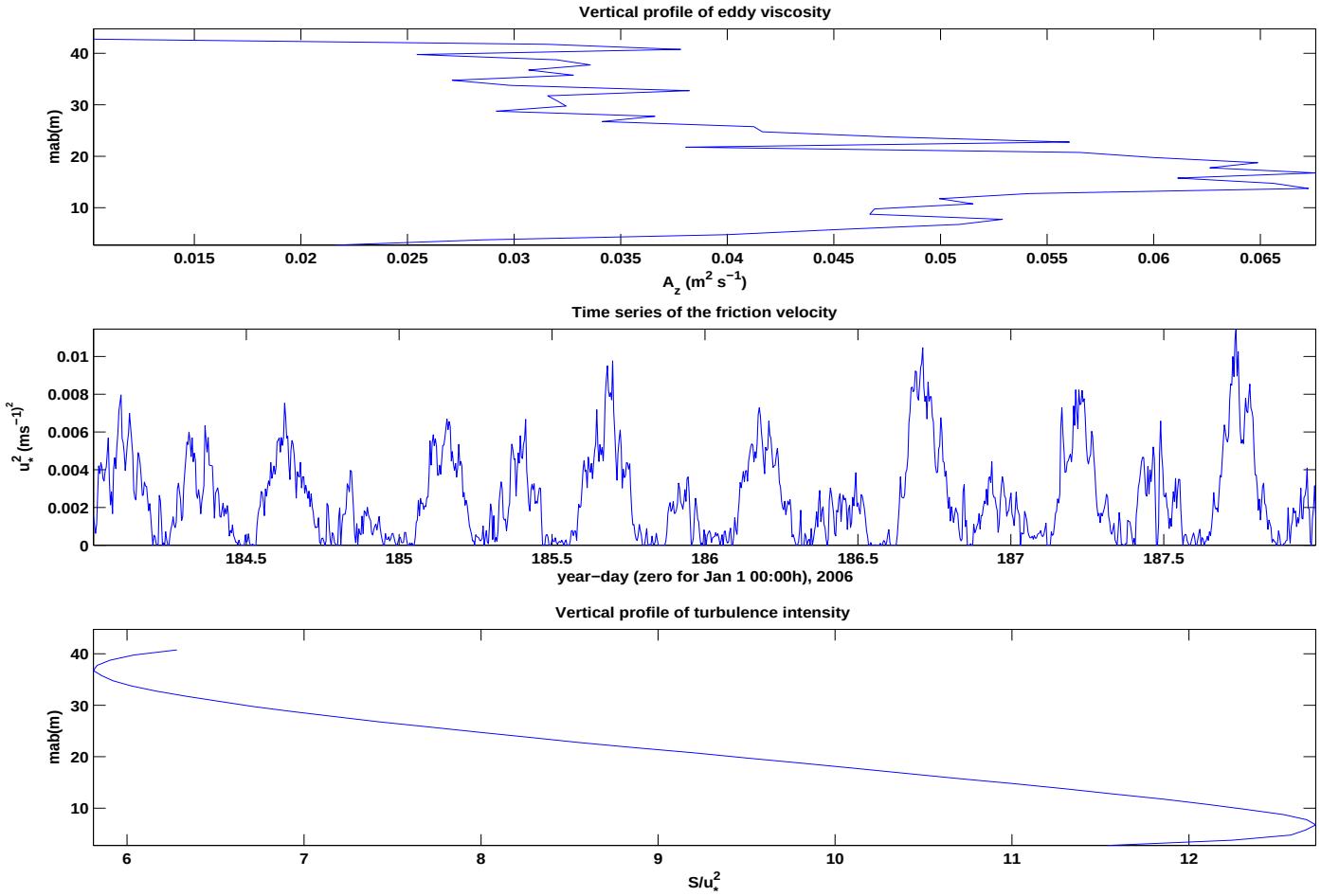

Figure 6.9: (a) Vertical profiles of eddy viscosity m^2s^{-1} (b) Time series of the friction velocity ms^{-1} (c) Vertical profile (mean) of turbulence intensity; (a… c)=(first… last panel) : DEPLOYMENT 1

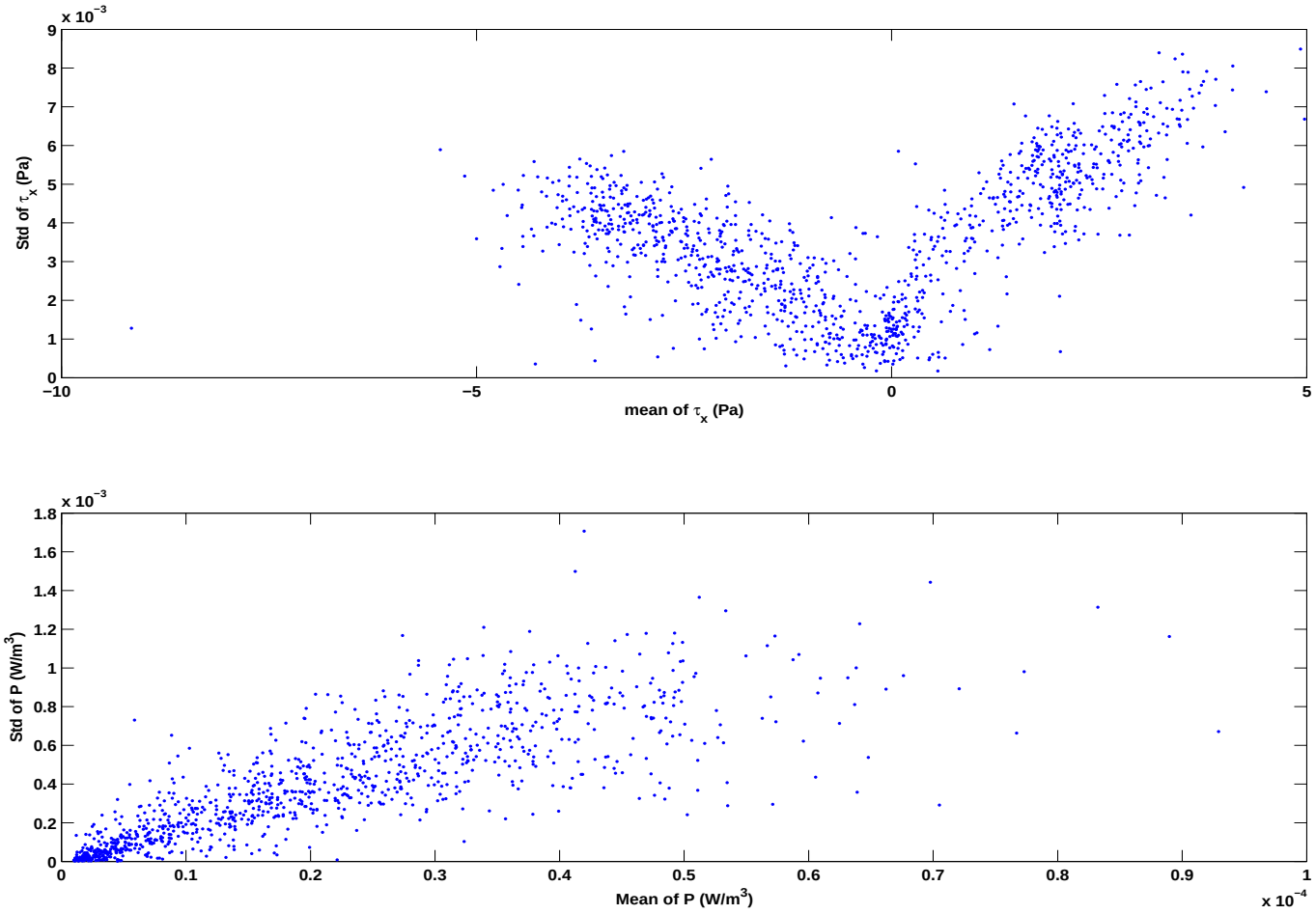

Figure 6.10: (a) Scatter plot of (a) The standard deviation of Reynolds stress calculated plotted as a function of mean stress (b) TKE production rate estimates plotted against the mean value of the TKE production rate (a… b)=(first… last panel): DEPLOYMENT 1

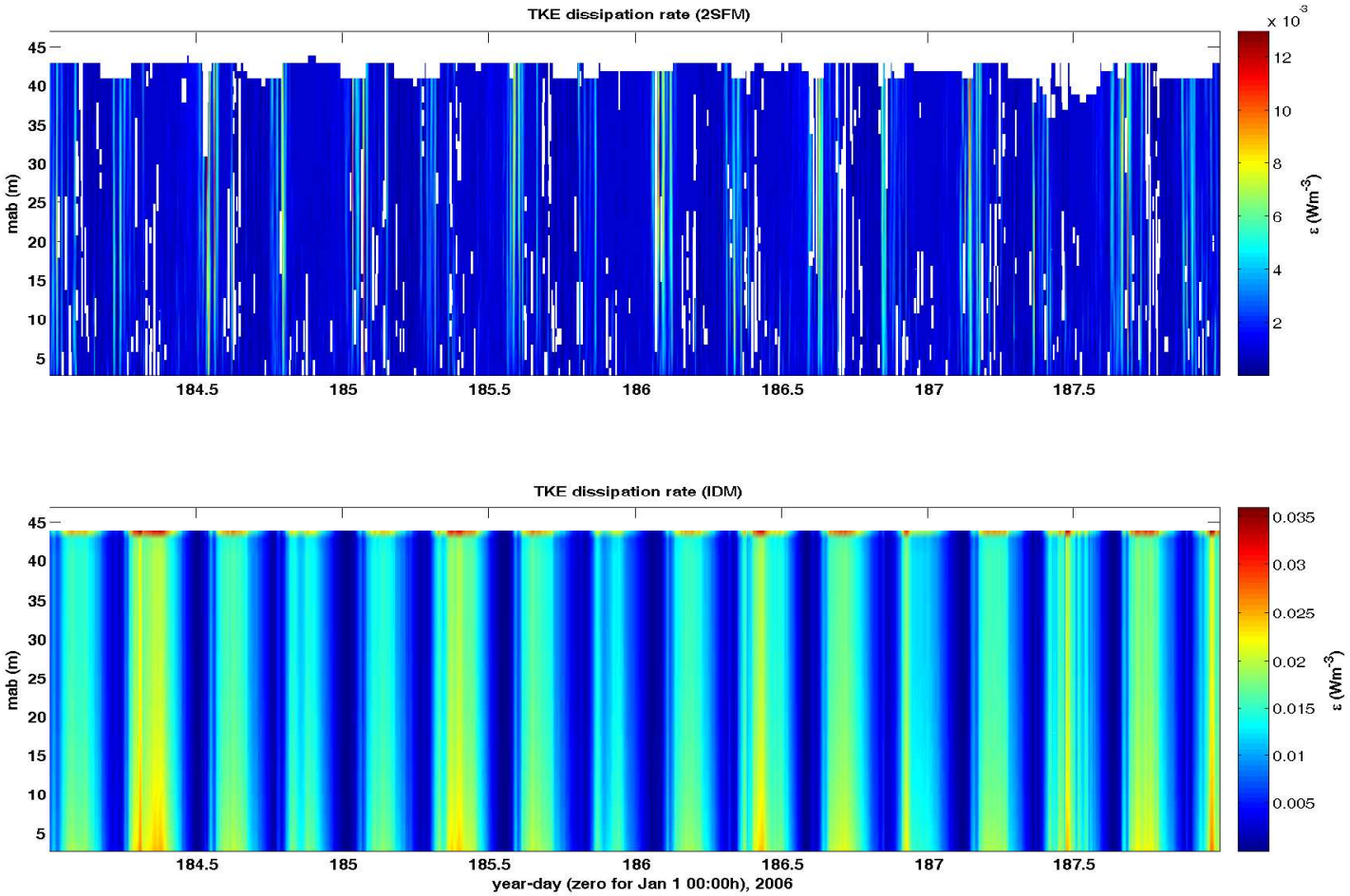

Figure 6.11: Depth-time series of (a) TKE dissipation rate using 2SFM (Wm^{-3}) and (b) TKE dissipation rate using IDM (Wm^{-3});(a… b)=(first… last panel) : DEPLOYMENT 1

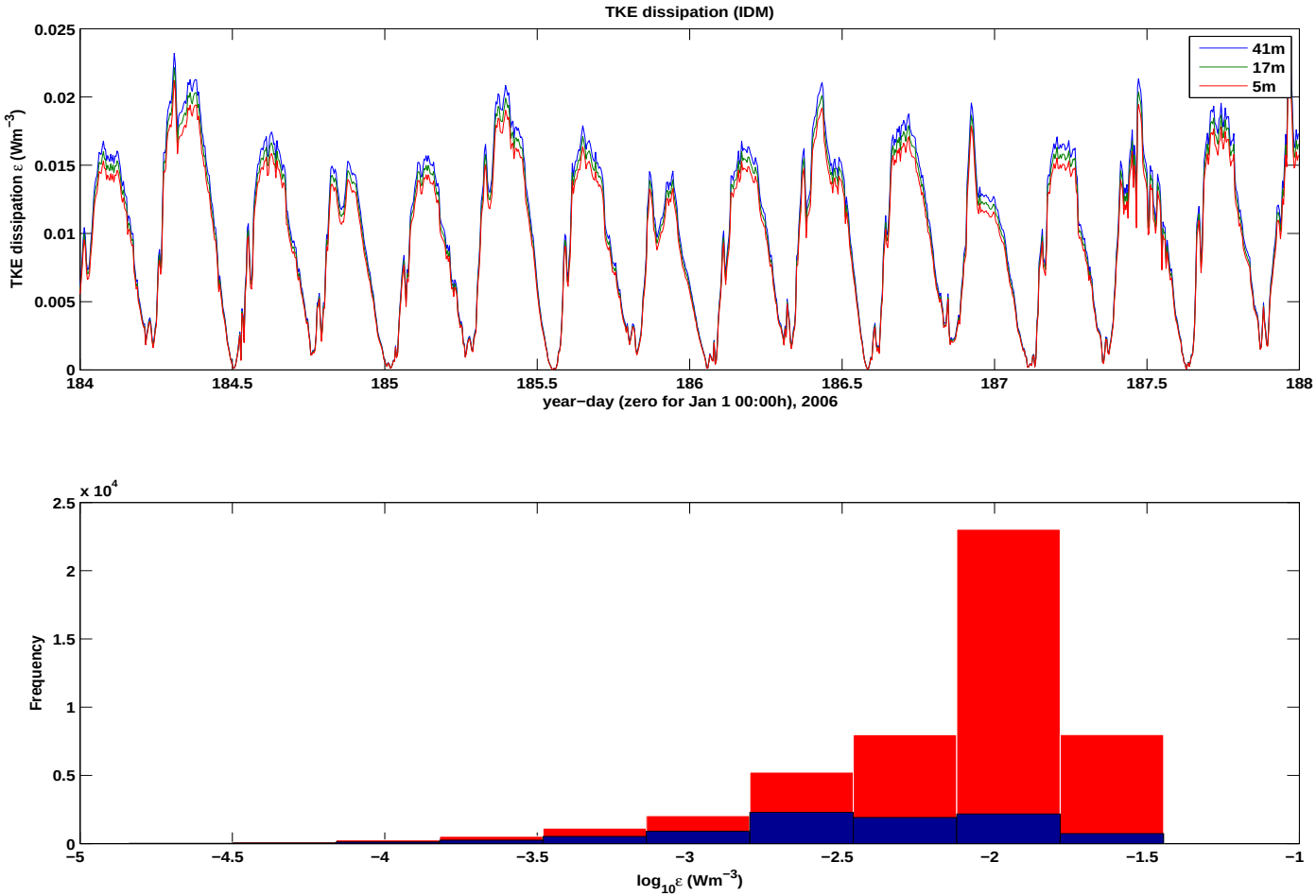

Figure 6.12: (a) Estimates of ε at 41, 17 and 5 m above bed (b) distribution of ε and TKE production P measurements in space and time. The overlaid black histogram shows the distribution of ε measurements corresponds to negative P estimates; negative values of TKE are dissipation: DEPLOYMENT 1

6.2.2 Deployment 2

The dataset from Deployment 2 covers both neap and spring tidal cycles. Figures 6.13-6.27 show similar profiles of turbulence structures as Deployment 1 with different mean water depth. As expected, the boundary layer thickness was seen to occupy the larger part of the water column with the surface wave effect seen to penetrate deeply into the water column especially during the spring tide (yeardays 280-286, 297-302) (Figures 6.13a and d). The values of Reynolds stress, TKE density, TKE (IDM) and eddy viscosity at $\sim 4m$ above seabed were $\sim 12Pa$, $\sim 0.2m^2s^{-2}$, $\sim 1.01Wm^{-3}$ and $\sim 8.7 \times 10^{-3}m^2s^{-1}$, respectively. However as observed in Deployment 1, the largest value of the turbulence intensity did not occur at the seabed but close to the water surface due to the influence of wave action (Figure 6.24c). This suggest that the intensity of turbulence in an energetic tidal flow is largely influenced by water depth and wave action. Interestingly, the value of ~ 14.3 was estimated for turbulence intensity near the seabed for Deployment 2 as compared to ~ 12.7 for Deployment 1. This suggests from these datasets that turbulence intensity at the seabed is site specific and mostly influenced by the magnitude of current velocity, wave action and water depth. The minimum and maximum values of vertical A_z from this deployment are found to be $\sim 0.0087m^2s^{-1}$ ($\sim 87cm^2s^{-1}$) and $\sim 0.0108m^2s^{-1}$ ($\sim 108cm^2s^{-1}$) (Figure 6.24a). From equation 2.5.14 and following Williams and Simpson [124], the linear regression equation from Deployment 2 data is:

$$\sigma_{st} = 0.0010\tau_x + 0.0004 \tag{6.2.2}$$

showing a slight reduction in the flow-related component of the uncertainty. This is assumed to be due to the larger vertical bin size used in Deployment 2 (1.5 m) compared to that used in Deployment 1 (1 m).

Figures 6.16-6.21 show mean Reynolds stress profiles at hourly intervals for a 12-h period (a tidal cycle) over 12 tidal cycles for both neap and spring tides. The profiles are obtained with a 60-min averaging period. The minimum value of the sum for each depth is determined and the lowest value of Reynolds stress per depth (given 20 m clearance above the seabed and 10 m clearance below water surface). The best installation position for a floating tidal turbine ranged between $\pm 13.60m$ (36.32%) with 95% confidence interval of $\sim 1.50m$ below mean water level (Table 6.3-6.5) $\sim 21 - 27$ m above bed. Table 6.3-6.5 list the 60 tidal cycles with their corresponding 'best position'

values for a floating tidal turbine installation. The 95% confidence intervals were calculated for each tidal cycle as the standard error multiplied by the critical two-tailed value of t-distribution. The mean of 36.32% (13.60 m below MWL) which fluctuates within the confidence interval $\sim 1.50m$ (Figure 6.22), found to be the best installation position for floating tidal turbine for a mean water depth of 37 m at the fall of Warness. The scatter plot of the standard deviation of Reynolds stress against the mean stress (Figure 6.25) shows an increased correlation than the scatter plot (Figure 6.10) in Deployment 1. This suggests that the bulk turbulence parameters estimate can be improved with a larger dataset. The TKE dissipation estimate from IDM performs better than the estimate from 2SFM (Figure 6.26). This confirms the earlier result obtained in section 6.2.1 (Figure 6.11). Three profiles of TKE dissipation rates ε are shown in Figure 6.27 (upper panel) overlaid with distribution of TKE production rates P (Figure 6.27). A general enhancement is seen between spring and neap tides, but there is no clear variance with depth. As discussed in Chapter 2, section 2.5.1, IDM performance with noisy data is very poor and this is expected, especially with the surface wave effect as seen in Figure 6.2. The discrepancies between ε and P (unbalanced turbulence kinetic energy budget) are expected since the isotropic assumption upon which IDM estimates are based, are not met.

Tidal Cycle	Best Turbine Position (Turbine position below MWL) (m)	Depth (below MWL) (%)	95% conf. (m) ($\pm$)
1	14.12	37.71	1.38
2	14.12	37.71	1.55
3	13.25	35.38	1.57
4	13.62	36.38	1.49
5	12.87	34.38	1.65
6	12.87	34.38	1.38
7	13.62	36.38	1.43
8	13.62	36.38	1.55
9	13.87	37.05	1.42
10	13.00	34.71	1.59
11	13.12	35.04	1.78
12	14.00	37.38	1.74
13	11.75	31.37	1.46
14	13.25	35.38	1.76
15	13.37	35.71	1.60
16	15.00	40.05	1.47
17	13.00	34.71	1.48
18	12.37	33.04	1.36
19	13.25	35.38	1.40
20	12.50	33.38	0.85

Table 6.3: Best turbine position (BTP) (bin position below MWL) at depth below water surface for 60 tidal cycles (Deployment 2): 5 October - 5 November 2007

Tidal Cycle	Best Turbine Position (Turbine position below MWL) (m)	Depth (below MWL) (%)	95% conf. (m) ($\pm$)
21	15.00	40.05	1.52
22	13.87	37.05	1.16
23	13.12	35.04	1.58
24	13.25	35.38	1.21
25	13.37	35.71	1.55
26	13.87	37.05	1.36
27	14.25	38.05	1.55
28	14.00	37.38	1.59
29	13.50	36.05	1.63
30	13.50	36.05	1.52
31	12.75	34.04	1.70
32	13.75	36.71	1.62
33	14.87	39.72	1.31
34	13.87	37.05	1.58
35	13.50	36.05	1.63
36	15.75	42.05	1.11
37	13.62	36.38	1.49
38	13.62	36.38	1.11
39	13.50	36.05	1.86

Table 6.4: Best turbine position (BTP) (bin position below MWL) at depth below water surface for 60 tidal cycles (Deployment 2): 5 October - 5 November 2007 (Cont.)

Tidal Cycle	Best Turbine Position (Turbine position below MWL) (m)	Depth (below MWL) (%)	95% conf. (m) (±)
40	13.87	37.05	1.78
41	13.12	35.04	1.42
42	13.37	35.71	1.75
43	12.62	33.71	1.49
44	13.00	34.71	1.96
45	12.87	34.38	1.65
46	13.25	35.38	1.51
47	13.87	37.05	1.82
48	13.37	35.71	1.79
49	13.25	35.38	1.34
50	14.25	38.05	1.70
51	13.75	36.71	1.51
52	14.25	38.05	1.55
53	13.25	35.38	1.62
54	14.12	37.71	1.38
55	13.00	34.71	1.31
56	12.87	34.38	1.70
57	14.87	39.72	1.38
58	15.00	40.05	1.41
59	14.87	39.72	1.03
60	13.62	36.38	1.49
Mean	**13.60**	**36.32**	**1.51**

Table 6.5: Best turbine position (BTP) (bin position below MWL) at depth below water surface for 60 tidal cycles (Deployment 2): 5 October - 5 November 2007 (Cont.)

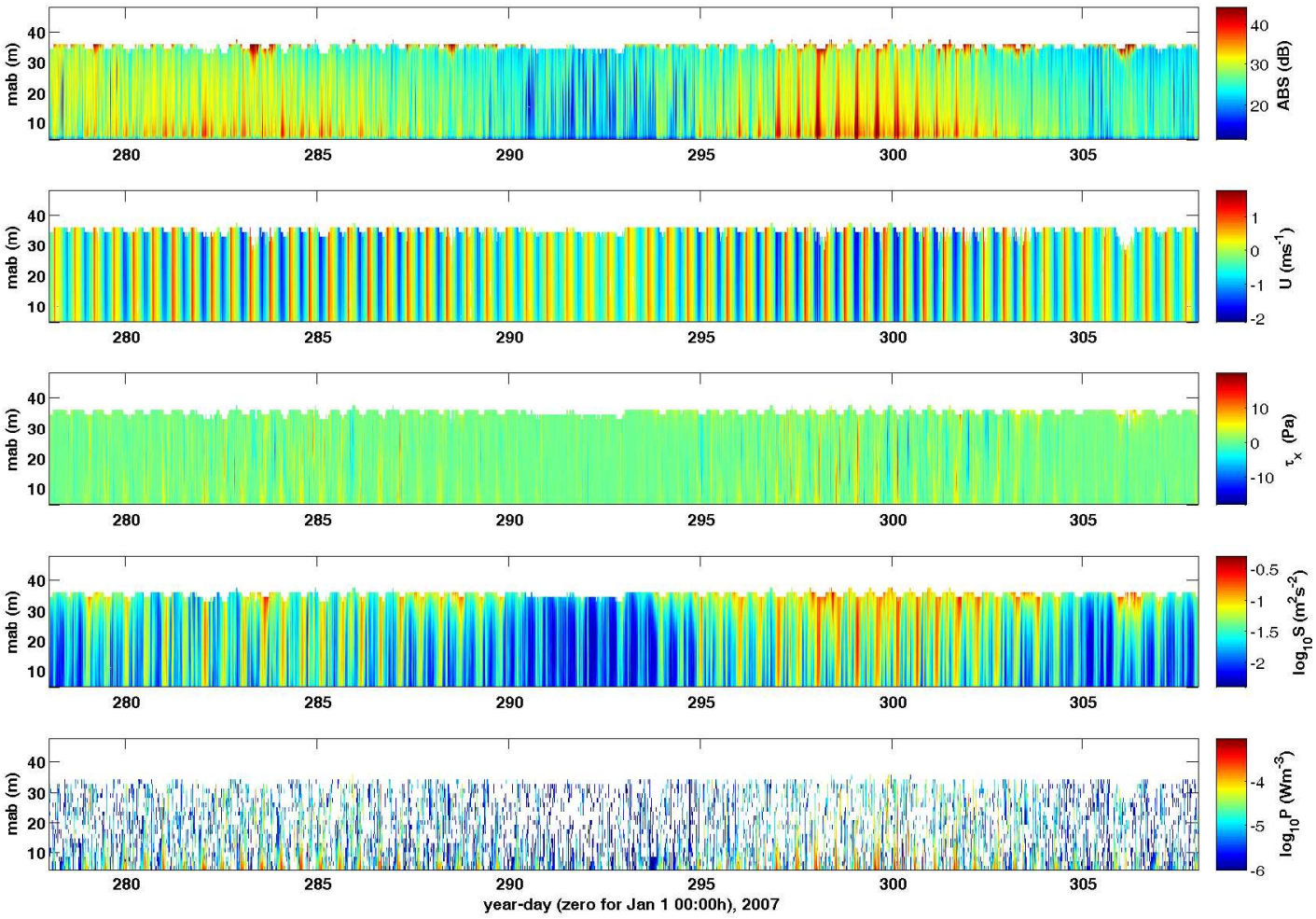

Figure 6.13: Depth-time series of (a) acoustic backscatter signal strength (dB) (b) stream velocity (ms^{-1}) (c) Reynolds stress (Pa) (d) TKE density (Jm^{-3}) (e) TKE production (Wm^{-3}) ; (a… e)=(first… last panel) : DEPLOYMENT 2

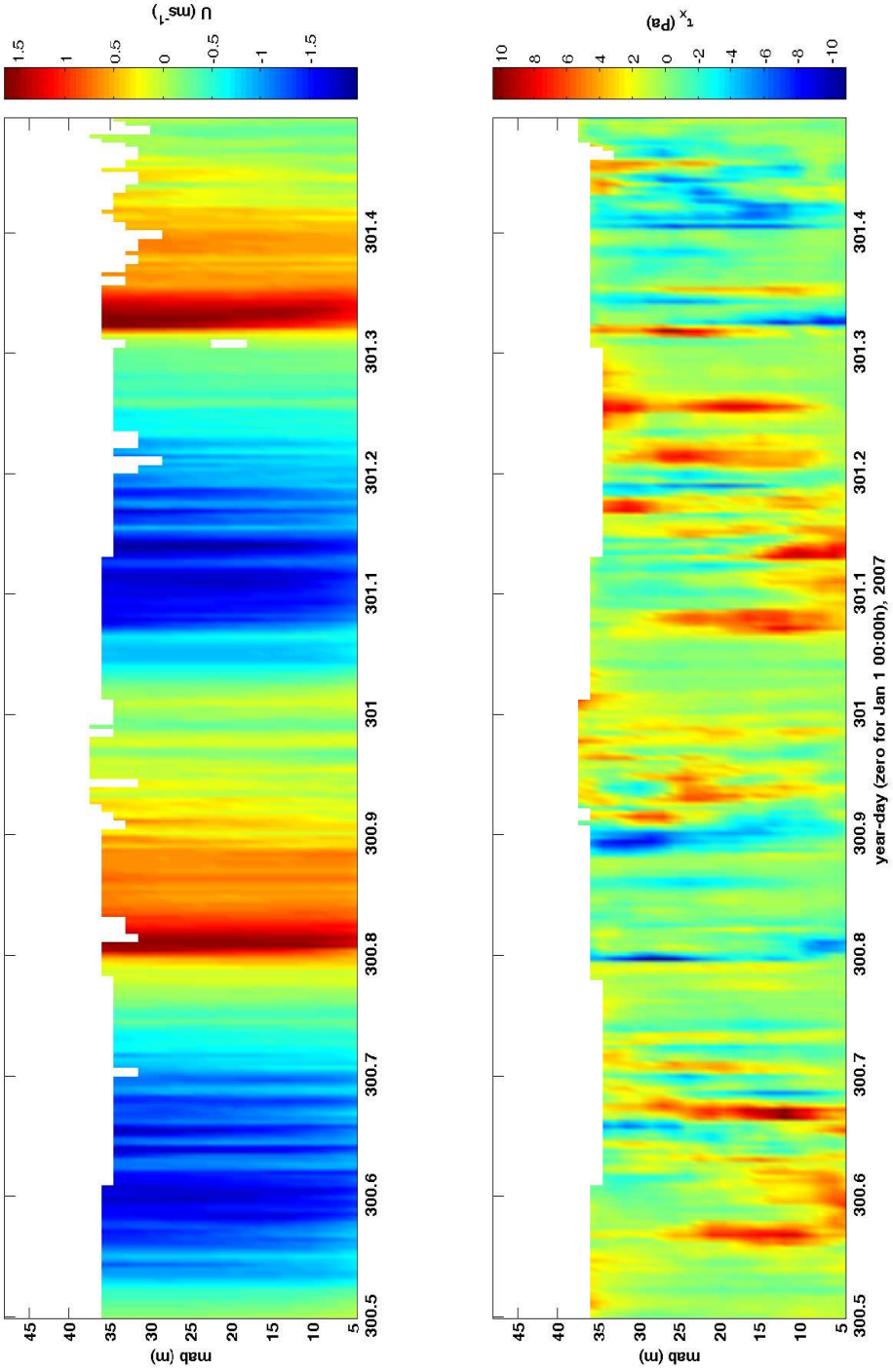

Figure 6.14: Depth-time series of (a) current velocity (ms^{-1}) and (b) Reynolds stress (Pa): DEPLOYMENT 2

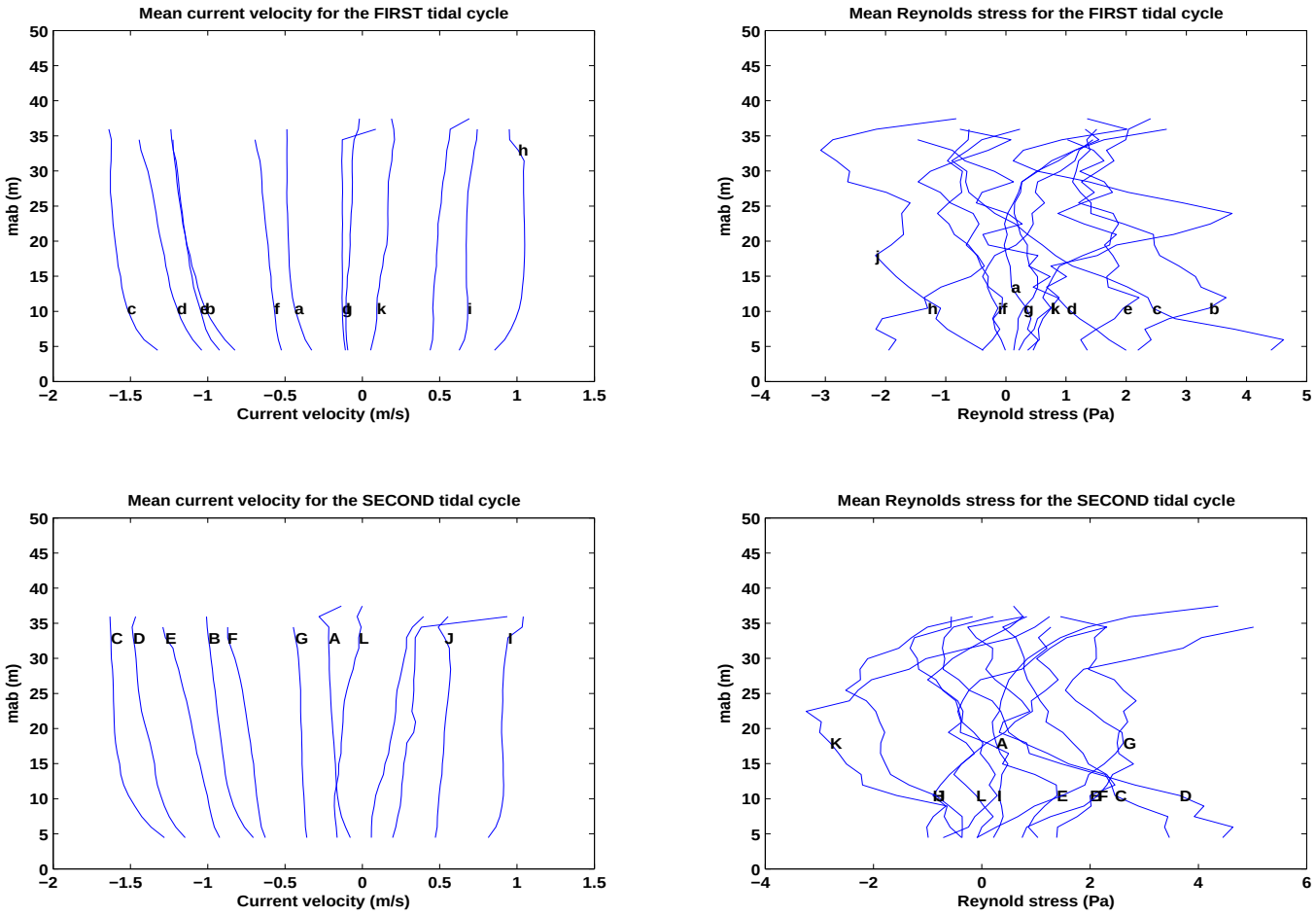

Figure 6.15: Mean velocity (ms^{-1}) profiles for 2 tidal cycles (24 hours) (yearday 300-301) (left). Hourly mean Reynolds stress (Pa) profiles at times corresponding to the stress profiles in (a) (right): Letters a-l and A-L correspond to mean profiles for currents and Reynolds stresses over 12 hours: DEPLOYMENT 2

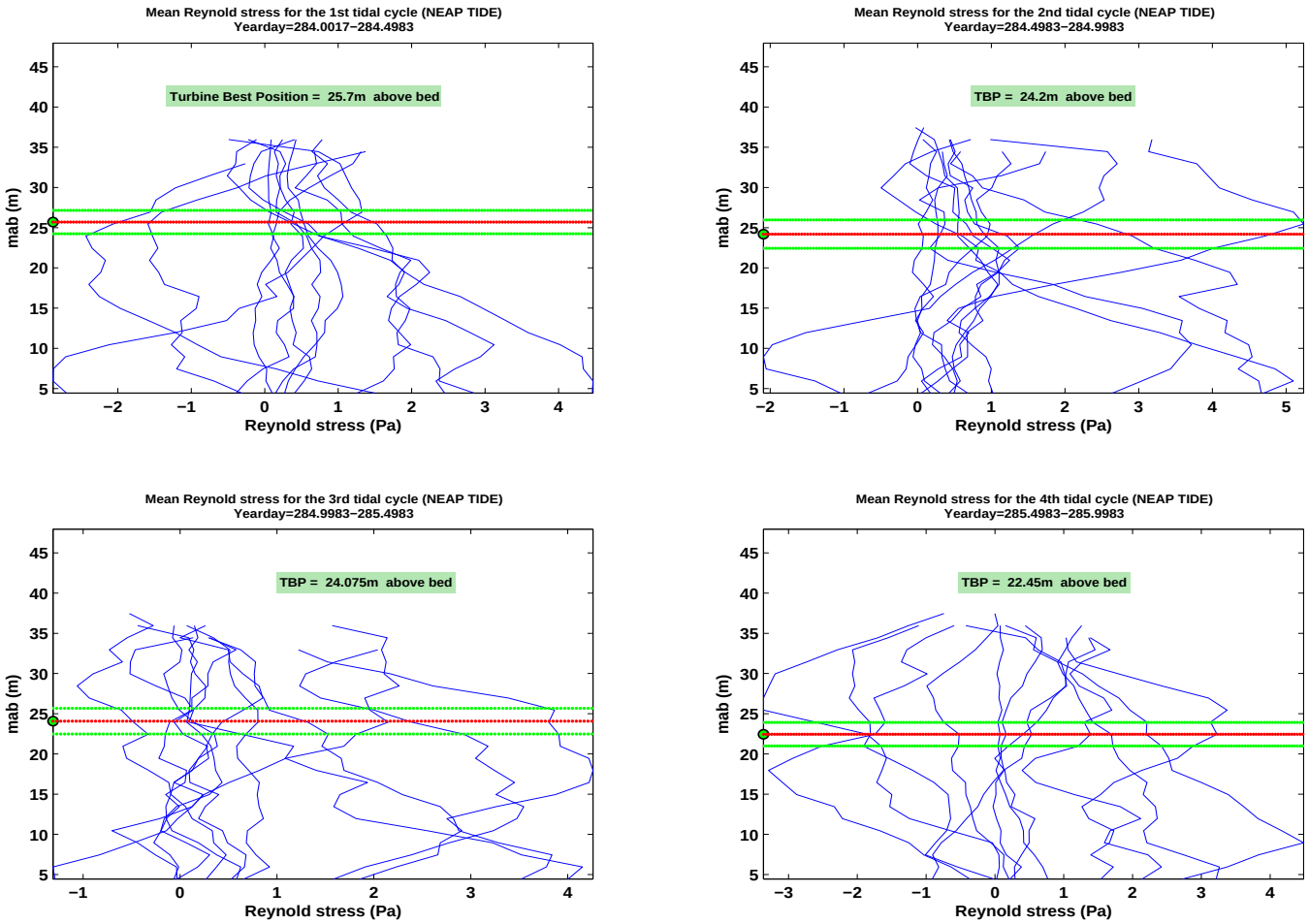

Figure 6.16: Hourly mean Reynolds stress (*Pa*) profiles for 4 tidal cycles (48 hours) (yearday 284.4983-286.4948); The red line is the (mean) best position and the green lines indicate the 95% confidence interval calculated as the standard error multiplied by the critical two-tailed value of t-distribution : DEPLOYMENT 2

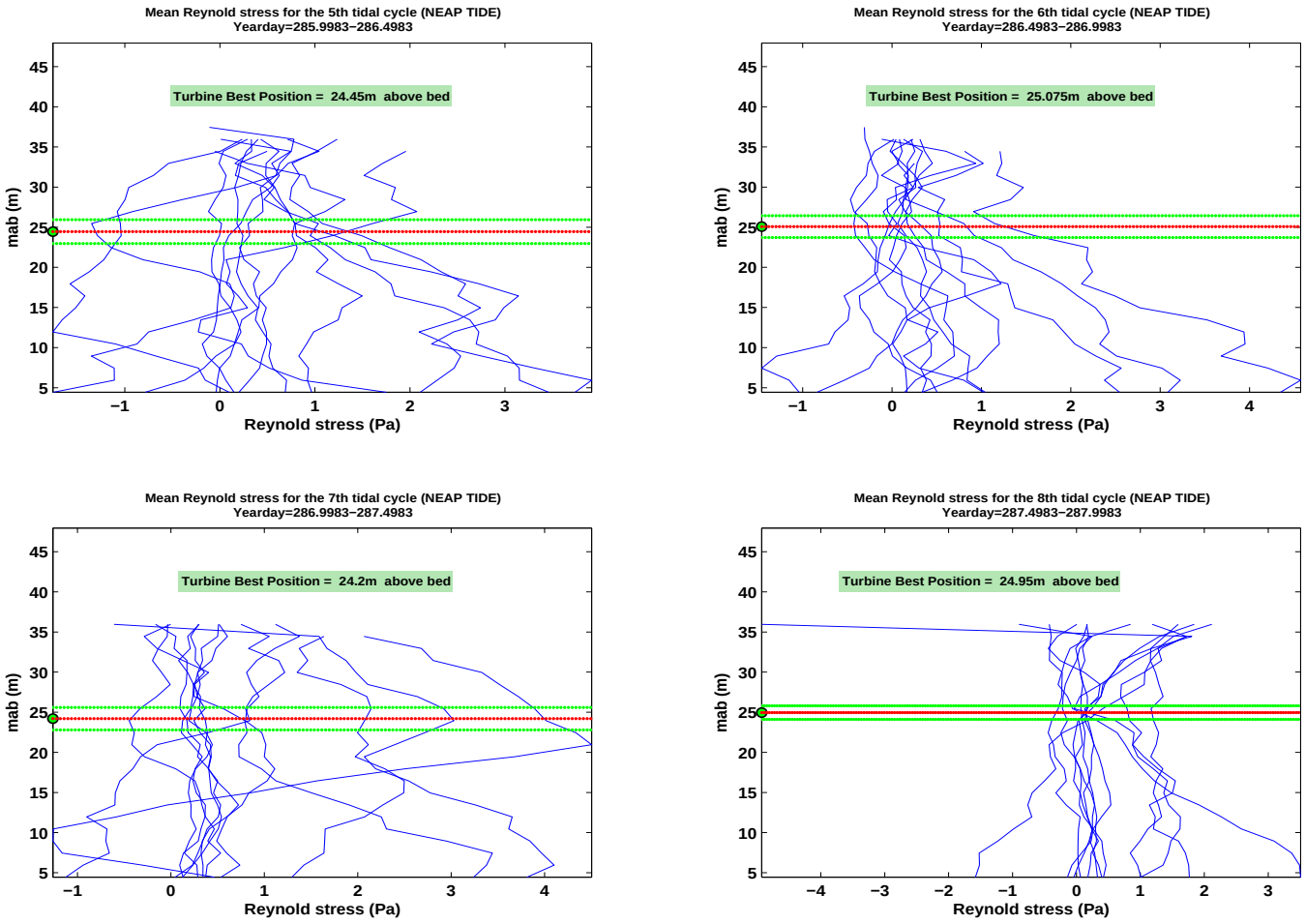

Figure 6.17: Hourly mean Reynolds stress (Pa) profiles for 4 tidal cycles (48 hours) (yearday 286.4948-288.4948); The red line is the (mean) best position and the green lines indicate the 95% confidence interval calculated as the standard error multiplied by the critical two-tailed value of t-distribution : DEPLOYMENT 2

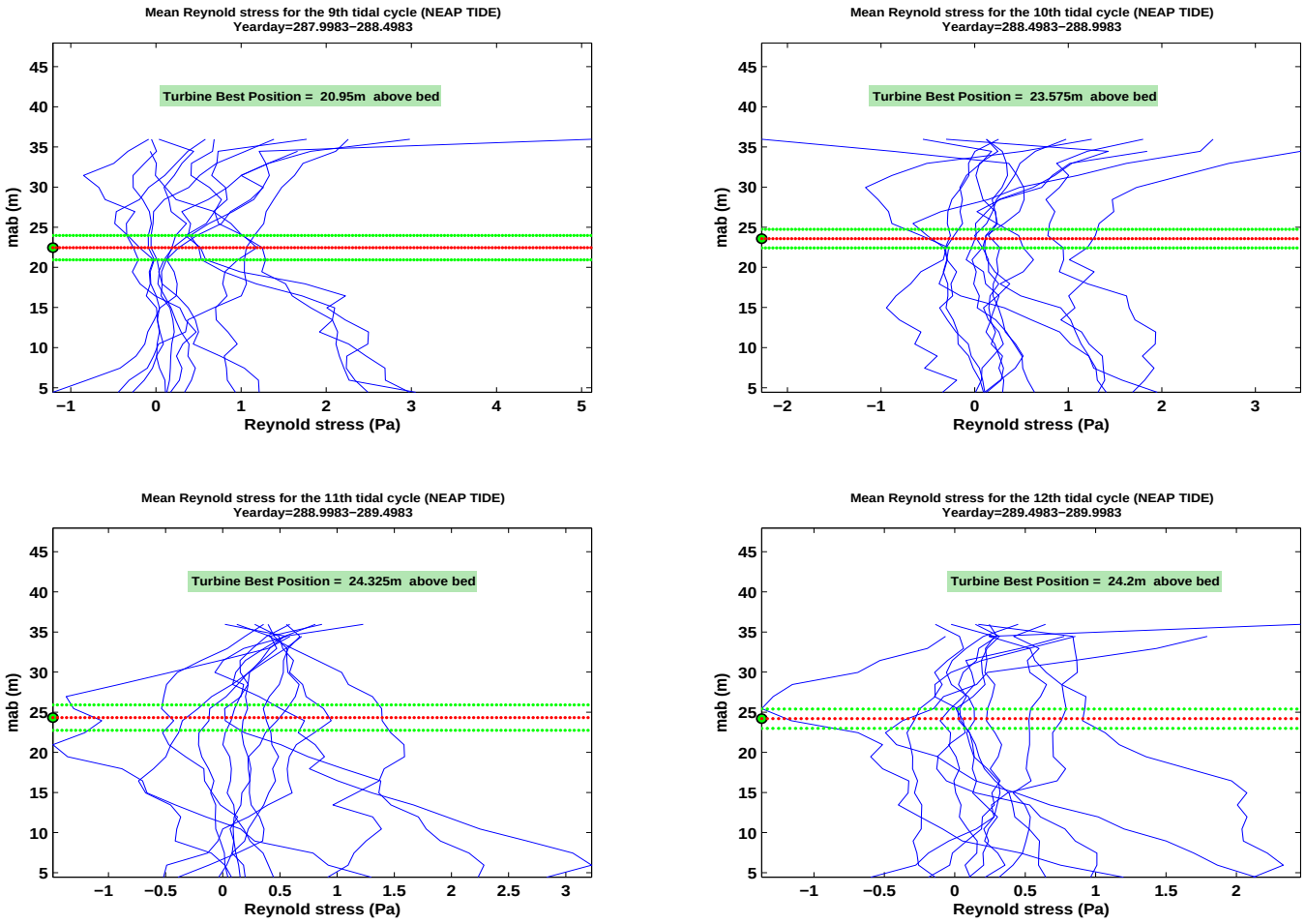

Figure 6.18: Hourly mean Reynolds stress (Pa) profiles for 4 tidal cycles (48 hours) (yearday 288.4948-290.4948);The red line is the (mean) best position and the green lines indicate the 95% confidence interval calculated as the standard error multiplied by the critical two-tailed value of t-distribution: DEPLOYMENT 2

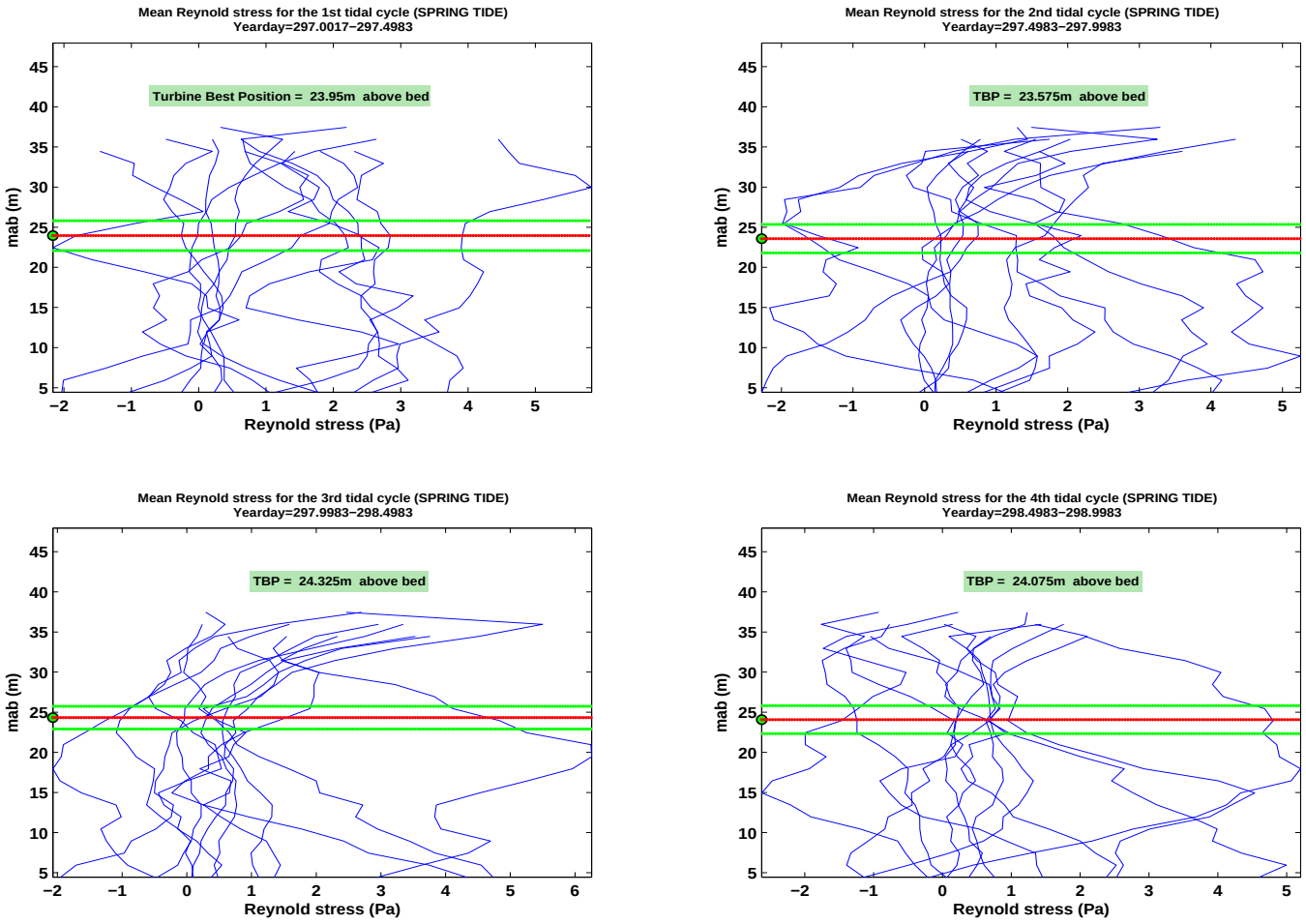

Figure 6.19: Hourly mean Reynolds stress (*Pa*) profiles for 4 tidal cycles (48 hours) (yearday 297.4983-299.4948); The red line is the (mean) best position and the green lines indicate the 95% confidence interval calculated as the standard error multiplied by the critical two-tailed value of t-distribution : DEPLOYMENT 2

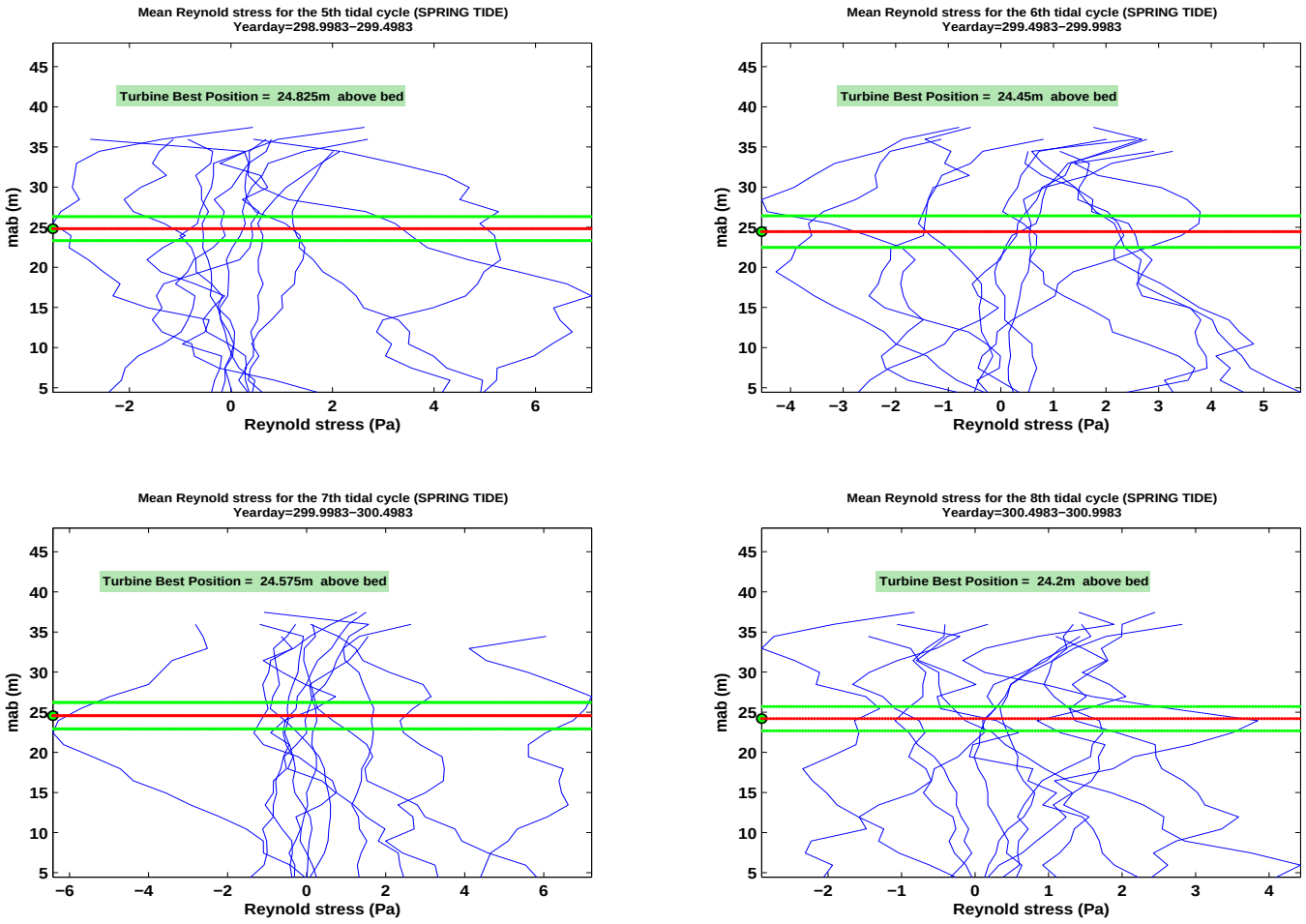

Figure 6.20: Hourly mean Reynolds stress (Pa) profiles for 4 tidal cycles (48 hours) (yearday 299.4948-301.4948); The red line is the (mean) best position and the green lines indicate the 95% confidence interval calculated as the standard error multiplied by the critical two-tailed value of t-distribution : DEPLOYMENT 2

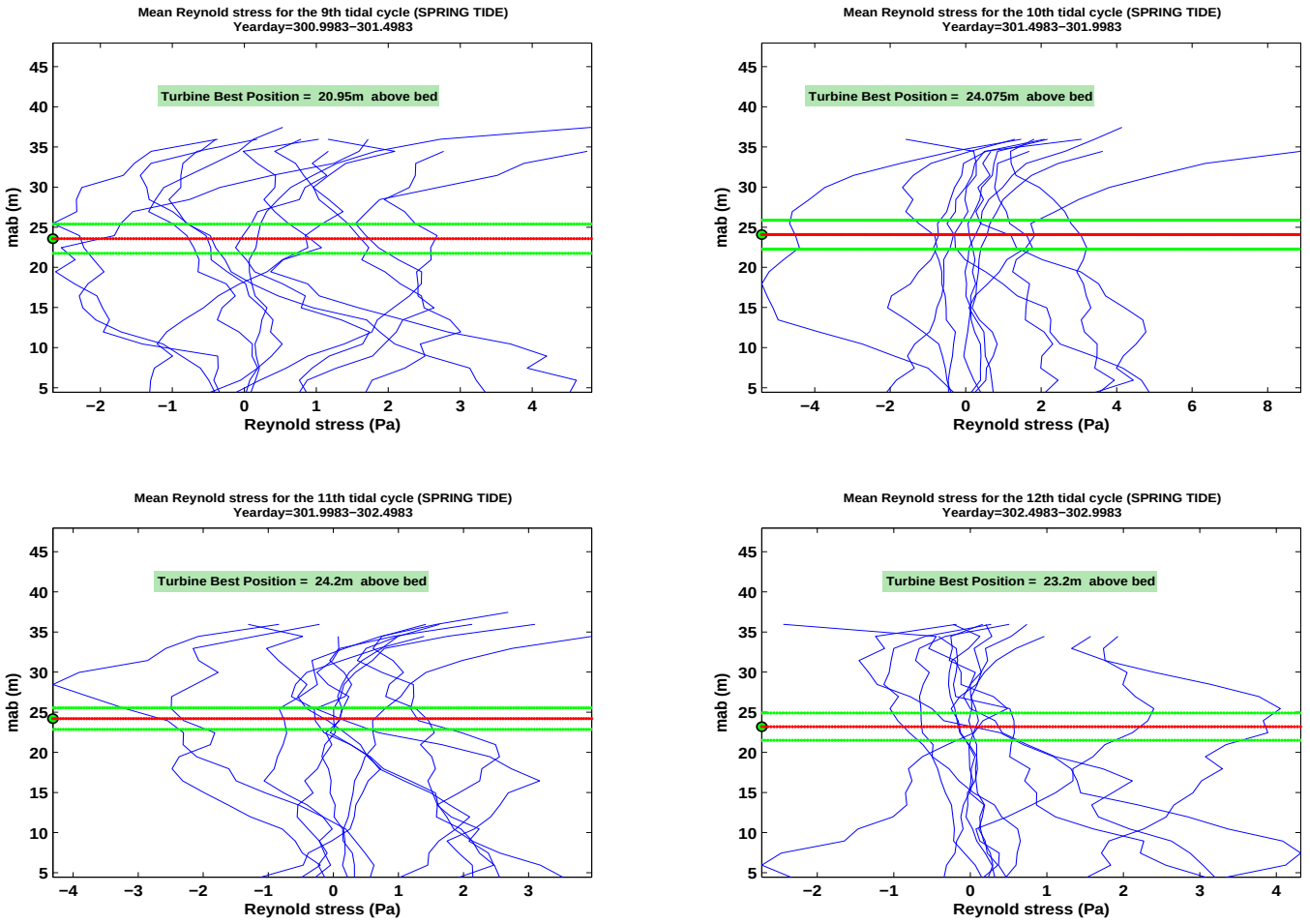

Figure 6.21: Hourly mean Reynolds stress (*Pa*) profiles for 4 tidal cycles (48 hours) (yearday 301.4948-303.4948); The red line is the (mean) best position and the green lines indicate the 95% confidence interval calculated as the standard error multiplied by the critical two-tailed value of t-distribution : DEPLOYMENT 2

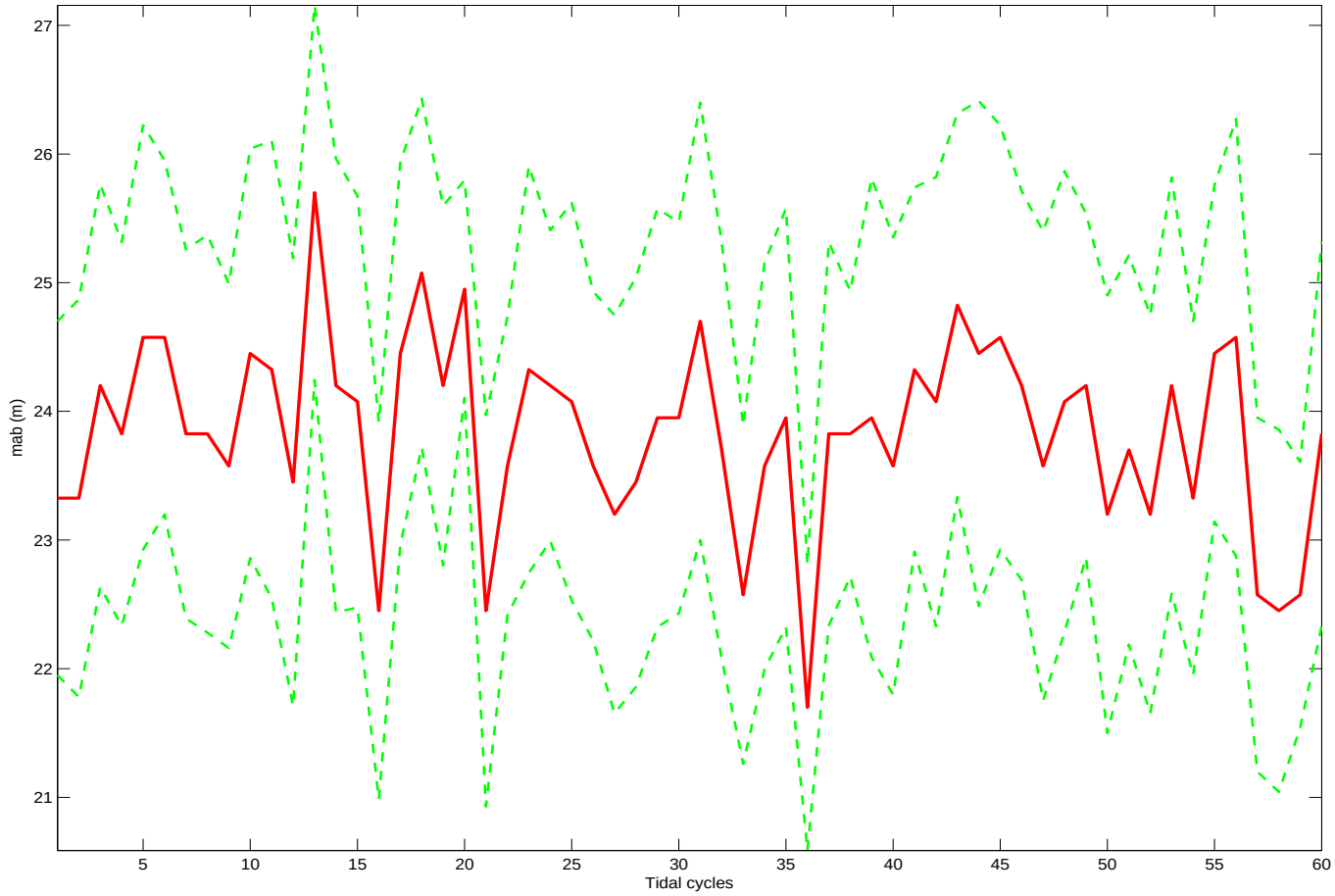

Figure 6.22: Mean of best turbine positions versus tidal cycles (red line) and the green lines indicate the 95% confidence interval calculated as the standard error multiplied by the critical two-tailed value of t-distribution: DEPLOYMENT 2

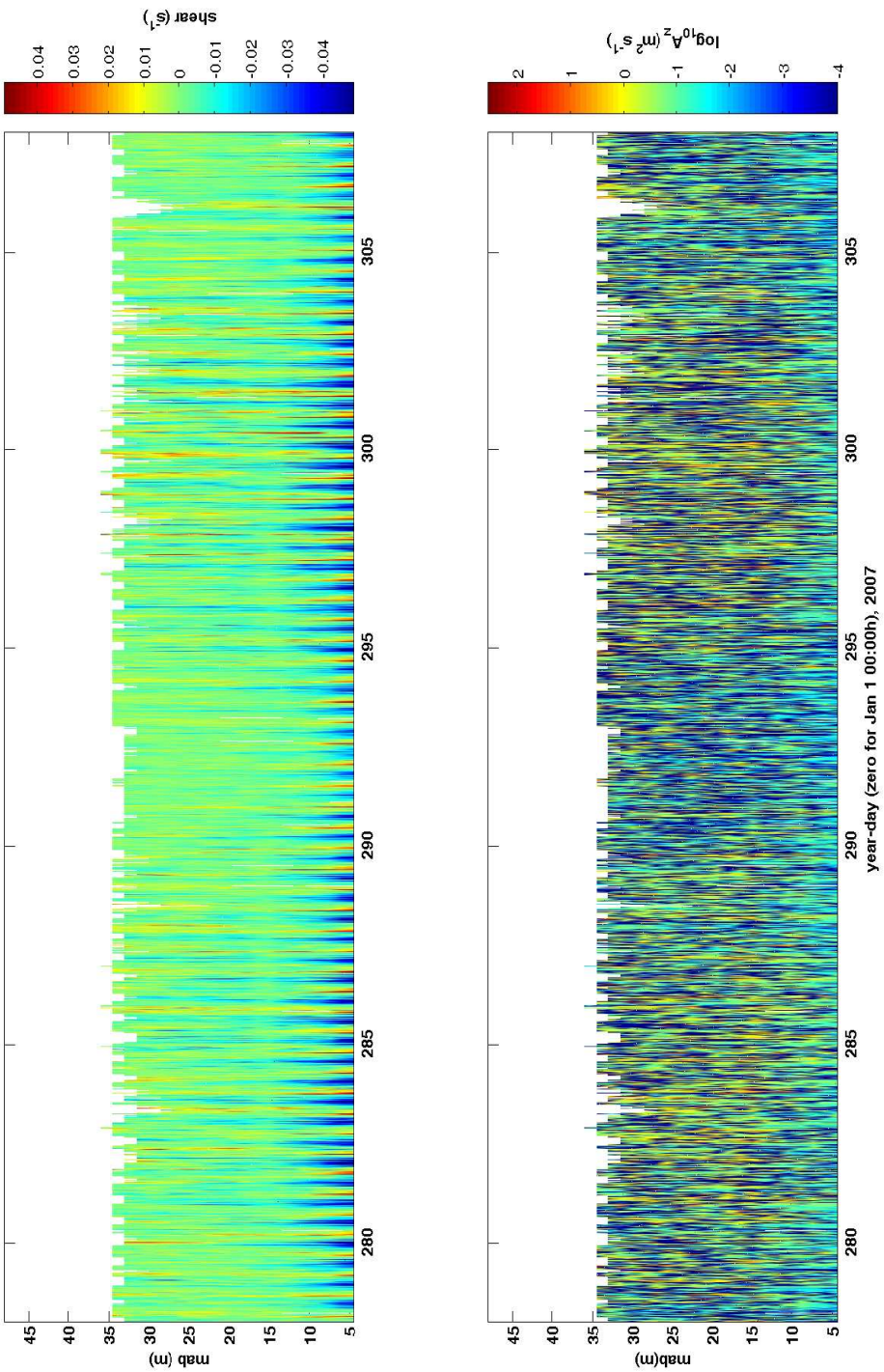

Figure 6.23: Depth-time series of (a) vertical shear (s^{-1}) (upper panel) (b) eddy viscosity ($m^2 s^{-1}$) (lower panel): DEPLOYMENT 2

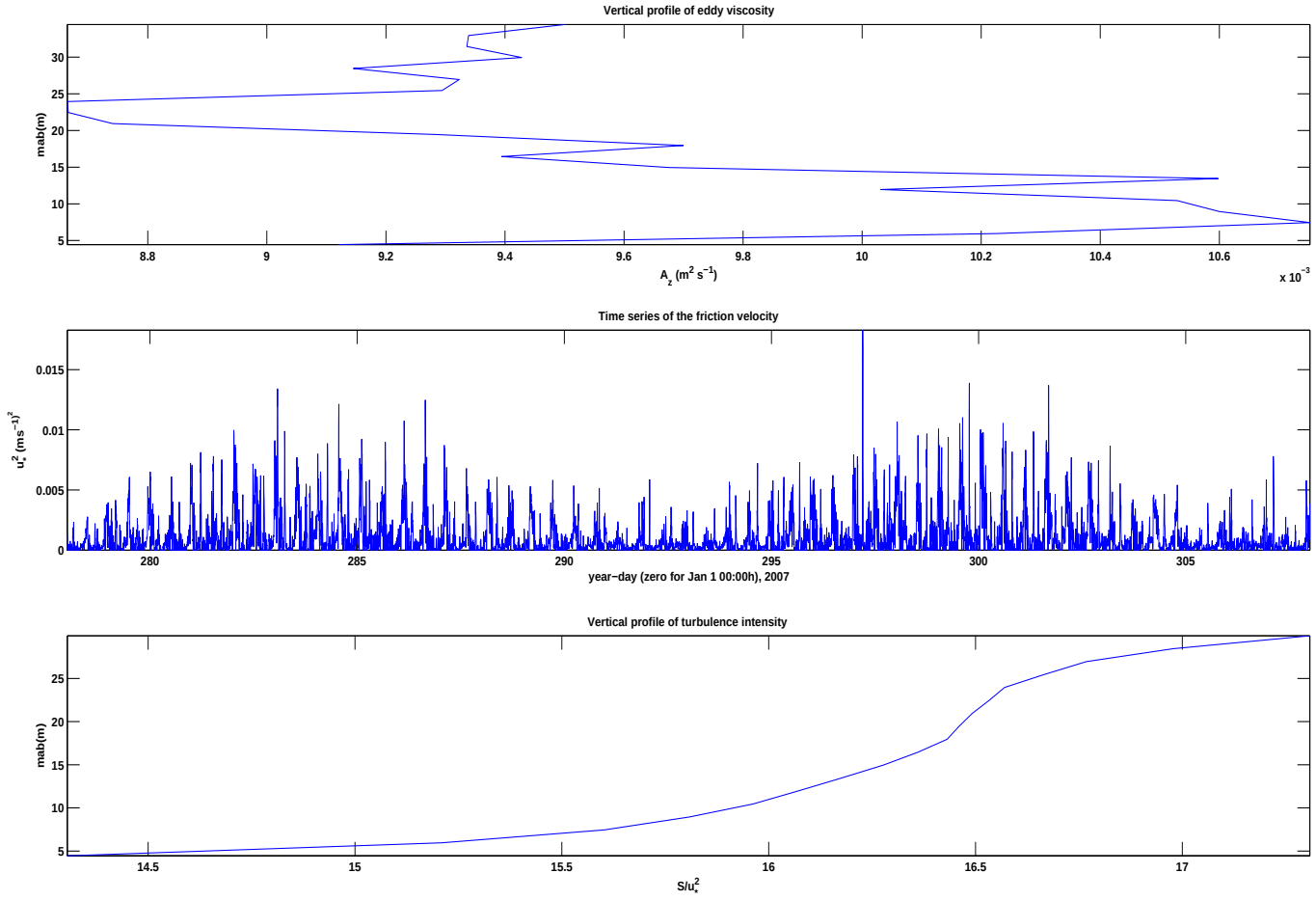

Figure 6.24: (a) Vertical profiles of eddy viscosity m^2s^{-1} (b) Time series of the friction velocity ms^{-1} (c) Vertical profile (mean) of turbulence intensity; (a… c)=(first… last panel) : DEPLOYMENT 2

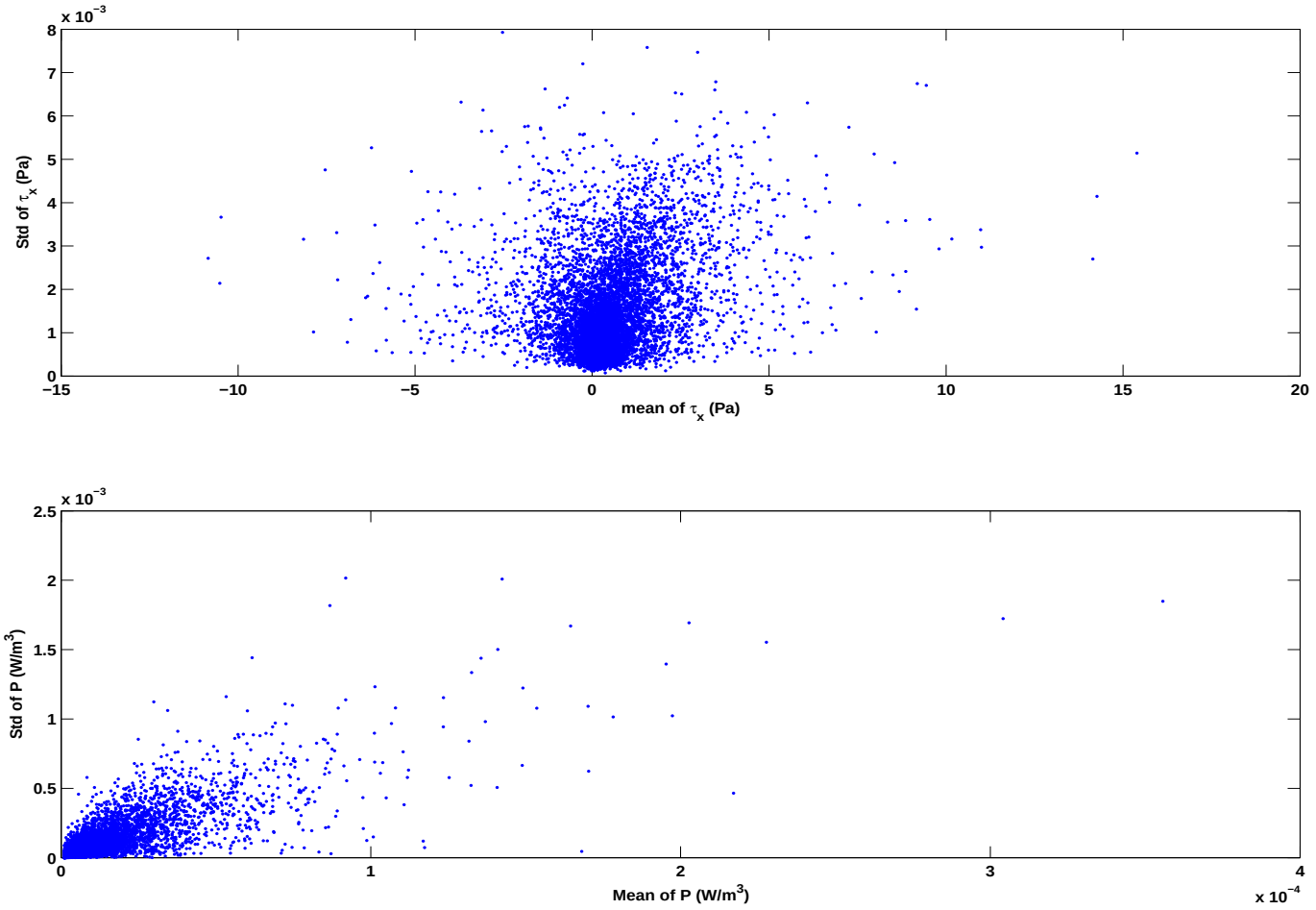

Figure 6.25: (a) Scatter plot of (a) The standard deviation of Reynolds stress calculated plotted as a function of mean stress (b) TKE production rate estimates plotted against the mean value of the TKE production rate (a… b)=(first… last panel): DEPLOYMENT 2

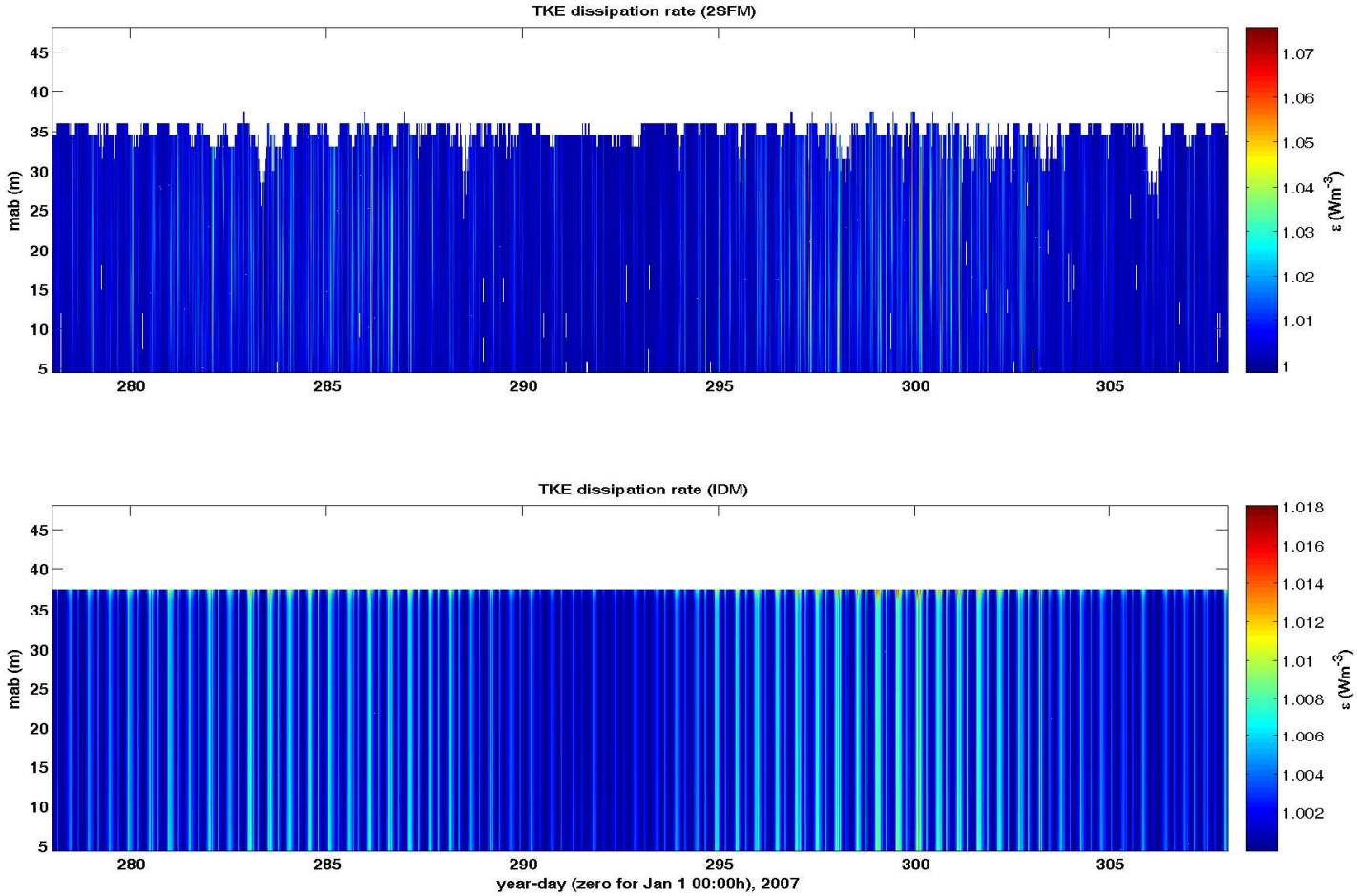

Figure 6.26: Depth-time series of (a) TKE dissipation rate using 2SFM (Wm^{-3}) and (b) TKE dissipation rate using IDM (Wm^{-3});(a… b)=(first… last panel) : DEPLOYMENT 2

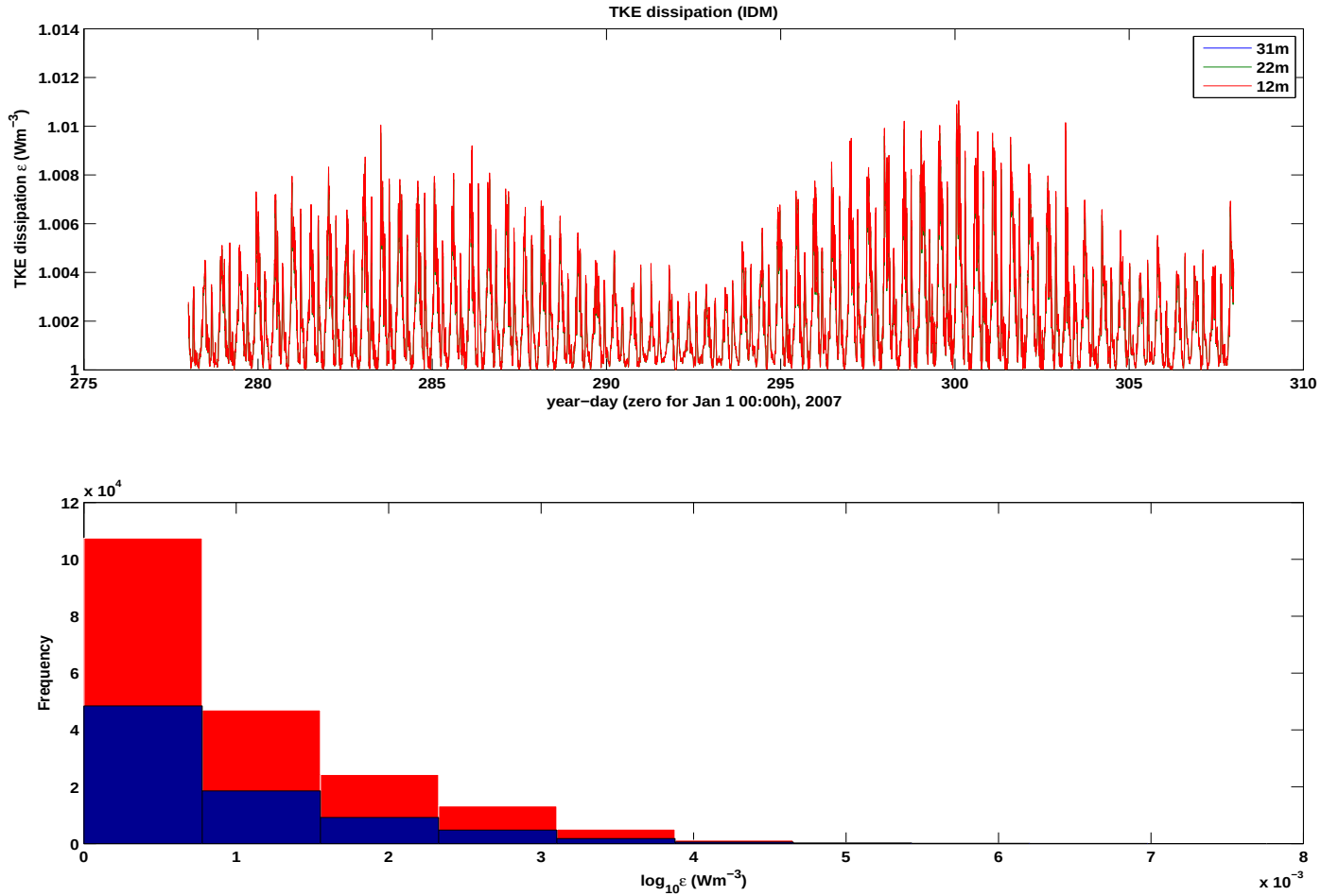

Figure 6.27: (a) Estimates of ε at 31, 22 and 12 m above bed (b) distribution of ε and TKE production P measurements in space and time. The overlaid black histogram shows the distribution of ε measurements corresponds to negative P estimates; negatives values of TKE are dissipation: DEPLOYMENT 2

Chapter 7

Conclusions and Recommendations

The goal of this thesis was to characterise a typical tidal stream site through measured data. This work has been successful in achieving these objectives. As an important step to reach this goal, various datasets collected at various times of the year, over the entire water column and at different sampling rates covering a large number of tidal cycles, have been processed, analysed and the results interpreted. While the findings from this work is of valuable interest to the marine tidal industry, this work has also provided data that will catalyse further research where other methods may be available to quantify and characterise the tidal stream site. In this Chapter, conclusions from key results discussed in the preceding Chapters are presented. Practical implications of these findings are highlighted and recommendations for future work are given.

7.1 Conclusions

This study began by reviewing research closely related to ADCP technology, waves and currents measurements, wave-current interaction and its effect on the flow kinematics, turbulence in the bottom boundary layer. In Chapter 2, a review of data analysis techniques employed in this study and their merits and limitations were presented, which was crucial in achieving the set objective of this work. Chapter 2 through 6 presented the analysis of data using the methods proposed in Chapter 2. The results were presented and discussed. A summary of the most important findings is as follows:

1. Based on four datasets analysed, the tidal stream velocity was greater than $\sim 2ms^{-1}$ at mean spring peak velocity close to the water surface and $\sim 1.4ms^{-1}$ during the neap tide. Asymmetry between flood and ebb was noticed with larger currents occurring on the flood than on the ebb. Maximum values were observed

at every second flood (Figure 6.2c) due to diurnal inequalities;

2. During the spring tide (20 August, 2005), the significant wave height H_s ranges between ~ 0.2 and ~ 3 m and ~ 0.4 and ~ 1.28 m during neap tide. During the storm event, H_s rose to about 7.9 m (Chapter 3, Table 4.2).

   This stormy event correlates with the West-Northwest sea development and decay. During the wave development, peak periods varied between ~ 4.3 to 20 s while the significant wave heights ranged from ~ 0.4 and ~ 7.9 m. This observation corresponds to some of the most severe sea states in the Fall of Warness in terms of significant wave heights due to WNW wind action over the longer dimension of the North Atlantic. The storm progressively decays due to the dispersive nature of WSW wind waves in term of wave periods and significant wave heights. Due to the superimposition of South-Southeast seas on the West-Northwest wave field as noticed during the observational period (Figure 4.2), a directional bimodal spectrum was observed;

3. An increase in the value of H_s corresponds to an increase in wave-induced orbital velocity (e.g., Figure 4.9);

4. The directional wave data collected in the Fall of Warness during summer and winter clearly show the wave response to the changing wind direction and intensity. The propagation direction of storm-generated sea waves is predominantly from West-Northwestly in response to the varying wind conditions during the storm event, while swell direction are mainly from East-Southeast;

5. The wave energy changes with the wind speed (e.g., Figure 4.2) but also influenced by tidal stream fluctuations. It was observed that near-bed orbital velocities fluctuates with tidal cycles (Tables 3.2- 3.3);

6. Wave-current interaction and bottom friction enhances wave energy dissipation;

7. There was a correlation between significant wave height and the current speed due to wave-current interaction confirming waves are generated in current (see Hedges *et al.* [38] and Figure 4.3).

8. The total bottom shear stress calculated from the combined wave and current flows is more than an order of magnitude greater than the computed values from

wave parameters alone. Before and after slack water when wave effect is significant, the maximum bottom shear stress from wave contributed less than 2% to the total shear stress at the seabed (e.g., Figure 5.5);

9. As expected, the intensities of Reynolds stress, TKE density, TKE production, TKE dissipation and vertical shear, fluctuate with tidal stream velocity and tidal cycles, and diminish towards slack water (e.g., Figures 6.2, 6.8);

10. Maximum values of Reynolds stress greater than $\sim 7Pa$ (with a current speed of $\sim 1.8ms^{-1}$) was obtained from a mean water depth of $\sim 46m$ from a 5 day dataset and $\sim 19Pa$ (with a current speed of $\sim 2.21ms^{-1}$) from a mean water depth of $\sim 37m$ from a 30 day dataset. As expected, an increase in current speed corresponds to an increase in the mean stress. Shear stress increases as water depth becomes shallower. Results from other investigators, though in low current speeds found corresponding values. For example, Rippeth *et al.* [93] found $\sim 4.5Pa$ for a current speed of $1.2ms^{-1}$, Rippeth *et al.* [94] observed $\sim 0.5Pa$ for a current speed of $\sim 0.6ms^{-1}$ and Williams and Simpson [124]) got $\sim 6Pa$ for a current speed of $\sim 1.2ms^{-1}$. The mean turbulence intensity near the seabed, for both high frequency measurements (about 68 tidal cycles) was found to be $\sim 13.5\%$ (Figures 6.9, 6.24). Dyer [22] proposed a turbulence intensity value of the order of 10% near the boundary of an estuary. The minimum values of mean stress for each tidal cycle were calculated in order to determine the best position for a floating tidal turbine (rotor) installation. The author is 95% confident that for a mean water depth of 46 m (Deployment 1), the best mean turbine position fall within the interval $\sim 12.58 \pm 2.8m$ below mean water level (Table 6.2). For the second deployment, with a larger dataset and mean water depth of 37 m, the best mean turbine position fall within the interval of $\sim 13.60 \pm 1.50m$ below mean water level (Table 6.3-6.5). This suggest that a mean water depth of $\sim 12.5 - 13 \pm 2m$ below the mean water depth can be regarded as the best and safest position for tidal turbine (rotor) installation. The implication of this result is that if the stroke of a floating tidal turbine for example, moves below or above this 'less turbulent' position (between each tidal cycle), the element member of this structure may experience a severe force coming from the fluctuating part of the velocity. Interestingly, this value coincides with the planned deployment position at the Fall of Warness for full scale SRTT during prototype testing in 2009;

11. Eddy viscosity, which is responsible for dynamic mixing in the water column, is subject to large uncertainties near slack water and increases with increasing flow speed. Maximum values of the vertical eddy viscosity of ~ 0.067 and $\sim 0.0108 m^2 s^{-1}$ were observed near the seabed for the two high frequency measurements (46 and 37 m mean water depth), respectively. The time-averaged eddy viscosity profile attained a maximum close to the middepth (for both high frequency measurements) and decreased gradually towards the water surface (Figures 6.9, 6.24). In the month of October, Pohlmann [87] found maximum A_z rates of more than $200 cm^2 s^{-1}$ in the central North Sea and in August, he found the smallest surface values of less than $50 cm^2 s^{-1}$. From this thesis, the maximum value of A_z in October (Deployment 2) was $\sim 0.0108 m^2 s^{-1}$ ($\sim 108 cm^2 s^{-1}$) (Figure 6.24a) and the smallest surface values of less than $\sim 0.013 m^2 s^{-1}$ ($\sim 130 cm^2 s^{-1}$) was found in the month of July (Deployment 1) (Figure 6.24). The values in Deployment 1 seem to be higher because of shorter dataset. It is expected that these values are subject to change with a longer dataset. The difference in summer (between May and September) and winter (between October and April) is due to the fact that vertical eddy viscosity increases as a result of the intensive cooling through the sea surface, combined with the intensification of wind stress during the winter months, when the thermocline has totally disappeared and convection reaches down to the seabed. Decreasing storm activities explain the strong decrease of A_z rates during summer.

12. In the calculation of TKE dissipation rates for Deployments 1 and 2 (Figures 6.11, 6.26), the 2SFM values were not reliable. The cause of this may be connected to the homogeneous assumption which was not met. The IDM method gave a more reliable result. The maximum values at the sea bed were $\sim 2.06 \times 10^{-2}$ and $\sim 1 W m^{-3}$ for Deployments 1 and 2 , respectively. This result, which is consistent with what other investigators have found, shows that ε increases with increasing flow speed.

It should be noted that there was no data from any other instruments recorded in a typical active tidal site such as the Fall of Warness to validate the wave data and analysis. It is hoped that future work can look more into the validation.

7.2 Design Implications

As discussed out in this study, the performance of a tidal stream device is based on accurate on-site measurements and adequate characterisation of the tidal stream environment before the deployment. This information will aid the design optimisation of the device and establish a more reliable means of estimating the energy capture at a site. The reasons being:

1. the sea state at the tidal stream environment, as demonstrated in this thesis, is most probably a multimodal directional sea. The effect of multimodal directional sea-current interaction can create a severe environment and as such the device can experience the following (Kjeldsen *et al.*[54], Batten *et al.* [4], Barltrop *et al.* [3]):

    - increase encounter probability for nonlinear wave groups that can significantly affect the stability and operation of a tidal stream device;
    - produce yaw motion that creates large forces and bending moments on a tidal stream device;
    - in the design stage help to assess accurately the accumulation of fatigue damage on device structures;
    - aid in estimating phase lag and coherence between sea loading and the response of various members of a structure.

2. The boundary-layer-induced turbulent fluctuation flow across the rotor and the entire structure of the tidal stream turbine is very crucial in order to quantify the transient performance of the device. Since turbulence is site-specific, the only reliable quantification is through site-measurements. Turbulence fluctuations can (Dyer [22], Berr [7], Barltrop *et al.* [3], Kelley *et al.* [50]):

    - produce unequal forces on the tidal turbine;
    - create cyclic loads on the blade which may result in yaw misalignment, oscillations and may degrade energy capture;
    - create dynamic response and increase fatigue damage;
    - higher heave response may occur from a developing sea with small significant waveheight and small peak period, since heave motions might tend to have higher natural frequencies. For instance, an increase in tube length of a tidal stream turbine will reduce heave motions.;

- cause wave attenuation which might excite roll motions since the natural frequency of roll tends to be relatively low. For instance an increase in the area of the rotor legs of a tidal turbine might reduce roll response.

This study has established the need to adequately understand the kinematics of a tidal stream site before a device is deployed. If a tidal stream device is designed without taking account of the site-measured parameters, for example, bulk turbulence parameters, and is deployed in flows that have such characteristics, a high level of approach-flow turbulence might create cyclic loads on the blades which may exceed the assumed design criteria. This may reduce power-take off and create a fatigue problem on the blades and the entire structure.

7.3 Recommendations for Future work

Despite the significant achievements made in the study on characterizing a typical tidal stream site, there are still areas which can improve the outcome. They are:

1. **ADCP measurement:**
   - Since the source of error as a result of instrument motions and turbulent fluctuation (tilt angle) cannot be removed (Lu and Lueck [68]), even by filtering, measurements with rigidly seabed mounted ADCP must be taken and the analysis method presented in this thesis can be used to validate the results;
   - The error due to wave-induced velocities, which is influenced by the strength and direction of the surface wave, may be significant (Rapo [89]). This can contaminate the Reynolds stress estimate. An improvement in the pre-processing techniques presented in Appendix B (Page 219) could reduce or eliminate this error. For instance by increasing the number of data points N (equation B.0.2);
   - The need for the turbulence anisotropy assumption introduces errors in bulk turbulent parameter estimates. A fifth beam on ADCPs is necessary so that the vertical velocity may be collected on-site and this will minimise the error incurred during the transformation from beam to radial velocities (Lu and Lueck [69]). This is further explained in section 2 below.
2. **Data Sampling and Analysis Methods:**

- The assumption of turbulence anisotropy (α in equation 2.5.10 of Chapter 2) which cannot be determined from an ADCP with four beams, biased the estimates of Reynolds stress and TKE density. Though the cost of using 2^o tilt angle threshold in this study is at most $\sim 17\%$ bias in the Reynolds stress (which is within the acceptable margin for turbulence estimation (e.g., Lu and Lueck [69], Williams and Simpson [124], Rippeth *et al.* [93]), the introduction of a fifth transducer fitted on an ADCP directed along the instrument axis measuring w' directly will eliminate this error. Likewise, the assumption of an anisotropy ratio of α (0.2 was used in this study (for an unstratified tidal channel Stacey [106])) would not have been necessary because a fifth transducer on the ADCP would have measured the vertical beam velocity directly. For the fifth beam ADCP configuration, the resolved velocities by all beams can be given as (from Figures 2.5 and 2.6):

$$rb_1 = -u_1 \sin\theta - w_1 \cos\theta \tag{7.3.1}$$

$$rb_2 = u_2 \sin\theta - w_2 \cos\theta \tag{7.3.2}$$

$$rb_3 = -v_3 \sin\theta - w_3 \cos\theta \tag{7.3.3}$$

$$rb_4 = v_4 \sin\theta - w_4 \cos\theta \tag{7.3.4}$$

$$rb_5 = -w_5 \tag{7.3.5}$$

  In a nonhomogeneous flow, the differences between two independent estimates of w called the *error velocity*, can be very large likewise the differences in horizontal velocities. Since the uncertainty in the homogeneity assumption is introduced into all velocities estimates, ADCPs fitted with a fifth beam pointing vertically upwards will be necessary to eliminate this bias;
- Secondly, the uncertainty in Reynolds stress estimate associated with the tilt (roll and pitch) angles can also be significant (Lu and Lueck [69]). Since the current is measured in beam coordinates, biases associated with tilt cannot be removed except by rigidly mounting the ADCP (Lu and Lueck [69], Williams and Simpson [124], Rippeth *et al.* [93]);
- The uncertainty due to random scatter motions within the sample volume (Doppler noise) can bias the estimate of TKE density (Lhermitte and Lemmin

[60]). The radial velocity estimates, are sensitive to the error associated with Doppler phase noise of an ADCP, which brings about a broadening of the Doppler spectral peak (Brumley *et al.* [11]). Doppler noise uncertainty is significant when turbulence intensities are low. The ADCP radial velocity estimates will have an uncertainty due to Doppler noise as (Voulgaris and Trowbridge [120]):

$$\sigma_{Dpn}^2 = \frac{\pi^{-1/2}}{16}\frac{c^2 D}{f^2 M \tau} \tag{7.3.6}$$

where σ_{Dpn} is the Doppler noise's uncertainty, c is the speed of sound in water, τ is the duration of acoustic pulse, M is the number of averaged acoustic pulses, $D\left(=\sqrt{D_r^2 + D_t^2 + D_d^2}\right)$ is the total Doppler bandwidth broadening, D_r is the broadening due to finite residence time, D_t is the broadening due turbulence within the sample volume D_t and D_d is the broadening due beam divergence. It is clear from equation (7.3.6) that the uncertainty due to flow related noise (e.g. Doppler noise) can be reduced by using a high number of averaged acoustic pulses M (ensembles) (Williams and Simpson [124]).

- The uncertainty in the Reynolds stress estimate may be underestimated using a small vertical cell size when configuring an ADCP for turbulence measurement. This is because the length scale of the turbulent fluctuations decreases near the seabed or boundary. For instance, Lu and Lueck [69] compared the estimates of Reynolds stresses using a vertical cell size of 1 m and 0.1 m. They found that the Reynolds stress estimate using 0.1 m vertical cell size were underestimated by 5% compared with vertical cell size of 1 m. In another observation, Rippeth *et al.* [93] found that a reduction of 5% in Reynolds stress estimate was recorded from the use of 0.5 and 0.25 vertical cell sizes. Since the standard deviation of the radial velocity of an ADCP varies approximately with the reciprocal of the vertical cell size (Williams and Simpson [124]), higher standard deviation of the along beam velocities can be avoided during the configuration of an ADCP if a large vertical cell size is chosen;
- The uncertainty in the Reynolds stress estimate can be reduced by using fast-pinging modes of sampling during ADCP configuration. Mode 12 allows raw ping rates near 20 Hz (compare to 2-4 Hz with Mode 1) (RDI [90]). For instance, Nidzieko *et al.* [76] compared the Reynolds stress estimate from

ADCP with Mode 1 and Mode 12. They found that Mode 1 overestimated stresses by 20% compared with fast-pinging water Mode 12. In another study, Williams and Simpson [124] compared the uncertainty in the Reynolds stress due to instrument noise for both Mode 1 and Mode 12. Their results showed a reduction of about 30% in the uncertainty using the fast ping rate, Mode 12. Since Reynolds stress and the rate of production of TKE uncertainties from instrument noise, are proportional to the square and cube of the velocity standard deviation, respectively, fast-pinging mode of sampling can reduce this flow related bias.

- The uncertainties in the estimates of TKE dissipation from ADCP data has always been a concern (e.g. Mohrholz *et al.* [74]). This is due to the fact that the velocity spectra are contaminated by wave motion in the inertial subrange and the assumption that the wave numbers at which the turbulence is produced and dissipated by viscosity, which is the basis for IDM, cannot be justified. A single-point measurement with an acoustic Doppler velocimeter (ADV) that can measure the vertical velocity directly or a fifth transducer pointing vertically upwards on the RDI ADCP will be of interest so that the vertical flow spectra, which will be less contaminated by wave motion in the inertial subrange can be used to estimate ε. Independent data sampled (at the same location and on the same mooring frame) from an ADV can be supplied which can then be used to estimate the TKE dissipation rates (e.g., Mohrholz *et al.* [74], Bowden and Fairbairn [8], Souza and Howarth [105]). It should also be noted that ADCPs can produce spurious data during strong waves because the instrument may not be accurately aligned in the vertical.
- Detailed investigations on the seasonal bulk turbulence parameters as well as analysis of the directional wave data at the tidal turbine installation location should be conducted using the same analytical procedures presented in this study.
- The variability in the meteorological forcing in the entire North Sea (and north Atlantic) has a strong impact on the vertical mixing throughout the water column and so if a realistic characterisation of an energetic tidal site is required, measurements should be collected during summer and winter months.

As shown above, Reynolds stress depends on tidal current velocities and wave action. On the other hand, the turbulent boundary layer thickness is influenced by strong bottom friction (or seabed roughness) due to increased shear. The non-linear interaction of these three quantities produces a complex hydrodynamic system. For that reason it is difficult to clearly quantify the influence of bulk turbulence parameters actually present in a specific tidal energy test site with just 6 weeks of high-frequency sampling. However, this disadvantage is compensated by the possibility to obtain for the first time in a comprehensive form, realistic space- and time-dependent distributions of the bulk turbulence parameters in the Fall of Warness tidal energy test site.

As far as the author is aware, this is the first time that ADCP Reynolds stress estimates have been used to determine the best and safest position (based on low Reynolds stress fluctuations) for tidal stream turbines in the water column in an energetic tidal test site. This study has also shown, for the first time, the use of ADCP data to characterise an energetic tidal test site before tidal turbine deployment. Nevertheless, ADCP Reynolds stress estimates can be unreliable during storm and strong waves as they will contribute to errors in spatial distribution in the along beam velocity variances especially during Northwestern wind storms which can influence long waves, and as such care must be taken when interpreting and analysing the ADCP data.

References

References

[1] Admiralty Sailing Direction, North coast of Scotland pilot, NP 52, Sixth Edition, (2006)

[2] A. M. Davies, *On using turbulence energy models to develop spectral viscosity models*, Continental Shelf Research, **11**, 1313-1353, (1991)

[3] N. Barltrop, K. S. Varyani, A. Grant, D. Clelland, X. Pham, *Wave-current interactions in marine current turbines*, Proceedings of the Institution of Mechanical Engineers, Part M: J. of Engineering for the Maritime Environment, **220**, 4, (2006)

[4] W.M.J. Batten, A.S. Bahaj, A.F. Molland, J.R. Chaplin,*Power and Thrust Measurements of Marine Current Turbines under various Hydrodynamic Flow Conditions in a Cavitation Tunnel and Towing Tank*, Renewable Energy, **32** (3), 407-426. Elsevier, (2007)

[5] A. Yu. Benilov, B. N. Filyushkin, *Application of the linear filtration methods to the fluctuation analysis in the sea upper layer*, Izvestiya, Fizika Atmosphery i Okeana 6, 477-482, (1970)

[6] M. Benoit, P. Frigaard, H. A. Schaffer, *Analysing multidirectional wave spectra: A tentative classification of available methods*, Proc. Seminar on Multidirectional Waves and their Interaction with Structures, San Francisco, CA, International Assembly of Hydraulic Research, 131-158, (1997)

[7] BERR Emerging Energies Technol. programme, *Development of a Design Tool for Axial Flow Tidal Stream Devices*, CONTRACT NUMBER: T/06/00231/00/00, URN NUMBER: 08/852

[8] K. F. Bowden, L.A. Fairbairn, *Measurements of turbulent fluctuations and Reynolds stresses in a tidal current*, Proc. Roy. Soc. London, Series A, **237**, 422-438, (1956)

[9] F. P. Bretherton, C. J. R. Garrett, *Wave trains in inhomogeneous moving media*, Proceedings of the Royal Society of London, A 302, 529554, (1969)

[10] P. Brissette, *Estimation of wave directional spectra and application to the study of surface gravity water waves*, PhD Thesis, McMaster University, Canada, (1992)

[11] B. H. Brumley, R. G. Cabrera, K. L. Deines, E. A. Terray, *Performance of a broad-band acoustic Doppler current profiler*, IEEE J. Oceanic Eng., 16, 402-40, (1991)

[12] I. G. BRYDEN, *Tidal Energy*, Encyclopedia of Energy, **6**, (2004)

[13] R. Burrows, T. S. Hedges, W. G. Mason, *The influence of wave-current interaction on induced fluid loading,* Proc. International Symposium on Hydrodynamics of Ocean Engineering, Trondheim, Norway, 491-507, (1981)

[14] J. Capon, *High resolution frequency-wavenumber spectrum analysis*, Proc. IEEE, **57**, 1408-1418, (1969)

[15] R. G. Dean, R. A. Dalrymple, *Water Wave Mechanics for Engineers and Scientists*, World Scientific, Singapore, 353pp, (1991)

[16] A. J. Chadwick, D. J. Pope, J. Borges, S. Ilic. *Shoreline directional wave spectra: Part 1. An investigation of spectral and directional analysis techniques*, Proceedings of Institution of Civil Engineering in Water Maritime and Energy, **112**, 198- 209, (1995)

[17] J. B. Christoffersen, I. G. Jonsson, *Bed friction and dissipation in a combined current and wave motion*, Ocean Eng., **12**, 5, 387423, (1985)

[18] J. M.B.P. Cruz, A. J.N.A. Sarmento, *Sea state characterisation of the test site of an offshore wave energy plant*, Ocean Engineering, **34**, 5-6, 763-775, (2007)

[19] R. A. Dalrymple, J. C. Heideman, *Nonlinear water waves on a vertically sheared current,* Proc. Workshop on Wave and Current Kinematics and Loading, E & P Forum, Paris, (1989)

[20] R. G. Dean, R. A. Dalrymple, *Water wave mechanics for engineers and scientists*, Advanced Series on Ocean Eng., **2**, World Scientific, Singapore, (1990)

[21] D. L. Donoho, I. M. Johnstone, *Ideal spatial adaptation by wavelet shrinkage*, Biometrika, **81**, 3, 425-455, (1994)

[22] K. R. Dyer, *Current velocity profiles in a tidal channel*, Geophys. J. R. Astronomical Soc. **22**, 153-161, (1970)

[23] *www.emec.org.uk/site_wide_projects.asp*

[24] *Floating structures: a guide for design and analysis*, The center for Marine and Petroleum Technol. (CMPT), volume 1, edited by N. D. P. Batrop, (1998)

[25] P. L. Fraenkel, *Marine Current Turbines: An emerging technology*, Hydraulic aspects of renewable energy, 16th Annual Seminar, Scottish Hydraulics Study Group, Glasgow, March (2004)

[26] P. L. Fraenkel, *Power from marine currents*, J. Power and Energy, **216**, 1, 1-14, (2002)

[27] D. C. Fugate, R. J. Chant, *Near-bottom shear stresses in a small, highly stratified estuary*, J. Geophys. Res., **110**, C03022, doi:10.1029/2004JC002563, (2005)

[28] A. E. Gargett, *Velcro measurement of turbulent kinetic energy dissipation rate* J. of Atmospheric and Oceanic Technol., **16**, 1973-1993, (1999)

[29] Y. Goda, *Directional wave spectrum and its engineering applications*, Advances in Coastal and ocean engineering, **3**, ed. P. Liu, World Scientific Publishing Co, Singapore, 67-102, (1995)

[30] D. G. Goring, V. I. Nikora, *Despiking Acoustic Doppler Velocimeter Data*, J. of Hydraulic Engineering, **128**, 1, 117-126, (2002)

[31] W. D. Grant, O. S. Madsen, *The continental shelf bottom boundary layer*, Annual Review of Fluid Mechanics, **18**, 265-305, (1986)

[32] S. Gant, T. Stallard, *Modelling a Tidal Turbine in Unsteady Flow*, Proceedings of the Eighteenth (2008) International Offshore and Polar Engineering Conference, Vancouver, BC, Canada, July 6-11, (2008)

[33] *Green Energy Study for British Columbia Phase 2: Mainland, Tidal current Energy*, Prepared by Triton Consultants Ltd. For BC Hydro, Engineering,(2002)

[34] T. F. Gross, A. R. M. Nowell, *Mean flow and turbulence scaling in a tidal boundary layer*, Cont. Shelf Res., **2**, 1109-1126, (1983)

[35] N. Hashimoto, *Analysis of the directional wave spectrum from field data*, Advances in Coastal and ocean engineering, **3**, ed. P. Liu, World Scientific Publishing Co, Singapore, 103-143, (1995)

[36] K. Hathaway; C. Long, *A comparison of directional wave measurements from an ADCP, AWAC, and pressure sensor array*, American Geophysical Union, Fall Meeting (2008)

[37] T. S. Hedges, *Combinations of waves and currents: an introduction*, Proc. ICE, Part 1, **82**, 567-585, (1987)

[38] T. S. Hedges, K. Anastasiou, and D. Gabriel, *Interaction of random waves and currents*, J. of Waterway, Port, Coastal and Ocean Engineering, **1**, I 1 (6): 27 5-288, (1985)

[39] K. Horikawa, *Nearshore Dynamics and Coastal Processes: Theory, Measurement and Predictive Models*, University of Tokyo Press, (1998)

[40] N. E. Huang, D. T. Chen, C. C. Tung, *Interaction between steady non-uniform currents and gravity waves with applications for current measurement*, J. Phys. Oceanogr., **2**, 420-431, (1972)

[41] W. Huang, C. Chou and J. Z. Yim, *Experiments on the reflection coefficients of a detached breakwater in a directional wave field*,Coastal Engineering **47**,4, 367-379, (2003)

[42] J. M. Huthnance,*Circulation, exchange and water masses at the ocen margin: the role of physical processes at the shelf edge*, Prog. Oceanogr., **35**, 353-431, (1995).

[43] J. M. Huthnance,*North sea interaction with the North Atlantic ocean*, German J. of Hydrography, **49**, 2-3, (1997)

[44] N. M. Ismail, *Wave-current models for design of marine structures,* J. Waterway, Port, Coastal and ocean Ocean Engg., **110**, 4, 432-447, (1984)

[45] M. Isobe, K. Kondo, K. Horikawa, *Extension of MLM for estimating directional wave spectrum*, Proc. Symp. on Description and Modeling of Directional Seas, Paper No.A-6., **15**, (1984)

[46] S. J. Jacobs, *On wave-current interaction in a turbulent boundary layer*, Geophysical & Astrophysical Fluid Dynamics, 1029-0419, **50**, 4, 203-227, (1990)

[47] G. Jeans, C. Primrose, N. Descusse, *A Comparison Between Directional Wave Measurements from the RDI Workhorse with Waves and the Datawell Directional Waverider*, Oceans 04 MTS/IEEE/ Techno-Oceans 04, Kobe Japan, (2004)

[48] E. R. Jefferys, *Measuring directional spectrum with the MLM*, Proc. Directional wave spectra App. Conf. University of Califonia, Berkely, Califonia, USA, 203-219, (1986)

[49] J. S. Jennings, *Future sustainable energy supply, Energy World*, 8-10, (1996)

[50] N. D. Kelly, B. J. Jonkman, G. N. Scott, *The great plains turbulence environment: Its origins, impact and simulation*, NREL/CP-500-40176, (2006)

[51] P.H. Kemp, R.R. Simons, *The interaction between waves and a turbulent current: waves propagating with the current*, J Fluid Mech., **116**, 227-250, (1982)

[52] J. T. Kirby, T. M. Chen, *Surface waves on vertically sheared flows: Approximate dispersion relations*, J. Geophysical Research, 94, C1, 1013-1027, (1989)

[53] S. A. Kitaigorodskii, M. A. Donelan, J. L. Lumley, E. A. Terray, *Wave-turbulence interactions in the upper ocean: Part II*, J. of Phys. Oceanogr. 13, 1988-1999, (1983)

[54] S. P. Kjeldsen, H. E. Krogstad, R. B. Olsen, *Some results from the Labrador sea extreme waves experiment*, Proc. ICCE, Malaga, Spain, 667-681, (1988)

[55] K. Kobune, N. Hashimoto, *Estimation of directional spectra from the maximum entropy principle*, Proc. 5th Int. Off. Mech. And Artic Eng. Symp., Tokyo, japan, 80-85, (1986)

[56] V. P. Kochergin, *Three-dimensional prognostic models: Three-dimensional coastal ocean models*, N. S. Heaps, editor, American Geophysical Union, Washington D. C., Coastal and Estuarine Science, **4**, 201-208, (1987)

[57] V. K. Kraav, *Computational of the semidiurnal tide and turbulence parameters in the North Sea*, Oceanology, **9**, 332-341, (1969)

[58] H. E. Krogstad, R. L. Gordon, M. C. Miller, *High resolution directional wave spectra from horizontally mounted acoustic Doppler current meters*, J. Atmos. Oceanic tech., **5**, 340-352, (1988)

[59] P. J. Kundu, I. M. Cohen, *Fluid Mechanics*, Academic Press, 730 pp., (2002)

[60] R. Lhermitte, U. Lemmin, *Open-channel flow and turbulence measurement by high-resolution Doppler sonar*, J. Atmos. Oceanic Technol., 11, 1295-1308, (1994)

[61] R. Lhermitte, *Turbulent air motion as observed by Doppler radar* , 13th Radar Meteorological Conference, Am. Meteorol. Soc., Montreal, Que., Canada, (1968)

[62] A. Lohrmann, B. Hackett, L. D. Roed, *High resolution measurements of turbulence, velocity, and stress using a pulse-to-pulse coherent sonar*, J. Atmos. Oceanic Technol., **7**, 19-37, (1990)

[63] A. Lohrmann, B. Hackett, and L. P. Roed, *High resolution measurements of turbulence, velocity, and stress using a pulse-to-pulse coherent sonar*, J. Atmos. Oceanic Technol., **7**, 19-37, (1990)

[64] M. S. Longuet-Higgins, R. W. Stewart, *The changes in amplitude of short gravity waves on steady non-uniform currents*, J. of Fluid Mechanics, **10**, 529-549, (1961)

[65] M. S. Longuet-Higgins, R. W. Stewart, *Radiation stresses in water waves: physical discussion, with applications*, Deep-Sea Res., **11**,4, 151-562, (1964)

[66] M. S. Longuet-Higgins, *On the statistical distribution of the heights of sea waves,* J. of Marine Research, **11**, 245-266, (1952)

[67] A.Lorke, A. Wuest, *Application of coherent ADCP for turbulence measurements in the bottom boundary layer*, J. Atmos. Ocean Tech., **22**, 11, 1821-1828, (2005)

[68] Y. Lu, R. G. Lueck, *Using a broadband ADCP in a tidal channel. Part II: Turbulence*, J. Atmos. Oceanic Technol., **16**, 1568-1579, (1999)

[69] Y. Lu, R. G. Lueck, *Using a broadband ADCP in a tidal channel. Part I: Mean flow and shear*, J. Atmos. Oceanic Technol., 16, 1556-1567, 1999b)

[70] A. Lygre, H. E. Krogstad, *Maximum entropy estimation of the directional distribution in ocean wave spectra*, J. Phys. Oceanogr., **16**,2052-2060, (1986)

[71] O. S. Madsen, *Spectral wave-current bottom boundary layer flows*, Coastal Engineering 1994: Proceedings, 24th International Conference, Coastal Engineering Research Council. American Society of Civil Engineers, Kobe, Japan, 384-398, (1994)

[72] www.mathworks.com

[73] R. L. P. Verley and G. Moe, *The effect of cylinder vibration on the drag force and the resultant hydrodynamic damping*, Technical Report STF60 A79061, Norwegian Institute of Technology, (1978)

[74] V. Mohrholz, H. Prandke, H. U. Lass, *Estimation of TKE dissipation rates in dense bottom plumes using pulse coherent acoustic Doppler profiler (PC-ADCP) - Structure function approach*, J. of Marine Systems, **70**, 217-239, (2008).

[75] I. Nezu, H. Nakagawa, *Turbulence in open-channel Flows*, Balkema, Rotterdam, The Netherlands, (1993)

[76] N. J. Nidzieko, D. A. Fong, J. L. Hench, *Comparison of Reynolds Stress Estimates Derived from Standard and Fast-Ping ADCPs*, J. Atmos. Oceanic Technol., **23**, 854-861, (2006)

[77] O. Nwogu, *Effect of steady currents on directional wave spectra*, Proceedings of the 12th International Conference on Offshore Mechanics and Arctic Engineering, **l**, 25-32, (1993)

[78] O. Nwogu, *Analysis of fixed and floating structures in random multi-directional waves*, PhD Thesis, University of British Columbia, Vancouver, BC, Canada, (1989).

[79] O. H. Oakley, J. B. Lozow, *Directional spectra measurements by small arrays*, Proc. Offsh. Tech. Conf., Houston, USA, 155-166, (1977) ob6M. J. Tucker, and E. G. Pitt, *Waves in Ocean Engineering*, Elsevier Ocean Engineering Book Series Volume 5, Elsevier Science Ltd, Oxford, (2001)

[80] M. K. Ochi, *Ocean Waves*, Cambridge University Press, Cambridge, 319pp., (1998)

[81] J. Oltman-shay, R. T. Guza, *A data adaptive ocean wave directional spectrum estimator for pitch/roll type measurements*, J. Phys. Oceanogr., **14**, 1800-1810, (1989)

[82] *www.absoluteastronomy.com/topics/Orkney_Islands*

[83] E. Osalusi, J. Side, R. Harris, *Reynolds stress and turbulence estimates in bottom boundary layer of Fall of Warness*, Int. Comm. Heat and Mass Transfer, **36**, 5, 412-421, (2009)

[84] E. Osalusi, J. Side, R. Harris, *Structure of turbulent flow in EMECs tidal energy test site*, Int. Comm. Heat and Mass Transfer, **36**,5, 422-431, (2009)

[85] J. C. Park, Y. Uno, T. Sato, H. Miyata and H. H. Chun, Numerical reproduction of fully nonlinear multi-directional waves by a viscous 3D numerical wave tank, Ocean Engineering, **31**,11-12, 1549-1565, (2004)

[86] S.S. Pawka, *Island shadows in wave directional spectra*, J. Geophys. Res., **88**, 2579-2591, (1983)

[87] T. Pohlmann, *Calculating the annual cycle of the vertical eddy viscosity in the North Sea with a three-dimensional baroclinic shelf sea circulation model*, Continental Shelf Research, **16**, 147-161, (1996)

[88] http://www.python.org/

[89] M. Rapo. *Error and uncertainty in estimates of Reynolds stress using an ADCP in an energetic ocean state* , Ph.D thesis, Massachusetts Institute of Technol., USA (2006)

[90] *www.rdinstruments.com/pdfs/waves_primer*_0504.*pdf*

[91] www.rdinstruments.com

[92] P.C. Reid, A. H. Taylor, J. A. Stephens, *The hydrography and hydrographic balances of the North Sea. In: Pollution of the North Sea, an assessment*, Ed. by W. Salomons, B.L. Bayne, E.K. Duursma, and U. Förstner. Springer-Verlag, Berlin, Heidelberg, 3-19,New York (1988)

[93] T. P. Rippeth, E. Williams, J. H. Simpson, *Reynolds stress and turbulent energy production in a tidal channel*, I. Phys. Oceanogr., **32**, 1242-1251, (2002)

[94] T. P. Rippeth, J. H. Simpson, E. Williams and M. E. Inall, *Measurement of the rates of production and dissipation of turbulent kinetic energy in an energetic tidal flow: Red Wharf Bay revisited*, J. Phys. Oceanogr., **33**, 1889-1901, (2003)

[95] I. Nezu, W. Rodi, *Open-channel flow measurements with a Laser Doppler Anemometer*, J. of Hydraulic Engineering, **112**, 5, 335-355, (1984)

[96] P. Rosales, F.J. Ocampo-Torres, P. Osuna, J. Monbaliu and R. Padilla-Hernández, *Wave-current interaction in coastal waters: Effects on the bottom-shear stress*, J. of Marine Systems, **71** 1-2,131-148, (2008)

[97] H. Sauvageot, *Radar Meteorology*, Artech House Books, (1992)

[98] Scotrenewables (http://www.scotrenewables.com).

[99] J. H. Simpson, E. Williams, L. H. Brasseur, J. M. Brubaker, *The impact of tidal straining on the cycle of turbulence in a partially stratified estuary*, Cont. Shelf Res., **25**, 51-64,(2005)

[100] S. Singer, *PowerSwitch! Climate change and the power sector*, Renewable Energy World July-August, **6**, James and James (Science Publishers) Ltd. London, (2003)

[101] R. A. Skop, *Approximate dispersion relation for wave-current interaction*, J. Waterway, Port, Coastal and ocean Ocean Engg., **113**, 2, 187-195, (1987)

[102] C. G. Soares, G. R. Rodriguez, P. Cavaco, L. and Ferrer, *Experimental study on the interaction of wave spectra and currents*, Proceedings of the 19th International Conference on Offshore Mechanics and Arctic Engineering, ASME, New York, (2000)

[103] A. Solovieva, R. Lukas, *Observation of wave-enhanced turbulence in the near-surface layer of the ocean during TOGA COARE*, Deep-Sea Research I **50**, 371-395, (2003)

[104] R. L. Soulsby, *Calculating bottom orbital velocity beneath waves*, Coastal Engineering, **11**, 371-380, (1987)

[105] A.J. Souza , M.J. Howarth, *Estimates of Reynolds stress in a highly energetic shelf sea*, Ocean Dynamics, **55**, 490-498, (2005)

[106] M. T. Stacey, S. G. Monismith, J. R. Burau, *Measurements of Reynolds stress profiles in unstratified tidal flow*, J. of Geophysical Research, **104**, 10933-10949, (1999)

[107] M. T. Stacey, S. G. Monismith, J. R. Burau, *Measurements of Reynolds stress profiles in unstratified tidal flow*, J. Geophys. Res., **104**, 10933-10949, (1999a)

[108] M. T. Stacey, S. G. Monismith, *Measuring estuarine turbulence with an ADCP*, The Proc. Congress of the IAHR, **B**, San Francisco, CA, 155-160, (1998)

[109] K. R. Stapleton, *Wave-current interaction in the coastal zone* , PhD thesis, Institute of Marine Studies, University of Plymouth, UL (1996)

[110] K. R. Stapleton, D. A. Huntley, *Seabed stress determinations using the inertial dissipation method and the turbulent kinetic energy method*, Earth Surface Processes and Landforms, **20**, 807-815, (1995)

[111] X. Sun, *Numerical and experimental investigation of tidal current energy extraction*, PhD thesis, The University of Edinburgh, (2008)

[112] N. Suzuki, N. Ebuchi, C. Zhao, I. Watabe and Y. Sugimori, *Study of the relationship between non-dimensional roughness length and wave age, effected by wave directionality*, Proc. Indian Acad. Sci. (Earth Planet. Sci.), **111**, No. 3, 305-313, (2002)

[113] R. E. Tailor, A. Rajagopalan, *Load spectra for slender offshore structures in waves and currents*, J. Earthquake Engineering and Structural Dynamics, **11**, 831-842, (1983)

[114] H. Tanaka, V. To Dang, *Geometry of Sand Ripples due to Combined Wave-Current Flows*, J. Waterways, Port, Coast. And Ocean Engrg., **122**, 6, 298-3000, (1996)

[115] M. Trevethan, *A Fundamental Study of Turbulence and Turbulent Mixing in a Small Subtropical Estuary*, Ph.D Thesis, University of Queensland, (2007)

[116] M. J. Tucker, and E. G. Pitt, *Waves in Ocean Engineering*, Elsevier Ocean Engineering Book Series Volume 5, Elsevier Science Ltd, Oxford, (2001)

[117] C. C. Tung and N. E. Huang, *Combined effects of current and waves on fluid force*, Ocean Engineering, **2**, 183-193, (1973)

[118] C. C. Tung and N. E. Huang, *Influence of wave-current interaction on fluid force*, Ocean Engineering, **2**, 207-218, (1973)

[119] J. VanZwieten, F. R. Driscoll, A. Leonessa, G. Deane, *Design of a prototype ocean current turbine part I: mathematical modelling and dynamics simulation*, Ocean Engineering, **33**, 11-12, 1485-1521, (2006)

[120] G. Voulgaris, J. H. Trowbridge, *Evaluation of the Acoustic Doppler Velocimeter (ADV) for Turbulence Measurements*, J. Atmos. Oceanic Technol., **15**, 272-289, (1998)

[121] X. Wang, N. Qian, *Turbulence characteristics of sediment-laden flow* , J. Hydraulic Engineering, ASCE, **115**, 6, 781-800, (1989)

[122] J. W. Wantz and R. E. Sinclair, *Distribution of extreme winds in the Bonneville power administration service area*, J. of Applied Met., 20, 1400-1411, (1981)

[123] P. J. Wiles, T. P. Rippeth, J. H. Simpson, P. J. Hendricks, *A novel technique for measuring the rate of turbulent dissipation in the marine environment*, Geophys. Res. Lett., **33**, (L21608), 15, (2006)

[124] E. Williams, J. H. Simpson, *Uncertainties in estimates of Reynolds stress and TKE production rate using the ADCP variance method*, J. Atmos. Oceanic Technol, **21**, 347-357, (2004)

[125] P. J. Wiles, T. P. Rippeth, J. H. Simpson, P. J. Hendricks, *A novel technique for measuring the rate of turbulent dissipation in the marine environment*, Geophys. Res. Lett., **33**, (L21608), 15, (2006)

[126] P. A. Work, *Nearshore directional wave measurements by surface-following buoy and acoustic Doppler current profiler*, Ocean Engineering, **35**, 727-737, (2008)

[127] Y. C. Li, *The transformation of wave spectrum in currents*, China Ocean Engineering, **1**,4, 1-11, (1987)

[128] P. K. Yeung, Y. Zhou, *On the universality of the Kolmogorov constant in numerical simulation of turbulence*, NASA/CR-97-206251, ICASE Report N. 97-64, (1997)

[129] J. ZhenGang, *Hydrodynamics and water quality: Modelling rivers, lakes and estuaries* , WileyBlackwell, (2008)

[130] C. Y. Zhou and J. M. R. Graham, *Numerical study of cylinders in waves and currents, Journal of Fluids and Structures*, **14**, 403-428, (2000)

[131] Z. You, *The statistical distribution of nearbed wave orbital velocity in intermediate coastal water depth*, Coastal Engineering, **56**, 844-852, (2009)

Appendix A

Theoretical Development

A.1 ADCP Measurements

A.1.1 ADCP Beam Velocities

The frequency the planktonic organisms in water encounter when travelling away or towards the sound source decreases or increases, respectively due to the time it takes one wavelength of sound source to pass through the scatterers. This change in frequency due to motion is known as the Doppler shift. The motion in the direction of sound propagation is calculated as:

$$\overline{S_{vrbi}} = \left(\frac{1}{2}\frac{C}{\sigma_f}\right)\hat{\sigma_{f_{Ds}}} \tag{A.1.1}$$

where $\overline{S_{vrbi}}$ is the velocity of the scatterer in the direction opposite to that of the sound propagation, C is the sound speed in water, σ_f is the transmit frequency and $\hat{\sigma_{f_{Ds}}}$ is the Doppler shift frequency. The factor of $(1/2)$ is the result of the scatterer acting as both receiver and source due to the scatterer's motion being accounted for twice.

$$\sigma_f{}'' \approx \left(1 + \frac{2\overline{S_{vrbi}}}{C}\right)\sigma_f \tag{A.1.2}$$

for $\overline{S_{vrbi}} \ll C$.

$$\sigma_f{}'' \approx \left(1 + \frac{2\overline{S_{vrbi}}}{C}\right)\sigma_f \tag{A.1.3}$$

for $\overline{S_{vrbi}} \ll C$.

Let T_s denotes the time for one wavelength to pass a stationary point and ΔT_s (positive for following source and receiver motion) be a small change in time T_s for one wavelength to pass the moving scatterers, then:

$$\sigma_f = \frac{1}{T_s}, \quad \sigma_f{}' = \frac{1}{T_s - \Delta T_s} \tag{A.1.4}$$

The distance moved by the scatterers (drifted with the current S_v) as one wavelength of sound passes through them in the direction of sound propagation is given as:

$$d = S_v t \quad \longrightarrow \quad \Delta d = (T_s - \Delta T_s) S_v \tag{A.1.5}$$

If C is considered constant, then

$$C = \frac{d}{t} \quad \longrightarrow \quad \Delta T_s = \frac{\Delta d}{C} \quad \longrightarrow \quad \Delta T_s = \frac{(T_s - \Delta T_s) S_v}{C} \tag{A.1.6}$$

and

$$C\Delta T_s = S_v T_s - S_v \Delta T_s \quad \longrightarrow \quad C\Delta T_s + S_v \Delta T_s = S_v T_s \quad \longrightarrow \quad \Delta T_s = \frac{S_v T_s}{C + S_v} \tag{A.1.7}$$

Using $T_s = 1/\sigma_f$ and substituting ΔT_s into $\sigma_f{}'$, equation (A.1.7) becomes:

$$\sigma_f{}' = \frac{1}{T_s - \Delta T_s} = \frac{1}{T_s - \frac{S_v T_s}{C + S_v}} = \frac{1}{\frac{1}{\sigma_f} - \frac{S_v}{(C + S_v)\sigma_f}} = \frac{(C + S_v)\sigma_f}{C + S_v - S_v} = \left(\frac{C + S_v}{C}\right)\sigma_f \tag{A.1.8}$$

The dilation or contraction time $\Delta T_s{}'$ which is the distance moved by the source for a sound propagation of one period T_s is given as:

$$\Delta T_s{}' = \frac{\Delta d'}{C} = \frac{S_v{}' T_s{}'}{C} \tag{A.1.9}$$

and the stationary receiver frequency $\sigma_f{}''$ is then estimated from equations (A.1.3)-(A.1.9) as:

$$\sigma_f{}'' = \frac{1}{T_s{}' - \frac{S_v{}' T_s{}'}{C}} = \frac{1}{\frac{1}{\sigma_f{}'} - \frac{S_v{}'}{\sigma_f{}' C}} = \left(\frac{C}{C - S_v{}'}\right)\sigma_f \tag{A.1.10}$$

The echo reflected back from the scatterers $\sigma_f{}'$ (moving source) makes the original source becomes the stationary receiver as such $\sigma_f{}''$ becomes the return echo. By replacing $\sigma_f{}'$ in equation (A.1.8) and using $S_v = S_v{}'$, the equation becomes:

$$\sigma_f{}'' = \left(\frac{C}{C - S_v{}'}\right)\left(\frac{C + S_v}{C}\right)\sigma_f = \left(\frac{C + S_v}{C - S_v}\right)\sigma_f \tag{A.1.11}$$

By subtracting σ_f from $\sigma_f{}''$ (equation (A.1.11) gives:

$$\begin{aligned} \sigma_{f_{Ds}} &= \left(\frac{C + S_v}{C - S_v}\right)\sigma_f - \sigma_f = \left(\frac{C + S_v}{C - S_v} - 1\right)\sigma_f \\ &= \left(\frac{C + S_v - C + S_v}{C - S_v}\right)\sigma_f \\ &= \left(\frac{2S_v}{C - S_v}\right)\sigma_f \\ &= \left(\frac{2S_v}{C}\right)\sigma_f \end{aligned} \tag{A.1.12}$$

since $C \gg S_v$ in the water.

A.1.2 ADCP Radial Velocities

The ADCP measures velocity in the direction of each beam. It uses the combination of the returned signals of four acoustic beams to estimate the mean velocity vector components. Figure 2.5 shows the relationship between the acoustic beams and the mean velocity vectors at a one water depth. The sound beams ($r_{bi}, i = 1, \ldots, 4$) are at an angle of $\theta (= 20^o$ in this context) from the vertical. The acoustic pulses travel through the water column, scatter off some suspended particles, and the return acoustic signals to the

ADCP transducer for analyses. The radial velocity is calculated from the combination of its component velocities. From Figure 2.5, the combination of r_{b1} and r_{b2} acoustic beams which are relative to each other can be used to estimate the mean horizontal and vertical velocity components as:

$$\overline{u} = \frac{\overline{r_{b2}} - \overline{r_{b1}}}{2\sin\theta} \tag{A.1.13}$$

and

$$\overline{w} = \frac{\overline{r_{b2}} + \overline{r_{b1}}}{2\cos\theta} \tag{A.1.14}$$

Similarly, the v component is estimated using r_{b3} and r_{b4} acoustic beams oriented perpendicular to the first pair of beams i.e.,

$$\overline{v} = \frac{\overline{r_{b4}} - \overline{r_{b3}}}{2\sin\theta} \tag{A.1.15}$$

and

$$\overline{w} = \frac{\overline{r_{b4}} + \overline{r_{b3}}}{2\cos\theta} \tag{A.1.16}$$

However, in non-homogeneous flow field, r_{b1} and r_{b2} or r_{b3} and r_{b4} acoustic beams prescribe different velocities. It is evident that equation (A.1.13)-(A.1.16) cannot be used to transform the velocities to radial velocities along the beam path. Figure 2.6, shows the transformation diagram for homogeneous a flow field. In this case, the transformation equation for the radial velocities r_{b1} and r_{b2} are given as:

$$r_{b1} = -u_1\sin\theta + w_1\cos\theta \tag{A.1.17}$$

and

$$r_{b2} = u_2\sin\theta + w_2\cos\theta \tag{A.1.18}$$

The mean current velocity (u) is computed as:

$$\overline{u} = \left(\frac{u_1 + u_2}{2}\right) + \left(\frac{w_1 - w_2}{2\tan\theta}\right) \tag{A.1.19}$$

$$\overline{w} = \left(\frac{w_1 + w_2}{2}\right) + \left(\frac{u_1 - u_2}{2}\right)\tan\theta \tag{A.1.20}$$

Similarly, the v component can be estimated as:

$$\overline{v} = \left(\frac{u_3 + u_4}{2}\right) + \left(\frac{w_3 - w_4}{2\tan\theta}\right) \tag{A.1.21}$$

$$\overline{w} = \left(\frac{w_3 + w_4}{2}\right) + \left(\frac{u_3 - u_4}{2}\right)\tan\theta \tag{A.1.22}$$

The second terms in equations (A.1.19) - (A.1.22) are the error term associated with u, v and w due to inhomogeneous flow.

A.1.3 ADCP Configurations

The ADCP operates by sending out pulses through its transducer and receives back scattered signals along the beam axis of the transducer. The Doppler shifted velocity can be resolved along the beam axis of the ADCP with a positive beam velocity representing a radial flow towards the transducer face (Figure 2.1). The resolved beam velocities without the heading, pitch and roll correction are given as (Lu and Lueck [68]):

$$\begin{aligned} rb_1 &= -u_1\sin\theta - w_1\cos\theta \\ rb_2 &= u_2\sin\theta - w_2\cos\theta \\ rb_3 &= -v_3\sin\theta - w_3\cos\theta \\ rb_4 &= v_4\sin\theta - w_4\cos\theta \end{aligned} \tag{A.1.23}$$

If the flow is homogeneous (spatially uniform), then there is no spatial variations in the flow between beam estimates of the primary flow velocities, which can then be

combined to give:

$$\begin{aligned} u_{12} &= \frac{rb_2 - rb_1}{2} = \frac{[u_2 + u_1]\sin\theta + [w_1 - w_2]\cos\theta}{2} \\ v_{34} &= \frac{rb_4 - rb_3}{2} = \frac{[v_4 + v_3]\sin\theta + [w_3 - w_4]\cos\theta}{2} \\ w_{12} &= -(\frac{rb_1 + rb_2}{2}) = \frac{[w_1 + w_2]\cos\theta + [u_1 - u_2]\sin\theta}{2} \\ w_{34} &= -(\frac{rb_3 + rb_4}{2}) = \frac{[w_3 + w_4]\cos\theta + [v_3 - v_4]\sin\theta}{2} \end{aligned} \tag{A.1.24}$$

where the primary flow velocities are given by $u = u_{12}$, $v = v_{34}$, and $w = (w_{12} + w_{34})/2$. This inversion is identical to applying the *instrument transformation matrix* as described in RDI's Technical Manuals [91]. The data used in this study were collected by EMEC using RDI sentinel, four-transducers 600 kHz broadband ADCP with a tilt angle of 20^o from the vertical axis. The data were collected over the entire water column. The ADCP was also equipped with pitch (ξ_2) and roll (ξ_3) sensors which measure the tilt about horizontal x and vertical y axis (Figure 2.1). Heading (ξ_1) was also recorded relative to the compass and coincide with the vector pointing North. If the flow is homogeneous, i.e. $\xi_1 = \xi_2 = \xi_3 \approx 0$, the measured instantaneous velocities $r_{bi}(i = 1 \ldots 4)$ can be transformed to instantaneous velocities vectors u and w velocities in x and z axis and v and w velocities in y and z directions. For homogeneous flow the error velocity is approximately equal to zero. Due to the inherent error associated with the individual ping, numbers of pings are averaged and the mean velocities u, v and w are given as (Lu and Lueck [68], RDI [91]):

$$\overline{u} = \frac{\overline{r_{b2}} - \overline{r_{b1}}}{2\sin\theta}, \quad \overline{v} = \frac{\overline{r_{b4}} - \overline{r_{b3}}}{2\sin\theta}, \quad \overline{w} = \sum_{i=1}^{4} \frac{\overline{r_{bi}}}{4\cos\theta} \tag{A.1.25}$$

In turbulent flow (e.g., tidal stream site), the assumption of homogeneity will fail and the concept leading to equation (A.1.25) will not be appropriate. This is because equation (A.1.25) averages out the fluctuating part of the velocities as the beams increasingly diverge away from the transducer. The velocities seen by opposite beams will not be the same i.e. $r_{b1} \neq r_{b2}$, $r_{b3} \neq r_{b4}$. It is this inhomogeneous flow that introduces high uncertainty in the ADCP measurements. Research has shown (e.g., Nezu and Nakagawa [75]) that even though the instantaneous velocities are chaotic, the statistics of this chaos can give very good information about the turbulence parameters. Based on

this, the Reynolds stress tensor approach, which is based on higher moment flow, has been used in this study to estimate the bulk turbulence parameters. The method, called the *variance method* was discussed in Chapter 2, section 2.5.

The Reynolds stress tensor per unit mass $-\overline{u_i' u_j'}$ can be defined as:

$$R_T = \begin{bmatrix} -\overline{u'u'} & -\overline{u'v'} & -\overline{u'w'} \\ -\overline{u'v'} & -\overline{v'v'} & -\overline{v'w'} \\ -\overline{u'w'} & -\overline{v'w'} & -\overline{w'w'} \end{bmatrix} \tag{A.1.26}$$

where the 'prime' indicates the fluctuating part of the flow ($u' = u - \overline{u}$), which is derived by subtracting the mean ($\overline{u}$) from instantaneous velocities (u) using Reynolds decomposition approach. In this thesis, an average of 10 minutes is used. The main diagonal terms, such as $-\overline{u'u'}$ represent the turbulent kinetic energy in the three components of the flow in the Cartesian coordinates x, y, and z. If turbulence is anisotropic (i.e. being directionally dependent), the off-diagonal terms, such as $-\overline{u'w'}$ which represent turbulent momentum fluxes are non-zero. These stress terms $-\overline{u'w'}$ represent the vertical flux (w') of the x momentum deficit (u') which depict the transport of momentum within the flow, either towards or away from boundaries. Understanding these terms is crucial in order to adequately characterised the complex flows at a typical tidal energy test site. However, the best models available cannot adequately estimate these terms. Measuring these terms is difficult but recently, Stacey *et al.* [106], Osalusi *et al.* [83], Osalusi *et al.* [84] have been successful in using ADCP data to quantify important Reynolds stress components.

A.2 Wave Spectra

The sea waves consist of an infinite number of wavelets which are assumed to represent an infinite number of superimpositions of small amplitude waves having different frequencies and directions of propagations. These wavelets contain wave energy which is distributed randomly. The distribution of these energies against their frequencies and directions is referred to as the wave spectrum. Longuet-Higgins [64] was the first to propose a mathematical representation of surface wave elevation of a random wave as a sum of infinite series of component waves. The water surface elevation can be represented as (Longuet-Higgins [64]):

$$\eta = \eta(x,y,t) = \sum_{n=1}^{\infty} a_n \cos(k_n x \cos\theta_n + k_n y \sin\theta_n - 2\pi f_n t + \epsilon_n) \tag{A.2.1}$$

where η is the surface elevation, above mean water level (MWL), a is the wave amplitude, $k = (2\pi/L)$ is the wavenumber, L is the wavelength, f is the wave frequency, θ is the angle between the x-axis and the direction of wave propagation, f is the wave frequency, ϵ is the phase angle and x,y and t are the space and time coordinates. The relationship between the wavenumber k and the frequency f, known as dispersion relation is given as:

$$\omega^2 = 4\pi^2 f^2 = gk \tanh kh \tag{A.2.2}$$

and

$$L = \frac{g}{2\pi} T^2 \tanh \frac{2\pi h}{L} \tag{A.2.3}$$

where $\omega = 2\pi f$ is the angular frequency and h is the water depth.

A.3 Directional Spectrum Estimators

The information of directional wave structure of waves that propagate through different sensors can be represented by Cross-Power Spectrum Density (CPSD) which is the coefficient of the Fourier transformation of the covariance function. Isobe *et al.* [45] proposed a relationship between CPSD and the directional wave spectra as:

$$\begin{aligned} \Phi_{mn}(f) \quad = \quad & \int_0^{2\pi} H_m(f,\theta) H_n^*(f,\theta) \Big(\cos\Big[k x_{mn} \cos\theta + k y_{mn} \sin\theta \Big] \\ & - \sin\Big[k x_{mn} \cos\theta + k y_{mn} \sin\theta \Big] \Big) S(f,\theta) d\theta \end{aligned} \tag{A.3.1}$$

where Φ_{mn} is the cross-power spectrum between the mth and the nth wave property, f is the wave frequency, $H_m(f,\theta)$ is the transfer function from water surface elevation to

the mth wave property, θ is the direction, k is the wave number, $S(f,\theta)$ is the directional wave spectrum and $\mathbf{X}_{mn}(x_{mn},y_{mn})$ is the vector of wave probes for the mth and nth wave property. The transfer function is given as:

$$H_m(f,\theta) = h_m(f)\cos^{m\alpha}\theta \sin^{m\beta}\theta \tag{A.3.2}$$

According to Isobe *et al.* [45] the transfer function is derived from small amplitude wave theory as listed in Table G.1.

Measured Quantities		$h(k,f)$	α	β
Surface elevation	η	1	0	0
Vertical acceleration	η_{tt}	$-4\pi^2 f^2$	0	0
Surface slope (x)	η_x	ik	1	0
Surface slope (y)	η_y	ik	0	1
Orbital velocity (x)	u	$2\pi f\frac{\cosh k(h+z)}{\sinh kh}$	1	0
Orbital velocity (y)	v	$2\pi f\frac{\sinh k(h+z)}{\sinh kh}$	0	1
Pressure variation	p	$\rho g\frac{\cosh k(h+z)}{\cos kh}$	0	0

Table A.1: Transfer function for directional spectral measurements

Note: z is the elevation measured upward from the mean water level, h the water depth, ρ the density of water, and g the acceleration of gravity.

The directional spectrum is expressed as a product of the frequency spectrum $S(f)$ and the directional spreading function $D(\theta,f)$ as:

$$E(f,\theta) = S(f)D(\theta,f) \tag{A.3.3}$$

where

$$\int_0^{2\pi} E(f,\theta)d\theta = S(f) \tag{A.3.4}$$

From equations (A.3.3) - (A.3.4)

$$\int_0^{2\pi} D(\theta,f)d\theta = 1 \tag{A.3.5}$$

$D(\theta,f)$ is to be estimated from the observed quantities $S(f)$.

A.3.1 Direct Fourier Transform Method (DFTM)

Direct Fourier transform method is based on the assumption that the directional spectrum could be regarded as a Fourier series, represented by:

$$S(f,\theta) = \frac{a_0}{2} + \sum_{n=1}^{N} \Big[a_n \cos n\theta + b_n \sin n\theta \Big] \tag{A.3.6}$$

where a_0, a_n and b_n are Fourier coefficients. Substituting equation (A.3.6) into equation (A.3.2) yields:

$$\begin{aligned} \Phi_{kj}(f) &= \frac{a_0}{2} 2\pi J_0(kD_{kj}) \\ &+ \sum_{n=1}^{N} \Big[a_n \cos n\alpha_{kj} + b_n \sin n\alpha_{kj} \Big] 2\pi (-i)^n J_n(kD_{kj}) \end{aligned} \tag{A.3.7}$$

where $J_n()$ denotes the Bessel function of the first type. Let

$$\begin{aligned} A_0^{kj} &= \pi J_0(kD_{kj}) \\ A_n^{kj} &= 2\pi (-i)^n J_n(kD_{kj}) \cos n\alpha_{kj} \\ B_n^{kj} &= 2\pi (-i)^n J_n(kD_{kj}) \cos n\alpha_{kj} \end{aligned} \tag{A.3.8}$$

then, equation (A.3.8) can be written as:

$$\mathbf{B} = \mathbf{A}\mathbf{R}^T \tag{A.3.9}$$

where

$$\mathbf{A} = \begin{bmatrix} A_0^{kj} & 0 & 0 & -A_2^{kj} & B_2^{kj} & 0 & 0 & A_4^{kj} & B_4^{kj} & \cdots & \cdots \\ 0 & A_1^{kj} & B_1^{kj} & 0 & 0 & -A_3^{kj} & B_3^{kj} & 0 & 0 & \cdots & \cdots \end{bmatrix} \tag{A.3.10}$$

$$\mathbf{B} = \begin{bmatrix} \mathbf{C} \\ \mathbf{Q} \end{bmatrix} \tag{A.3.11}$$

$$\mathbf{R} = \begin{bmatrix} a_0 & a_1 & b_1 & a_2 & b_2 & \cdots & \cdots \end{bmatrix} \tag{A.3.12}$$

The matrix of the array of four wave sensors can be represented as:

$$\begin{bmatrix} C_{12} \\ C_{13} \\ C_{14} \\ C_{23} \\ C_{24} \\ C_{34} \end{bmatrix} = \begin{bmatrix} A_0^{12} & A_2^{12} & B_0^{12} & A_4^{12} & B_0^{12} \\ A_0^{13} & A_2^{13} & B_0^{13} & A_4^{13} & B_0^{13} \\ A_0^{14} & A_2^{14} & B_0^{14} & A_4^{14} & B_0^{14} \\ A_0^{23} & A_2^{23} & B_0^{23} & A_4^{23} & B_0^{23} \\ A_0^{24} & A_2^{24} & B_0^{24} & A_4^{24} & B_0^{24} \\ A_0^{34} & A_2^{34} & B_0^{34} & A_4^{34} & B_0^{34} \end{bmatrix} \begin{bmatrix} a_0 \\ a_2 \\ b_2 \\ a_4 \\ b_4 \end{bmatrix} \tag{A.3.13}$$

$$\begin{bmatrix} Q_{12} \\ Q_{13} \\ Q_{14} \\ Q_{23} \\ Q_{24} \\ Q_{34} \end{bmatrix} = \begin{bmatrix} -A_1^{12} & B_1^{12} & A_3^{12} & B_3^{12} \\ -A_1^{13} & B_1^{13} & A_3^{13} & B_3^{13} \\ -A_1^{14} & B_1^{14} & A_3^{14} & B_3^{14} \\ -A_1^{23} & B_1^{23} & A_3^{23} & B_3^{23} \\ -A_1^{24} & B_1^{24} & A_3^{24} & B_3^{24} \\ -A_1^{34} & B_1^{34} & A_3^{34} & B_3^{34} \end{bmatrix} \begin{bmatrix} a_1 \\ b_1 \\ a_3 \\ b_3 \end{bmatrix} \tag{A.3.14}$$

where C_{kj} is the co-spectrum which is the real part of Φ_{kj}, Q_{kj} is the imaginary part of Φ_{kj}. The coefficients can be calculated using least squares.

A.3.2 Iterative Maximum Likelihood Method (IMLM)

The Maximum Likelihood Method (MLM) was first used by Capon [14] to obtain high resolution wavenumber spectra from an array of sensors. Oakley and Lozow [79] and Jefferys *et al.* [48] extended MLM to study wave data from probes array. The CPSD

matrix from array of wave probes array is given as:

$$\hat{C_{ij}}(f) = \left[\frac{f_i(f)}{|f_i(f)|} \frac{f_j(f)}{|f_j(f)|} \right] \tag{A.3.15}$$

where $f_i(f)$ and $f_j(f)$ are the Fourier transform of the signals from the ith and jth sensors and f is the frequency. In order to obtain a reliable statistical estimate of the CPSD, Jefferys *et al.* [48] proposed that equation (A.3.15) must be average over frequency bands or within the number of sensors. The CPSD of a monochromatic wave of power $S(\omega,\theta_j)$ from direction θ_j is expressed as:

$$C(f) = \sum_{j=1}^{N} Y(f,\theta_j) X^*(f,\theta_j) S(f,\theta_j) \tag{A.3.16}$$

$$Y_p(f,\theta_j) = e^{i\mathbf{k}(\cos\theta_j \mathbf{r}_p + \sin\theta_j \mathbf{r}_p)} = e^{i\mathbf{k}.\mathbf{r}_p} \tag{A.3.17}$$

where $*$ denotes the complex Hermitian transpose, $Y(f,\theta_j)$ is the number of sensors, $\mathbf{r}_p(= r_{xp},r_{yp})$ are the x,y components of the pth sensor, $\mathbf{k}(\cos\theta_i r_{xp} + \sin\theta_i r_{yp})$ is the phase difference between the pth sensor and the origin and $e^{i\mathbf{k}.\mathbf{r}_p}$ is the phase lag between the same sensor and the origin. If a monochromatic wave of one unit energy propagates in direction θ_j, equation (A.3.17) can be written as:

$$C(f) = Y(f,\theta_j) Y^*(f,\theta_j) \tag{A.3.18}$$

where Y is the array response. The estimate of directional spectrum is done by finding the estimate of $\hat{C}(f)$ of the true CPSD and the inverse of equation (A.3.17) that yields an estimate of directional spectrum $S(f,\theta)$. This is given as:

$$\hat{S}(f,\theta_j) = A^*(f,\theta_j) C(f) A(f,\theta_j) \tag{A.3.19}$$

where A^* is a complex column vector.

Equation (A.3.19) can be written as:

$$\begin{aligned}\hat{S}(\theta_j) &= A^*(\theta_j)\left[\sum_{i=1}^{N} X(\theta_i)X^*(\theta_i)S(\theta_i)\right]A(\theta_j) \\ &= \sum_{i=1}^{N}\left[A^*(\theta_i)\left[X(\theta_i)X^*(\theta_i)\right]A(\theta_j)S(\theta_i)\right] \\ &= \sum_{j=1}^{N}\left[|A^*(\theta_j)X(\theta_i)|^2 S(\theta_i)\right] \\ &= |A^*(\theta_j)X(\theta_i)|^2 S(\theta_i) + \sum_{i\neq j}\left[|A^*(\theta_j)X(\theta_i)|^2 S(\theta_i)\right]\end{aligned} \tag{A.3.20}$$

Equation (A.3.20) shows that MLM estimate will always be positive. The constrained optimisation problem defined as:

$$|A^*(\theta_j)X(\theta_i)|^2 = 1 \tag{A.3.21}$$

correctly estimates the energy from direction θ_j while minimizing the contribution from other directions θ_i. From Jefferys *et al.* [48], equation (A.3.21) can be solved using Lagrange multiplier theory which gives the function to be minimized as:

$$L(A(\theta_j),\Omega) = A^*(\theta_j)CA(\theta_j) + \Omega(A^*(\theta_j)X(\theta_j) - 1) \tag{A.3.22}$$

where Ω is a Lagrange multiplier.

To find the stationary values of the unconstrained function in equation (A.3.22) , the solution is defined as:

$$\hat{S}(f,\theta) = \frac{\epsilon_s}{X^*(f,\theta_i)C^{-1}(f)X(f,\theta_i)} \tag{A.3.23}$$

where $C^{-1}(f)$ is the inverse of CPSD and ϵ_s is the scaling factor which equates the total energy at frequency f to the energy in the frequency spectrum. Capon [14] proposed a perturbation in order to avoid singularity in CPSD matrix as:

$$C(f) = (1-r)C(f) + r.I, \quad 0 < r < 1 \tag{A.3.24}$$

where I is an identity matrix. Jefferys *et al.* [48] suggested a typical values of r between $O(10^{-5})$ and $O(10^{-9})$ because the perturbation equation (A.3.24) will add incoherent noise to the sensors which decrease the resolution of the MLM.

One of the drawbacks of MLM is that the reconstructed CPSD $C^R(f)$ from energy estimate $S(f,\theta)$ is different from the measured CPSD $C(f)$. Pawka [86] and Oltmanshay and Krogstad *et al.* [58] proposed an iterative scheme to force the directional estimate to be consistent with the measured CPSD. This procedure is refers to as IMLM. From Krogstad *et al.* [58],

$$S_{n+1} = S_n + \nu\left(S_{MLM} - S^R_{MLM}\right) \tag{A.3.25}$$

with a threshold value

$$\xi = \frac{max|S_{n+1} - S_n}{S_n} \tag{A.3.26}$$

where S_{MLM} is the estimate from MLM and S^R_{MLM} is the MLM estimate from the reconstructed CPSD matrix, S is the directional spectrum, and a value of $\nu = 1.2$ ensures the fastest convergence rate is reached (Krogstad *et al.* [58]).

A.3.3 Extended Maximum Entropy Program (EMEP)

Maximum Entropy Program (MEP) was developed to determine the probability density function of a random variable from data in which information about the distribution is not sufficient. Lygre and Krogstad [70] used this concept to derive the probable expression for directional spreading function as:

$$H(F) = -\int_{-\pi}^{\pi} \texttt{log}(F(\theta))d\theta \tag{A.3.27}$$

which is maximized subject to the constrain:

$$\int_{-\pi}^{\pi} F(\theta)e^{-k\theta}d\theta = c_n \tag{A.3.28}$$

where F is the entropy. The maximizing function can be written as (Lygre and Krogstad [70]):

$$D(\theta) = \frac{1}{2\pi} \frac{(1 - \phi_1 c_1^* - \cdots - \phi_N c_N^8)}{|1 - \phi_1 e^{i\theta} - \cdots - \phi_N e^{-iN\theta}|^2} \tag{A.3.29}$$

which is the spectral density of the autoregressive system:

$$\begin{bmatrix} 1 & c_1^* & \cdots & c_{N-1}^* \\ c_1 & 1 & \vdots & \vdots \\ \vdots & \vdots & \ddots & c_1^* \\ c_{N-1} & \cdots & c_1 & 1 \end{bmatrix} \begin{bmatrix} \phi_1 \\ \phi_1 \\ \vdots \\ \phi_N \end{bmatrix} = \begin{bmatrix} c_1 \\ c_1 \\ \vdots \\ c_N \end{bmatrix} \tag{A.3.30}$$

The directional spectrum estimate is obtained from equation (A.3.29).

For a mixed instrument arrays, Kobune and Hashimoto [55] proposed a more general relationship as:

$$H(F) = -\int_{-\pi}^{\pi} F(\theta) \mathtt{In}[F(\theta)] d\theta \tag{A.3.31}$$

Hashimoto [35] discovered that the iterative procedure to solve equation (A.3.31) fails with number of arrays greater than four. Nwogu [77] and Hashimoto [35] proposed a complex iterative scheme to solve the problem with arrays of wave gauges greater than four. From Hashimoto [35], the entropy can be written as:

$$H = -\int F(\theta) \Big[\mathtt{In}[F(\theta)] + \sum_{j=0}^{n} \lambda_j \theta^j \Big] d\theta \tag{A.3.32}$$

where H is maximized with respect to $F(\theta)$ by making $\partial H / \partial F = 0$. This results in probability density function defined as:

$$F(\theta) = \mathtt{exp}\Big(-1 - \sum \lambda_j \theta^j \Big) \tag{A.3.33}$$

where λ_j is chosen such that the sample moments equals to the theoretical moments evaluated based on the estimated probability density function, given as:

$$\int \theta^k \exp\Big(-1-\sum \lambda_j \theta^j\Big) d\theta = m_k, \quad k = 1,2,\cdots \tag{A.3.34}$$

where $m_0 = 1$, $m_k (k \neq 0)$ are sample moments from data.

In order to estimate directional spreading function $D(\theta, f)$ from the field data obtained from an array of wave sensors, Hashimoto [35] proposed the following relationship between CPSD and directional spectrum:

$$\Phi_{mn}(f) = \int_0^{2\pi} \exp\Big(ik(x_n - x_m)\Big) S(f,\theta) \tag{A.3.35}$$

and in dimensionless form:

$$\phi(f) = \frac{\Phi_{mn}(f)}{S(f)} = \int_0^{2\pi} q_j(\theta) D(\theta, f) d\theta, \quad j = 1,\cdots,(M+1) \tag{A.3.36}$$

where $M = N(N-1)$, N is the number of wave sensors and

$$\begin{aligned} \phi_j(f) &= \frac{\mathrm{Re}\Phi_{mn}(f)}{[S_m(f) S_n(f)]^{1/2}}, \quad \texttt{for} \quad j = 1,\cdots,(M/2) \\ &= \frac{\mathrm{Im}\Phi_{mn}(f)}{[S_m(f) S_n(f)]^{1/2}}, \quad \texttt{for} \quad j = (M/2)+1,\cdots,M \\ &= 1 \quad \texttt{for} \quad j = M+1,\cdots, \end{aligned} \tag{A.3.37}$$

$$\begin{aligned} q_j(\theta) &= \cos\Big(kr_i \cos(\beta_j - \theta)\Big) \quad \texttt{for} \quad j = 1,\cdots,(M/2)+1 \\ &= \sin\Big(kr_i \cos(\beta_j - \theta)\Big) \quad \texttt{for} \quad j = (M/2)+1,\cdots,M \\ &= 1 \quad \texttt{for} \quad j = M+1,\cdots \\ & r_j = \Big((x_n - x_m)^2 + (y_n - y_m)^2\Big)^{1/2} \\ & \beta_j = \tan^{-1}\left[\frac{(y_n - y_m)}{(x_n - x_m)}\right] \end{aligned} \tag{A.3.38}$$

The estimated directional spreading function becomes:

$$D(\theta,f) = \exp\left(-1 + \sum_{j=1}^{M+1} \lambda_j q_j(\theta_j) \right) \tag{A.3.39}$$

The general expression for EMEP directional spreading function $G(\theta,f)$ is given as (Benoit *et al.* [6]):

$$G(\theta,f) = \frac{\exp\left[\sum_{n=1}^{M} \left\{ a_n(f)\cos n\theta + b_n(f)\sin n\theta \right\} \right]}{\int_{-\pi}^{\pi} \exp\left[\sum_{n=1}^{M} \left\{ a_n(f)\cos n\theta + b_n(f)\sin n\theta \right\} \right] \mathrm{d}\theta} \tag{A.3.40}$$

where $a_n(f)$ and $b_n(f)$ are the unknown parameters and M is the order of the model. Hashimoto [35] gave more detailed expressions and discussions concerning procedures of the iterative computation. The application of equation (A.3.40) to the field data need to account for the errors in the cross-power spectra. The error in the EMEP estimation is given as:

$$\epsilon_n = \left[\int_{-\pi}^{\pi} (\phi_i - H_i(\theta)) \right] \times \frac{\exp\left[\sum_{n=1}^{M} \left\{ a_n(f)\cos n\theta + b_n(f)\sin n\theta \right\} \right]}{\int_{-\pi}^{\pi} \exp\left[\sum_{n=1}^{M} \left\{ a_n(f)\cos n\theta + b_n(f)\sin n\theta \right\} \right] \mathrm{d}\theta}, \quad i = 1,2,\ldots,M \tag{A.3.41}$$

where M is the number of remaining independent equations following the elimination of meaningless equations.

A.3.4 The Spectral Matrix

The spectral matrix structure contains:

- vector of length nf defining bin centers of the spectral matrix frequency axis
- vector of length nd defining bin centres of the spectral matrix direction axis

- the compass direction of the x axis from which angles are measured and
- matrix size $[nf, nd]$ containing the spectral density.

The layout of the spectral matrix is specified as a vector of evenly spaced frequencies and a vector of evenly spaced directions. These form the bin structure for the matrix and the values are the centre of the bin (see Figure A.1). Frequency f, in Hz and directions θ, in degrees are measured anticlockwise from the positive x axis. The orientation of a wave component is relative to the x direction of the ADCP layout and wave recorder directional components.

The spectral density itself is a matrix such that S_{ij} contains values of the spectral power density for the i^{th} frequency and the j^{th} direction. The energy is per unit $Hz.degree$. Therefore to convert to component wave amplitudes you need to multiply by bin sizes df and $d\theta$:

$$a_{ij} = \sqrt{2S_{ij}df d\theta} \tag{A.3.42}$$

where a_{ij} is the amplitude of the component with the i^{th} frequency and the j^{th} direction and S_{ij} is the value in the spectral density matrix.

A.4 Spectral Estimates of Wave-generated Bottom Orbital Velocities

Practically, the characteristics of a surface wave field which contains wave frequency spectra are presented in terms of significant wave heights, root-mean squared (RMS) peak or dominant wave periods over a given sampling interval. The moment of the surface spectra is given as (Tucker and Pitt [116]):

$$m = \int_0^n f^n S_\eta(f) df \tag{A.4.1}$$

The significant wave height H_s (or H_{m0} in term of the moment) is defined as (Longuet-Higgins, [64], Dean and Dalrymple, [15], Tucker and Pitt [116]):

$$H_s = 4\sqrt{m_0} = 4\sqrt{\int S_\eta(f) df}, \qquad n = 0, 1, \ldots \tag{A.4.2}$$

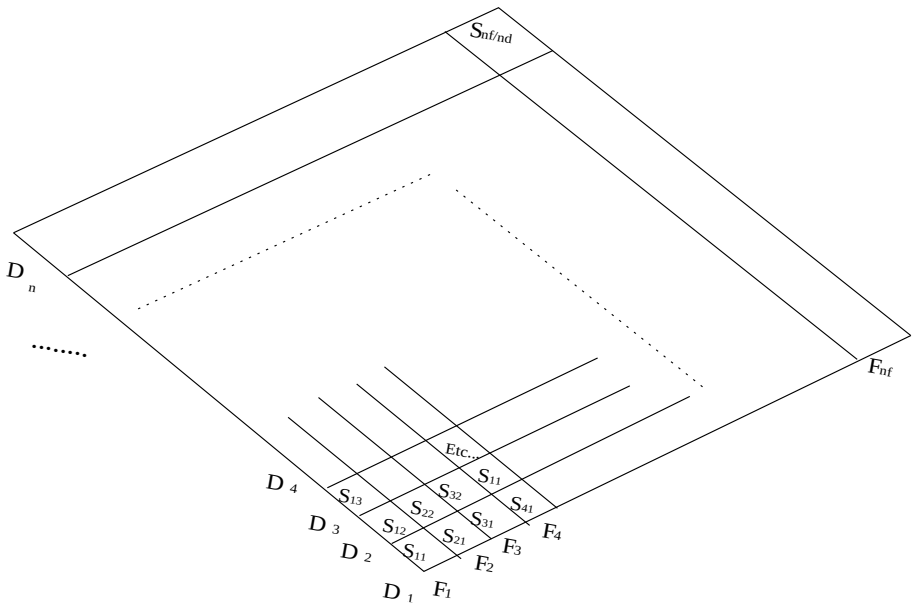

Figure A.1: Spectral matrix layout components S_{ij}. The frequency bin vector is $F_i(1:nf)$ and the direction bin vector is $D_j(1:nd)$

where m_0 is the variance (or zero-order moment) of water surface elevation η, and S_η is the spectra density of surface elevation as a function of frequency. For discrete sampling, H_s is approximated as:

$$H_s = 4\sqrt{\sum S_{\eta,i}\Delta f_i} \tag{A.4.3}$$

in which $\sum$ is the sum over all frequency bins in the spectrum and i is a positive index. The average zero-crossing period ($T_z = \sqrt{m_0/m_2}$) is the interval between consecutive times when surface elevation crosses zero going up or down (Tucker and Pitt [116]), where m_2 is the second-order moment of the wave height spectrum calculated from equation (A.4.1). The mean and the energy period is defined as $T_m = m_0/m_1$ and $T_e = m_{-1}/m_0$, respectively. The energy period corresponds to the weighted average of the wave energy.

At the seabed boundary layer, the spectrum of the wave-induced orbital velocity given

as:

$$u_b = \frac{H\pi}{T\sinh kh} = \frac{\omega a}{\sinh kh} \tag{A.4.4}$$

can be calculated from each frequency band i of the surface-wave spectrum as:

$$S_{u,i} = \frac{4\pi^2}{T_i^2 \sinh^2(k_i h)} S_{\eta,i} = \frac{\omega_i^2}{\sinh^2(k_i h)} S_{\eta,i} \tag{A.4.5}$$

where T is the wave period, h is the water depth, k is the wavenumber. Summing up the $S_{u,i}$ in equation (A.4.5) over each frequency gives:

$$u_{br}^2 = 2\sum_i S_{u,i}\Delta f_i \tag{A.4.6}$$

(Note: $a_{rms}^2 = H_{rms}^2/4 = 2m_0 = 2\int S_\eta df$ and $u_b =$ amplitude of wave orbital velocity at the bed). The bottom orbital velocity can be derived by substituting equation (A.4.5) into equation (A.4.6) to yield (Madsen [71]):

$$u_{br} = \sqrt{2}\left(\sum_i \left[\frac{4\pi^2}{T_i^2 \sinh^2(k_i h)} S_{\eta,i}\Delta f_i\right]\right)^{0.5} \tag{A.4.7}$$

The u_{br} can also be defined as the root-mean squared value of the bottom orbital velocity. The significant orbital velocity can be defined with respect to significant wave height as (Madsen [71]):

$$u_{bs} = \sqrt{2}u_{br} = 2\left(\sum_i \left[\frac{4\pi^2}{T_i^2 \sinh^2(k_i h)} S_{\eta,i}\Delta f_i\right]\right)^{0.5} \tag{A.4.8}$$

The representative wave frequency f_{br} and bottom frequency f_{bz} are defined as:

$$f_{br} = \frac{\sum_i f_i S_{u,i}\Delta f_i}{\sum_i S_{u,i}\Delta f_i} \tag{A.4.9}$$

and

$$f_{bz} = \left(\frac{\sum f_i^2 S_{u,i} \Delta f_i}{\sum S_{u,i} \Delta f_i} \right)^{0.5}, \tag{A.4.10}$$

respectively.

Appendix B

Pre-processing of ADCP data

ADCP data must undergo extensive quality control analysis in order to ensure that the uncertainties in the output are reduced to the minimum. Before the ADCP deployment, certain thresholds are set in order to flag bad data, for example, data that fall outside of broad error specifications or against a narrower range of error specifications or error due to strong reflections from the water surface that overcome the sidelobe suppression of the ADCP transducer. However, during pre-processing of ADCP data, some data may be questionable. Such suspected data, called spikes, are not removed; rather, they are detected and possibly replaced. Spikes in the data may corrupt, overestimate wave spectra or skew smoothed estimates. Spikes in the ADCP data are mainly caused by fish, ship, turbulence and floating debris. The total source of noise in ADCP beam velocity is given as:

$$\sigma_t^2 = \sigma_{spl}^2 + \sigma_{dn}^2 + \sigma_{msh}^2 \tag{B.0.1}$$

where σ_t^2 is the total velocity error variance, σ_{spl}^2 represents the sampling error which is related to the system's phase uncertainty, σ_{dn}^2 is the Doppler noise which is related to the total Doppler bandwidth broadening ($D^2 = D_r^2 + D_t^2 + D_d^2$), where D_r is the broadening due to finite residence time, D_t represents broadening due to turbulence and D_d is the broadening due to beam divergence). σ_{msh}^2 is the error variance due to mean velocity shear within the sample volume. While the error due to σ_{spl}^2 is independent of flow, σ_{dn}^2 and σ_{msh}^2 are flow related. The dominant noise term is due to turbulence (i.e. in σ_{dn}^2) and the mean velocity shear error (i.e. in σ_{msh}^2) becomes significant close to the seabed (Lhermitte and Lemmin [60]).

Acceleration and phase-space (or 3D Poincaré map) threshold methods have proved to be effective in detecting erroneous data (spikes) from acoustic sampling (Goring and

Nikora [30], Dohoho and Johnstone [21]). These methods are based on the observation that the derivative of a signal amplifies the high-frequency components (the spikes domain). The separation of these erroneous data is amplified as the order of derivative increases i.e. $d^j\hat{u}(\omega,t)/dt^j \propto \omega^j\hat{u}(\omega,t)$, where $\hat{u}(\omega,t)$ is the Fourier series transform of $u(t)$ (the instantaneous velocity), ω is the radial frequency and j is a positive index.

The acceleration threshold method is based on the assumption that in uniform flow, the instantaneous acceleration in flow cannot be greater than gravitational acceleration (Goring and Nikora [30]). However, the drawback of this method is that the spike detection is based on the choice of thresholds (which is a product of a constant (between 1 and 1.5) and the standard deviation) and this would not be able to differentiate between fluctuations in the records and spikes, most especially in turbulent flow if appropriate thresholds were not chosen. The phase-space threshold is based on the wavelet threshold method proposed by Donoho and Johnstone [21]. This method has proved successful in recent years (e.g., Goring and Nikora [30], Trevethan [115]) in detecting erroneous data from Acoustic Doppler Velocimeters (ADV). The description of phase-space method is given below.

B.0.1 Phase-Space Threshold Method

A three dimensional Poincaré map (phase-space plot) is used to plot the variable and its derivatives (first and second) against each other (Goring and Nikora [30]). The data points, cluster within an ellipsoid, defined by Universal criterion, are considered good while those lying outside are suspected to be spikes. The Universal criterion is defined as (Goring and Nikora [30]):

$$\alpha_c = \sqrt{2ln(N)}\sigma \tag{B.0.2}$$

where α_c is the Universal criterion, σ is the standard deviation of the sample volume (variable) and N is the number of data points. The first and second derivatives are defined as:

$$\frac{\partial u_k}{\partial t} = \frac{1}{2}\Big(u_{k+1} - u_{k-1}\Big) \tag{B.0.3}$$

$$\frac{\partial^2 u_k}{\partial t^2} = \frac{1}{2}\left(\frac{\partial u_{k+1}}{\partial t} - \frac{\partial u_{k-1}}{\partial t}\right) \tag{B.0.4}$$

where u is the velocity (or variable) and k is an index. α_c is calculated for each of equations (B.0.3) and (B.0.4) and these provide the major and minor ellipse threshold values. The datapoints lying outside the ellipsoid (spikes) are found and replaced by curve fitting using cubic spline data interpolation. This iteration continues until all erroneous data found are replaced. Figure B.1 illustrates the application of 3D phase space method on ADCP instantaneous velocity data collected at the Fall of Warness on the 26 August 2005. The blue cluster points are the good data inside the three dimensional ellipse and the red points found outside the ellipsoid are the suspected 'spikes'.

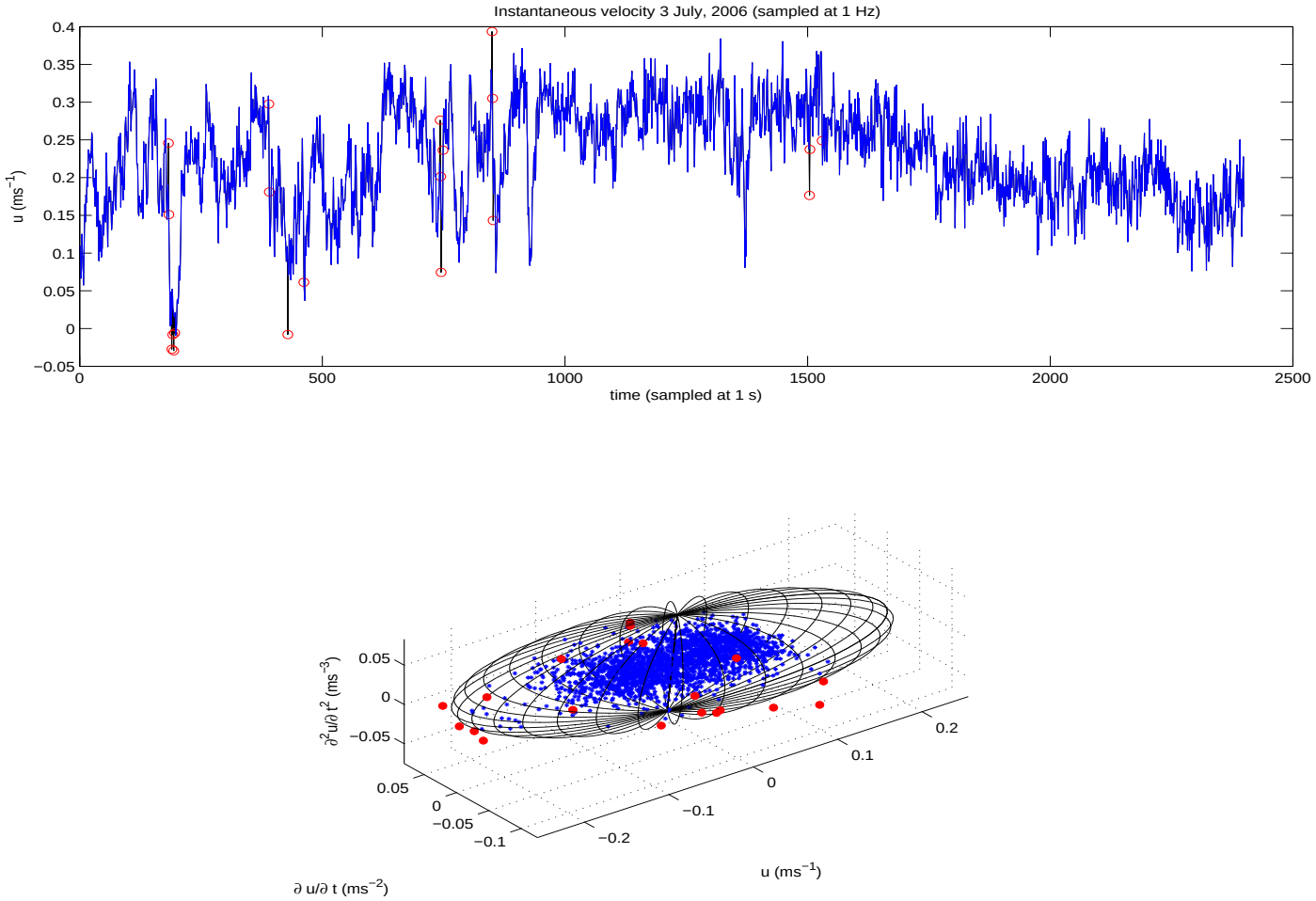

Figure B.1: The instantaneous velocity (upper panel) and 3D phase space method showing cluster of ADCP data measurement (lower panel): blue points are good data and red points are spikes

Appendix C

Wave-Turbulence Filtration

Linear filtration methods proposed by Benilov and Filyushkin [5] can be used to separate wave and turbulence ADCP data. This method has the capability of distinguishing turbulence from linear waves (Kitaigorodskii *et al.* [53], Trevethan [115]). Benilov and Filyushkin proposed that if water level $\eta(t)$ and velocity $U(t)$ are sampled at the same frequency and their spectral densities are known, then, any fluctuations in velocity that correlate with the water surface displacement are considered to be caused by the surface waves. The instantaneous velocity $U(t)$ is made up of turbulent fluctuations $U'(t)$ and noise generated waves $U_w(t)$ given as:

$$U(t) = U'(t) + U_w(t) \tag{C.0.1}$$

The displacement $\eta(t)$ is related to the wave noise as:

$$U_w(t) = \Gamma\eta(t) \tag{C.0.2}$$

where Γ is an unknown linear operator. Equation (C.0.2) establishes $U'(t)$ if the corresponding spectral densities of water surface displacement S_η and velocity S_{vel} are known, i.e.:

$$\overline{U'(t)\eta(t)} = 0 \tag{C.0.3}$$

Figure C.1 show an ADCP data from the Fall of Warness tidal test site, sampled at 1 Hz between 2 and 5 July 2006. The water level and the three velocity components spectra were plotted in Figure C.1. Figure C.1 (upper panel) shows the correlation between the spectra frequency band for both S_η and S_{vel}. By visual inspection, the cor-

relation between the spectra of water level and velocity spectra were found to be in the range of ~ 0.020 to ~ 0.174 Hz. The beam velocities signals contained in this range ($\sim 0.020 - \sim 0.174$) were band-pass filtered using Matlab® 3rd order Butterworth filter coefficients applied with the *filtfilt* function. The *filtfilt* function filters in both forward and backward direction in order to preserve the phase characteristics of the signal (Matlab [72]). The output of filtfilt was then subtracted from the raw beam data to obtain the turbulence (filtered) data.

It is assumed that data outside the frequency range were not affected by waves except non-linear components of surface waves. Figure C.1 (lower panel) shows the same spectra as in Figure C.1 (upper panel) when this frequency range containing waves has been removed. This section of the turbulence data removed has proved to be acceptable (e.g., Soloviev and Lukas [103], Trevethan [115]) since it covers a narrow frequency band.

Figure C.1 was used as an example and the limitations associated with it are recognised.

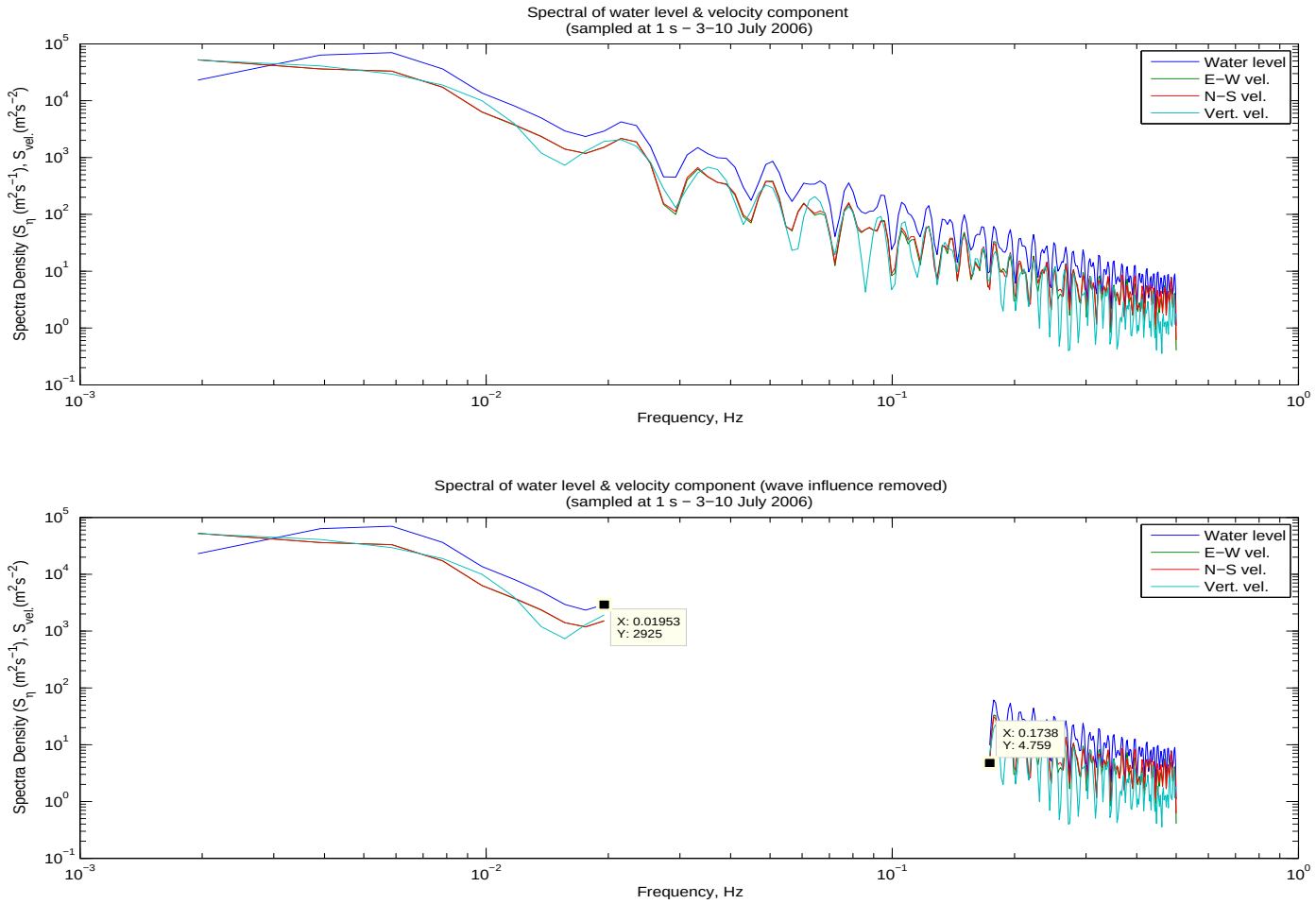

Figure C.1: The spectra of water level and velocity data sampled at 1 Hz with wave influence (upper panel) and without wave influence (lower panel)

Appendix D

Directional Wave Spectra Output: Comparing WavesMon® and the Present Study

Directional wave spectrum output from this thesis has been compared with the RDI ADCP's software, WavesMon® [90]. WavesMon® chooses twelve time series of beam radial velocities from three layers close to the water surface for directional wave computations. WavesMon® uses the range data as well. The range data is the along beam distance from the ADCP transducer to the water surface for each four beams. However, it is not known when WavesMon® switches to range data for directional spectrum computations. It uses the iterative maximum likelihood method (IMLM) for directional spreading estimation as its default setting.

Figures D.1 - D.12 show the comparison between directional spectra output from this study and WavesMon®. The ADCP data was sampled at 2Hz every 20 minutes in one hour from 15 March 2007 12:00 hours to 16 March 2007 11:00 hours and 18 March 2007 00:00 hours to 18 March 2007 23:00 hours. The corresponding wave parameters are shown in Table D.1. The Highlighted data are assumed to be questionable. For instance on the 15 March 2007 16:00 Hours, the H_s of 0.49 m seems to be odd during the wave decay as compared with the neighouring values and on the 15 March 2007 16:00 Hours to 15 March 2007 16:00 Hours, the values of H_s (0.59 and 0.87 m) suppose to be increasing (when compared with the neighouring values) during wave development. WavesMon® default settings of directional resolution of 4^o and frequency resolution of 0.00781250 Hz going from 0 to 1 Hz were used. The directional resolution of 2^o and frequency resolution of 0.01 Hz going from 0.1 to 0.5 Hz were used in this thesis. In addition to this, the preprocessing procedure described in section B.0.1 was performed on beam radial velocities, ranges and pressure data before processing of directional spectra computations were carried out.

It is unclear why WavesMon®'s frequency resolution extended to 1 Hz since the sampling rate (Nyquist frequency) of the ADCP is 2 Hz. The number of IMLM iterations determines the number of improved corrections on each frequency for the original solution. Higher values may result in negative energy anomalies and distorted spectra. For this reason, one iteration was used in both computations.

The polar plots (Figures D.1 - D.12) show that the generated spectrum from this study follow the WavesMon® output fairly well. However, the directional resolution from this study (upper panels, Figures D.1 - D.12) compare favourably with WavesMon®'s (lower panels). Tables D.1 and D.2 show the comparison of wave parameters (significant wave height H_s, peak period T_p and direction of peak period DT_p) between WavesMon® and the result from this study. The T_p values presented in column 2 in Tables D.1 and D.2 (WavesMon®) are derived from pressure data (as oppose to the values shown on the left corners of WavesMon® polar plots (lower panels, Figures D.1 - D.12) in order to compare it with the author's result. Generally, the values of H_s (columns 2 and 3) from WavesMon® seem to be larger than H_s from this study except during the storm events of 18 March 2007 02:00 to 18 March 2007 04:00 (Table D.2). It seems that WavesMon® filtered out the storm data. The T_p values from (column 4 and 5) WavesMon® seem to be constant, at least for several hours while T_p from this present study changes with time. However the DT_p from both computations seems to track each other very well. The cause of this difference between H_s and T_p is not clear. It is reasonable to assume that the differences are due to the inherent errors in the three bins of beam radial velocities WavesMon® chosen for directional computations and the algorithm used to detect and remove spikes from the data. Since WavesMon® is a 'blackbox' software, it is not certain what algorithms were used for the preprocessing of the data.

Because ADCP measurements are subject to numerous errors and uncertainties, some of which are amplified or generated by motion of the instrument during data collection. None of these fitting methods described in section A.3 will perform satisfactorily unless random errors associated with the instrument's internal electronics and velocity ambiguity errors which are large when stream flow velocities are large relative to the instrument velocity, are minimized.

Date	$H_s(m)$		$T_p(s)$		$D_p(^o)$	
	WavesMon®	Present study	WavesMon®	Present study	WavesMon®	Present study
15 March 2007 12:00	1.65	1.53	7.71	7.69	333	336
15 March 2007 13:00	1.81	1.70	7.71	7.69	333	342
15 March 2007 14:00	1.96	1.88	7.71	7.14	335	334
15 March 2007 15:00	1.55	1.14	7.71	5.88	300	338
15 March 2007 16:00	1.37	0.49	7.71	16.67	152	296
15 March 2007 17:00	1.96	0.85	7.71	7.14	326	322
15 March 2007 18:00	2.19	0.92	7.71	7.69	322	318
15 March 2007 19:00	1.58	0.87	8.01	8.33	322	328
15 March 2007 20:00	1.20	0.70	8.01	6.25	155	320
15 March 2007 21:00	0.88	0.66	8.01	6.67	182	172
15 March 2007 22:00	1.04	0.66	7.71	9.09	318	320
15 March 2007 23:00	1.54	1.46	7.71	9.09	345	344
16 March 2007 00:00	2.08	1.80	7.71	9.09	339	340
16 March 2007 01:00	2.04	1.81	7.71	8.33	342	332
16 March 2007 02:00	2.06	1.60	7.71	9.09	322	318
16 March 2007 03:00	1.43	1.07	7.71	7.14	309	294
16 March 2007 04:00	1.12	0.59	7.71	6.67	329	330
16 March 2007 05:00	1.43	0.87	7.71	7.14	205	168
16 March 2007 06:00	2.77	1.16	7.71	7.14	304	270
16 March 2007 07:00	1.78	1.02	8.01	7.69	331	326
16 March 2007 08:00	1.82	1.13	8.01	7.14	350	152
16 March 2007 09:00	1.77	1.15	8.01	6.25	331	160
16 March 2007 10:00	1.64	1.07	8.01	5.26	148	168
16 March 2007 11:00	1.76	1.47	7.71	11.11	321	322

Table D.1: Comparison between WavesMon® and present study wave statistics (15 March 2007 12:00 -16 March 2007 11:00); red coloured data are regarded as suspects

Date	$H_s(m)$		$T_p(s)$		$D_p(^o)$	
	WavesMon®	Present study	WavesMon®	Present study	WavesMon®	Present study
18 March 2007 00:00	2.00	1.93	9.40	9.09	329	338
18 March 2007 00:01	2.19	2.65	9.40	10.00	336	338
18 March 2007 00:02	3.78	4.50	8.80	16.67	307	346
18 March 2007 00:03	2.78	7.65	7.30	16.67	318	318
18 March 2007 00:04	2.18	3.23	5.90	20.00	320	314
18 March 2007 00:05	3.19	3.14	3.40	20.00	326	164
18 March 2007 00:06	3.97	3.31	2.10	20.00	335	294
18 March 2007 00:07	3.01	2.76	2.20	20.00	309	260
18 March 2007 00:08	3.19	1.59	2.10	16.67	321	310
18 March 2007 00:09	2.82	1.32	2.00	14.29	327	316
18 March 2007 00:10	1.74	1.18	3.70	4.35	319	322
18 March 2007 00:11	1.69	1.79	5.90	5.26	152	328
18 March 2007 00:12	4.44	2.99	2.20	7.69	153	356
18 March 2007 00:13	5.36	3.84	2.10	11.11	328	336
18 March 2007 00:14	3.19	2.43	2.00	11.11	348	348
18 March 2007 00:15	2.64	2.65	2.10	11.11	311	320
18 March 2007 00:16	2.09	2.06	8.20	7.69	342	330
18 March 2007 00:17	1.48	1.41	7.30	7.14	303	336
18 March 2007 00:18	2.05	0.93	2.00	12.50	292	302
18 March 2007 00:19	2.34	1.01	2.10	12.50	313	306
18 March 2007 00:20	2.66	0.92	2.00	16.67	290	58
18 March 2007 00:21	1.71	0.64	2.00	11.11	332	310
18 March 2007 00:22	1.64	0.59	2.10	7.14	321	318
18 March 2007 00:23	0.83	0.42	2.10	16.67	309	314

Table D.2: Comparison between WavesMon® and present study wave statistics (18 March 2007 00:00 - 18 March 2007 23:00)

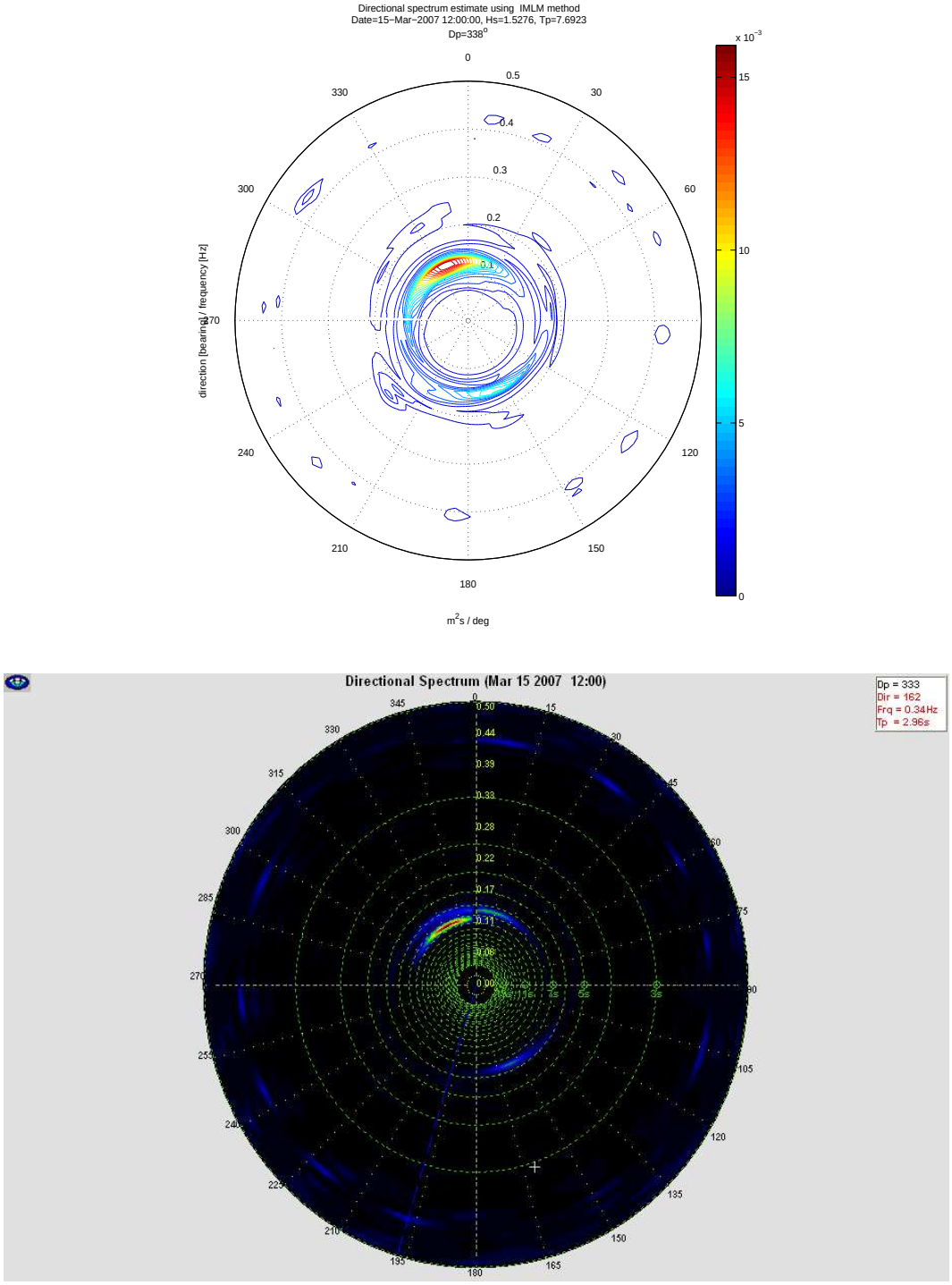

Figure D.1: Directional spectrum estimated using author's toolbox (upper) and RDI WavesMon (lower); 15 March 2007 12:00:00

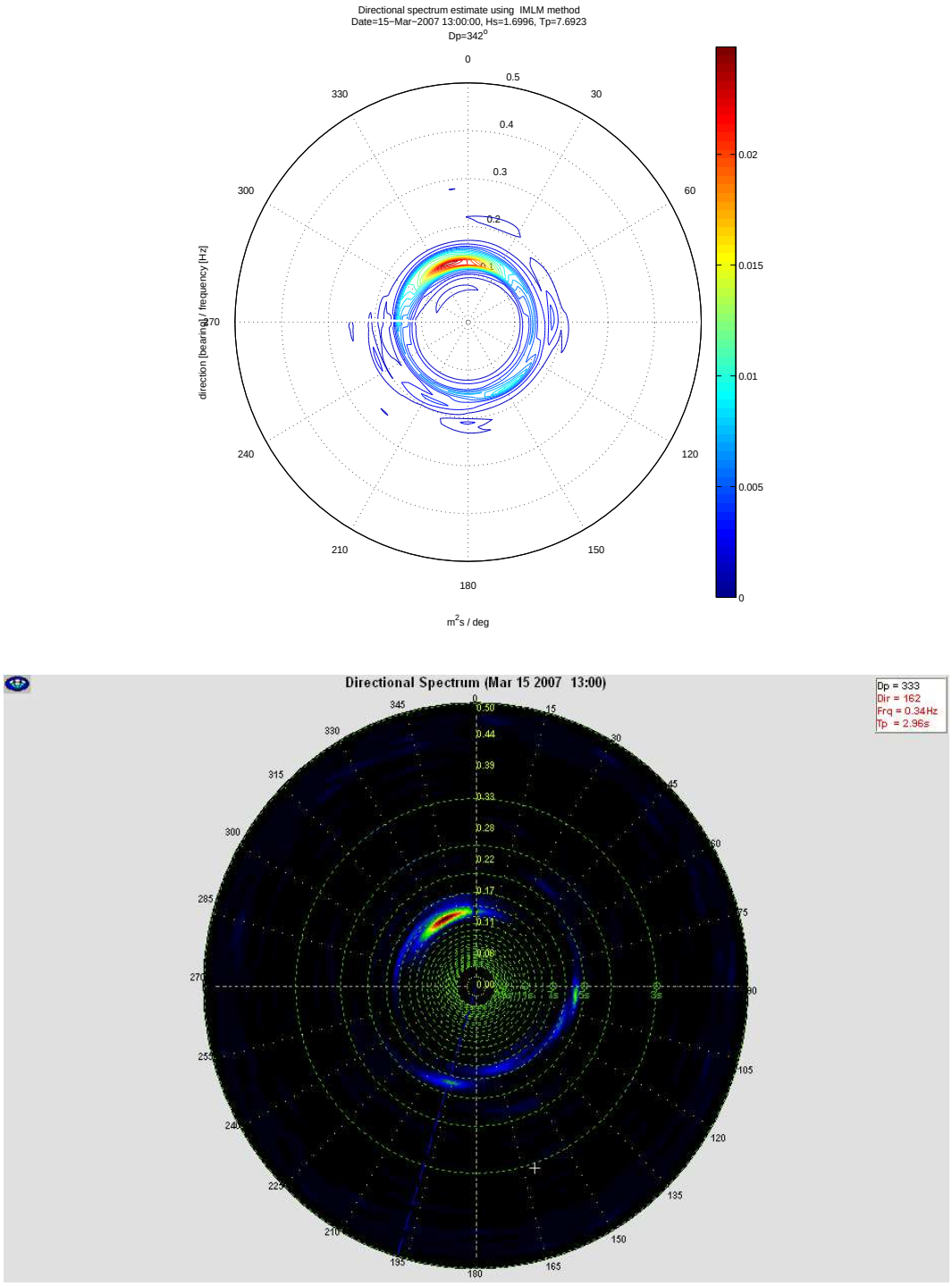

Figure D.2: Directional spectrum estimated using author's toolbox (upper) and RDI WavesMon (lower); 15 March 2007 13:00:00

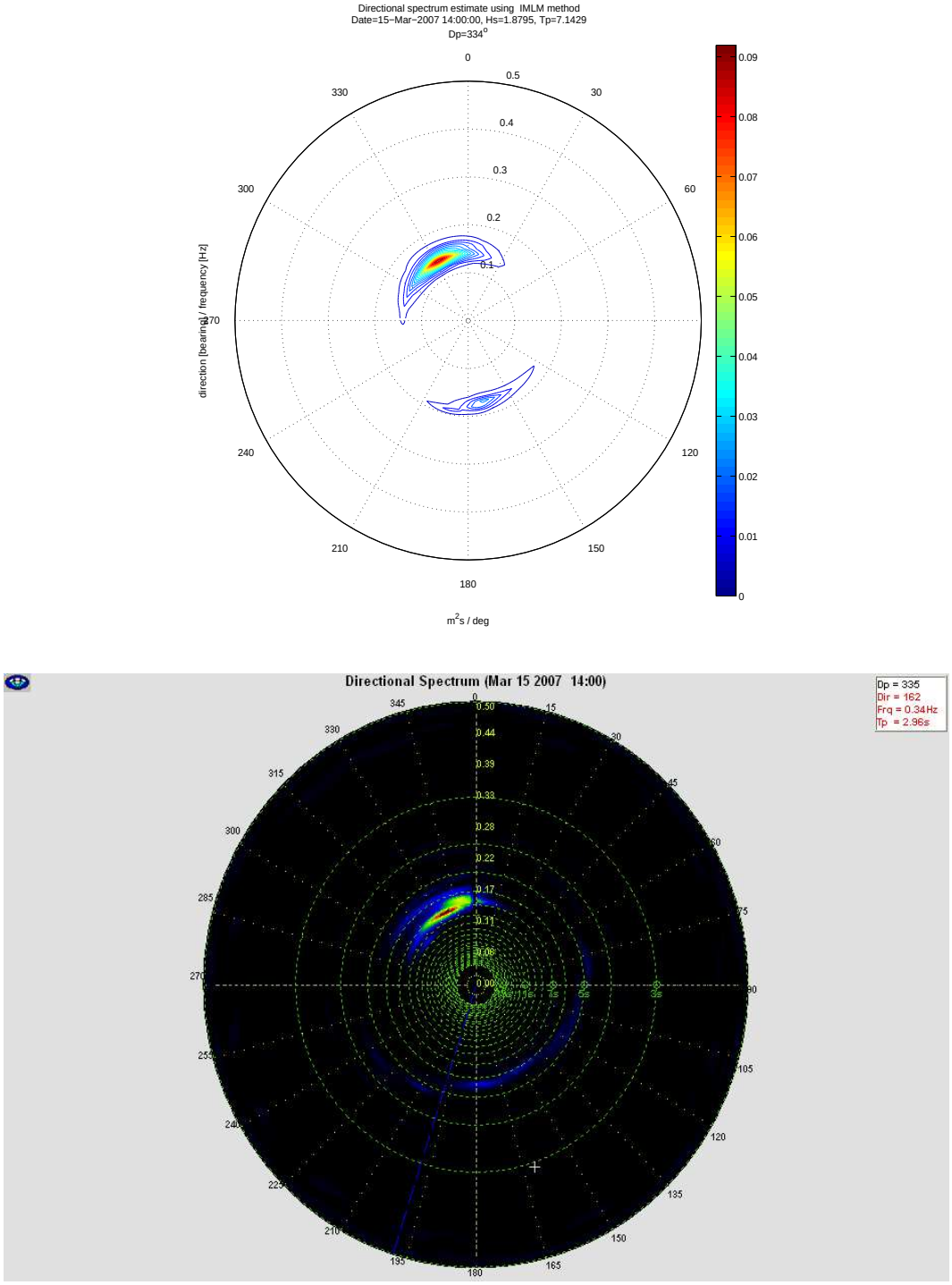

Figure D.3: Directional spectrum estimated using author's toolbox (upper) and RDI WavesMon (lower); 15 March 2007 14:00:00

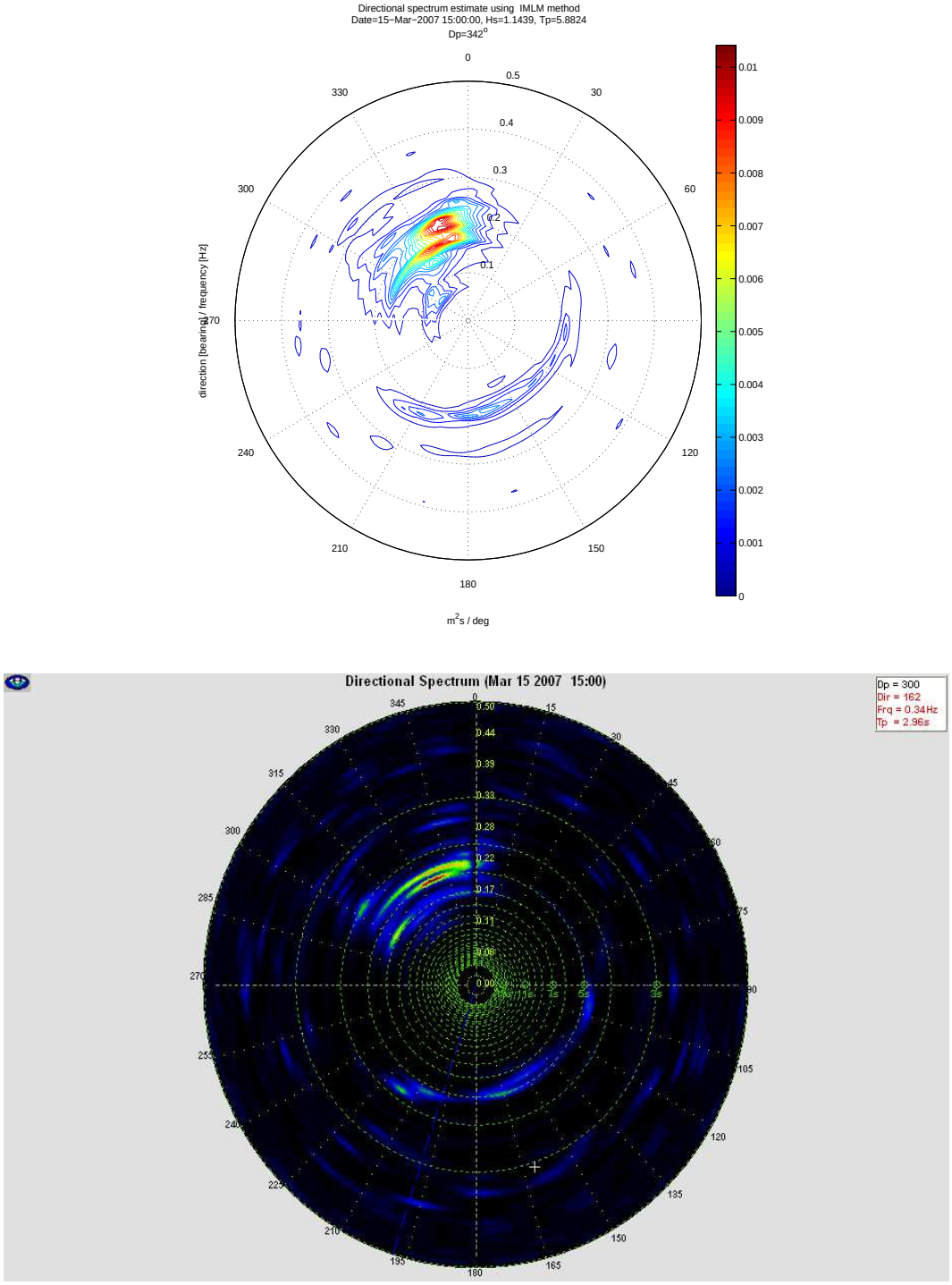

Figure D.4: Directional spectrum estimated using author's toolbox (upper) and RDI WavesMon (lower); 15 March 2007 15:00:00

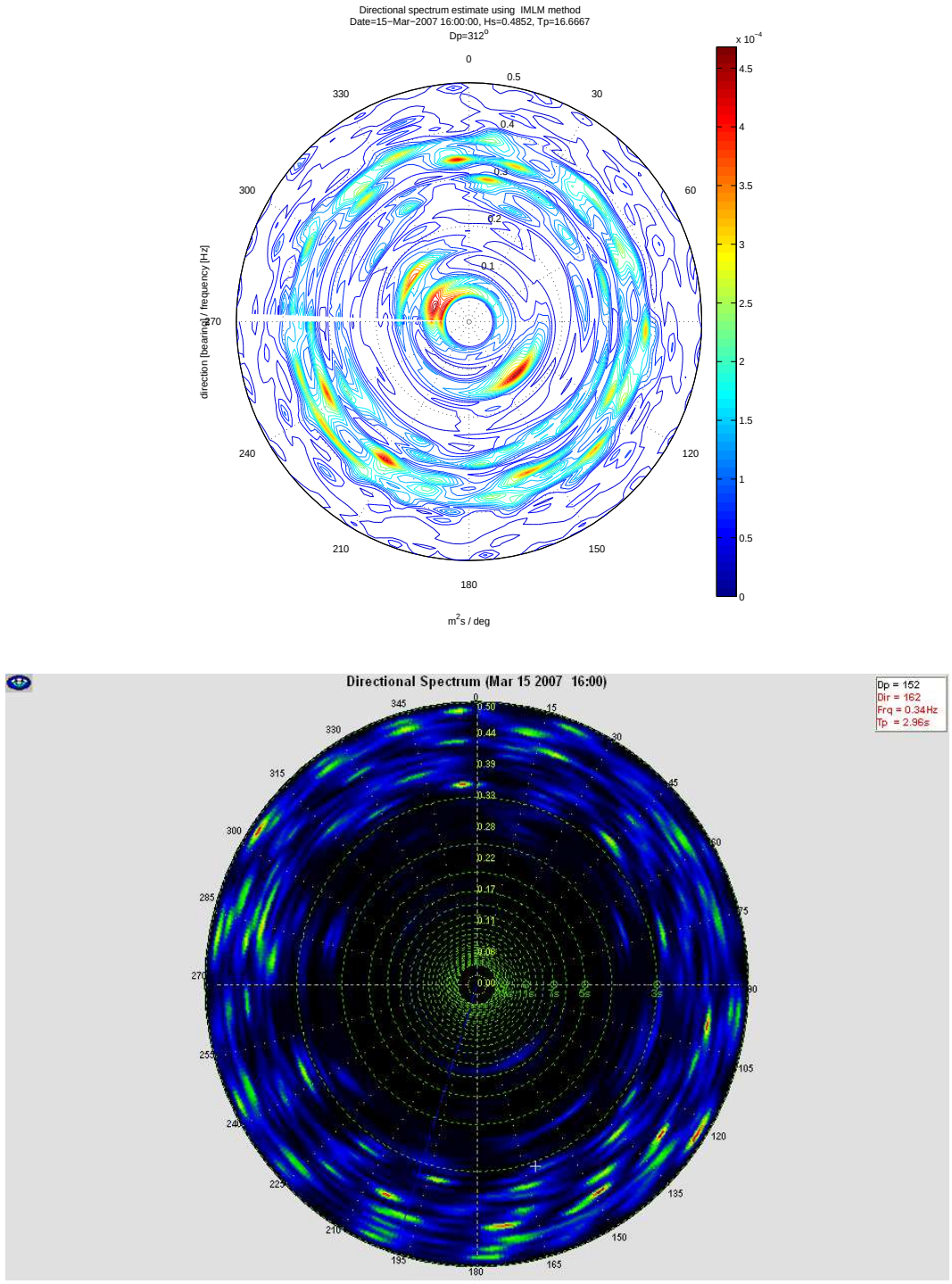

Figure D.5: Directional spectrum estimated using author's toolbox (upper) and RDI WavesMon (lower); 15 March 2007 16:00:00

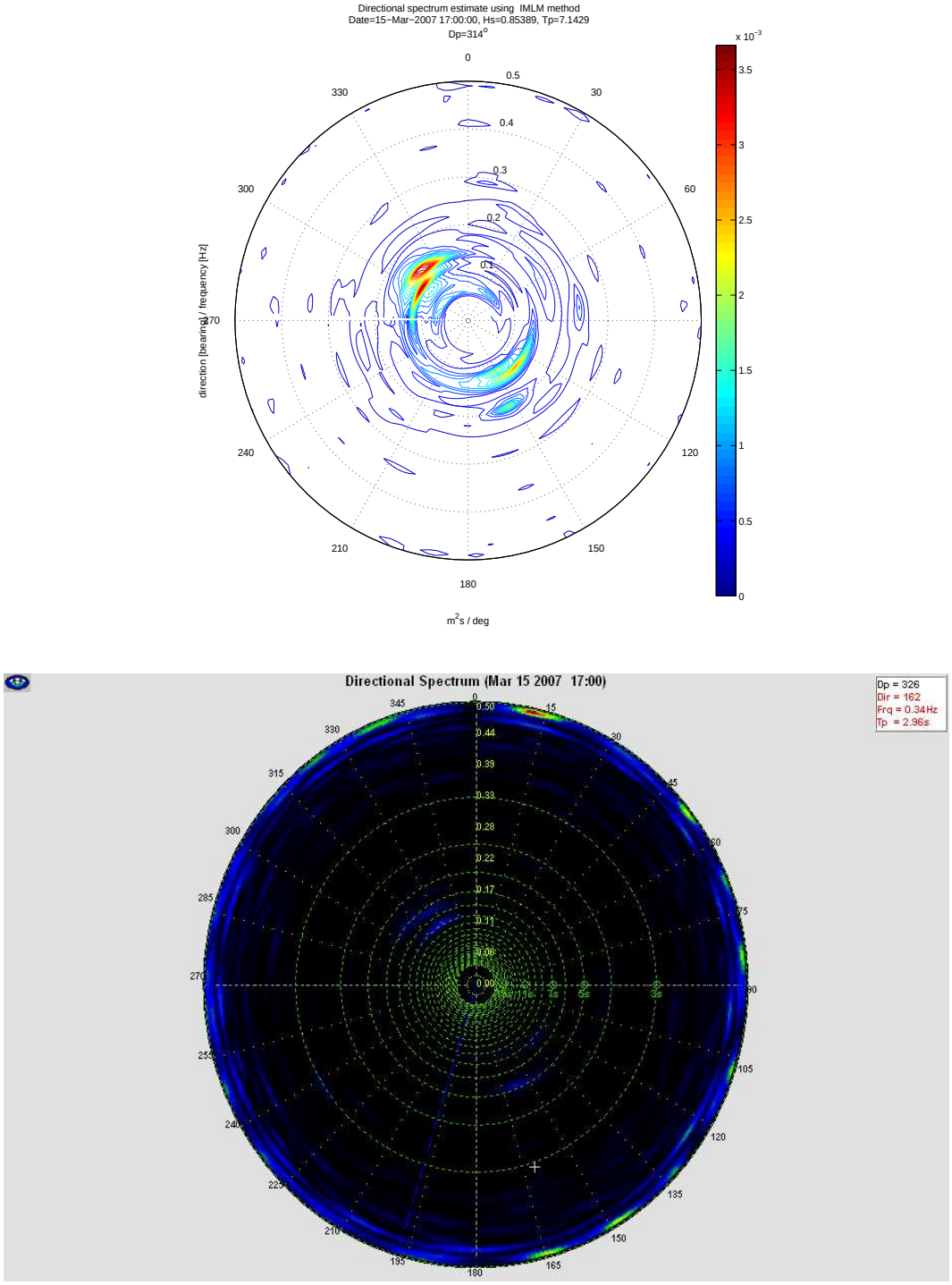

Figure D.6: Directional spectrum estimated using author's toolbox (upper) and RDI WavesMon (lower); 15 March 2007 17:00:00

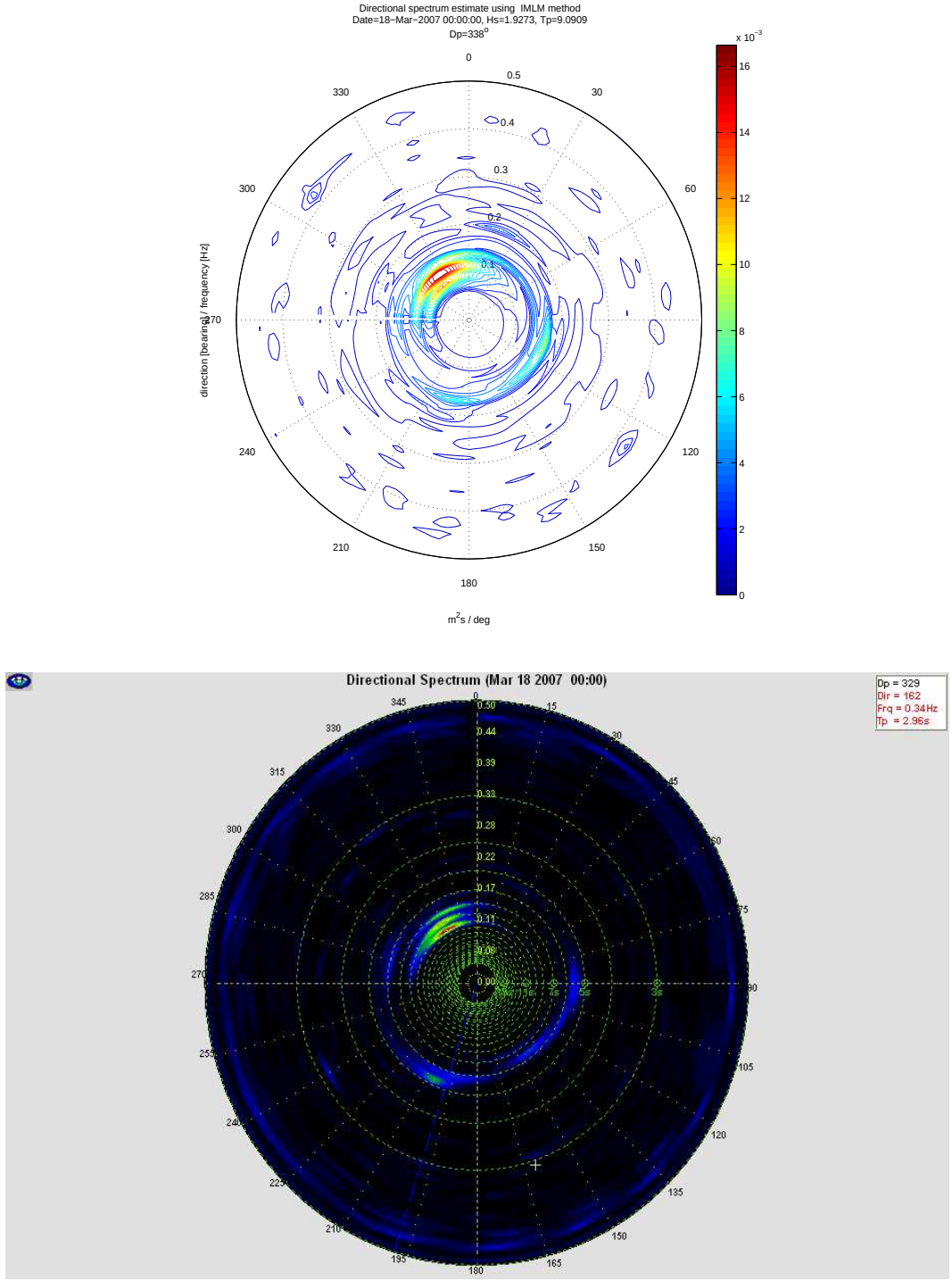

Figure D.7: Directional spectrum estimated using author's toolbox (upper) and RDI WavesMon (lower); 18 March 2007 00:00:00

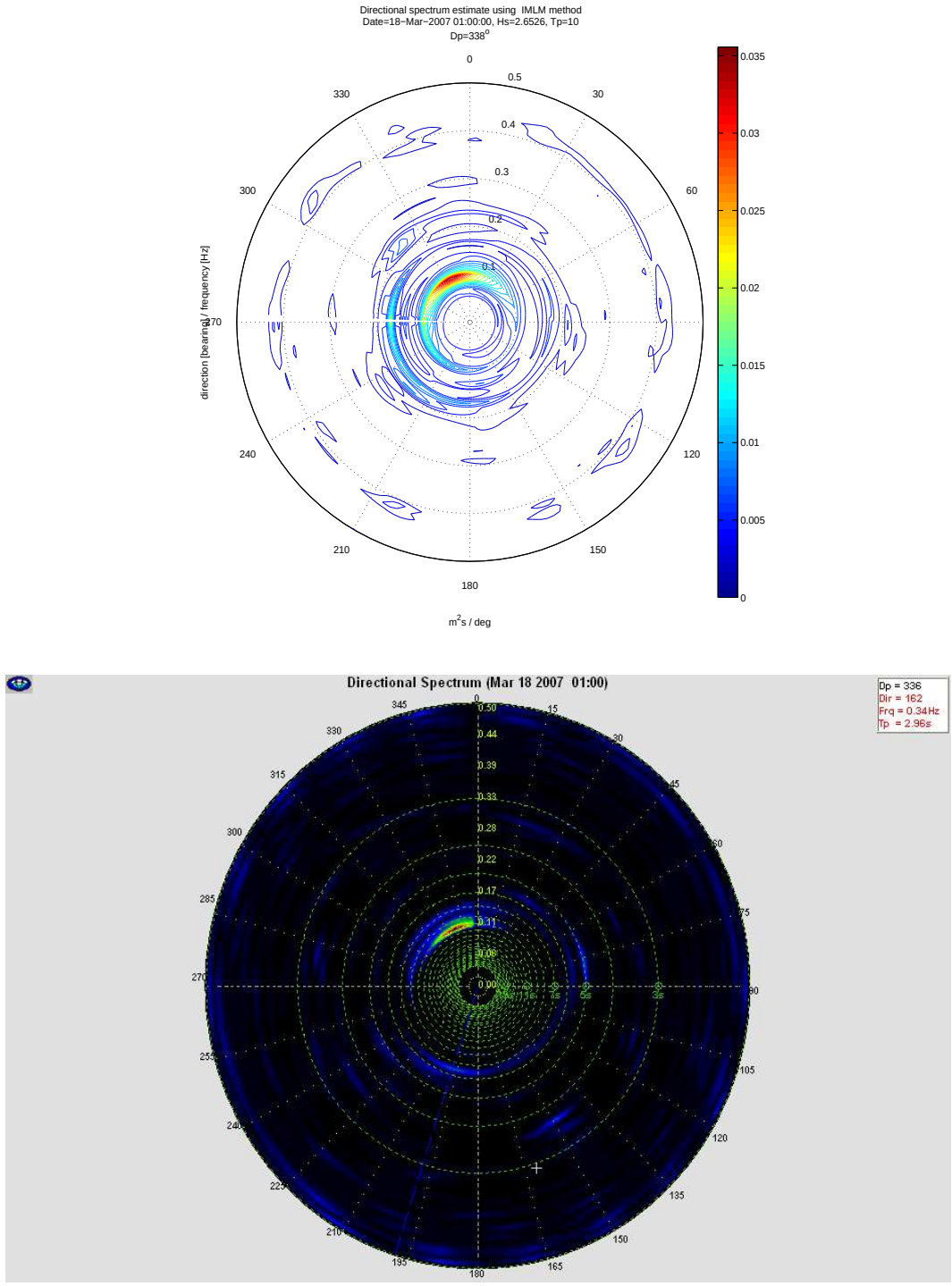

Figure D.8: Directional spectrum estimated using author's toolbox (upper) and RDI WavesMon (lower); 18 March 2007 01:00:00

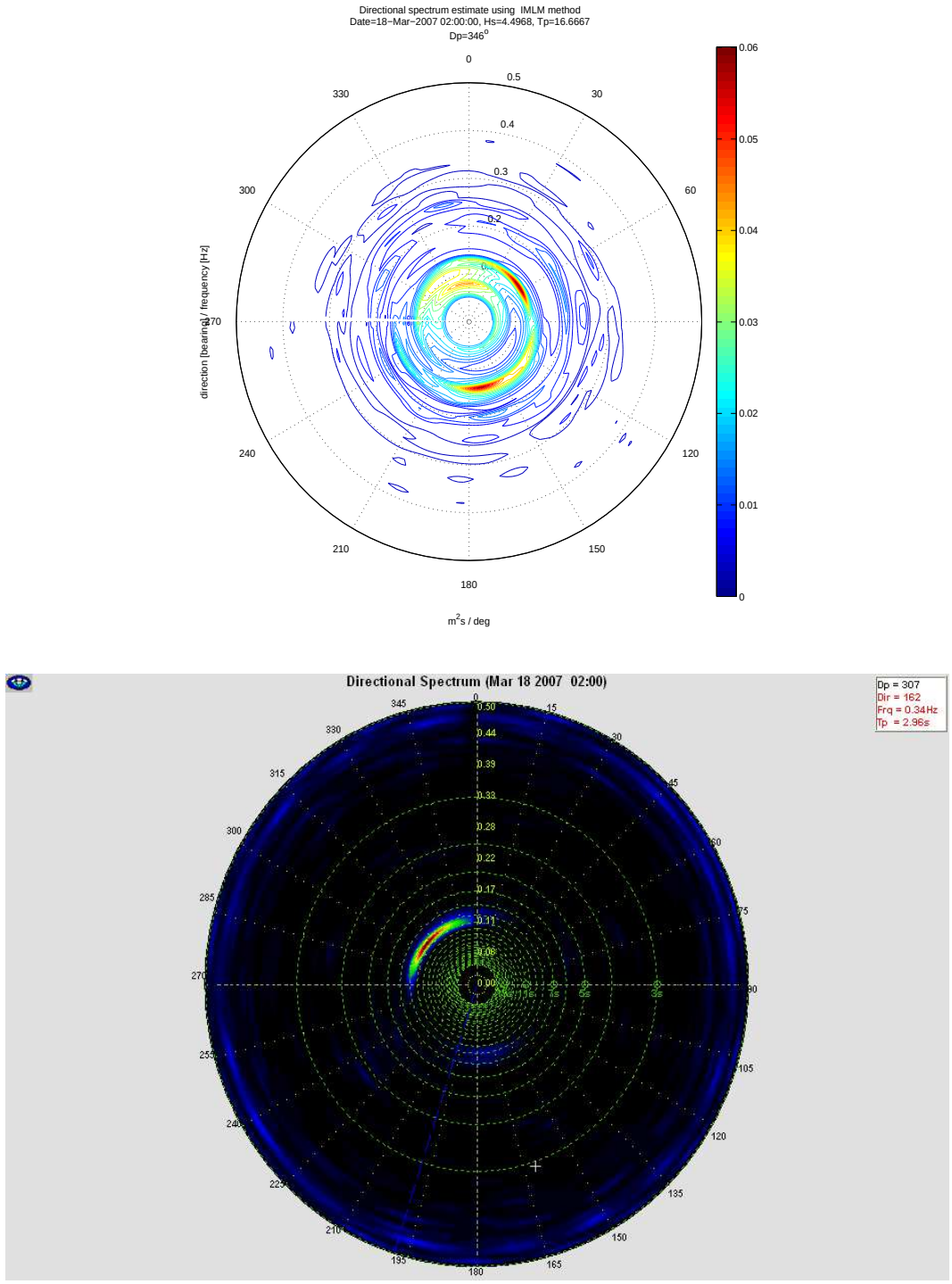

Figure D.9: Directional spectrum estimated using author's toolbox (upper) and RDI WavesMon (lower); 18 March 2007 02:00:00

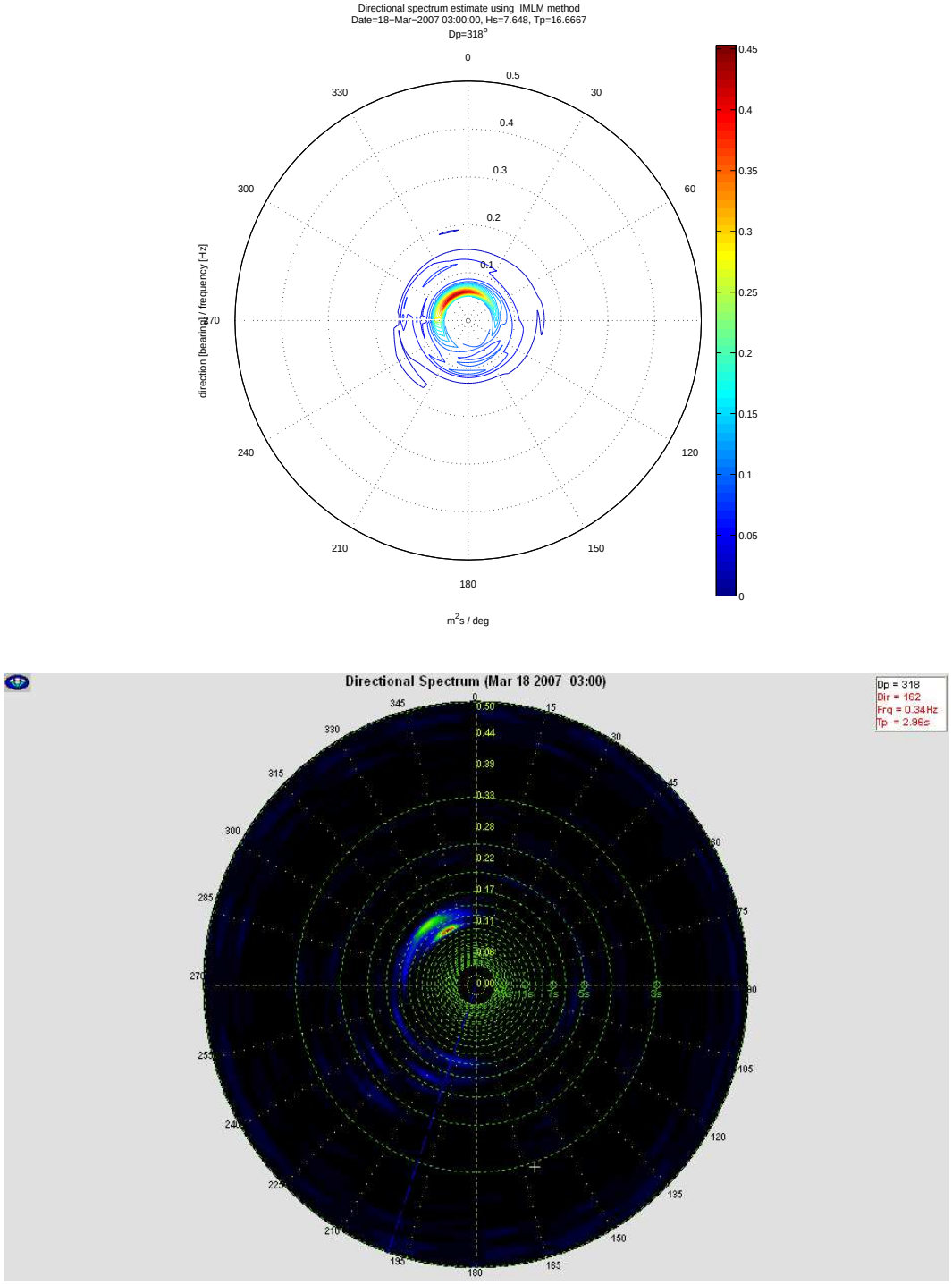

Figure D.10: Directional spectrum estimated using author's toolbox (upper) and RDI WavesMon (lower); 18 March 2007 03:00:00

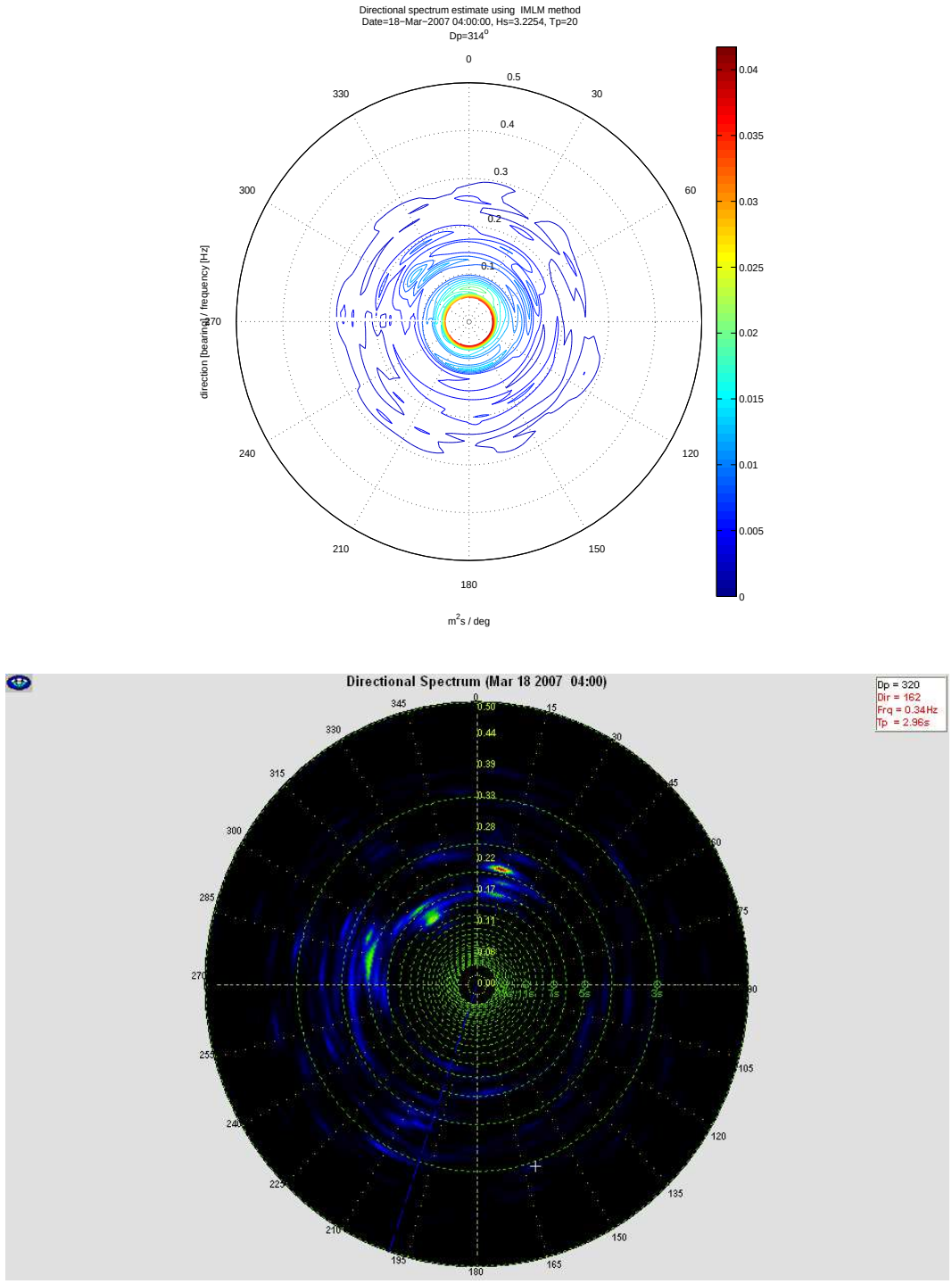

Figure D.11: Directional spectrum estimated using author's toolbox (upper) and RDI WavesMon (lower); 18 March 2007 04:00:00

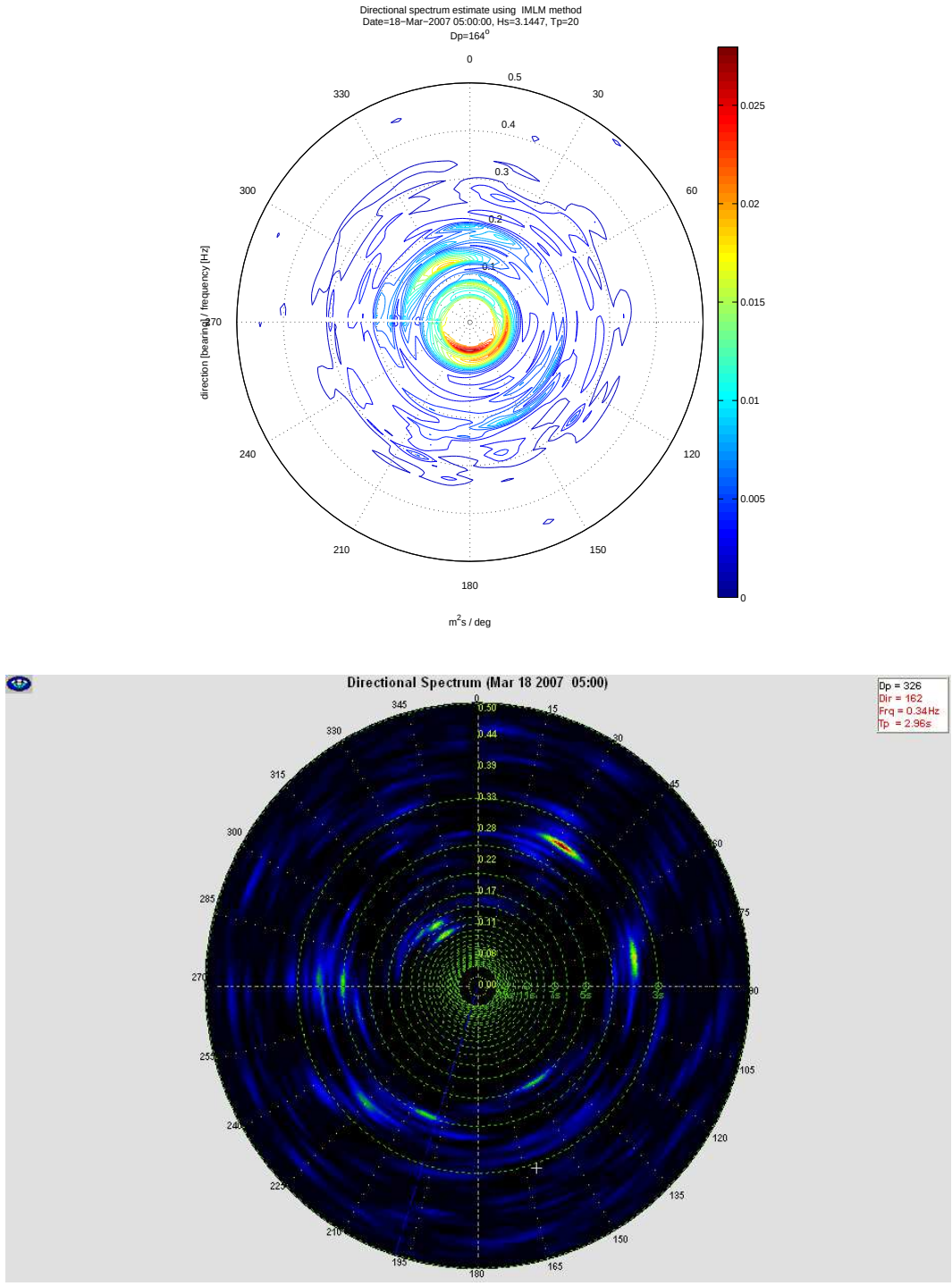

Figure D.12: Directional spectrum estimated using author's toolbox (upper) and RDI WavesMon (lower); 18 March 2007 05:00:00

Appendix E

Osalusi *et al.* (2009a)

E.1 **E. Osalusi, J. Side, R. Harris,** *Reynolds stress and turbulence estimates in bottom boundary layer of Fall of Warness*, **Int. Comm. Heat and Mass Transfer, 36, 5, 412-421, (2009)**

International Communications in Heat and Mass Transfer 36 (2009) 412–421

Contents lists available at ScienceDirect

International Communications in Heat and Mass Transfer

journal homepage: www.elsevier.com/locate/ichmt

Reynolds stress and turbulence estimates in bottom boundary layer of Fall of Warness☆

Emmanuel Osalusi *, Jonathan Side, Robert Harris

Renewable Energy Group, International Centre for Island Technology (ICIT), Institute of Petroleum Engineering, Heriot-Watt University, Old Academy, Back Road, Stromness, Orkney KW16 3AW, Scotland, United Kingdom

ARTICLE INFO

Available online 21 March 2009

Keywords:
Reynolds stress
Turbulent kinetic energy
ADCP
TKE production

ABSTRACT

A broadband acoustic Doppler current profiler (ADCP) moored on the seabed at 42 m depth has been used to observe the mean and turbulent flow components in the tidally energetic Fall of Warness channel over two tidal cycles. The Reynolds stress has been estimated from the difference in variance between the along-beam velocities of opposing acoustic beams. Near bed stress at 2.63 m above seabed (mab) exceeds 7.5 Pa at the time of mean flow (speed of ~1.3 m s^{-1}) while the ebb stresses are limited to ~3.31 Pa during the peak ebb, mean, flow of ~1.3 m s^{-1}. The production of turbulent kinetic energy (TKE), P was found to be negative below 2×10^{-9} W m^{-3} and up to 6×10^{-4} W m^{-3} was estimated during flood flows and decreasing to 3×10^{-4} W m^{-3}. The TKE dissipation rate ε was estimated by inertial dissipation method (IDM) with the greatest value of 2.43×10^{-2} W m^{-3} observed near the seabed around maximum ebb, falling to 5.75×10^{-5} W m^{-3} around slack water. The comparison between P and ε was performed by calculating individual ratios of P corresponding to ε using a bootstrap resampling technique. The study shows that the ratio ε/P averaged over whole flood and ebb were found to be ~0.4138 and ~0.4177, respectively, indicating that production exceeded dissipation. The uncertainties in Reynolds stress estimates due to instrument noise were found to be 3×10^{-4} Pa while 4.52×10^{-2} Pa can be attributed to the uncertainties due to the increase in the flow-related component.

1. Introduction

The global drive for renewable energy research and development arose from the need to; reduce green house effect, combat the inevitable decline, in traditional energy provision by fossil fuels and to reduce the level of environmental pollution due to energy production and consumption. Tidal current energy conversion systems have been noted as one of the viable technologies owing to other inherent predictability, reliability and minimal environmental impact. In addition, the natural resource is cheap and continuous. Unlike wind and solar energy, it is not considered weather dependent.

The World Offshore Renewable Energy Report 2002–2007, released by the Department of Trade and Industry, suggests that an estimated 3000 GW of tidal energy is available. Scottish Enterprise has estimated that, about 34% of UK electricity demand can be produced from tidal currents; this represents a huge untapped resource. Alternative energy sources hold the key towards the future, without them, energy crises are inevitable.

A typical site for a tidal current energy device is a challenging environment; exhibiting large scales of turbulent motion. A better understanding of the nature of turbulence in tidal channels is therefore, a key goal in the successful installation and operation of tidal energy devices. Understanding the structure of turbulence, will make it possible to be able to predict its appearance and possibly manage or control its influence. Large scale motion has been observed from previous work carried out on real flows and these may take the form of volumes of random motion or more organised vortices and shear flows. Rapid velocity changes within large scale turbulence imply that significant fluctuations in loading may be applied to a submerged tidal current energy device by such flow behaviour.

The design of modern marine current turbines is currently being driven by the extreme loads imposed upon the turbine. These loads come in two forms, both of equal importance to the design of a reliable turbine. The first comprises the extreme loads associated with the strongest tide and the second is the cyclic loads that continually pose a treat of fatigue damage to the turbine by turbulence in the inflow. As noted by Madsen et al. [1], the extreme loads during normal operation in turbulent conditions may exceed the design loads in wind turbine. The fatigue damage to critical components, such as the blades, is dominated disproportionately by the highest operating loads even though their rate-of-occurrence is relatively small. (Most of the flows occurring in nature are turbulent (McDonough [3])). Turbulence

☆ Communicated by W.J. Minkowycz.

* Corresponding author.
E-mail address: eo26@hw.ac.uk (E. Osalusi).

0735-1933/$ – see front matter © 2009 Elsevier Ltd. All rights reserved.
doi:10.1016/j.icheatmasstransfer.2009.02.004

Nomenclature

u_*	shear velocity, m s^{-1}
u	along-stream velocity, m s^{-1}
z	height above bed, m
v	across-stream velocity, m s^{-1}
P	TKE production, W m^{-3}
w	vertical velocity, m s^{-1}
A_z	Eddy viscosity, m^2 s^{-1}
S	TKE density, J m^{-3}
b_i	along-beam velocities, m s^{-1}
Re	Reynolds number, $\Omega r^2/v$
$\ddot{u}, \ddot{v}, \ddot{w}$	velocities instrument coordinate system, m s^{-1}
k	wavenumber
f	frequency
$\bar{u}$	mean velocity, m s^{-1}
M	ensemble number
$\bar{u}$	mean velocity, m s^{-1}
$\overline{x_i'^2}$	along-beam velocity variance due to turbulent fluctuations

Greek symbols

τ	shear stress, Pa
μ	dynamic viscosity, N s m^{-2}
τ_b	bed shear stress, Pa
ρ	fluid density, kg m^{-3}
τ_x	along-stream vertical turbulent stress, Pa
τ_y	across-stream vertical turbulent stress, Pa
ε	TKE dissipation, W m^{-3}
θ	beam angle, °
ϕ_1	pitch angle, °
ϕ_2	roll angle, °
γ	constant
α	Kolmogorov constant
σ_b^2	along-beam velocity variance due to instrument noise
σ_{st}	Reynolds stress uncertainties, Pa
σ_{sh}	Shear estimate uncertainties, 1 s^{-1}
σ_{pr}	TKE production uncertainties, W m^{-3}

Subscripts

n	integer
i	integer

is a manifestation of the flow and originates in the instability of shear flows. It can be characterised by a rotational three-dimensional motion, which generates large gradients of velocity at small scales and therefore promotes dissipation of kinetic energy into heat. This makes turbulence a highly dissipative process and therefore a source of energy that must be present to maintain the process. In 1883 Osborne Reynolds published the first paper, which described the transition from laminar to turbulent flow. He concluded that the transition occurs at higher speeds, when Reynolds number (Re), which determines resistance to the flow, exceeds 1.3×10^{10} ($Re = UD/v$ where U is an average velocity in the water column, D is a stream distance, v is a kinematic viscosity) (Reynolds [2]).

In coastal boundary layers the transition from laminar to turbulent flow is affected several parameters: such as pressure distribution in the external flow, roughness of the seabed and the nature of disturbances. The presence of bed roughness favours the transition by decreasing the critical value of the Reynolds number. The existence of irregularities on the seabed gives rise to additional disturbances in the flow and, as a consequence, a lower degree of amplification is sufficient to effect a transition from laminar to turbulent flow. Another important parameter affecting the stability of the flow is density variation. When the flow has density stratification, turbulent mixing can be strongly affected. This is true especially in the vertical direction where the parcels of fluid must be moved against hydrostatic forces.

At high water velocities and because of edge effects and surface roughness of structures, given that water is a viscous fluid, flows in a marine current turbine system are turbulent, rather than laminar. The tendency of water molecules to resist shear forces, due to the presence of viscosity, causes them to move irregularly. The shear stresses within a flow field tear the fluid into highly energetic, irregular, and three-dimensional eddies, with scales ranging from the size of the flow passage down to unity (Miller [4]). These eddies exist randomly in space and time in turbulent shear flows (Nezu and Nakagawa [5]). Within a turbine system, it would be difficult to separate the effects of normal forces (that cause pressure) from tangential forces (that cause shear stress), but rather the fluid stress will be a combination of the two.

At the bottom of the ocean the water flowing above the seabed causes stress which extends into the water column. Near the bed, the velocity decreases due to the friction. The part of the flow where the velocity is affected by the bed is called the boundary layer. In the laminar boundary layer the velocity shear ($\partial u/\partial z$) increases linearly with increase in shear stress (τ):

$$\tau = \mu \frac{\partial u}{\partial z}, \tag{1}$$

where μ is the dynamic viscosity. At a sufficiently high Reynolds number the flow in the boundary layer becomes turbulent due to instability present in the flow. As a consequence the flow develops a highly random character with rapid irregular fluctuations of velocity in space and in time. The velocity at any point in space (u) can be described by its time average ($\bar{u}$) and fluctuating part (u'): $u = \bar{u} + u'$. It can be seen that the fluctuating parts of velocity vector give rise to additional stresses in the flow, called Reynolds stresses which increase with distance from the boundary and with the intensity of turbulence.

Therefore, a total shear stress in the turbulent bottom boundary layer is a product of viscous and Reynolds stress. It varies with height above the bed, but near the bed, reaches the constant value defined as the bed shear stress (τ_b). This parameter makes it possible to define a shear velocity (u_*) that represents the strength of turbulent velocity fluctuations near the bed: $u_* = \sqrt{\tau_b/\rho}$: $u_* \approx \sqrt{\overline{u'w'}}$. From experimental studies, for relatively smooth bottoms the friction velocity was found to be around 0.2 cm s^{-1} for flat bottoms (Chriss and Cadwell [6]), 1 cm s^{-1} when a surface swell occurred (Grant et al. [7]), and few cm s^{-1} when bottom roughness was present (Cacchione et al. [8]).

The measurement of turbulent parameters in tidal flows presents oceanographers with a difficult problem, since it is necessary to obtain rapid measurements of velocity at small spatial scales in an environment in which large stresses operate and where, away from the bottom boundary, there is no fixed reference for velocity measurement. Turbulent stresses, or Reynolds stresses, represent the transport of momentum by turbulence and thus can control the vertical structure of turbulent environmental flows. Knowledge of Reynolds stresses along with mean velocity profiles allows the eddy viscosity, the most common parameterization of vertical mixing due to turbulence, to be computed. In the shallow coastal ocean, measurement of Reynolds stresses is complicated by the presence of surface waves. Although for small-amplitude irrotational waves the horizontal and vertical components of wave orbital velocities are 90° out of phase and therefore should have zero covariance, very small tilts in sensor alignment, or real wave stress associated with a sloping bed, for example, lead to a covariance between horizontal and vertical velocities that can contaminate or even dominate Reynolds stress measurements. Additionally, waves often occupy the same frequency range as turbulence in the shallow coastal ocean, and therefore wave

contamination cannot be removed by simple frequency filtering. Lohrmann et al. [9] introduced a method for calculating Reynolds stress profiles from four-beam current profiler measurements using the difference between the velocity variances along opposing beams. Stacey et al. [10], Lu and Lueck [11], and Williams and Simpson [12] extended this work with analyses of the confidence in Reynolds stress measurements. The variance method has since been applied successfully in a number of studies of stratified tidal systems (Stacey et al. [13]; Rippeth et al. [14]; Fugate and Chant [15]). Comparisons with independent collocated Acoustic Doppler Velocimeter (ADV) measurements have validated the method (Souza and Howarth [16]; Nidzieko et al. [17]) and illustrated that the fast pinging rate mode 12 maintains accuracy while reducing noise relative to the single ping mode 1 (Nidzieko et al. [17]; Williams and Simpson [12]). Mode 12 is an operational mode that allows Teledyne RDI's ADCPs to measure fast flows in shallow gauging sites. It can measure a large range of flow velocities and uses smaller depth cells, making it capable of taking measurements in much shallower flows. It works by reducing the size of the depth cell, making it possible to measure the highly sheared profile of fast flows near boundaries. It 12 gets around this by increasing the ping rate, allowing the depth cell size to be small without increasing the averaging time or data noise [18]. However, application of the variance method to coastal seas has illustrated that the method fails in the presence of energetic surface waves (Rippeth et al. [19]; Howarth and Souza [20]; Souza and Howarth [16]).

The measurement of Bottom Boundary Layer (BBL) characteristics in the seas and oceans is necessary for researches into the main mechanisms of interaction between the bed and water column. The information about BBL structure and dynamics is important for the prediction of sediment cover formation and bottom geomorphology, vertical diffusion and bottom friction processes, as well as for completion of various engineering works near the bed and the execution of geological survey and provides important data for ecological projects. Despite the significance of the BBL for various modern geophysics topics, it remains the least investigated oceanographic studies. This is a consequence of the difficulties of measurement near to bed surfaces.

ADCPs are capable of measuring profiles of the current velocity by applying run-time windowing of backscattered acoustic pings along three, or four, beams pointing in different directions. Whereas normal-mode ADCP measurements evaluate the Doppler frequency shift of the backscattered signal to estimate the in-beam velocity of the scattering particles, the pulse-coherent mode evaluates the phase shift between the echoes of two subsequent pings, resulting in much higher measurement accuracy but shorter profiling ranges. With the assumption that the velocity is the same within the respective depth bins of each beam, a three-dimensional velocity vector can be constructed from the measured along-beam velocities of at least three beams. A typical beam geometry is such that the beams are inclined by 20°–30° to the vertical and are symmetrically arranged, within a horizontal plane projection (e.g. in a Janus configuration). Depending on the range from the instrument and the slant angle, the above assumption is equivalent to a velocity field that is horizontally homogeneous on the scale of a few meters. For the mean velocity field this is usually an appropriate assumption for most flows in natural water bodies; however, it is not valid for turbulent velocity fluctuations, the data basis of the Inertial Dissipation Method (IDM).

The IDM applicability had been tested (Locke and Wuest [21]) for estimating profiles of dissipation rates of turbulent kinetic energy from the three-dimensional current velocities measured by conventional ADCPs operated in pulse-coherent mode. The IDM is based on the existence of an inertial subrange in the wavenumber spectrum of velocity fluctuations and is a well established and widely accepted method to estimate dissipation rates from measured time series of two- or three-dimensional current velocities. A detailed outline of the procedure to calculate a three-dimensional current vector based on the measured in-beam velocities of a three-beam ADCP is given in Ref. [21]. For a four-beam ADCP the calculus is given, for instance, in Lu and Lueck [11]. For the same instrument, it was shown by Lu and Lueck [22] that the statistical properties of the measured in-beam velocity fluctuations can be used to estimate selected Reynolds stresses as well as a term that is related to the turbulent kinetic energy (TKE) density. This procedure, known as the variance method, was applied to a variety of oceanic systems (e.g., Lohrmann et al. [9]; Stacey et al. [10]; Rippeth et al. [14]). The application of the variance method, however, is restricted to ADCPs with at least four beams, as well as to highly energetic systems, such as tidal channels.

Thus, assuming an appropriate resolution and signal-to-noise ratio, ADCPs in principle allow determination of the in-beam components of the turbulent velocity fluctuations. However, due to the geometrical spreading of the acoustic beams it cannot be assumed that each beam measures the same fluctuation. Hence the calculus, which provides the three-dimensional velocity vector based on the measured in-beam velocities, fails and will result in incorrect estimates of the directions and magnitudes of the velocity fluctuations. Under the conditions of homogeneous within the beam area, it can be assumed that the statistical properties of the velocity fluctuations, such as their spectral energy distribution, are the same for all beams. The spectral properties also remain unaltered by the linear transformation from beam to orthogonal coordinates, and the IDM can be applied independently of the orientation and velocity fluctuations relative to the mean flow.

In the present paper we present ADCP observations of turbulence, principally profiles of the turbulent shear stress, showing the evolution of the tidal flow in a channel in the Fall of Warness throughout two tidal cycles, attempting to define important features of turbulence in unstratified tidal flows. The Reynolds stress has been estimated from the difference in variance between the along-beam velocities of opposing acoustic beams. The IDM was used to calculate the turbulent energy dissipation rate in a zero mean field, assuming the turbulent cascade follows a $-5/3$ law in the inertial subrange (Locke and Wuest [21]). In what follows, the turbulence methods and the general physical setting in which the measurements were made together with the estimates of uncertainty are outlined and discussed.

2. Study area and ADCP deployment

A 600-kHz four-beam broadband ADCP (RD Instruments Workhorse monitor) was deployed on the bottom, looking upward, in approximately 42 m (mean water depth) of water between 3 July and 10 July 2006. The instrument was programmed to operate in fast pinging mode 12, recording one velocity profile per second. Velocities were recorded in beam coordinates; that is, one along-beam velocity was obtained for each of the instrument's four acoustic beams. The survey was conducted approximately 4 km west of the Island of Eday in the Orkney Islands, the tidal test site at the Fall of Warness, (59°08.147N;2°48.391W) of the European Marine Energy center (EMEC). This location is characterised by high velocity marine currents which reach almost 4 m s^{-1} at spring tides and 2.5 m s^{-1} during neap tides.

The ADCP was mounted in a $\pm 20°$ gimbal to adjust for uneven bottoms. The instrument was slightly tilted with respect to the vertical which varied between 0° and 8° during the experiment because of scour around the frame. For an isotropic flow typical of the coastal ocean, 2° tilts resulted in no more than a 17% bias in stress estimate (Lu and Lueck [11]) and thus, 2° was used as a reasonable cutoff for a maximum instrument tilt. The ADCP bin size was 1 m, with the first bin 1.63 m above bottom. Tidal current was predominantly semi-diurnal. Current speeds regularly exceeded 2 m s^{-1} at the surface, and the majority of the velocity shear was near the seabed. The ambiguity velocity (the maximum allowable radial motion for phase measurements [18]) was set at 2 m s^{-1} and the standard deviation of the

uncertainty associated with each horizontal velocity estimate was 0.0393 m s^{-1}.

3. Governing equations

3.1. The variance method

A four-beam ADCP typically has two pairs of opposing transducers that emit acoustic pulses along beams. Along-beam velocities are calculated by the instrument firmware, from the Doppler shift in the sound signal returned to the transducers, yielding four along-beam velocities (b_1, b_2, b_3, b_4), defined to be positive toward the instrument. Beam velocities can be resolved into an orthogonal coordinate system that is fixed relative to the ADCP. We use the coordinate system defined by Lu and Lueck [11], where $\ddot{x}$ is the direction from beam 1 to beam 2, and $\ddot{y}$ is the direction from beam 3 to beam 4. Beam velocities (b_1, b_2, b_3, b_4), expressed in terms of velocities in the instrument coordinate system ($\ddot{u}$, $\ddot{v}$, $\ddot{w}$), are

$$\begin{aligned} b_1 &= -\ddot{u}\sin\theta - \ddot{w}\cos\theta \\ b_2 &= \ddot{u}\sin\theta - \ddot{w}\cos\theta \\ b_3 &= -\ddot{v}\sin\theta - \ddot{w}\cos\theta \\ b_4 &= \ddot{v}\sin\theta - \ddot{w}\cos\theta \end{aligned} \tag{2}$$

where θ is the half angle between opposing beams (20° for an RDI Workhorse ADCP). In the case of a perfectly level instrument, $\ddot{u}$ and $\ddot{v}$ correspond to horizontal velocities and $\ddot{w}$ corresponds to the vertical velocity. If an ADCP is tilted by a pitch angle ϕ_1 about the x axis (positive counterclockwise) or by a roll angle ϕ_2 about the y axis (positive counterclockwise), the transform from the instrument coordinate system ($\ddot{u}$, $\ddot{v}$, $\ddot{w}$), to a level coordinate system (u, v, w), is

$$\begin{bmatrix} u \\ v \\ w \end{bmatrix} = \begin{bmatrix} \cos\phi_2 & 0 & \sin\phi_2 \\ \sin\phi_1\sin\phi_2 & \cos\phi_1 & -\sin\phi_1\cos\phi_2 \\ -\cos\phi_1\sin\phi_2 & \sin\phi_1 & \cos\phi_1\cos\phi_2 \end{bmatrix} \begin{bmatrix} \ddot{u} \\ \ddot{v} \\ \ddot{w} \end{bmatrix}. \tag{3}$$

For small ϕ_1 and ϕ_2 this expression can be simplified using Taylor expansions. Retaining only terms to first order in ϕ_1 and ϕ_2 yields

$$\begin{bmatrix} u \\ v \\ w \end{bmatrix} = \begin{bmatrix} 1 & 0 & \phi_2 \\ 0 & 1 & -\phi_1 \\ -\phi_2 & \phi_1 & 1 \end{bmatrix} \begin{bmatrix} \ddot{u} \\ \ddot{v} \\ \ddot{w} \end{bmatrix}. \tag{4}$$

Inverting this equation gives an expression for ($\ddot{u}$, $\ddot{v}$, $\ddot{w}$) in terms of the coordinates (u, v, w):

$$\begin{bmatrix} \ddot{u} \\ \ddot{v} \\ \ddot{w} \end{bmatrix} = \begin{bmatrix} 1 & 0 & -\phi_2 \\ 0 & 1 & \phi_1 \\ \phi_2 & -\phi_1 & 1 \end{bmatrix} \begin{bmatrix} u \\ v \\ w \end{bmatrix}. \tag{5}$$

In the absence of waves, each component of the velocity can be decomposed into a mean (e.g., $\bar{u}$) associated with slowly varying flow and into a fluctuation (e.g., u') associated with turbulence. Mean values are calculated over an appropriate time interval (e.g., 20 min) for which the flow is statistically stationary. If each quantity in Eq. (3) is decomposed in this way, it can be shown (Lohrmann et al. [9]; Stacey et al. [10]) that

$$\frac{\tau_x}{\rho} = \overline{\ddot{u}'\ddot{w}'} = \frac{\overline{b_3'^2} - \overline{b_4'^2}}{4\sin\theta\cos\theta} \tag{6}$$

$$\frac{\tau_y}{\rho} = \overline{\ddot{v}'\ddot{w}'} = \frac{\overline{b_1'^2} - \overline{b_2'^2}}{4\sin\theta\cos\theta}. \tag{7}$$

This is the variance method for calculating Reynolds stresses from ADCP beam velocities. Substituting the transformation in Eq. (5) into Eqs. (6) and (7) yields

$$\frac{\tau_x}{\rho} = \overline{u'w'} = \frac{\overline{b_3'^2} - \overline{b_4'^2}}{4\sin\theta\cos\theta} + \phi_2\left(\overline{u'^2} - \overline{w'^2}\right) - \phi_1\overline{u'v'}. \tag{8}$$

$$\frac{\tau_y}{\rho} = \overline{v'w'} = \frac{\overline{b_1'^2} - \overline{b_2'^2}}{4\sin\theta\cos\theta} - \phi_1\left(\overline{v'^2} - \overline{w'^2}\right) + \phi_2\overline{u'v'}. \tag{9}$$

where ρ is the water density, θ is the angle each beam of the ADCP makes with the vertical ($\theta = 20°$ for the RDI Workhorse used here). The second and the third terms of Eqs. (8) and (9) are the bias introduced to Reynolds stress estimates by instrument tilt in the absence of waves. The turbulent kinetic energy $q^2/2 = \left(\overline{u^2} + \overline{v^2} + \overline{w^2}\right)/2$ cannot be computed with data from either ADCP without additional assumptions. Defining $\xi = \overline{w'^2}/q^2$ and

$$S = \frac{1}{4\sin^2\theta}\sum_{i=1}^{4}\overline{b_i'^2} = \frac{1}{2}\left(\overline{u'^2} + \overline{v'^2}\right) + \overline{w'^2}\cot^2\theta, \tag{10}$$

for the four-beam ADCP e.g., Lohrmann et al. [9] allows the TKE to be expressed as

$$\frac{q^2}{2} = \frac{S^2}{1 + \xi(2\cot^2\theta - 1)}. \tag{11}$$

Computing TKE with Eq. (11) requires a value of ξ to be assumed. Lohrmann et al. [9] argued that $\overline{w'^2} < \left(\overline{u'^2} + \overline{v'^2}\right)/2$, and thus that isotropy ($\xi = 1/3$) would be a limiting case. For their measurements in a tidal, unstratified channel flow, Stacey et al. [10] used measurements of Nezu and Nakagawa [5], which yield $\xi = 0.17$. This value was used here.

The rate at which energy is transferred from the mean flow to TKE through the interaction of the turbulence with the shear is estimated from the product of the Reynolds stress and the velocity shear according to Rippeth et al. [19]

$$P = -\rho\left(\overline{u'w'}\frac{\partial\bar{u}}{\partial z} + \overline{v'w'}\frac{\partial\bar{v}}{\partial z}\right), \tag{12}$$

where both the stress and velocity shear are estimated from the ADCP data. As a result of the alignment of the ADCP to the tidal flow, we would expect the main contribution to the rate of production to come from the second term on the right-hand side of Eq. (12). The estimate of the vertical viscosity coefficient A_z can be can be calculated from the TKE production rate and the magnitude of shear, that is, (Lu and Lueck [22])

$$A_z = \frac{1}{\rho}\frac{P}{\left[\left(\frac{\partial\bar{u}}{\partial z}\right)^2 + \left(\frac{\partial\bar{v}}{\partial z}\right)^2\right]}. \tag{13}$$

The sign of A_z is the same as P. It should be noted that the estimates of A_z are subject to large uncertainties, particularly when the magnitudes of shear are small.

3.2. Estimates of turbulent kinetic energy dissipation

The TKE dissipation rate ε is a very important parameter and cannot be neglected when considering the turbulence energy balance. This term is always positive and it is controlled by the largest scales of eddies (energy suppliers). Therefore the dissipation rate together with viscosity determines the velocity gradients and size of dissipative scales. At high enough Reynolds numbers, turbulent energy dissipates due to an energy cascade from larger to smaller eddies (Bradshaw [24]). Firstly, the kinetic energy is transferred from the mean flow and large scale eddies are formed. The large eddies continuously supply the energy to the small eddies, which then transfer it to even smaller eddies and so on. The

energy is then dissipated into heat by the smallest scales of turbulent eddies. In this study, IDM is adopted to estimate the rate of TKE dissipation. This method is based on the assumption that if the wavenumbers at which the turbulent energy is produced and dissipated are well separated, (the region of separation is known as the inertial subrange) the flux of energy from low to high wavenumber is equal to the dissipation rate, as there are no sinks or sources of energy within the wavenumbers of the subrange (Locke and Wuest [21]).

There, the spectra often show the characteristic $k^{-5/3}$ slope as a function of the wavenumber k. In homogeneous turbulent flow and with the assumption of isotropy, the diagonal components ϕ_i ($i=1,\ldots,3$) of the associated spectrum tensor, in a given direction within this range, is given by:

$$\phi_i = \alpha_i \varepsilon^{2/3} k^{-5/3}. \tag{14}$$

The index i refers to the along-stream ($i=1$) and cross-stream ($i=2,3$) components of the spectrum tensor, and α_i refers to the one-dimensional Kolmogorov constant α_k ($\alpha_1=\alpha_k$, $\alpha_2=\alpha_3=4/3\alpha_k$). Eq. (14) can be estimated from frequency f by means of the frozen-turbulence hypothesis ($k=2\pi f/\bar{u}$) (Locke and Wuest [21]), as

$$\phi_i = \alpha \varepsilon^{2/3} \left(\frac{2\pi}{\bar{u}}\right)^{-2/3} f^{-5/3} \tag{15}$$

where $\bar{u}$ is the mean velocity in the i direction. By applying Taylor's hypothesis, ϕ_i is calculated from the measured time series of the three-dimensional velocity, and thus ε is estimated by spectral fitting (e.g., Gross and Nowell [23]; Locke and Wuest [21]).

Since ADCPs do not resolve the directions of the turbulent velocity fluctuations, along-stream and cross-stream velocity spectra cannot be separated. Thus the isotropy constant α_i in Eq. (15) remains undetermined within the range $\alpha_k \le \alpha_i \le 4/3\alpha_k$. Using spectral fitting Eq. (15) leads to an uncertainty for the dissipation rate estimation of up to a factor of $(4/3)^{-3/2} \approx -0.65$, which is well within the range of uncertainties of conventional methods (e.g. Locke and Wuest [21]).

Segments of the measured time series of the velocities at all depths were first analyzed for the mean current direction and speed. Wavenumber spectra were calculated from the measured in-beam velocities and averaged over the four beams. Segment sizes were 1024 samples (17 min). If the spectra exhibited an inertial subrange, a straight line representing a $-5/3$ slope was fitted to a double logarithmic spectrum plot, and ε was estimated by rearranging Eq. (15) using a Kolmogorov constant $\alpha_k = 1.56 \times 18/55$ for the streamwise spectral component (Wolk et al. [25]).

3.3. Variance method uncertainties

The level of uncertainty in stress estimates is determined by instrument noise, velocity variability, and averaging. Lu and Lueck [22] present useful statistical methods for determining uncertainty, using either bootstrap or random lag covariance approaches. The latter approach is also discussed by Rippeth et al. [19]. A semi-empirical equation for the standard error (σ_{st}) in stress estimates was derived by Williams and Simpson [12] as:

$$\sigma_{st}^2 = \rho^2 \gamma \left(\frac{\sigma_b^2 + \overline{x_i'^2}}{M \sin^2 2\theta}\right)^2, \tag{16}$$

where σ_b^2 is the variance in beam velocity due to instrument noise, $\overline{x_i'^2}$ is the variance due to velocity variability, M is the number of samples

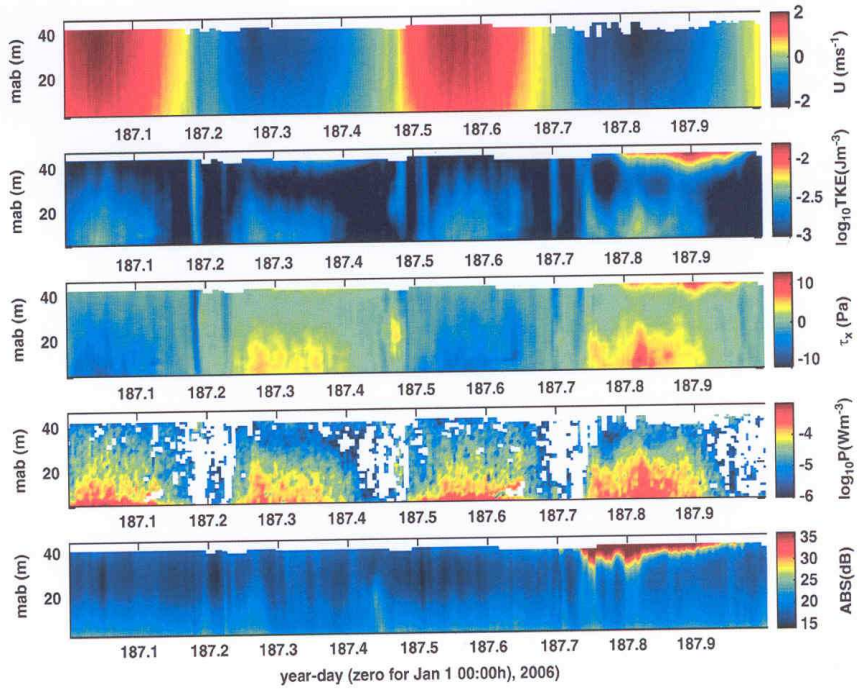

Fig. 1. Depth–time series of (a) along-stream velocity (m s^{-1}), (b) TKE density (J m^{-3}), (c) Reynolds stress (Pa), (d) TKE production (W m^{-3}) and (e) acoustic backscatter signal strength (dB); (a...e) = (first...last panel).

in a variance computation period (1200 samples was used in this study).

Williams and Simpson's [12] proposed uncertainty in shear estimates is computed as

$$\sigma_{sh} = \gamma_s \frac{\left(\mathrm{var}\left[u_{2(n+1)} - u_{1(n+1)} - u_{2(n-1)} + u_{1(n-1)}\right]\right)}{4M(\Delta z)^2 \sin^2\theta}. \quad (17)$$

It should be noted that the assumption that the vertical velocity is the same in both beams will increase the calculated variance if the two vertical velocities are not the same; hence, Eq. (17) will tend to overestimate the variance of the shear. It is readily seen from this equation that the uncertainty in the shear can be reduced by increasing the number of ensembles to be averaged. It can also be reduced by increasing the depth cell size, at the expense of the vertical resolution. The error in the estimates of rate of shear production can be determined using the formula for the variance of a product. For two independent variables, this is

$$\sigma_{pr}^2 = (\overline{u'w'})^2 \sigma_{sh}^2 + \left(\frac{\partial u}{\partial z}\right)^2 \sigma_{st}^2 + \sigma_{st}^2 \sigma_{sh}^2. \quad (18)$$

For the low-flow case, $\overline{u'w'} \to 0$ and $(\partial u/\partial z) \to 0$, so it is expected that the last term will dominate. The other two terms are expected to dominate at times of higher flow. However, there are a number of limitations of our observational method, which should be born in mind in interpreting the data. A region close to the bed and another close to the surface cannot be sampled because of acoustic constraints. In addition, the vertical bin size of 1 m limits the scale of eddy motions which can contribute to the variance.

4. Results and discussions

In the series of figures presented, white gaps occur in the following: (a) side-lobe contamination near the sea surface, (b) statistical non-homogeneity of b_i over the variance computation period, (c) statistical non-homogeneity of u, v and w over the distance between beams, (d) frequent values below the noise floor, (e) surface or internal wave bias, and (f) ADCP motion.

Figs. 1–5 show a summary of the processed one-day data during the observational period which indicate the general character of flow in the Fall of Warness flood and ebb tides. Velocity and stress data have been rotated into along and cross-channel components and it is the former which is presented here and in subsequent figures. Fig. 1 depicts contour plots for current velocity u, turbulent kinetic energy (TKE) intensity, Reynolds stress, τ_k, TKE production, P, and acoustic backscatter, ABS. The velocity at the surface reaches 2 m s^{-1} on the flood and ebb flows and decreases as depth increases. The velocity at 2.63 m above the bed Fig. 1a reaches 1.51 m s^{-1} on the flood with generally much stronger flows (1.56 m s^{-1} maximum) on the ebb. The data show a generally consistent behaviour over successive tidal cycles. The TKE intensity, Fig. 1b, the Reynolds stress Fig. 1c and the TKE production Fig. 1d all exhibit larger magnitudes on the ebb than the flood. It can be noted in Fig. 1c that the fluctuating parts of the velocity vector, u', arising from additional stress in the flow increase with distance from the bed together with the intensity of the turbulence. The TKE production rate (P) varied with velocity and maximum P coincides with the strongest flows. Production rates were highest near the bed where the frictional forces from the seabed were strongest. The P estimates miss the bottom 2.63 m due to the height of the bed frame and the blanking interval of the ADCP.

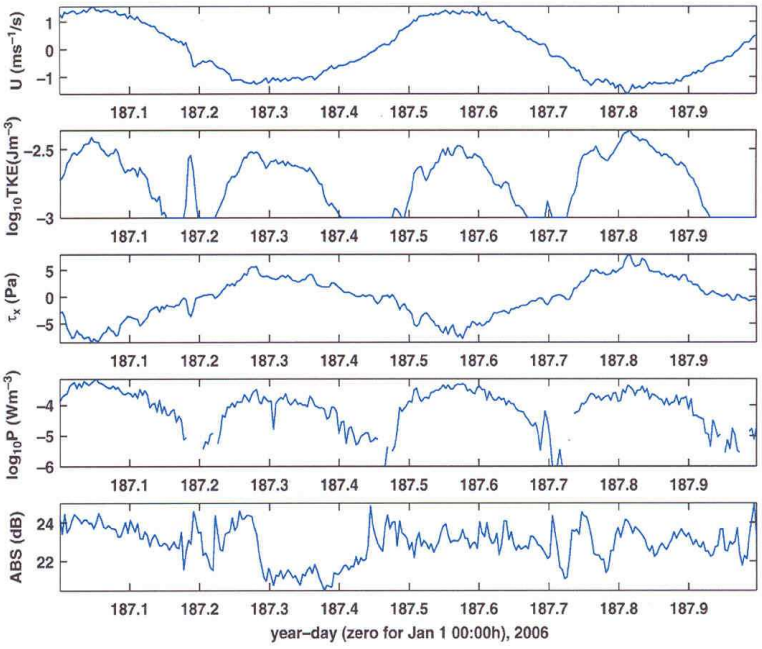

Fig. 2. Time series observation at 2.63 mab of (a) along current velocity (m s^{-1}), (b) TKE density (J m^{-3}), (d) Reynolds stress (Pa), (e) TKE production (W m^{-3}) and (f) acoustic backscatter; (a...f) = (first...last panel).

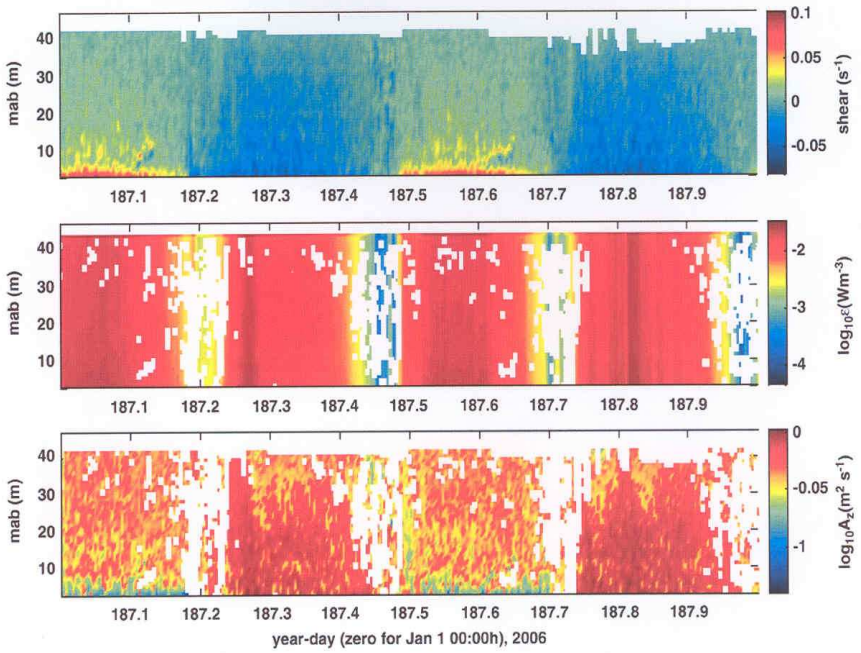

Fig. 3. Depth–time series of (a) vertical shear (s^{-1}), (b) TKE dissipation (W m^{-3}) and (c) turbulent viscosity (m^2 s^{-1}); (a...c) = (first...last panel).

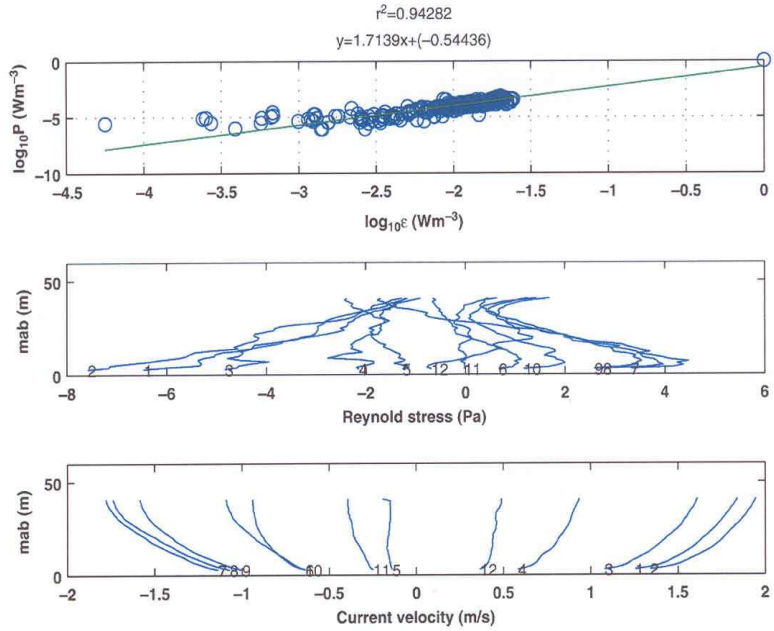

Fig. 4. (a) Scatter plot of TKE production and Reynolds stress. (b) Hourly mean current profiles (middle panel) and Reynolds stress (Pa) profiles (lower panel) for the 12 h of the experiment.

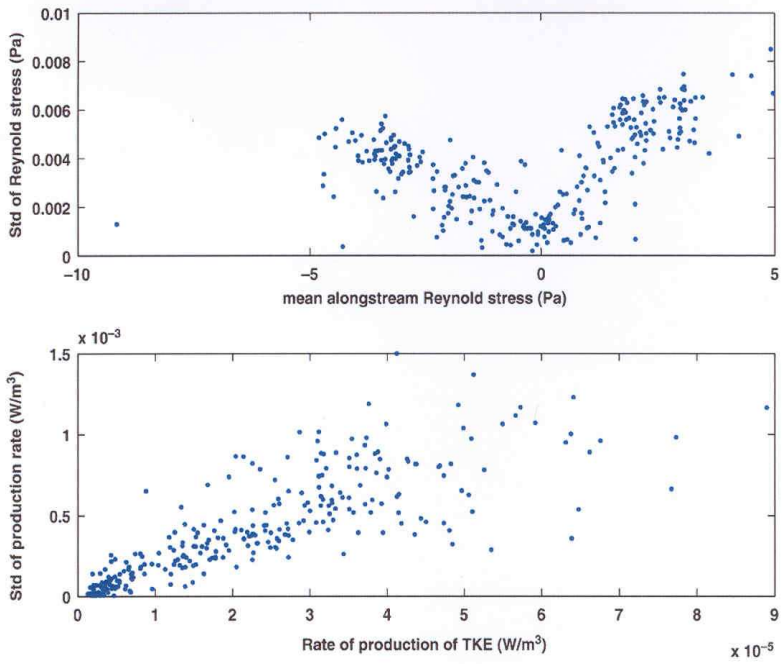

Fig. 5. The standard deviation of (a) Reynolds stress calculated plotted as a function of mean stress and (b) TKE production rate estimates plotted against the mean value of the TKE production rate (a...b) = (first...last panel).

The rate of TKE production, P at which energy is transferred from the mean flow to turbulent kinetic energy is estimated from the product of the Reynolds stress and the velocity shear. A contoured plot of P during the flood and ebb flow (Fig. 1d) that shows the highest rate of production is consistently found near the seabed (where the mean shear is maximum) with levels decreasing by about two orders of magnitude between the lowest and highest bins.

Near the bed (2.63 mab) at peak ebb flow, the maximum P exceeds ~2.99 W m^{-3} while lowest values occur at low water slack when production falls to ~2.2 W m^{-3}. Production rates of up to 6×10^{-4} W m^{-3} occurred on the flood tide, while on the ebb tide P was limited to 3×10^{-4} W m^{-3}. The noise threshold for the TKE production estimates was of the order 1.36×10^{-6} W m^{-3}. Contour plots of the time series of the vertical shear, rates of dissipation of turbulent kinetic energy and turbulent viscosity are given in Fig. 3. There is a semidiurnal variation ε which is clearly related to the phase of the tidal current. The largest values of ~2.43×10^{-2} W m^{-3} are observed near the seabed around maximum ebb, falling off -5.75×10^{-5} W m^{-3} around slack water. The eddy viscosity coefficient A_z is calculated by dividing P with the squares of the shear. The estimates of A_z Fig. 3c are subject to large uncertainties, particularly when the magnitudes of the shear are small (Eq. (13)). Fig. 3c indicates a variation of A_z with tidal flow, ranging from about ~0.12 m^2 s^{-1} during the weak flood to ~0.85 m^2 s^{-1} during the ebb. During the strong ebb between days 187.2 and 187.4, A_z is about ~0.84 m^2 s^{-1}. The turbulent viscosity increases with increasing height in the lower half of the water column, and reaches a maximum near mid-depth.

The upper panel of Fig. 4, estimated at 2.63 m above the seabed, compares the estimates of ε against the estimates of P. Fig. 4 (upper panel) shows the relationship between the rate of TKE production and the TKE dissipation rate. The two parameters track each other. Both flood and ebb data show a satisfactory fit ($r^2>0.94$) to a straight line with comparable slopes. Fig. 4 (middle and lower panel) gives a general impression of the cycle of stress variation over a semidiurnal cycle. The plot shows 1-h mean vertical stress profiles acting in the direction parallel to the direction of the tidal flow together with the corresponding along-stream current profiles. The stresses generally decrease more or less linearly from extreme values near the seabed (2.63 mab) to negligible values at the highest level observed (~1 m below the surface). The velocity profiles show maximum near surface flood flows of >1.8 m s^{-1}. (e.g., profiles 1 and 2) while the maximum near-surface ebb flows are ~1.8 m s^{-1}. (e.g., profiles 7, 8). The largest velocities are generally observed near the surface with the velocities in the lower part of the water column conforming to a logarithmic profile. During the flood, near-bed stress (height = 2.63 m above the seabed) exceeds ~7.5 Pa at the time of maximum depth mean flow speed (~1.3 m s^{-1}) while during the ebb stresses are limited to ~3.31 Pa during the peak ebb, depth mean, flow of ~1.13 m s^{-1}. Around slack water the stresses throughout the water column are close to zero. We noticed that around ebb high waters (e.g., profiles 5 and 11) there is negligible stress throughout the water column. There are exceptions with profiles that show high stress (1.25–1.69 Pa) in the upper part of the water column (e.g., profiles 7, 8 and 9). These occur during the latter part of the ebb flows. There are also profiles that show a linear increase in stress from values of ~−1.69 Pa (e.g. profile 12) to maximum (~1.35 Pa) in the middle of the water column, and decreases linearly to ~−0.69 Pa at the seabed. A further interesting observation is the curling back of the stress profile in the bottom two bins during maximum flow (e.g., profile 7), with a maximum stress of ~4.46 Pa observed at a height of 6.76 m above the seabed decreasing to (~3.31 Pa) at a height of 2.63 m above the seabed (mab).

Fig. 5 shows the standard deviation of the Reynolds stresses calculated from the observations using Eq. (16) plotted against the

associated Reynolds stress. The y intercept of the calculated Reynolds stress standard deviation plotted against the along-channel stress is proportional the instrument noise (Williams and Simpson [12]). Using a least squares fit, and calculating a standard deviation from Stacey et al. [13] (their Eqs. (26) and (28)), had a minimum uncertainty of $\sim 1.75 \times 10^{-4}$ Pa (Fig. 5). The linear regression equation obtained is

$$\sigma_{st} = 0.0020\tau_x + 0.0008. \quad (19)$$

By referring to Eq. (19), it is apparent that the uncertainty can be reduced by the combination of increasing the number of pings per ensemble, which reduces σ_b and hence σ_{st}, and increasing M, which also reduces σ_b. At higher stress levels, there are two components in the uncertainty in the Reynolds stress. These are the instrument noise component and the flow-related component due to turbulent motions. The gradient in the equation above represents the increase in the flow-related component of the uncertainty and is affected only by the number of ensembles used to estimate the stress. The standard deviation of the TKE production rate calculated from Eqs. (16)–(18) plotted against the production rate is shown in Fig. 5b. Williams and Simpson [12] showed that about 85% of the variance in the TKE production rate estimates is due to the second term in Eq. (18) $[\rho^2(\partial u/\partial z)^2\sigma_{st}^2]$ at times of high flow, with most of the remaining 15% due to the first term $[\rho^2\overline{uw}2\sigma_{sh}^2]$ and the last term $(\rho^2\sigma_{st}^2\sigma_{sh}^2)$ making a negligible contribution at least an order of magnitude smaller than either of the other two terms. At times of low flow, the last term is of the same order as the second term, and the first term is negligible. This indicates that in order to reduce the uncertainty in the estimates of the rate of turbulent production, we particularly need to reduce the uncertainty in the Reynolds stress estimates, σ_{st}^2. Since this involves increasing the number of ensembles, M, used to calculate the variance, it is apparent that σ_{sh}^2 will also be decreased by the same factor at times when turbulent fluctuations dominate over instrument noise. The ratio of the rates of dissipation to production of turbulent kinetic energy has been calculated by calculating individual ratios of P corresponding to ε for flood (day 187.0–187.15) and ebb (day 187.25–187.40) following the removal of P estimates made during periods when the stress estimates are unreliable (i.e., around slack water, near the surface). The error shown is the 95% confidence limits of the ratios calculated using a bootstrap resampling technique of Lu and Lueck [22]. During the tidal cycle the ratios of ε/P on the flood and ebb, 0.4138, and 0.4177, are not significantly different from one another. This reported ratio indicates that the production exceeded dissipation, which has a significant deviation from the expected, theoretical value of unity. Previous studies also showed a deviation of ε/P ratio from unity which was much greater than reported here (Lu and Lueck [11]; Rippeth et al. [14]). This discrepancy is considerably less than those reported for other comparisons of in situ measurements of marine turbulence. For example, Lu and Lueck [11] found $\varepsilon/P \sim 0.2$ for mid-water column estimates of P using the variance method and ε measured at one height using a moored velocity shear probe. However, the difference between the ε/P estimates and unity could be caused by errors associated with the methods used in this research to estimate both parameters. For example, Stacey et al. [13] proposed a method for examining the assumption about temporal stationarity of the flow of the flow and velocity variances using an ADCP.

Additional bias in the ADCP measurements may be due to its vertical resolution. The greater the bin size the greater the error in the velocity fluctuation caused by the ADCP spatial averaging within its bins. The depth cell size chosen for the studies was 1 m. Near the boundary, as the length scale of the turbulent fluctuations decreases, some undersampling of the variance may result. Lu and Lueck [11] estimate that using a depth cell size of 1 m produces an underestimate of the Reynolds stress of 5% compared with a depth cell size of 0.1 m, and Rippeth et al. [14] estimate a loss of less than 5% when comparing depth cells of 0.5 and 0.25 m. It should also be noted that an additional effect of decreasing the depth cell size is to increase the instrument noise, which may have serious implications in a low energy regime.

5. Conclusions

A bottom-mounted ADCP moored at 1.63 m above the seabed, measured turbulence, flow in Fall of Warness tidal energetic site. The flow in the channel is mainly tidal and with peak speeds of $\sim 1\ m\ s^{-1}$. The data enable us to derive estimates of Reynolds stress, TKE density, the rates of TKE production and dissipation and eddy viscosity using the variance method. Depth–time variations of turbulence in the channel are revealed by measurements with the ADCP. The variation of the Reynolds stress with depth corresponds to the vertical structure of the mean shear. The along-stream component of the stress contains clear tidal variations. The production of turbulent kinetic energy is generally enhanced near the bottom, bearing the character of wall-bounded turbulence. The TKE density changes more strongly with time than with depth. The eddy viscosity has a maxima at mid-depth. The TKE dissipation was found to be greatest ($\sim 2.43 \times 10^{-2}$) near the bed when the fastest flow occurred. The results are useful in two ways. First, they provide a set of observations that define the cycles of the production and dissipation of TKE in an energetic seawater column. Second, they allow us to test the two techniques employed, since we would expect ε and P to closely track each other and covary with mean values that are equal. There is good agreement between the patterns of variation of P and ε. Both parameters closely track each other and follow a semidiurnal pattern. The comparison between P and ε was performed by calculating individual ratios of P corresponding to ε. The study found that the ratio ε/P averaged over whole flood and ebb were found to be ~0.4138 and ~0.4177, respectively, indicating that production exceeded dissipation.

Result from this study is of great importance in the deployment of marine energy devices in energetic environment like the Fall of Warness. This is because the velocity of the flow at a given location can vary greatly across the actuator area of the turbine. This could lead to significant variations in loading across the actuator and associated fatigue and vibration problems. Understanding the turbulence levels is important not only to the siting of individual units (e.g. avoiding areas with strongly stratified flow) but can also inform the device design. Understanding what these levels will be is important to setting realistic limits to design.

Acknowledgement

This work is based upon work funded by the TOTAL E&P (UK) PhD studentship research in Marine Renewable Energy. The authors would like to thank EMEC for providing the ADCP data.

References

[1] P.H. Madsen, K. Pierce, M. Buhl, Predicting ultimate loads for wind turbine design, 1999 ASME Wind Energy Symposium, 1999, p. 355.
[2] O. Reynolds, An experimental investigation of the circumstances which determine whether the motion of water shall be direct or sinuous, and of the law of resistance in parallel channels, Philos. Trans. R. Soc. Lond. 174 (1883) 935–982.
[3] J.M. McDonough, Introductory Lectures on Turbulence, Departments of Mechanical Engineering and Mathematics, University of Kentucky, 2004.
[4] D.S. Miller, Internal Flow Systems Design and Performance Prediction, 2nd edition, Gulf Publishing Company, Houston, Texas, 1990. 396 pp.
[5] I. Nezu, H. Nakagawa, Turbulence in Open-channel Flows, Balkema, Rotterdam, The Netherlands, 1993.
[6] T.M. Chriss, D.R. Cadwell, Universal similarity and the thickness of the viscous sublayer at the ocean floor, J. Geophys. Res. (1984) 6403–6414.
[7] W.D. Grant, A.J. Williams, S.M. Glenn, Bottom stress estimates and their prediction on the Northern California Continental Shelf during CODE-1, J. Phys. Oceanogr. 14 (1984) 506–527.
[8] D.A. Cacchione, D.E. Drake, G.B. Tate, J.T. Ferreira. Bottom stress estimates and sand transport on the northern California inner continental shelf American Geophysical Union, 75, 181, 1994.

[9] A. Lohrmann, B. Hackett, L.P. Roed, High resolution measurements of turbulence, velocity, and stress using a pulse-to-pulse coherent sonar, J. Atmos. Ocean. Technol. 7 (1990) 19–37.
[10] M.T. Stacey, S.G. Monismith, J.R. Burau, Observations of turbulence in a partially stratified estuary, J. Phys. Oceanogr. 29 (1999) 1950–1970.
[11] Y. Lu, R.G. Lueck, Using a broadband ADCP in a tidal channel. Part II: turbulence, J. Atmos. Ocean. Technol. 16 (1999) 1568–1579.
[12] E. Williams, J.H. Simpson, Uncertainties in estimates of Reynolds stress and TKE production rate using the ADCP variance method, J. Atmos. Ocean. Technol. 21 (2004) 347–357.
[13] M.T. Stacey, S.G. Monismith, J.R. Burau, Measurements of Reynolds stress profiles in unstratified tidal flow, J. Geophys. Res. 104 (C5) (1999) 10 933–10 949.
[14] T.P. Rippeth, E. Williams, J.H. Simpson, Reynolds stress and turbulent energy production in a tidal channel, J. Phys. Oceanogr. 32 (2002) 1242–1251.
[15] D.C. Fugate, R.J. Chant, Near-bottom shear stresses in a small, highly stratified estuary, J. Geophys. Res. 110 (2005) C03022, doi:10.1029/2004JC002563.
[16] A.J. Souza, M.J. Howarth, Estimates of Reynolds stress in a highly energetic shelf sea, Ocean Dyn. 55 (2005) 490–498.
[17] N.J. Nidzieko, D.A. Fong, J.L. Hench, Comparison of Reynolds stress estimates derived from standard and fastping ADCPs, J. Atmos. Ocean. Technol. 23 (2006) 854–861.
[18] www.rdinstruments.com.
[19] T.P. Rippeth, J.H. Simpson, E. Williams, M.E. Inall, Measurement of the rates of production and dissipation of turbulent kinetic energy in an energetic tidal flow: Red Wharf Bay revisited, J. Phys. Oceanogr. 33 (2003) 1889–1901.
[20] M.J. Howarth, A.J. Souza, Reynolds stress observations in continental shelf seas, Deep-Sea Res., II 52 (2005) 1075–1086.
[21] A. Locke, A. Wuest, Application of coherent ADCP for turbulence measurements in the bottom boundary layer, J. Atmos. Ocean. Technol. 22 (11) (2005) 1821–1828.
[22] Y. Lu, R.G. Lueck, Using a broadband ADCP in a tidal channel. Part I: mean flow and shear, J. Atmos. Ocean. Technol. 16 (1999) 1556–1567.
[23] T.F. Gross, A.R.M. Nowell, Mean flow and turbulence scaling in a tidal boundary layer, Cont. Shelf Res. 2 (1983) 1109–1126.
[24] P. Bradshaw, An Introduction to Turbulence and Its Measurement, Pergamon Press, Oxford, 1971.
[25] F. Wolk, H. Yamazaki, L. Seuront, R.G. Lueck, A new free-fall profiler for measuring biophysical microstructure, J. Atmos. Ocean. Technol. 19 (2002) 780–793.

Appendix F

Osalusi *et al.* (2009b)

F.1 **E. Osalusi, J. Side, R. Harris,** *Structure of turbulent flow in EMECs tidal energy test site*, **Int. Comm. Heat and Mass Transfer, 36,5, 422-431, (2009)**

International Communications in Heat and Mass Transfer 36 (2009) 422–431

Contents lists available at ScienceDirect

International Communications in Heat and Mass Transfer

journal homepage: www.elsevier.com/locate/ichmt

Structure of turbulent flow in EMEC's tidal energy test site☆

Emmanuel Osalusi *, Jonathan Side, Robert Harris

Renewable Energy Group, International Centre for Island Technology (ICIT), Institute of Petroleum Engineering, Heriot-Watt University, Old Academy, Back Road, Stromness, Orkney KW16 3AW, Scotland, United Kingdom

ARTICLE INFO

Available online 25 March 2009

Keywords:
ADCP
TKE production
TKE dissipation
Turbulent viscosity

ABSTRACT

Measurements of bulk turbulent parameters (Kinetic energy, dissipation rates, Reynolds stress, etc.) were performed in the bottom boundary layer of the European Marine Energy Centre (EMEC) tidal test site using Acoustic Doppler Current Profilers (ADCPs). Flood and ebb currents exceed 1.4 ms−1 near the seabed (at 2.63 mab) and generate >7 Pa stresses. The production of turbulent kinetic energy (TKE) P, was found to be negative below 2×10^{-9} Wm^{-3} and, of up to 5×10^{-4} Wm^{-3} was estimated during flood flows and decreasing to 10^{-5} Wm^{-3} during slack water. The TKE dissipation rate ε was estimated using the structure function method with greatest value of up to 5×10^{-1} Wm^{-3} near the seabed around maximum flood, falling to 4×10^{-3} Wm^{-3} around slack water. The comparison between P and ε was performed by calculating individual ratios of P corresponding to ε using a bootstrap resampling technique. The study shows that the ratio ε/P averaged over whole flood and ebb were found to be ~0.3553 and ~0.3266, respectively, indicating that production exceeds dissipation. The uncertainties in Reynolds stress estimates due to instrument noise was found to be 4×10^{-4} Pa.

1. Introduction

Tidal current energy conversion system has been noted as one of the viable technologies for its inherent predictability, reliability and minimal or no negative environmental impact. In addition, the natural resource is cheap and continuous. Unlike wind and solar energy, it is not considered as weather dependent. The World Offshore Renewable Energy Report 2002–2007, released by the Department of Trade and Industry, suggests that an estimated 3000GW of tidal energy be available. Scottish Enterprise has estimated that, about 34% of UK electricity demand can be produced from tidal currents; this represents a huge untapped resource. Alternative energy sources hold the key towards the future, without them, energy crises are inevitable. A typical site for a tidal current energy device is a challenging environment; exhibiting large scales of turbulent motion. A better understanding of the nature of turbulence in tidal channels is therefore, a key goal in the successful installation and operation of tidal energy devices. Understanding the structure of turbulence, will make it possible to be able to predict its appearance and possibly manage or control its influence. Large scale motion has been observed from previous work carried out on real flows and these may take the form of volumes of random motion or more organised vortices and shear flows. Rapid velocity changes within large scale turbulence imply that significant fluctuations in loading may be applied to a submerged tidal current energy device by such flow behavior.

The design of modern marine current turbines is currently being driven by the extreme loads imposed upon the turbine. These loads come in two forms, both of equal importance to the design of a reliable turbine. The first comprises the extreme loads associated with strongest tide and the second is the cyclic loads that continually pose a treat of fatigue damage to the turbine by turbulence in the inflow. As noted by [1], the extreme loads during normal operation in turbulent conditions may exceed the design loads in wind turbine. The fatigue damage to critical components, such as the blades, is dominated disproportionately by the highest operating loads even though their rate-of-occurrence is relatively small. (Most of the flows occurring in nature are turbulent [3]. Turbulence is a manifestation of the flow and originates in the instability of shear flows. It can be characterised by a rotational three-dimensional motion, which generates large gradients of velocity at small scales and therefore promotes dissipation of kinetic energy into heat. This makes turbulence a highly dissipative process and therefore a source of energy must be present to maintain the process. In 1883 Osborne Reynolds published the first paper, which described the transition from laminar to turbulent flow. He concluded that the transition occurs at higher speeds, when Reynolds number (Re), which determines resistance to the flow, exceeds 1.3×10^{10} ($Re = UD/\nu$ where U is an average velocity in the water column, D is a stream distance, ν is a kinematic viscosity) [2].

In coastal boundary layers the transition from laminar to turbulent flow is affected several parameters: such as pressure distribution in the external flow, roughness of the seabed and the nature of

☆ Communicated by W.J. Minkowycz.

* Corresponding author.
E-mail address: eo26@hw.ac.uk (E. Osalusi).

0735-1933/$ – see front matter © 2009 Elsevier Ltd. All rights reserved.
doi:10.1016/j.icheatmasstransfer.2009.02.010

Nomenclature

u_*	shear velocity, m/s
u	along-stream velocity, m/s
z	height above bed, m
v	across-stream velocity, m/s
P	TKE production, W/m^3
w	vertical velocity, m/s
Az	Eddy viscosity, m^2/s
S	TKE density, J/m^3
b_i	along-beam velocities, m/s
Re	Reynolds number, $\Omega r^2/\nu$
ü, $\ddot{v}$, $\ddot{w}$	velocities instrument coordinate system, m/s
k	wavenumber
f	frequency
$\bar{u}$	mean velocity, m/s
M	ensemble number
$\overline{\bar{u}}$	mean velocity, m/s
$\overline{x_i'^2}$	along-beam velocity variance due to turbulent fluctuations

Greek symbols

τ	shear stress, Pa
μ	dynamic viscosity, Ns/m^2
τ_b	bed shear stress, Pa
ρ	fluid density, kg/m^3
τ_x	along-stream vertical turbulent stress, Pa
τ_y	across-stream vertical turbulent stress, Pa
ε	TKE dissipation, W/m^3
θ	beam angle, °
ϕ_1	pitch angle, °
ϕ_2	roll angle, °
γ	constant
α	Kolmogorov constant
σ_b^2	along-beam velocity variance due to instrument noise
σ_{st}	Reynolds stress uncertainties, Pa
σ_{sh}	Shear estimate uncertainties, 1/s
σ_{pr}	TKE production uncertainties, W/m^3

Subscripts

n	integer
i	integer

disturbances. The presence of bed roughness favours the transition by decreasing the critical value of the Reynolds number. The existence of irregularities on the seabed gives rise to additional disturbances in the flow and, as a consequence, a lower degree of amplification is sufficient to effect a transition from laminar to turbulent flow. Another important parameter affecting the stability of the flow is density variation. When the flow has density stratification, turbulent mixing can be strongly affected. This is true especially in the vertical direction where the parcels of fluid must be moved against hydrostatic forces.

At high water velocities and because of edge effects and surface roughness of structures, given that water is a viscous fluid, flows in a marine current turbine system are turbulent, rather than laminar. The tendency of water molecules to resist shear forces, due to the presence of viscosity, causes them to move irregularly. The shear stresses within a flow field tear the fluid into highly energetic, irregular, and three-dimensional eddies, with scales ranging from the size of the flow passage down to unity [4]. These eddies exist randomly in space and time in turbulent shear flows [5]. Within a turbine system, it would be difficult to separate the effects of normal forces (that cause pressure) from tangential forces (that cause shear stress), but rather the fluid stress will be a combination of the two.

At the bottom of the ocean the water flowing above the seabed causes stress which extends into the water column. Near the bed, the velocity decreases due to the friction. The part of the flow where the velocity is affected by the bed is called the boundary layer. In the laminar boundary layer the velocity shear ($\partial u/\partial z$) increases linearly with increase in shear stress (τ):

$$\tau = \mu \frac{\partial u}{\partial z}, \tag{1}$$

where μ is the dynamic viscosity. At a sufficiently high Reynolds number the flow in the boundary layer becomes turbulent due to instability present in the flow. As a consequence the flow develops a highly random character with rapid irregular fluctuations of velocity in space and in time. The velocity at any point in space (u) can be described by its time average ($\bar{u}$) and fluctuating part (u'): $u = \bar{u} + u'$. It can be seen that the fluctuating parts of velocity vector give rise to additional stresses in the flow, called Reynolds stresses which increase with distance from the boundary and with the intensity of turbulence.

Therefore, a total shear stress in the turbulent bottom boundary layer is a product of viscous and Reynolds stress. It varies with height above the bed, but near the bed, reaches the constant value defined as the bed shear stress (τ_b). This parameter makes it possible to define a shear velocity (u_*) that represents the strength of turbulent velocity fluctuations near the bed: $u_* = \sqrt{\tau_b/\rho}$: $u_* \approx \sqrt{\overline{u'w'}}$. From experimental studies, for relatively smooth bottoms the friction velocity was found to be around 0.2 cms^{-1} for flat bottoms [6], 1 cms^{-1} when a surface swell occurred [7], and few cms^{-1} when bottom roughness was present [8].

The measurement of turbulent parameters in tidal flows presents oceanographers with a difficult problem, since it is necessary to obtain rapid measurements of velocity at small spatial scales in an environment in which large stresses operate and where, away from the bottom boundary, there is no fixed reference for velocity measurement. Turbulent stresses, or Reynolds stresses, represent the transport of momentum by turbulence and thus can control the vertical structure of turbulent environmental flows. Knowledge of Reynolds stresses along with mean velocity profiles allows the eddy viscosity, the most common parameterization of vertical mixing due to turbulence, to be computed. In the shallow coastal ocean, measurement of Reynolds stresses is complicated by the presence of surface waves. Although for small-amplitude irrotational waves the horizontal and vertical components of wave orbital velocities are 90° out of phase and therefore should have zero covariance, very small tilts in sensor alignment, or real wave stress associated with a sloping bed, for example, lead to a covariance between horizontal and vertical velocities that can contaminate or even dominate Reynolds stress measurements. Additionally, waves often occupy the same frequency range as turbulence in the shallow coastal ocean, and therefore wave contamination cannot be removed by simple frequency filtering. Lohrmann et al. [9] introduced a method for calculating Reynolds stress profiles from four-beam current profiler measurements using the difference between the velocity variances along opposing beams. Stacey et al. [10], Lu and Lueck [11], and Williams and Simpson [12] extended this work with analyses of the confidence in Reynolds stress measurements. The variance method has since been applied successfully in a number of studies of stratified tidal systems [13–15]. Comparisons with independent collocated Acoustic Doppler Velocimeter (ADV) measurements have validated the method [16,17] and illustrated that the fast pinging rate mode 12 maintains accuracy while reducing noise relative to the single ping mode 1 [12,16]. Mode 12 is an operational mode that allows Teledyne RDI's ADCPs to measure fast flows in shallow gauging sites. It can measure a large range of flow velocities and uses smaller depth cells, making it capable of taking

measurements in much shallower flows. It works by reducing the size of the depth cell, making it possible to measure the highly sheared profile of fast flows near boundaries. It (mode 12) gets around this by increasing the ping rate, allowing the depth cell size to be small without increasing the averaging time or data noise [18]. However, application of the variance method to coastal seas has illustrated that the method fails in the presence of energetic surface waves [17,19,20].

The measurement of Bottom Boundary Layer (BBL) characteristics in the seas and oceans is necessary for researches into the main mechanisms of interaction between the bed and water column. The information about BBL structure and dynamics is important for the prediction of sediment cover formation and bottom geomorphology, vertical diffusion and bottom friction processes, as well as for completion of various engineering works near the bed and the execution of geological survey and provides important data for ecological projects. Despite the significance of the BBL for various modern geophysics topics, it remains the least investigated oceanographic studies. This is a consequence of the difficulties of measurement near to bed surfaces.

ADCPs are capable of measuring profiles of the current velocity by applying run-time windowing of backscattered acoustic pings along, three or four beams pointing in different directions. Whereas normal-mode ADCP measurements evaluate the Doppler frequency shift of the backscattered signal to estimate the in-beam velocity of the scattering particles, the pulse-coherent mode evaluates the phase shift between the echoes of two subsequent pings, resulting in much higher measurement accuracy but shorter profiling ranges. With the assumption that the velocity is the same within the respective depth bins of each beam, a three-dimensional velocity vector can be constructed from the measured along-beam velocities of at least three beams. A typical beam geometry is such that the beams are inclined by 20°–30° to the vertical and are symmetrically arranged, within a horizontal plane projection (e.g. in a Janus configuration). A detailed outline of the procedure to calculate a three-dimensional current vector based on the measured in-beam velocities of a three-beam ADCP is given in [21]. In analogy, for a four-beam ADCP the calculus is given, for instance, in [11]. For the same instrument, it was shown by [22] that the statistical properties of the measured in-beam velocity fluctuations can be used to estimate selected Reynolds stresses as well as a term that is related to the turbulent kinetic energy (TKE) density. This procedure, known as the variance method, was applied to a variety of oceanic systems (e.g., [9,10,14]. The application of the variance method, however, is restricted to ADCPs with at least four beams, as well as to highly energetic systems, such as tidal channels.

Turbulent mixing generated by current shear and wave breaking is, besides differential advection [23], the key process leading to an entrainment of ambient water into propagating dense bottom plumes. However, measuring of turbulence parameters in the ocean is far from being a standard method. Turbulence measurements require state-of-the-art technology and experienced staff. Single-point measurements are well established and are carried out with acoustic Doppler velocimeters (ADVs) that measure all three velocity components in the same small sampling volume. The advantage of this method is that both, the turbulent kinetic energy (TKE) and its dissipation rate (ε) can be estimated from a single instrument, but it is obviously impossible to estimate the vertical shear, and thus the TKE shear production, from this instrument alone. Vertical profiles of turbulence parameters are obtained by microstructure shear profilers [24] and temperature microstructure profilers [25]. Both types of instruments yield estimates of the TKE dissipation rate. Due to the intermittency of turbulence, this method requires repeated profiling in order to obtain stable averages of statistical quantities. This is laborious work, and longer time series are rare. To overcome these shortcomings new measuring technologies were developed during the recent decade. Very promising is the use of acoustic Doppler current profilers (ADCP). Reynolds stress and TKE production can be derived from ADCPs with four beams (Janus configuration) using the variance method [9,11,14]. This method requires horizontally homogeneous statistical properties of the turbulence over the distance between the opposite beams of the ADCP, typically in the order of 10 m. Another necessary precondition is the strictly vertical orientation of the ADCP. Any deviation from the vertical axis causes errors in the Reynolds-stress estimates [12]. The application of moored, self-contained ADCPs enables profile measurements of turbulence parameters over long time periods. However, if the ADCP is operated in the normal Doppler mode the variance method is restricted to systems with a high turbulence level, since the turbulent length scale must be sufficiently large compared to the vertical cell size of the ADCP and the accuracy of the velocity estimates is limited by the Doppler noise. There are new developments to derive also the TKE dissipation rate from ADCP data. Two different approaches are employed. The spectral method [21] fits the measured velocity spectrum in the inertial subrange to the theoretical $k^{-5/3}$ law, where k denotes the wave number. The required high accuracy of the velocity estimates with small measuring volumes can be only provided by the pulse coherent mode (PC-mode) ADCP, which exploits the phase shift between two subsequent transmitted pulses to estimate the velocity. The limitation of the spectral method, using stream-wise fluctuation spectra, is the uncertainty in the isotropy constant. Thus, the spectral method estimates an upper limit ε^* of the true dissipation rate ε ranging between $0.65\varepsilon \leq \varepsilon \leq \varepsilon^*$ [21]. The second new approach is the structure function method. It uses the theory of spatial velocity correlations in case of homogeneous turbulence [26]. This method was originally developed for radar-based measurements of dissipation rate in the atmosphere [27]. Wiles et al. [26] applied the structure function method to ADCP measurements in a shelf sea with strong tidal forcing. They found a reasonable agreement between TKE dissipation rates estimated from a microstructure shear profiler (Fly) and TKE production rates derived from the variance method. However, the high Doppler noise in the used broad band mode of the ADCP restricts the application to environments with a high turbulence level (order of $\varepsilon > 10^{-6}$ Wkg^{-1}), e.g. areas with strong tidal currents. Also, they found different dissipation rates for the upstream and downstream directed beams, which can be explained by the anisotropy of the large turbulent eddies. The application of the structure function method to a pulse coherent mode ADCP may allow for the estimation of dissipation rates also in environments with weaker turbulence intensity, since the higher accuracy yields an enhanced temporal and spatial resolution of the current field.

In the present paper we present ADCP observations of turbulence, principally profiles of the turbulent shear stress, showing the evolution of the tidal flow in EMEC's tidal energy test site over two tidal cycles. The Reynolds stress has been estimated from the difference in variance between the along-beam velocities of opposing acoustic beams. The structured function method was used to calculate the turbulent energy dissipation rate ε. In what follows, the turbulence methods and the general physical setting in which the measurements were made together with the estimate of uncertainties were outlined and discussed.

2. Study area and ADCP deployment

A 600-kHz four-beam broadband ADCP (RD Instruments Workhorse monitor) was deployed on the bottom, looking upward, in approximately 42 m (mean water depth) of water between 3 July and 10 July 2006. The instrument was programmed to operate in fast pinging mode 12, recording one velocity profile per second. Velocities were recorded in beam coordinates; that is, one along-beam velocity was obtained for each of the instrument's four acoustic beams. The survey was conducted approximately 4 km west of the Island of Eday in the Orkney Islands, the tidal test site at the Fall of Warness, (59°08.147N; 2°48.391W) of the European Marine Energy center (EMEC). This location is characterized by high velocity marine currents which reach almost 4 ms^{-1} at spring tides and 2.5 ms^{-1} during neap tides.

The ADCP was mounted in a ±20° gimbal to adjust for uneven bottoms. The instrument was slightly tilted with respect to the vertical which varied between 0° and 8° during the experiment because of scour around the frame. For an isotropic flow typical of the coastal ocean, 2° tilts resulted in no more than a 17% bias in stress estimate [11] and thus, 2° was used as a reasonable cutoff for a maximum instrument tilt. The ADCP bin size was 1 m, with the first bin 1.63 m above bottom. Tidal current was predominantly semidiurnal. Current speeds regularly exceeded 2 ms^{-1} at the surface, and the majority of the velocity shear was near the seabed. The ambiguity velocity (the maximum allowable radial motion for phase measurements [18]) was set at 2 ms^{-1} and the standard deviation of the uncertainty associated with each horizontal velocity estimate was 0.0393 ms^{-1}.

3. Governing equations

3.1. The variance method

A four-beam ADCP typically has two pairs of opposing transducers that emit acoustic pulses along beams. Along-beam velocities are calculated by the instrument firmware, from the Doppler shift in the sound signal returned to the transducers, yielding four along-beam velocities (b_1, b_2, b_3, b_4), defined to be positive toward the instrument. Beam velocities can be resolved into an orthogonal coordinate system that is fixed relative to the ADCP. We use the coordinate system defined by [11], where $\ddot{x}$ is the direction from beam 1 to beam 2, and $\ddot{y}$ is the direction from beam 3 to beam 4. Beam velocities (b_1, b_2, b_3, b_4), expressed in terms of velocities in the instrument coordinate system ($\ddot{u}$, $\ddot{v}$, $\ddot{w}$), are

$$\begin{aligned} b_1 &= -\ddot{u}\sin\theta - \ddot{w}\cos\theta \\ b_2 &= \ddot{u}\sin\theta - \ddot{w}\cos\theta \\ b_3 &= -\ddot{v}\sin\theta - \ddot{w}\cos\theta \\ b_4 &= \ddot{v}\sin\theta - \ddot{w}\cos\theta \end{aligned} \tag{2}$$

where θ is the half angle between opposing beams (20° for an RDI Workhorse ADCP). In the case of a perfectly level instrument, $\ddot{u}$ and $\ddot{v}$ correspond to horizontal velocities and $\ddot{w}$ corresponds to the vertical velocity. If an ADCP is tilted by a pitch angle ϕ_1 about the x axis (positive counterclockwise) or by a roll angle ϕ_2 about the y axis (positive counterclockwise), the transform from the instrument coordinate system ($\ddot{u}$, $\ddot{v}$, $\ddot{w}$), to a level coordinate system (u, v, w), is

$$\begin{bmatrix} u \\ v \\ w \end{bmatrix} = \begin{bmatrix} \cos\phi_2 & 0 & \sin\phi_2 \\ \sin\phi_1\sin\phi_2 & \cos\phi_1 & -\sin\phi_1\cos\phi_2 \\ -\cos\phi_1\sin\phi_2 & \sin\phi_1 & \cos\phi_1\cos\phi_2 \end{bmatrix} \begin{bmatrix} \ddot{u} \\ \ddot{v} \\ \ddot{w} \end{bmatrix} \tag{3}$$

For small ϕ_1 and ϕ_2 this expression can be simplified using Taylor expansions. Retaining only terms to first order in ϕ_1 and ϕ_2 yields

$$\begin{bmatrix} u \\ v \\ w \end{bmatrix} = \begin{bmatrix} 1 & 0 & \phi_2 \\ 0 & 1 & -\phi_1 \\ -\phi_2 & \phi_1 & 1 \end{bmatrix} \begin{bmatrix} \ddot{u} \\ \ddot{v} \\ \ddot{w} \end{bmatrix} \tag{4}$$

Inverting this equation gives an expression for ($\ddot{u}$, $\ddot{v}$, $\ddot{w}$) in terms of the coordinates (u, v, w):

$$\begin{bmatrix} \ddot{u} \\ \ddot{v} \\ \ddot{w} \end{bmatrix} = \begin{bmatrix} 1 & 0 & -\phi_2 \\ 0 & 1 & \phi_1 \\ \phi_2 & -\phi_1 & 1 \end{bmatrix} \begin{bmatrix} u \\ v \\ w \end{bmatrix}. \tag{5}$$

In the absence of waves, each component of the velocity can be decomposed into a mean (e.g., $\bar{u}$) associated with slowly varying flow and into a fluctuation (e.g., u') associated with turbulence. Mean values are calculated over an appropriate time interval (e.g., 20 min) for which the flow is statistically stationary. If each quantity in Eq. (3) is decomposed in this way, it can be shown [9,10] that

$$\frac{\tau_x}{\rho} = \overline{\ddot{u}'\ddot{w}'} = \frac{\overline{b_3'^2} - \overline{b_4'^2}}{4\sin\theta\cos\theta} \tag{6}$$

$$\frac{\tau_y}{\rho} = \overline{\ddot{v}'\ddot{w}'} = \frac{\overline{b_1'^2} - \overline{b_2'^2}}{4\sin\theta\cos\theta}. \tag{7}$$

This is the variance method for calculating Reynolds stresses from ADCP beam velocities. Substituting the transformation in Eq. (5) into Eqs. (6) and (7) yields

$$\frac{\tau_x}{\rho} = \overline{u'w'} = \frac{\overline{b_3'^2} - \overline{b_4'^2}}{4\sin\theta\cos\theta} + \phi_2\left(\overline{u'^2} - \overline{w'^2}\right) - \phi_1\overline{u'v'}. \tag{8}$$

$$\frac{\tau_y}{\rho} = \overline{v'w'} = \frac{\overline{b_1'^2} - \overline{b_2'^2}}{4\sin\theta\cos\theta} - \phi_1\left(\overline{v'^2} - \overline{w'^2}\right) + \phi_2\overline{u'v'}. \tag{9}$$

where ρ is the water density, θ is the angle each beam of the ADCP makes with the vertical ($\theta = 20°$ for the RDI Workhorse used here). The second and the third terms of Eqs. (8) and (9) are the bias introduced to Reynolds stress estimates by instrument tilt in the absence of waves. The turbulent kinetic energy $q^2/2 = (\overline{u^2} + \overline{v^2} + \overline{w^2})/2$ cannot be computed with data from either ADCP without additional assumptions. Defining $\xi = \overline{w'^2}/q2$ and

$$S = \frac{1}{4\sin^2\theta}\sum_{i=1}^{4}\overline{b_i'^2} = \frac{1}{2}\left(\overline{u'^2} + \overline{v'^2}\right) + \overline{w'^2}\cot^2\theta, \tag{10}$$

for the four-beam ADCP e.g., [9] allows the TKE to be expressed as

$$\frac{q^2}{2} = \frac{S^2}{1 + \xi(2\cot^2\theta - 1)}. \tag{11}$$

Computing TKE with Eq. (11) requires a value of ξ to be assumed. Lohrmann et al. [9] argued that $\overline{w'^2} < (\overline{u'^2} + \overline{v'^2})/2$, and thus that isotropy ($\xi = 1/3$) would be a limiting case. For their measurements in a tidal, unstratified channel flow, Stacey et al. [10] used measurements of Nezu and Nakagawa [5], which yield $\xi = 0.17$. This value was used here.

The rate at which energy is transferred from the mean flow to TKE through the interaction of the turbulence with the shear is estimated from the product of the Reynolds stress and the velocity shear according to Rippeth et al. [19].

$$P = -\rho\left(\overline{u'w'}\frac{\partial\bar{u}}{\partial z} + \overline{v'w'}\frac{\partial\bar{v}}{\partial z}\right), \tag{12}$$

where both the stress and velocity shear are estimated from the ADCP data. As a result of the alignment of the ADCP to the tidal flow, we would expect the main contribution to the rate of production to come from the second term on the right-hand side of Eq. (12). The estimate of the vertical viscosity coefficient A_z can be can be calculated from the TKE production rate and the magnitude of shear, that is, [22].

$$A_z = \frac{1}{\rho}\frac{P}{\left[\left(\frac{\partial\bar{u}}{\partial z}\right)^2 + \left(\frac{\partial\bar{v}}{\partial z}\right)^2\right]}. \tag{13}$$

The sign of A_z is the same as P. It should be noted that the estimates of A_z are subject to large uncertainties, particularly when the magnitudes of shear are small.

3.2. Estimates of turbulent kinetic energy dissipation

In a homogeneous turbulent flow with a spatial and temporal constant background flow the velocity difference between two points of distance r is mainly determined by turbulent eddies of a spatial

scale near to r. The mean square of the velocity difference defines as radial structure function $Z(z, r)$ at depth z (e.g. [28–29], where u is the velocity component along the line connecting both measuring points.

$$Z(z,r) = \overline{(u(z) - u(z+r))^2} \tag{14}$$

Assuming that the velocity difference is also proportional to an associated velocity scale u' one obtains the relation

$$Z(z,r) \sim u'^2. \tag{15}$$

In case of isotropic turbulence the relationship between the characteristic length scale, the velocity scale of turbulent eddies in the inertial sub range and the TKE dissipation rate ε follows from the Taylor cascade theory [30].

$$\varepsilon \sim \frac{u'^3}{r}. \tag{16}$$

Combining Eqs. (14) and (15) one can derive a relationship between the structure function $Z(z, r)$ and the TKE dissipation rate ε.

$$Z(z,r) = C\varepsilon^{2/3} r^{2/3}. \tag{17}$$

For isotropic turbulence C is assumed to be a constant. Its value was estimated empirically by measurements in the atmosphere [27] and ocean [31]. C varies between 2.0 and 2.2, depending on the ratio r/η where η is the Kolmogoroff microscale. In this paper $C = 2.1$ was used, which seemed to be a good approximation in the observed range of dissipation rate. It should be mentioned that the structure function approach is only valid for the inertial subrange, typically $l_0/6 \geq r \gg \eta$. The structure function approach was applied to each of the four beams. For each depth bin z_i a set of structure functions $Z(z_i, r_k)$ for increasing distances of r_k was calculated using a centered difference scheme.

$$Z(z_i, r_k) = \overline{(u(z_{i-k}) - u(z_{i+k}))^2} \tag{18}$$

with $k = 1,\ldots n$, and $r_k = 2 \cdot k \cdot$ binsize.

According to the structure of Eq. (15) the sets of $Z(z_i, r_k)$ were fitted to an equation of the form

$$Z(z_i, r) = Ar^{2/3} + n, \text{with } A = C\varepsilon^{2/3}. \tag{19}$$

using a least-square algorithm. Then, the TKE dissipation rate is derived from the value of the estimated slope, A. The offset parameter n may be interpreted as noise, but it is not the inherent Doppler noise as in the case of measurements in the Doppler mode, instead n contains that part of velocity variance, which is not proportional to $r^{2/3}$. The equations above are valid for isotropic turbulence with a spatially constant background flow. According to Eq. (14) a constant shear in the background flow will contribute to the structure function, although it is not related to velocity fluctuations in the inertial subrange. Thus, before calculating Z the mean flow must be removed. The raw beam velocities were temporally averaged over the averaging interval that is used for the structure function calculation. Then this mean is subtracted from the raw beam velocities. Afterwards, the dissipation rates were calculated for each single beam of the ADCP, and then spatially averaged over the three beams, within each depth cell [26].

3.3. Variance method uncertainties

The level of uncertainty in stress estimates is determined by instrument noise, velocity variability, and averaging. Lu and Lueck [22] present useful statistical methods for determining uncertainty, using either bootstrap or random lag covariance approaches. The latter approach is also discussed by Rippeth et al. [19]. A semi-empirical equation for the standard error (σ_{st}) in stress estimates was derived by Williams and Simpson [12] as:

$$\sigma_{st}^2 = \rho^2 \gamma \left(\frac{\sigma_b^2 + \overline{x_t'^2}}{M \sin^2 2\theta} \right)^2, \tag{20}$$

where σ_b^2 is the variance in beam-velocity due to instrument noise, $\overline{x_t'^2}$ is the variance due to velocity variability, M is the number of samples in a variance computation period (1200 samples were used in this study).

Williams and Simpson ([12]) proposed uncertainty in shear estimates is computed as

$$\sigma_{sh} = \gamma_s \frac{\left(var\left[u_{2(n+1)} - u_{1(n+1)} - u_{2(n-1)} + u_{1(n-1)} \right] \right)}{4M(\Delta z)^2 \sin^2 \theta}. \tag{21}$$

It should be noted that the assumption that the vertical velocity is the same in both beams will increase the calculated variance if the two vertical velocities are not the same; hence, Eq. (21) will tend to overestimate the variance of the shear. It is readily seen from this equation that the uncertainty in the shear can be reduced by increasing the number of ensembles to be averaged. It can also be reduced by increasing the depth cell size, at the expense of the vertical resolution. The error in the estimates of rate of shear production can be determined using the formula for the variance of a product. For two independent variables, this is

$$\sigma_{pr}^2 = \overline{(u'w')}^2 \sigma_{sh}^2 + \left(\frac{\partial u}{\partial z} \right)^2 \sigma_{st}^2 + \sigma_{st}^2 \sigma_{sh}^2. \tag{22}$$

For the low-flow case, $\overline{u'w'} \to 0$ and $(\partial u/\partial z) \to 0$, so it is expected that the last term will dominate. The other two terms are expected to dominate at times of higher flow. However, there are a number of limitations of our observational method, which should be born in mind in interpreting the data. A region close to the bed and another close to the surface cannot be sampled because of acoustic constraints. In addition, the vertical bin size of 1 m limits the scale of eddy motions which can contribute to the variance.

4. Results and discussions

In the series of figures presented, white gaps occur where (a) side-lobe contamination near the sea surface (b) statistical non-homogeneity of b_i over the variance computation period (c) statistical non-homogeneity of u, v and w over the distance between beams (d) frequent values below the noise floor (e) surface or internal wave bias, and (f) ADCP motion. Fig. 1 gives a general impression of the cycle of stress variation over two tidal cycles. The plot shows 1-h mean vertical stress profiles acting in the direction parallel to the direction of the tidal flow together with the corresponding along-stream current profiles. Interestingly, asymmetry pattern between the ebb and flood is considerably noticed. The stresses generally decrease more or less linearly from extreme values near the seabed (2.63 mab) to negligible values at the highest level observed (~1 m below the surface). The velocity profiles show maximum near surface flood flows of $>1.7\ ms^{-1}$. (e.g., profiles 1 and 2) while the maximum near-surface ebb flows are $\sim 2.0\ ms^{-1}$. (e.g., profiles 8,9). The largest velocities are generally observed near the surface with the velocities in the lower part of the water column conforming to a logarithmic profile. During the ebb, near-bed stress (height = 2.76 m above the seabed) exceeds ~7.5 Pa at the time of maximum depth–mean flow speed ($\sim 1.76\ ms^{-1}$) while during the flood stresses are limited to ~4.84 Pa during the peak flood, depth–mean, flow of $\sim 1.33\ ms^{-1}$.

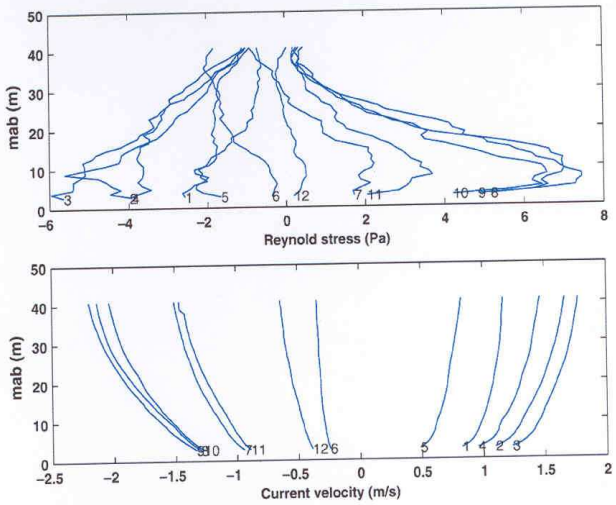

Fig. 1. Hourly mean Reynolds stress (Pa) profiles for the 12 h of the experiment (upper panel). The numbers indicate the time of the profile in yeardays: (lower panel) Mean velocity (ms^{-1}).

Around slack water the stresses throughout the water column are close to zero. We noticed that around ebb high waters (e.g., profile 12) there is negligible stress throughout the water column. There are also profiles that show a linear increase in stress from values of ~0.45 Pa (e.g. profile 10) to maximum (~6.9 Pa) near the middle of the water column, and decreases linearly to (~4.2 Pa) at the seabed. A further interesting observation is the curling back of the stress profile in the bottom two bins during maximum flow (e.g., profile 5), with a maximum stress of ~ −2.32 Pa observed at a height of 9.76 m above the seabed decreasing to (~ − 1.96 Pa) at a height of 7.76 m above the seabed (mab). Fig. 2 shows the contours of backscatter intensity, current velocity, TKE density, Reynolds stress and TKE production rate, P. We notice a higher magnitude in the backscatter intensity at the water surface (Fig. 2A) between day 184.6 and 184.7 (second flood flow) and during the turning of the tide. The higher value at the surface is assumed to be due to the interference of fish or marine vehicles. The pattern at these dates are reflected in the contour plots of TKE density S, the Reynolds stress τ_x and the TKE production P.

Current velocity (Fig. 2B) are tidally dominated and this is reflected in the Reynolds stress variability (Fig. 2C). Currents typically exceed 1.8 ms^{-1} on flood at the surface but peak at values closer to ~1.9 ms^{-1} on ebb. Contour plots of Reynolds stress estimate (Fig. 2C) exceeds 7.9 Pa on ebb flow and typically reach −7.1 Pa on ebb tide. Reynolds stress decreases roughly linearly with height above the bottom. The quantity S, which relates to the TKE density $q^2/2$ by Eq. (11), is illustrated in Fig. 2D. The blank area around day noticed at the surface, corresponds to negative S. Here S is smallest during the weak ebb, and largest estimates of S are obtained during the strongest ebb tide. Generally, the magnitude of S increases toward the seabed for both flood and ebb flows. The strength of the TKE production rate P estimated by Eq. (12) is shown in (Fig. 2E). Peak values exceed 5×10^{-4} Wm^{-3} near the bed. The bottom-generated turbulence can extend to nearly the surface on both flood and ebb but is typically trapped within a 4–6 m of the bottom. The threshold for the TKE production estimates due to noise is estimated to be of order 2.25×10^{-5} Wm^{-3} [12] and so P estimates are not reliable in the upper part of the water column around slack water. Fig. 3A shows the contour plot of vertical shear. It was noticed that shear is maximum near the bed (2.63 mab) and decreases to less than 0.04 within 7.63 mab. Above this height the shear on ebb extends to the surface and is essentially zero on flood. The TKE dissipation rate ε was estimated using the structure function method described in Section 2. The contour of ε is shown in Fig. 3B. The TKE dissipation rate varied with a semidiurnal pattern with maximum dissipation on the flood phase of the tide than the ebb. The maximum value of ε observed during this region is about 10^{-1} Wm^{-3}. Variation in dissipation rate correlates with the Reynolds stress (Fig. 2C) and shear (Fig. 3A) — i.e. the dissipation rate increased with both increasing Reynolds stresses and shear.

By using Eq. (13), the sign of A_z is the same as P. The estimates of A_z are subject to large uncertainties, particularly when the magnitudes of the shear are small especially in the near surface when wave breaking, rather than mean shear, is the source of energy. Fig. 3C indicates a variation of A_z with tidal flow, ranging from about $10^{-4}-3\times10^{-2}$ m^2s^{-1} in this region. The turbulent viscosity increases with increasing height in the lower half of the water column, and reaches a maximum near mid depth. Fig. 4A, estimated at 2.63 m above the sea bed, compares the estimates of ε against the estimates of P. The plot (upper panel) shows that both flood and ebb data show a satisfactory fit ($r^2>0.6$) to a straight line with comparable slopes. Fig. 4B shows the standard deviation of the Reynolds stresses calculated from the observations using Eq. (20) plotted against the associated Reynolds stress. The y intercept of the calculated Reynolds stress standard deviation plotted against the along-channel stress is proportional to the instrument noise [12]. Using a least squares fit, and calculating a standard deviation from Stacey et al. [13] [their Eqs. (26) and (28)], had a minimum uncertainty of ~3.51×10^{-4} Pa (Fig. 4B). The linear regression equation is obtained as

$$\sigma_{st} = 0.0019\tau_x + 0.0009. \tag{23}$$

By referring to Eq. (23), it is apparent that the uncertainty can be reduced by the combination of increasing the number of pings per ensemble, which reduces σ_b and hence σst, and increasing M, which also reduces σ_b. At higher stress levels, there are two components in the uncertainty in the Reynolds stress. These are the instrument noise component and the flow-related component due to turbulent motions. The gradient in the equation above (0.0039) represents the increase in the flow-related component of the uncertainty and is affected only by the number of ensembles used to estimate the stress. The standard deviation of the TKE production rate calculated from Eqs.

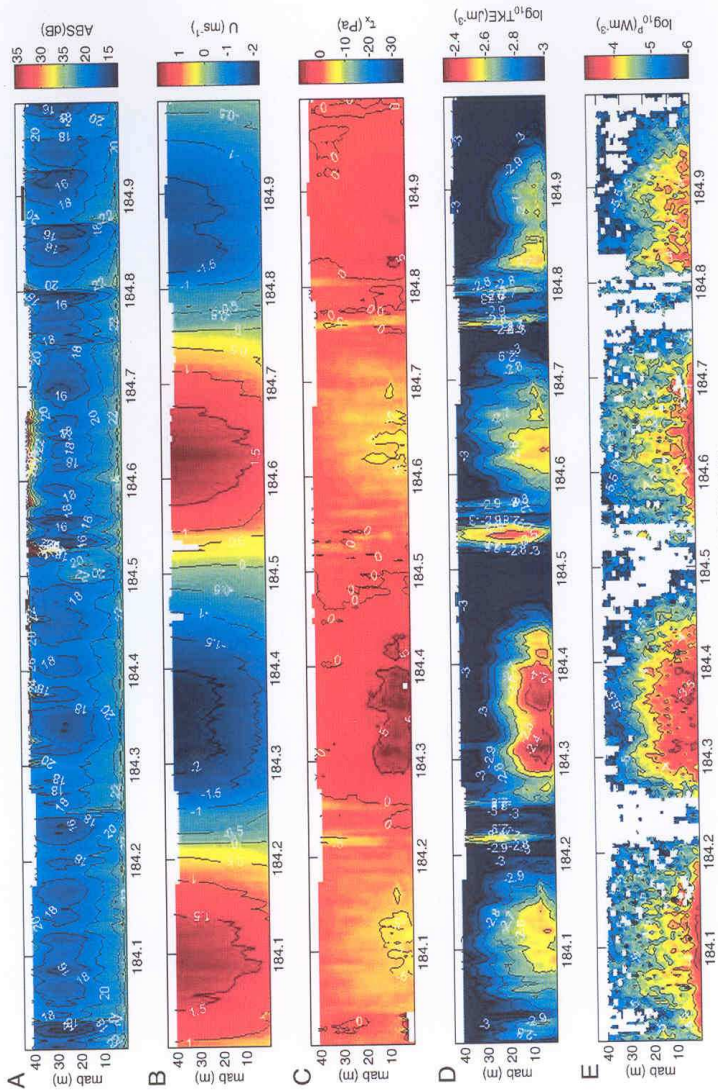

Fig. 2. Depth–time series of (A) acoustic backscatter along signal strength (*dB*), (B) stream velocity (ms^{-1}), (C) Reynolds stress (Pa), (D) TKE density (Jm^{-3}) and (E) TKE production (Wm^{-3}); (A... F)=(first... last panel).

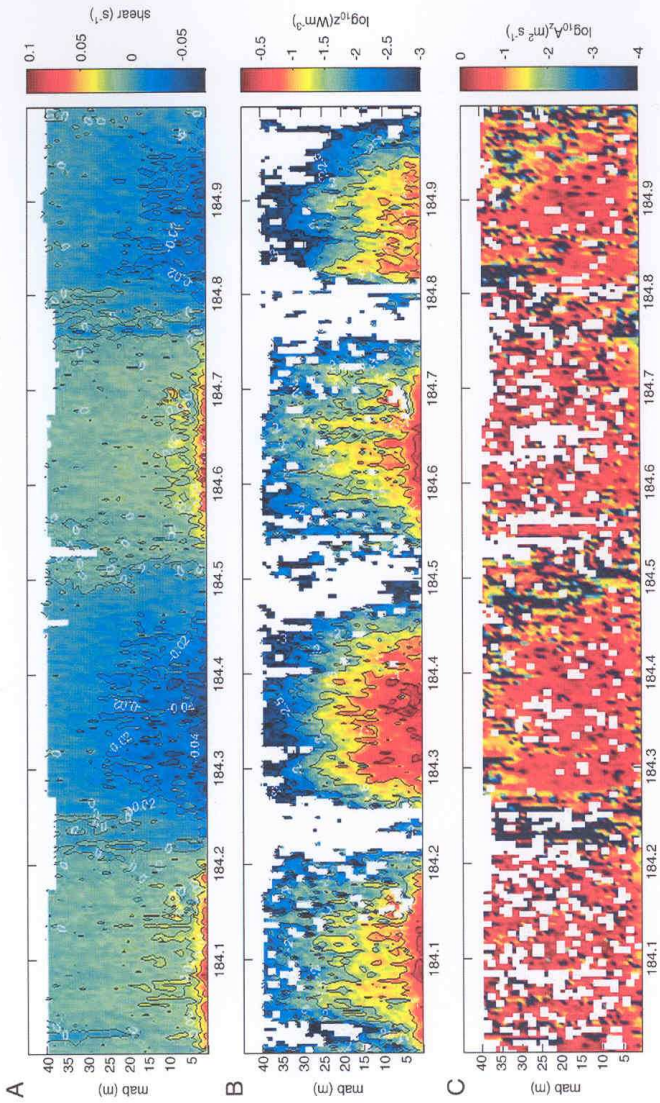

Fig. 3. Depth–time series of (A) vertical shear (s^{-1}), (B) TKE dissipation (Wm^{-3}) and (C) turbulent viscosity (m^2s^{-1});(A... C)=(first... last panel).

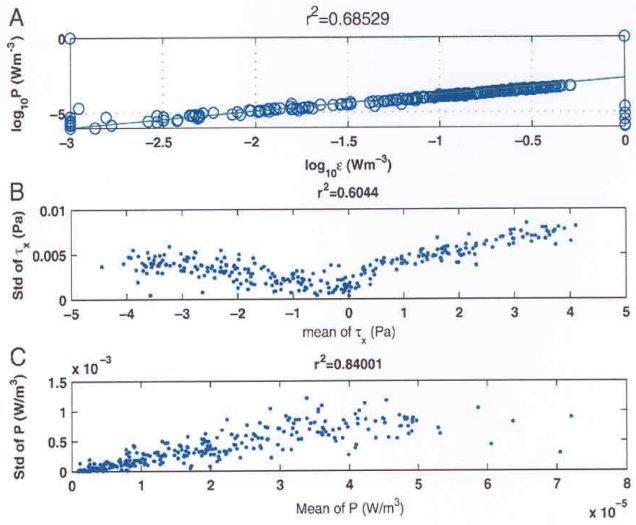

Fig. 4. (A) Scatter plot of (A) P and ε at 2.63 mab. (B) The standard deviation of (A) Reynolds stress calculated plotted as a function of mean stress. (C) TKE production rate estimates plotted against the mean value of the TKE production rate (A… C)=(first… last panel).

(20)–(22) is plotted against the production rate are shown in Fig. 4C. Williams and Simpson [12] showed that about 85% of the variance in the TKE production rate estimates is due to the second term in Eq. (22) $[\rho^2(\partial u/\partial z)^2\sigma_{st}^2]$ at times of high flow, with most of the remaining 15% due to the first term $[\rho^2\overline{uw}^2\sigma_{sh}^2]$ and the last term $(\rho^2\sigma_{st}^2\sigma_{sh}^2)$ making a negligible contribution of at least an order of magnitude smaller than either of the other two terms. At times of low flow, the last term is of the same order as the second term, and the first term is negligible. This indicates that in order to reduce the uncertainty in the estimates of the rate of turbulent production, we particularly need to reduce the uncertainty in the Reynolds stress estimates, σ_{st}^2. Since this involves increasing the number of ensembles, M, used to calculate the variance, it is apparent that σ_{sh}^2 will also be decreased by the same factor at times when turbulent fluctuations dominate over instrument noise. The ratio of the rates of dissipation to production of turbulent kinetic energy has been calculated by calculating individual ratios of P corresponding to ε for flood (day 184.0–184.15) and ebb (day 184.25–184.40) following the removal of P estimates made during periods when the stress estimates are unreliable (i.e., around slack water, near the surface).

The error shown is the 95% confidence limits of the ratios calculated using a bootstrap re-sampling technique of Lu and Lueck [22]. During the tidal cycle the ratios of ε/P on the flood and ebb, 0.3549, and 0.3262, are not significantly different from one another. This reported ratio indicates that the production exceeded dissipation, which has a significant deviation from the expected, theoretical value of unity. Previous studies also showed a deviation of ε/P ratio from unity which was much greater than reported here [11,14]. This discrepancy is considerably less than those reported for other comparisons of in situ measurements of marine turbulence. For example, Lu et al. [12] found ε/P ~0.2 for mid-water column estimates of P using the variance method and ε measured at one height using a moored velocity shear probe. However, the difference between the ε/P estimates and unity could be caused by errors associated with the methods used in this research to estimate both parameters. For example, Stacey et al. [13] proposed a method for examining the assumption about temporal stationarity of the flow of the flow and velocity variances using an ADCP. Additional bias in the ADCP measurements may be due to its vertical resolution. The greater the bin size the greater the error in the velocity fluctuation caused by the ADCP spatial averaging within its bins. The depth cell size chosen for the studies was 1 m. Near the boundary, as the length scale of the turbulent fluctuations decreases, some undersampling of the variance may result. Lu et al. [12] estimate that using a depth cell size of 1 m produces an underestimate of the Reynolds stress of 5% compared with a depth cell size of 0.1 m, and Rippeth et al. [14] estimate a loss of less than 5% when comparing depth cells of 0.5 and 0.25 m. It should also be noted that an additional effect of decreasing the depth cell size is to increase the instrument noise, which may have serious implications in a low energy regime.

5. Conclusions

A bottom-mounted ADCP moored at 1.63 m above the seabed, measured turbulence flow in the EMEC's tidal energy test site. The flow in the channel is mainly tidal and with peak speeds of ~1 ms^{-1}. The data enable us to derive estimates of Reynolds stress, TKE density, the rates of TKE production and dissipation and eddy viscosity using the variance method. Depth–time variations of turbulence in the channel are revealed by measurements with the ADCP. The variation of the Reynolds stress with depth corresponds to the vertical structure of the mean shear. The along-stream component of the stress contains clear tidal variations. The production of turbulent kinetic energy is generally enhanced near the bottom, bearing the character of wall-bounded turbulence. The TKE density changes more strongly with time than with depth. The eddy viscosity has a maxima at mid depth. The TKE dissipation was found to be greatest $(\sim 5\times 10^{-1})$ near the bed when the fastest flow occurred. The results are useful in two ways. First, they provide a set of observations that define the cycles of the production and dissipation of TKE in an energetic seawater column. Second, they allow us to test the two techniques employed, since we would expect ε and P to closely track each other and covary with mean values that are equal. There is good agreement between the patterns of variation of P and ε. Both parameters closely track each other and follow a semidiurnal pattern. The comparison between P and ε was performed by calculating individual ratios of P corresponding to ε. The study found that the ratio ε/P averaged over whole flood and ebb were found

to be ~0.3549 and ~0.3265, respectively, indicating that production exceeded dissipation.

Result from this study is of great importance in the deployment of marine energy devices in energetic environment like the Fall of Warness. This is because the velocity of the flow at a given location can vary greatly across the actuator area of the turbine. This could lead to significant variations in loading across the actuator and associated fatigue and vibration problems. Understanding the turbulence levels is important not only to the siting of individual units (e.g. avoiding areas with strongly stratified flow) but can also inform the device design. Understanding what these levels will be is important to setting realistic limits to design.

Acknowledgement

This work is based upon work funded by TOTAL E&P (UK) PhD studentship research in Marine Renewable Energy. The authors would like to thank EMEC for providing the ADCP data.

References

[1] P.H. Madsen, K. Pierce, M. Buhl, Predicting Ultimate Loads for Wind Turbine Design, 1999 ASME Wind Energy Symposium, 1999, p. 355.
[2] O. Reynolds, An experimental investigation of the circumstances which determine whether the motion of water shall be direct or sinuous, and of the law of resistance in parallel channels, Philos. Trans. R. Soc. 174 (1883) 935–982.
[3] J.M. McDonough, Introductory Lectures on Turbulence, Departments of Mechanical Engineering and Mathematics, University of Kentucky, 2004.
[4] D.S. Miller, Internal Flow Systems Design and Performance Prediction, 2nd edition, Gulf Publishing Company, Houston, Texas, 1990, p. 396.
[5] I. Nezu, H. Nakagawa, Turbulence in Open-Channel Flows, Balkema, Rotterdam, The Netherlands, 1993.
[6] T.M. Chriss, D.R. Cadwell, Universal similarity and the thickness of the viscous sublayer at the ocean floor, J. Geophys. Res. (1984) 6403–6414.
[7] W.D. Grant, A.J. Williams, S.M. Glenn, Bottom stress estimates and their prediction on the Northern California Continental Shelf during CODE-1, J. Phys. Oceanogr. 14 (1984) 506–527.
[8] D.A. Cacchione, D.E. Drake, G.B. Tate, J.T. Ferreira, Bottom Stress Estimates and Sand Transport on the Northern California Inner Continental Shelf, vol. 75, American Geophysical Union, 1994, p. 181.
[9] A. Lohrmann, B. Hackett, L.P. Roed, High resolution measurements of turbulence, velocity, and stress using a pulse-to-pulse coherent sonar, J. Atmos. Ocean. Technol. 7 (1990) 19–37.
[10] M.T. Stacey, S.G. Monismith, J.R. Burau, Observations of turbulence in a partially stratified estuary, J. Phys. Oceanogr. 29 (1999) 1950–1970.
[11] Y. Lu, R.G. Lueck, Using a broadband ADCP in a tidal channel. Part II: Turbulence, J. Atmos. Ocean. Technol. 16 (1999) 1568–1579.
[12] E. Williams, J.H. Simpson, Uncertainties in estimates of Reynolds stress and TKE production rate using the ADCP variance method, J. Atmos. Ocean. Technol. 21 (2004) 347–357.
[13] M.T. Stacey, S.G. Monismith, J.R. Burau, Measurements of Reynolds stress profiles in unstratified tidal flow, J. Geophys. Res. 104 (C5) (1999) 10 933–10 949.
[14] T.P. Rippeth, E. Williams, J.H. Simpson, Reynolds stress and turbulent energy production in a tidal channel, J. Phys. Oceanogr. 32 (2002) 1242–1251.
[15] D.C. Fugate, R.J. Chant, Near-bottom shear stresses in a small, highly stratified estuary, J. Geophys. Res. 110 (C03022) (2005), doi:10.1029/2004JC002563.
[16] A.J. Souza, M.J. Howarth, Estimates of Reynolds stress in a highly energetic shelf sea, Ocean Dyn. 55 (2005) 490–498.
[17] N.J. Nidzieko, D.A. Fong, J.L. Hench, Comparison of Reynolds stress estimates derived from standard and fastping ADCPs, J. Atmos. Ocean. Technol. 23 (2006) 854–861.
[18] www.rdinstruments.com.
[19] T.P. Rippeth, J.H. Simpson, E. Williams, M.E. Inall, Measurement of the rates of production and dissipation of turbulent kinetic energy in an energetic tidal flow: Red Wharf Bay revisited, J. Phys. Oceanogr. 33 (2003) 1889–1901.
[20] M.J. Howarth, A.J. Souza, Reynolds stress observations in continental shelf seas, Deep-Sea Res. II 52 (2005) 1075–1086.
[21] A. Locke, A. Wuest, Application of coherent ADCP for turbulence measurements in the bottom boundary layer, J. Atmos. Ocean. Technol. 22 (11) (2005) 1821–1828.
[22] Y. Lu, R.G. Lueck, Using a broadband ADCP in a tidal channel. Part I: Mean flow and shear, J. Atmos. Ocean. Technol. 16 (1999) 1556–1567.
[23] H.M. van Aken, The onset of stratification in shelf seas due to differential advection in the presence of a salinity gradient, Cont. Shelf Res. 5 (1986) 475–485.
[24] H. Prandke, Microstructure sensors, in: H. Baumert, J. Simpson, J. Suendermann (Eds.), Marine Turbulence: Theories, Models, and Observations, Cambridge University Press, 2005, pp. 101–109.
[25] O. Kocsis, H. Prandke, A. Stips, A. Simon, A. Wüest, Comparison of dissipation of turbulent kinetic energy determined from shear and temperature microstructure, J. Mar. Syst. 21 (1999) 67–84.
[26] P.J. Wiles, T.P. Rippeth, J.H. Simpson, P.J. Hendricks, A novel technique for measuring the rate of turbulent dissipation in the marine environment, Geophys. Res. Lett. 33 (L21608) (2006) 15.
[27] H. Sauvageot, Radar Meteorology, Artech House Books, 1992.
[28] L.D. Landau, E.M. Lifschitz, Lehrbuch der theoretischen Physik, Hydrodynamik Band, vol. 6, Akademie Verlag, Berlin, 1991.
[29] S.B. Pope, Turbulent Flows, Cambridge University Press, 2000, p. 771.
[30] G.I. Taylor, The statistical theory of isotropic turbulence, J. Aeronaut. Sci. 4 (1937) 311.
[31] S.G. Saddoughi, S.V. Veeravalli, Local isotropy in turbulent boundary layers at high Reynolds number, J. Fluid Mech. 268 (1994) 333–372.

Appendix G

Code Functions

G.1 Code Index

G.1.1 poincare3D.m

```
clc
Clear all
Close all
%\begin{verbatim}
%% A THREE DIMENSIONAL POINCARE  MAP (3D PHASE PLOT):
%%%% Code excludes the points outside of ellipsoid in
%%% two-dimensional domain
 function [U_output, index] = poincare3D(U, plot, option )
%=========================================================================
%
% Input
%   U            : input data with dimension (n,1)
```

```
%   plot         : =9 plot results (optional)
%   option     : =0 or not specified  ; return spike noise as NaN
%                  = 1 ; remove spike noise and variable becomes shorter
%than input length
%                 = 2            ; interpolate NaN using cubic polynomial
%
% Output
%   U_output    : output (filterd) data
%   index        : excluded array element number in U
%==========================================================================

nvar = nargin;
if nvar==1
    option  = 0;
    plot = 0;
elseif nvar==2
    option = 0;
end

%
% --- initial setup
%

% number of maximum iteration
n_iter = 20;
n_out  = 999;

n      = size(U,1);
f_mean = nanmean(U);
f      = U - f_mean;
lambda = sqrt(2*log(n));

if nargin==1
  plot = 0;
end
```

```
%
% --- loop
%

n_loop = 1;

while (n_out~=0) & (n_loop <= n_iter)

%
% --- main
%

% step 0
f = f - nanmean(f);
%nanstd(f)

% step 1: first and second derivatives
f_t  = gradient(f);
f_tt = gradient(f_t);

% step 2: estimate angle between f and f_tt axis
if n_loop==1
  theta = atan2(sum(f.*f_tt), sum(f.^2) );
end

% step 3: checking outlier in the 3D phase space
[xp,yp,zp,index,coef] = func_excludeoutlier_ellipsoid3d(f,f_t,f_tt,theta);

% --- excluding data
%
n_nan_1 = size(find(isnan(f)==1),1);
f(index)  = NaN;
n_nan_2 = size(find(isnan(f)==1),1);
n_out   = n_nan_2 - n_nan_1;
```

```
%
% --- end of loop
%

n_loop = n_loop + 1;

end

%
% --- post process
%

go = f + f_mean;
index = find(isnan(go));

if n_loop < n_iter
  disp(...
    ['>> Number of outlier   = ', num2str(size(find(isnan(f)==1),1)), ...
     ' : Number of iteration = ', num2str(n_loop-1)] ...
  )
else
  disp(...
    ['>> Number of outlier   = ', num2str(size(find(isnan(f)==1),1)), ...
     ' : Number of iteration = ', num2str(n_loop-1), ' !!!
 exceed maximum value
!!!'] ...
  )
end

%
% --- interpolation or shorten NaN data
%

if abs(option) >= 1
```

```
    % remove NaN from data
    inan = find(~isnan(go));
    U_output = go(inan);
    % interpolate NaN data
    if abs(option) == 2
        x   = find(~isnan(go));
        y   = go(x);
        xi  = 1:max(length(U));
        U_output = interp1(x, y, xi, 'cubic')';
    end
else
    % output despiked value as NaN
    U_output = go;
end
%
% --- for check and  plot
%

if plot == 9

%theta/pi*180
F    = U - f_mean;
F_t  = gradient(F);
F_tt = gradient(F_t);
RF = [ cos(theta) 0  sin(theta); 0 1 0 ; -sin(theta) 0 cos(theta)];
RB = [ cos(theta) 0 -sin(theta); 0 1 0 ;  sin(theta) 0 cos(theta)];

% making ellipsoid data
a = coef(1);
b = coef(2);
c = coef(3);
ne  = 32;
dt  = 2*pi/ne;
dp  = pi/ne;
t   = 0:dt:2*pi;
```

```
p   = 0:dp:pi;
n_t = max(size(t));
n_p = max(size(p));

% making ellipsoid
for it = 1:n_t
  for is = 1:n_p
    xe(n_p*(it-1)+is) = a*sin(p(is))*cos(t(it));
    ye(n_p*(it-1)+is) = b*sin(p(is))*sin(t(it));
    ze(n_p*(it-1)+is) = c*cos(p(is));
  end
end
xer = xe*RB(1,1) + ye*RB(1,2) + ze*RB(1,3);
yer = xe*RB(2,1) + ye*RB(2,2) + ze*RB(2,3);
zer = xe*RB(3,1) + ye*RB(3,2) + ze*RB(3,3);

% plot figures
% scrsz = get(0,'ScreenSize');
%     fig1=figure('Position',[scrsz]);
%     orient landscape
figure
plot(U);
ylabel('u (ms^{-1})');
xlabel('time (sampled at 1 s)');
title('Instantaneous velocity 3 July, 2006 (sampled at 1 Hz)')
scrsz = get(0,'ScreenSize');
    fig1=figure('Position',[scrsz]);
    orient landscape
subplot(211)
plot(U,'k-');
hold on
plot(index,U(index),'ro');
ylabel('u (ms^{-1})');
xlabel('time (sampled at 1 s)');
title('Instantaneous velocity 3 July, 2006 (sampled at 1 Hz)')
```

```
if option==2
    plot(U_output,'b-');
    ylabel('u (ms^{-1})');
xlabel('time (sampled at 1 s)');
title('Instantaneous velocity 3 July, 2006 (sampled at 1 Hz)')

end

subplot(212)
plot3(f,f_t,f_tt,'b*','MarkerSize',3)
hold on

plot3(F(index),F_t(index),F_tt(index),'ro','MarkerFaceColor','r','MarkerSize',5)
  plot3(xer,yer,zer,'k-');
hold off
axis equal
grid on
xlabel('u (ms^{-1})');
ylabel('\partial u/\partial t (ms^{-2})');
zlabel('\partial^2u/\partial t^2 (ms^{-3})');
%title('Instantaneous velocity 3 July, 2006 (sampled at 1 Hz)')

% scrsz = get(0,'ScreenSize');
%     fig1=figure('Position',[scrsz]);
%     orient landscape

figure
plot(U_output);
ylabel('u (ms^{-1})');
xlabel('time (sampled at 1 s)');
title('Preprocessed instantaneous velocity 3 July, 2006 (sampled at 1 Hz)')
 hold off
%pause

end
```

G.1.2 spikesRemoval.m

```
%%Points outside of ellipsoid in two-
% dimensional domain are excluded
function [U_output,V_output,W_output,Index,coeffi] = spikesRemoval(U,V,W,phi)
%=========================================================================

% Input
%   U                   : input U data
%   V                   : input V data
%   W                   : input W data
%   phi                 : angle between U and W
%
% Output
%   U_output            : excluded U data
%   V_output            : excluded V data
%   W_output            : excluded V data
%   Index               : excluded array element number in U and V
%   coeffi              : coefficients for ellipsoid

%=========================================================================

%
% --- initial setup
%

n = max(size(U));
lambda = sqrt(2*log(n));

U_output = [];
V_output = [];
```

```
W_output = [];
Index = [];

%
% --- rotate data
%

%phi = atan2(sum(U.*W), sum(U.^2) );

if phi == 0
  X = U;
  Y = V;
  Z = W;
else
  R = [ cos(phi) 0  sin(phi); 0 1 0 ; -sin(phi) 0 cos(phi)];
  X = U*R(1,1) + V*R(1,2) + W*R(1,3);
  Y = U*R(2,1) + V*R(2,2) + W*R(2,3);
  Z = U*R(3,1) + V*R(3,2) + W*R(3,3);
end

%test
%plot3(U,V,W,'b*')
%hold on
%  plot3(X,Y,Z,'r*')
%hold off
%pause

%
% --- preprocess
%

a = lambda*nanstd(X);
b = lambda*nanstd(Y);
c = lambda*nanstd(Z);
```

```
%
% --- main
%

m = 0;
for i=1:n
  x1 = X(i);
  y1 = Y(i);
  z1 = Z(i);
  % point on the ellipsoid
  x2 = a*b*c*x1/sqrt((a*c*y1)^2+b^2*(c^2*x1^2+a^2*z1^2));
  y2 = a*b*c*y1/sqrt((a*c*y1)^2+b^2*(c^2*x1^2+a^2*z1^2));
  zt = c^2* (1 - (x2/a)^2 - (y2/b)^2 );
  if z1 < 0
    z2 = -sqrt(zt);
  elseif z1 > 0
    z2 = sqrt(zt);
  else
    z2 = 0;
  end

  % check outlier from ellipsoid
  dis = (x2^2+y2^2+z2^2) - (x1^2+y1^2+z1^2);
  if dis < 0
    m = m + 1;
    Index(m) = i;
    U_output(m) = U(i);
    V_output(m) = V(i);
    W_output(m) = W(i);
  end
end

coeffi(1) = a;
coeffi(2) = b;
coeffi(3) = c;
```

G.1.3 dftm_estimator.m

```
function [DSPEC]=dftm_estimator(cpsdd,trans,wn,spec,dsp}
%INPUT:
%cpsdd= output (vector) from CPSD calculations
%trans=transfer parameters - using transfer functions;
%wn= dirsavenumber
%spec= One dimensional spectra output (e.g. calculated from the pressure data)
%dirsa= directional bins which cover the whole circle (in radians)
%itn=Number of iterations
%dsp=output progress [>2]


%OUTPUT:
%DSPEC=Data Structure containing spetral elements
%%%%%%%%%%%%%%%%%%%%%%%%

SIZ=size(cpsdd,1);
FREQS=size(cpsdd,3);
DIRR=size(trans,3);
DIRR2=8*atan(1.0)/DIRR;

if(dsp<2)
   warning off;
end

for ff=1:FREQS
   if(dsp>=1)
      disp(['calculating for frequency' blanks(1)...
 num2str(ff) ' of' blanks(1) num2str(FREQS)]);
   end
      ncpsd=cpsdd(:,:,ff);
   Sftmp=zeros(DIRR,1)+i*zeros(DIRR,1);
   for m=1:SIZ
      for n=1:SIZ
```

```
          H(1:DIRR)=trans(n,ff,1:DIRR);
         Hs(1:DIRR)=conj(trans(m,ff,1:DIRR));

          expx(1:DIRR)=exp(i*wn(m,n,ff,1:DIRR));
             xtemp=ncpsd(m,n).*H.*Hs.*expx;
             Sftmp(:)=Sftmp(:)+xtemp';


       end
   end
    E=Sftmp(:)';
   E=E./(DIRR2*sum(E));
   DSPEC(ff,:)=spec(1,ff)*E;
end
 warning on;
```

G.1.4 emep_estimator.m

```
function [DSPEC]=emep_estimator(cpsdd,trans,WN,spec,dirsa,itn,dsp)


%INPUT:
%cpsdd= output (vector) from CPSD calculations
%trans=transfer parameters - using transfer functions;
%wn= dirsavenumber
%spec= One dimensional spectra output (e.g. calculated from the presure data)
%dirs= directional bins which cover the whole circle (in radians)
%itn=Number of iterations
%dsp=output progress [VALUE > 2]


%OUTPUT:
%DSPEC=Data Structure containing spetral elements
%%%%%%%%%%%%%%%%%%%%%%%%%%
```

```
%%%%%%%%%%%%%%%%%%%%%%%%

if(dsp<2)
   warning off;
end


SIZZ=size(cpsdd,1);
FREQS=size(cpsdd,3);
DIRR=size(trans,3);

DIRR2=abs(dirsa(2)-dirsa(1));
pi=4.0*atan(1.0);

if(dsp<2)
   warning off;
end


Co=real(cpsdd);
Quad=-imag(cpsdd);

for ff=1:FREQS

   xpsx(:,:,ff)=diag(cpsdd(:,:,ff))*(diag(cpsdd(:,:,ff))');
   sigCo(:,:,ff)=sqrt(0.5*(xpsx(:,:,ff)+Co(:,:,ff).^2-Quad(:,:,ff).^2));
   sigQuad(:,:,ff)=sqrt(0.5*(xpsx(:,:,ff)-Co(:,:,ff).^2+Quad(:,:,ff).^2));
end


for ff=1:FREQS
```

```
index=0;
for m=1:SIZZ
   for n=m:SIZZ
      expx(1:DIRR)=exp(-i*WN(m,n,ff,1:DIRR));
      Hh(1:DIRR)=trans(m,ff,1:DIRR);
      Hhs(1:DIRR)=conj(trans(n,ff,1:DIRR));
      Htemp=(Hh.*Hhs.*expx);


      if(Htemp(1)~=Htemp(2))
      index=index+1;
      phi(index,ff)=real(cpsdd(m,n,ff))./(sigCo(m,n,ff)*spec(1,ff));
      H(1:DIRR,index,ff)=real(Htemp)./sigCo(m,n,ff);

         if(WN(m,n,1,1)+WN(m,n,1,2)~=0)
            index=index+1;
            phi(index,ff)=imag(cpsdd(m,n,ff))./(sigQuad(m,n,ff)*spec(1,ff));
            H(1:DIRR,index,ff)=imag(Htemp)./sigQuad(m,n,ff);
        end
      end
     end
  end
  end
  M=index;


  for eni=1:M/2+1
    cosnt(1:DIRR,1:M,eni)=cos(eni*dirsa')*ones(1,M);
    sinnt(1:DIRR,1:M,eni)=sin(eni*dirsa')*ones(1,M);
  end

  cosn=cos([1:M/2+1]'*dirsa);
  sinn=sin([1:M/2+1]'*dirsa);
```

```
  for ff=1:FREQS
     if (dsp>=1)
        disp(['calculating for frequency' blanks(1) ...
num2str(ff) ' of' blanks(1) num2str(FREQS)]);
     end
   Hi(1:DIRR,1:M)=H(1:DIRR,1:M,ff);
   Phione=(ones(size(dirsa'))*phi(1:M,ff)');

   keepgoing=1;
   n=0;
   AIC=[];


   while(keepgoing==1)
      n=n+1;

      if(n<=M/2+1)
      if(dsp>0)
           disp(strcat('model :',num2str(n)));
      end
      a1(1:n)=0.0;
      b1(1:n)=0.0;

      a2(1:n)=100.0;
      b2(1:n)=100.0;

      count=0;
      rlx=1.0;
      while(max(abs(a2(1:n)))>0.01 | max(abs(b2(1:n)))>0.01)
         count=count+1;
         Fn=(a1(1:n)*cosn(1:n,:)+b1(1:n)*sinn(1:n,:))';

         Fnexp=exp(Fn)*ones(1,M);
         PhiHF=(Phione-Hi).*Fnexp;
         Z(1:M)=sum(PhiHF)./sum(Fnexp);
```

```
    for eni=1:n
       X(eni,1:M)=Z.*(...
          (sum(Fnexp.*cosnt(:,:,eni))./sum(Fnexp) ) -...
          (sum(PhiHF.*cosnt(:,:,eni))./sum(PhiHF) )...
          );
       Y(eni,1:M)=Z.*(...
          (sum(Fnexp.*sinnt(:,:,eni))./sum(Fnexp) )-...
          (sum(PhiHF.*sinnt(:,:,eni))./sum(PhiHF) )...
          );
    end
   C(:,1:n)=(X(1:n,1:M))';
    C(:,n+1:2*n)=(Y(1:n,1:M))';

    out=C(:,1:n*2)\Z';
    out=out';

    a2old=a2(1:n);
    b2old=b2(1:n);
    a2=out(1:n);
    b2=out(n+1:2*n);
    if sum((abs(a2)-abs(a2old))>100) | ...
sum((abs(b2)-abs(b2old))>100 |count>itn)
       if(rlx>0.0625)
          rlx=rlx*0.5;
          if(dsp==2)
             disp(['relaxing computation...factor:' ...
num2str(rlx,4)]);
          end

          count=0;
          a1(1:n)=0.0;
          b1(1:n)=0.0;
       else
          if(dsp==2)
             warning('computation fully relaxed... ...
```

```
bailing out');
               end
                keepgoing=0;
                break;
            end
         else
             a1=a1(1:n)+rlx*a2;
          b1=b1(1:n)+rlx*b2;
         end
      end

      error=Z-a2(1:n)*X(1:n,:)-b2(1:n)*Y(1:n,:);

      AIC(n)=M*(log(2*pi*var(error))+1)+4*n+2;

      if(n>1)
           if((AIC(n)>AIC(n-1))| isnan(AIC(n)))
              keepgoing=0;
           end
      end



          a1held(n,1:n)=a1(1:n);
         b1held(n,1:n)=b1(1:n);
         best=n;

         if~(keepgoing)
            if(n>1)
            a1=a1held(n-1,1:n-1);
            b1=b1held(n-1,1:n-1);
            best=n-1;
            else
            a1=0.0;
            b1=0.0;
            end
```

```
            end

   else
      keepgoing=0;
   end

end
   if(dsp==2)
        disp(['best: ' num2str(best)]);
   end

   G=exp(a1*cosn(1:best,:)+b1*sinn(1:best,:))';

   SG=G/(sum(G)*DIRR2);

    DSPEC(ff,1:DIRR)=spec(1,ff)*SG';

    end

warning on;
```

G.1.5 imlm_estimator.m

```
function [DSPEC]=imlm_estimator(cpsdd,trans,wn,spec,itn,dsp)



%INPUT:
%cpsdd= output (vector) from CPSD calculations
%trans=transfer parameters - using transfer functions;
%wn= dirsavenumber
%spec= One dimensional spectra output...
 (e.g. calculated from the presure data)
```

```
%dirsa= directional bins which cover the whole circle (in radians)
%itn=Number of iterations
%dsp=output progress [>2]


%OUTPUT:
%DSPEC=Data Structure containing spetral elements
%%%%%%%%%%%%%%%%%%%%%%%%


SIZZ=size(cpsdd,1);
FREQS=size(cpsdd,3);
DIRRS=size(trans,3);

DIRR2=8*atan(1.0)/DIRRS;

if(dsp<2)
   warning off;
end


gamma=0.1;
beta=1.0;
alpha=0.1;

for ff=1:FREQS
   if(dsp>=1)
      disp(['calculating for frequency' blanks(1) ...
num2str(ff) ' of' blanks(1) num2str(FREQS)]);
  end

   for m=1:SIZZ
      for n=1:SIZZ
        H(1:DIRRS,m,n)=trans(n,ff,1:DIRRS);
      Hs(1:DIRRS,m,n)=conj(trans(m,ff,1:DIRRS));
```

```
   expx(1:DIRRS,m,n)=exp(i*wn(m,n,ff,1:DIRRS));
   iexpx(1:DIRRS,m,n)=exp(-i*wn(m,n,ff,1:DIRRS));
   Htemp(:,m,n)=H(:,m,n).*Hs(:,m,n).*expx(:,m,n);
   iHtemp(:,m,n)=H(:,m,n).*Hs(:,m,n).*iexpx(:,m,n);
end
end


invcps=inv(cpsdd(:,:,ff));
Sftmp=zeros(DIRRS,1);
for m=1:SIZZ
   for n=1:SIZZ
         xtemp=invcps(m,n)*Htemp(:,m,n);
         Sftmp(:)=Sftmp(:)+xtemp;
     end
end
Eo=(1./Sftmp(:));
kappa=1./(DIRR2*sum(Eo));
Eo=kappa*Eo;
E=Eo;
T=Eo;

for it=1:itn
   for m=1:SIZZ
     for n=1:SIZZ
         expG(m,n,:)=iHtemp(:,m,n).*E(:);
         ixps(m,n)=sum(expG(m,n,:))*DIRR2;
     end
   end
   invcps=inv(ixps);
   Sftmp=zeros(DIRRS,1);
   for m=1:SIZZ
     for n=1:SIZZ
         xtemp=invcps(m,n)*Htemp(:,m,n);
         Sftmp(:)=Sftmp(:)+xtemp;
```

```
            end
          end
          Told=T;
        T=(1./Sftmp(:));
        kappa=1./(DIRR2*sum(T));
        T=kappa*T;

        %lambda=ones(size(T))-(T./Eo)
        %ei=gamma*lambda.*E;
        ei=gamma*((Eo-T)+alpha*(T-Told));
        E=E+ei;
        kappa=1./(DIRR2*sum(E));
     E=kappa*E;


   end

   DSPEC(ff,:)=spec(1,ff)*E';
end

warning on;
```

G.1.6 variance_method.m

```
function [Reyds,RDIs]=variance_method(data_fluc,RDIs)
% function Reyds=reynoldstress(data_fluc,RDIs)
% function Reyds=uvwpc(data_fluc,RDIs)
% compute mean and variance over n-points
% preaverage m points
% oversample jn times
% all variable are in instrument coordinates
%
% Also: computes target strength using targs.m
%
```

```
% INST: instrument coordinate system, ...
where u is in direction of beam 1, v is in direction of beam 3
% EARTH: earth coordinate system
%

%INPUT:
%data_fluc= data structure containing ...
flunctuating velocities, tilt angles
%RDIs=data structure containing RDI stantdards

%OUTPUT:
%Reyds= data structure containing Reynolds...
 stress estimates and fluctuating velocities

%%%%%%%%%%%%%%%%%%%%%%%%%%%%%%%%%%%%%%%%%
%%%%%%%%%%%%%%%%%%%%%%%%%%%%%%%%%%%%%%%%%%%%%%%%%
%global pp;
maxnans = 20; %20 percent
maxnans2 = 90;
samprate = 0.5;% / (median(diff(data_fluc.time_jul))*24*3600);
RDIs=setdefv(RDIs,'get_hscale',0); ...
 %sets this default if field not found
RDIs=setdefv(RDIs,'shear_average',15);
RDIs=setdefv(RDIs,'SD_wavespex',0);

% density of water
rhow=1025;
F=data_fluc.freq;
 %acoustic frequency, used for calculating sound absorption...
 -- very important to normalizing TS computation
S=35;   %salinity, used for calculating sound absorption...
 -- somewhat important to normalizing TS computation
P=10;   %pressure, used for calculating sound absorption, ...
though relatively unimportant in the computation
dz=diff(data_fluc.z(1:2));
```

```
% convert to local variable
beamangle=RDIs.beamangle;
n=RDIs.timeaverage;
jn=RDIs.timeoversample;


disp(' Getstress: compute Reynolds Stress')

% size of arrays
[len,wid]=size(data_fluc.rb1);
n2=fix(n/jn);
in=fix((wid-n+n2)/n);

% detect empty files
if in<1, disp('time series too short'), return, end

% loop over beams to get along beam mean and variance
for nb=1:4
   disp(['  variance for beam: ',int2str(nb)])
   eval(['xv=data_fluc.rb',int2str(nb),'v;']); xv=xv';
   %transposing variables so that we can take mean ...
and variance along columns (time) later
   eval(['x=data_fluc.rb',int2str(nb),';']);   x=x';

%   [len,wid]=size(xv');
% loop over bins
   for i=1:len
% loop over subsample
      for j=1:jn
         ii=j:jn:in*jn;
         xmv(:,ii)=reshape(xv([1:(in*n)]+(j-1)*n2,i),n,in);
         xm(:,ii)=reshape(x([1:(in*n)]+(j-1)*n2,i),n,in);
      end
      y(i,:)=meannan2(xm([1:n2]+floor((n-n2)/2),:),maxnans);
```

```
      [m2(i,:) m3(i,:)]=filtmom(xmv,fix(n*RDIs.var_omit),RDIs.timepolyfilt);
      if RDIs.get_hscale,
        for k=1:size(xmv,2);
          C=filtacf(xmv(:,k),round(n/2),fix(n*RDIs.var_omit));
          R(i,k,nb)=sum(C)/2/samprate;
            %for lengthscale (see below) - ...
integrate autocorrelation function from time 0 to n
%          figure; plot(-n/2:n/2,C,'.'); title(['height: '...
,num2str(data_fluc.z(i)),'m  R: ',num2str(R(i,k,nb))]); pause;close
        end
      end
    end
   eval(['Reyds.rb',int2str(nb),'=y;'])
   eval(['Reyds.rb',int2str(nb),'_m2=m2;'])
   eval(['Reyds.rb',int2str(nb),'_m3=m3;'])
end


% compute 1st bin reynolds stress directly from covariance...
 in U and V, for cross-comparison
x=data_fluc.u_earth(1,:); y=data_fluc.v_earth(1,:); z=data_fluc.w(1,:);
for j=1:jn
   ii=j:jn:in*jn;
   xm(:,ii)=reshape(x([1:(in*n)]+(j-1)*n2),n,in);
   ym(:,ii)=reshape(y([1:(in*n)]+(j-1)*n2),n,in);
   zm(:,ii)=reshape(z([1:(in*n)]+(j-1)*n2),n,in);
end; clear x y
Reyds.taux1_earth = -filtvar2(xm,zm,fix(n*RDIs.var_omit),...
RDIs.timepolyfilt) * rhow;
   %estimate of taux1 as calculated directly from mean(U' V')
Reyds.tauy1_earth = -filtvar2(ym,zm,fix(n*RDIs.var_omit),...
RDIs.timepolyfilt) * rhow;


%compute mean squared shear, for instability analyses...
```

```
 (e.g. Richardson number)
%   as in Peters, 1999 , but with xx-sample ...
temporal averaging (xx is RDIs.shear_average)
xx=RDIs.shear_average;  %
us_earth=boxfilt(data_fluc.u_earth',xx)';
vs_earth=boxfilt(data_fluc.v_earth',xx)';
dudzs_earth=gradient(us_earth',dz)';
dvdzs_earth=gradient(vs_earth',dz)';
x=dudzs_earth'.^2;
y=dvdzs_earth'.^2; clear us_earth vs_earth ...
dvdzs_earth dudzs_earth xm ym xa ya
for i=1:len
   for j=1:jn
      ii=j:jn:in*jn;
      xm(:,ii)=reshape(x([1:(in*n)]+(j-1)*n2,i),n,in);
      ym(:,ii)=reshape(y([1:(in*n)]+(j-1)*n2,i),n,in);
   end
   xa(i,:)=meannan2(xm([1:n2]+floor((n-n2)/2),:),maxnans);
   ya(i,:)=meannan2(ym([1:n2]+floor((n-n2)/2),:),maxnans);
end
Reyds.dudz2=xa+ya;
clear x y


% process target strength data
x=data_fluc.ts';
iindex=1:wid;
%range-normalization is further below, after averaging...
for i=1:len
   for j=1:jn
      ii=j:jn:in*jn;
      tim(:,ii)=reshape(data_fluc.time_jul([1:(in*n)]+(j-1)*n2),n,in);
      index(:,ii)=reshape(iindex([1:(in*n)]+(j-1)*n2),n,in);
      xm(:,ii)=reshape(x([1:(in*n)]+(j-1)*n2,i),n,in);
   end
```

```
   y(i,:)=meannan2(xm([1:n2]+floor((n-n2)/2),:),maxnans);
end
Reyds.ea=y; %y is TS here - swapping

%get average depth for each period (skipping nans)
if existf(data_fluc,'depth'),
   for c=1:in*jn;
      ii=(1:n)+(c-1)*round(n/jn);
%      plot(data_fluc.depth(ii),'k.');...
 title([num2str(100*length(find(isnan(data_fluc.depth(ii)))))...
/length(ii)),' percent bad depths']); pause
      depthf=data_fluc.depth(ii)'; mdepth=meannan(depthf);
sdepth=stdnan(depthf);
      bad=find(depthf<mdepth-2*sdepth | depthf>mdepth+2*sdepth);
 depthf(bad)=nan;
      depthstdf=data_fluc.depthstd(ii); depthstdf(bad)=nan;
%      plot(data_fluc.depth(ii),'r.'); ...
hold on; plot(depthf,'k.'); pause; clf
      Reyds.depth(c)=meannan2(depthf,maxnans2);
 Reyds.depthstd(c)=meannan2(depthstdf,maxnans2);
   end
end

if RDIs.SD_wavespex, getwavedata; end


% save time pitch roll heading
Reyds.time_jul=meannan(tim);
Reyds.ii=round(meannan(index));
Reyds.rol=data_fluc.rol(Reyds.ii);
Reyds.pit=data_fluc.pit(Reyds.ii);
Reyds.hdg=data_fluc.hdg(Reyds.ii);
Reyds.temp=data_fluc.temp(Reyds.ii);
Reyds.xmc=data_fluc.xmc(Reyds.ii);
```

```
% rotate bottom bin stress back to instrument coordinates
[Reyds.taux1_inst,Reyds.tauy1_inst]=...
uvrot(Reyds.taux1_earth,Reyds.tauy1_earth,-Reyds.hdg);

Reyds.z=data_fluc.z;
%ea_sise=size(Reyds.ea)
%tj_size=size(Reyds.time_jul)
%z_size=size(Reyds.z)

Reyds.ts=real(targs(Reyds.ea,meshgrid(Reyds.z,Reyds.time_jul)',...
.5,80,2,adp_sndabs(F,S,P)));

% compute Reynolds stress using the variance method
dz=diff(Reyds.z(1:2));
Reyds.taux_inst=(Reyds.rb2_m2-Reyds.rb1_m2)/(2*sind(2*beamangle))*rhow;
 %note the trig property:  sin(2*a)=2*sin(a)*cos(a)
Reyds.tauy_inst=(Reyds.rb4_m2-Reyds.rb3_m2)/(2*sind(2*beamangle))*rhow;
 %no negative in equation -- our convention is for tau to be positive
 %...
if it represents an upward flux of upriver momentum
Reyds.S=(Reyds.rb1_m2+Reyds.rb2_m2+Reyds.rb3_m2+Reyds.rb4_m2)/(4*sind(beamangle).^2)
...
  %S is related to TKE, see Lu and Lueck  99b eq.3 OR Stacey et al,...
 1999a Eqs 7a,7b
Reyds.K3=(Reyds.rb1_m3+Reyds.rb2_m3+Reyds.rb3_m3+Reyds.rb4_m3);...
 %related to turb diffusion of TKE - see Stacey 2003 Eqs. 13,24


Reyds.u_inst=(Reyds.rb2-Reyds.rb1)/(2*sind(beamangle));
Reyds.v_inst=(Reyds.rb4-Reyds.rb3)/(2*sind(beamangle));
Reyds.wv_inst=(-Reyds.rb4-Reyds.rb3)/(2*cosd(beamangle));
Reyds.wu_inst=(-Reyds.rb2-Reyds.rb1)/(2*cosd(beamangle));

if RDIs.get_hscale,
  %compute the horizontal lengthscale of Stacey et al. 1999a
```

```
  for c=1:4,
 lambda_ix(:,:,c)=hypot(Reyds.u_inst,Reyds.v_inst).*R(:,:,c);...
 lambda_iy(:,:,c)=hypot(Reyds.u_inst,Reyds.v_inst).*R(:,:,c); end ...
%taylor frozen turb, with SPEED
  lambda_uwx=abs(Reyds.rb2_m2.*lambda_ix(:,:,2)...
-Reyds.rb1_m2.*lambda_ix(:,:,1)) ./ (2*sind(2*beamangle)....
*hypot(Reyds.taux_inst,Reyds.tauy_inst)/rhow);
  lambda_vwy=abs(Reyds.rb4_m2.*lambda_iy(:,:,4)-Reyds.rb3_m2.*...
lambda_iy(:,:,3)) ./ (2*sind(2*beamangle).*...
hypot(Reyds.taux_inst,Reyds.tauy_inst)/rhow);
  Reyds.lambda=sqrt(lambda_uwx.^2 + lambda_vwy.^2);
end

dt=diff(Reyds.time_jul(1:2))*24*3600;

[Reyds.dudz_inst]=gradient(Reyds.u_inst',dz)';
%used for computing P and Kz
[Reyds.dvdz_inst]=gradient(Reyds.v_inst',dz)';

Reyds.Px_inst=Reyds.taux_inst.*Reyds.dudz_inst;
Reyds.Py_inst=Reyds.tauy_inst.*Reyds.dvdz_inst;
Reyds.P=Reyds.Px_inst+Reyds.Py_inst;
%Equation (3) of Lu et al 2000 JPO 30:855, ...
yet multiplied by rhow to have units of   W / m^3

Reyds.kz=(Reyds.taux_inst./Reyds.dudz_inst ...
+ Reyds.tauy_inst./Reyds.dvdz_inst)/rhow;

%Loads all subsets and joins them together in a full dataset.
...  Processes data
%  further (rotations, etc.) and makes several calculations.  ...
```

```
Smoothes ending
%  variables.
%
%%%%%%%%%%%%%%%%%%%%%%%%%%%%%%%%%%%%%%%%%%%%%%%%%%%%%%%%%%%%%%%%%%%%%%%%%%%%
rhow=1025;
if exist('pp')==0, load subset-1 p; pp=p; end

loadall
dz=diff(da.z(1:2));
[len,wid]=size(da.taux_inst);

if wid>10

disp(['rotate velocity (and stress) onto velocity principal axis... '])
%Rotate stress and velocity using determination of velocity principal axis
%NOTE that velocities here are already in earth coordinates, ...
yet stresses and shears are in beam coordinates.
%First, rotate earth velocities so that x-axis is ...
along principal axis of velocities
clear i;  %just a precaution to avoid surprising errors ...
- i is sqrt(-1) and set aside for complex numbers
nn=pp.izrot;
[da.theta_princax,maj,min,wr]=princax(da.u_earth(nn,:)+...
da.v_earth(nn,:)*i);  %rotates using data from height index
      %pp.izrot....
  theta is CCW from east - math convention
%Second, rotate every ensemble of velocity, stress and shear to ...
this principal axis (accounting for variable heading)
earth2paxis=repmat(da.theta_princax,size(da.u_earth)); ...
%x-axis points into direction of maximum velocity variance,...
 keeping right-handed coordinate frame
[da.u,da.v]=uvrot(da.u_earth,da.v_earth,earth2paxis);
inst2paxis=repmat(da.theta_princax+da.hdg,[length(da.z) 1]);
 %x-axis points into direction of maximum velocity variance,...
 keeping right-handed coordinate frame
```

```
[da.taux,da.tauy]=uvrot(da.taux_inst,da.tauy_inst,inst2paxis);
[da.taux1,da.tauy1]=uvrot(da.taux1_inst,da.tauy1_inst,inst2paxis(1,:));

[da.dudz]=gradient(da.u',dz)';
[da.dvdz]=gradient(da.v',dz)';

fprintf(['remove shear values below ',num2str(pp.minshear)]);
dz=diff(da.z(1:2));

disp('recalculate production and eddy viscosity using new shear data')
shear2 =(da.dvdz.^2 + da.dudz.^2);
da.P = (da.taux.*da.dudz + da.tauy.*da.dvdz);
 %units- W/m3 (TKE Production)
da.kz = (da.taux./da.dudz + da.tauy./da.dvdz)./rhow;
 %units- m2/s
da.Ee=da.taux.*da.dudz;
beamangle=20; alpha=1.5;
%doS=(do.rb1_m2+do.rb2_m2+do.rb3_m2+do.rb4_m2)...
/(4*sind(beamangle).^2);
%da.S=(doS)/(1+Zxx*( (2*cotd(beamangle).^2)-1)) ;

da.S=(do.rb1_m2+do.rb2_m2+do.rb3_m2+do.rb4_m2)/(4*sind(beamangle).^2);
%TKE density
gamma=(1/(1+alpha))*(1+( (2*alpha)/(tan(20)^2)  ) );
da.q=sqrt( (2*da.S)./gamma   );

bad=find(da.kz<0.000001); da.kz(bad)=ones(size(bad)).*0.000001;

disp('compute Prandtl mixing length scale l_m')
da.l_m=sqrt(sqrt(da.taux.^2+da.tauy.^2)./rhow./shear2);

disp('compute and filter various bedstresses and u_* by...
 extrapolating Reynolds stress data to the bed');
 % (from lowest bin up to [pp.ustarcalc_datarange]
dr=1:pp.ustarcalc_datarange;
```

```
for c=1:wid,
   P=polyfit(da.z(dr),sqrt(da.taux(dr,c).^2 + da.tauy(dr,c).^2),1);
   Q=polyfit(da.z(dr),da.taux(dr,c),1);
   da.taub(c)=P(2); da.taux0(c)=Q(2);
    %taux0 is the alongchannel component
   %figure(3); plot(abs(da.tauy_r(:,c)),da.z,'o'...
,[0 6]*P(c,1)+P(c,2),[0 6],'r-');
title(['V_{100}=',num2str(da.v_r(1,c)),'
   U*=',num2str(ustar(c),3)]); pause
end
da.ustar=sqrt(da.taub./rhow); %friction or shear velocity


else
disp(' too few data')
end

%remove_badtilts
da.ds=da.time_jul-2440000+datenum(1968,5,23,0,0,0);


save allresults -v7.3
return

%================================
function [ur,vr]=uvrot(u,v,rot);
% [ur,vr]=rotate(u,v,rot);
% rotate velocity vector clockwise
% by angle rot in deg -- ...
either be a scalar or matrix of size(u)
rot=-rot*pi/180;
cr=cos(rot);
sr=sin(rot);
ur=u.*cr-v.*sr;
vr=u.*sr+v.*cr;
```

G.1.7 tke_idm.m

```
function [epsilo]=tke_idm(east,north,vert,adcpheight)
%program to calculate a value epsilon...
 (TKE dissipation rates) using the Inertial Dissipation

%INPUT:
%east= adcp east-west velocity data
%north=adcp north-south velocity data
%vertadcp vertical velocity data
%adcpheight=adcp height above bed

%OUTPUT:
%epsilo=TKE dissipation estimates

[xa,xb]=size(east);
for i=1:xb
    cross=east(:,i);
    long=north(:,i);
    vertical=vert(:,i);
    B1=east(:,i);
    adcpheight=1.63;

    cross(isnan(cross))=0;
    long(isnan(long))=0;
    vertical(isnan(vertical))=0;
    B1(isnan(B1))=0;

    a=nanmean(cross);
    b=nanmean(long);
    c=nanmean(vertical);
    %[VelMag,VelDir]=UVtoSpDir(east,north);
    %magvel=(a.^2+b.^2+c.^2).^.5;
```

```
    magvel=nanstd(B1);
    urmsB1=nanstd(B1);



    % Calcualte spectrum of vertical time series
        [p,f]=psd(B1,512,256,512,8);

        %Calculaate predicted limits on inertial subrange

            f1=magvel/adcpheight;
            f2=2.3*magvel/(2*pi*.055);

            g=256;
            p=p(:,1)/4;
            ef1=(ceil(f1*64))+1;
            ef2=(floor(f2*64))+1;

            if ef2>g
                ef2=g;
            end



            alpha=.69;

            meanfreq=mean(log10(f(ef1:ef2)));
            meanphi=mean(log10(p(ef1:ef2)));
            logconst=(meanphi)+ (5/3)*(meanfreq);
            [VelMag,VelDir]=UVtoSpDir(east,north);
            %VelMag=(cross.^2+long.^2+vertical.^2).^.5;
            %EE= ((10^(logconst) * ((2*pi)/magvel)^(2/3)/.69)^.5  )^(3/2);
            epsilo(:,i)= ((10^(logconst) *...
 ((2*pi)./nanstd(east,0,2) ).^(2/3)./.69).^.5  ).^(3/2);
end
```

G.1.8 tke_2sfm.m

```
function [epsilo]=tke_2SFM(east)

%INPUT:
%east= adcp east-west velocity data

%OUTPUT:
%epsilo=TKE dissipation estimates

uux=east;
uum=nanmean(east,2);

[ax,bx]=size(uux);
for i=1:bx
    xx1(:,i)=uux(:,i)-uum;
end


%xx1=uu1;
%xx1=rand(45,60);
[n,m]=size(xx1);
% aa=xx1([2:2:end],:);
% bb=xx1([1:2:end],:);
N=0;
%xx1=detrend(xx1);
for i=1:n
    for j=2:m-1
        if (isodd(i)==0) || (i)<=n  || (j+(N+1))<m
            hhg=xx1(i,j+1)-xx1(i,j-1);

        elseif (isodd(i)==1) || (j+(N+1))<m || ...
```

```
i<n || (j-(N+1))<0
            hhg=( xx1( i , (j+(N+1)))- ...
xx1(i, (j-N) ) ) + (xx1(i,(j+N ))) - xx1(i,(j-(N+1)));
        else

            hhg=NaN;
        end
        C=2.1;
        [x,y]=size(hhg);
        r=1:x;
        DD1(i,j)=(hhg/(C.*r.^(2/3))).^(3/2);

        N=N+1;
    end
end
end
```